Imperial College London

Department of Mechanical Engineering

Phosphorescent thermal history sensors for extreme environments

Álvaro Yáñez González

Submitted in part fulfilment of the requirements for the degree of Doctor of Philosophy in Mechanical Engineering of Imperial College London and the Diploma of Imperial College London

September 2015

DECLARATION OF ORIGINALITY

I, Álvaro Yáñez González, certify that the thesis entitled "Phosphorescent thermal history sensors for extreme environments" and the work presented herein are my own and any information derived from published or unpublished work of others has been properly acknowledged and a list of references is provided at the end of the thesis.

COPYRIGHT DECLARATION

ABSTRACT

The measurement of the surface temperature of many components in gas turbines has become increasingly important as the firing temperature raises to improve thermal efficiency and reduce CO_2 emissions. Traditional methods to measure temperatures in real time, such as thermocouples or pyrometers, are sometimes not suitable and an alternative must be sought. Thermal history sensors record the maximum temperatures reached during operation, which can then be measured after the engine has cooled down. Currently, temperature sensitive paints are mainly used to obtain temperature profiles on gas turbine components but they present some limitations such as subjectivity of the measurement, poor resolution and toxicity. Permanent changes in the optical properties of thermographic phosphors have been proposed as an alternative to record temperatures and can potentially overcome some of the difficulties associated with traditional paints.

The changes in the optical properties of some europium doped phosphors after oxidation can be used to sense temperatures up to 1400 °C. The oxidation mechanism of $BaMgAl_{10}O_{17}$:Eu are investigated in detail by means of standard material characterisation techniques and laser induced phosphorescence. Variations in the luminescence properties of the phosphor (intensity ratio and lifetime decay) are related to microstructural and chemical changes and permitted to measure temperatures in the range 700 - 1200 °C. The influence of practical factors that can affect the measurement accuracy and sensitivity are thoroughly characterised. These include the energy fluence used for excitation, duration of the exposure at high temperatures, dopant concentration, time spent during cooling down, composition of the atmosphere during the heat treatment and particle size. The reversibility of the changes in the optical properties of the phosphor is studied by applying a heat treatment in a reducing atmosphere, and thus reusability of the sensor demonstrated.

The development of a coating made of this phosphor is explored for the first time with regards to its application as a sensor. The difficulties to manufacture such a coating are mainly related to the complex stoichiometry and high processing temperature of the phosphor material. $BaMgAl_{10}O_{17}$:Eu coatings onto metallic substrates are manufactured by the screen printing method. In these coatings, diffusion of elements from the substrate undesirably affects the optical properties of the sensor after exposure to high temperatures. The use of a diffusion

barrier permits to perform temperature measurements at temperatures up to 1100 °C comparable to the powder material.

Thermal gradients across the ceramic coating can drastically affect the accuracy of the temperature measurements performed by using luminescence. Investigations in thermal barrier coating sensors in controlled gradient conditions are performed that permit evaluation of the temperature error introduced by these gradients. Comparison of experimental data and a theoretical model indicates that significant temperature measurement errors can be expected in BAM:Eu coatings when a thermal gradient is present.

PUBLICATIONS

The work conducted during the PhD and presented in this thesis is associated with the following publications.

Journal Publications

1. Yáñez González, Á., Ruiz Trejo, E., van Wachem, B., Skinner, S., Beyrau, F., Heyes, A.L., *A detailed characterization of $BaMgAl_{10}O_{17}$:Eu phosphor as a thermal history sensor for harsh environments*, Sensors and Actuators A: Physical, **234** 339-345 (2015) [1].

2. Yáñez González, Á., Pilgrim, C.C., Feist, J.P., Sollazzo, P.Y., Beyrau, F., Heyes, A.L., *On-line temperature measurement inside a thermal barrier sensor coating during engine operation*, Journal of Turbomachinery, **137**(10) 101004-101004, (2015) [2].

3. Yáñez González, Á., Skinner, S., Beyrau, F., Heyes, A.L., *Reusable thermal history sensing via oxidation of a divalent rare earth ion based phosphor synthesized by the sol-gel process*, **36**(14-15) 1275-1281, (2015) [3].

Conference proceedings

4. Yáñez González, Á., Ruiz Trejo, E., van Wachem, B., Skinner, S., Beyrau, F., Heyes, A.L., *Development of an optical thermal history sensor based on the oxidation of divalent rare earth ion phosphor.* Proceedings of the 14th UK Heat Transfer Conference, Edinburgh, UK, 2015 [4].

5. Araguas Rodriguez, S., Feist, J.P., Pilgrim, C.C., Berthier, S., Biswas, K., Skinner, S., Yáñez González, Á., Heyes, A.L., *Luminescent Thermal History Sensors: Fundamentals and Applications for Thermal Profiling*, NATO AVT Symposium, Rzeszów, Poland, 2015 [5].

6. Yáñez González, Á., Pilgrim, C.C., Feist, J.P., Sollazzo, P.Y., Beyrau, F., Heyes, A.L., *On-line temperature measurement inside a thermal barrier sensor coating during engine operation*, ASME Turbo Expo 2014, Düsseldorf, Germany, 2014 [6].

7. Yáñez González, Á., Skinner, S., Beyrau, F., Heyes, A.L., *A reusable thermal history sensor based on the oxidation of a divalent rare earth ion based phosphor synthesized*

by the sol-gel process, IET & ISA 60th International Instrumentation Symposium, London, UK, 2014 [7].

8. Yáñez González, Á., Pilgrim, C.C., Sollazzo, P.Y., Heyes, A.L., Feist, J.P., Nicholls, J.R., Beyrau, F., *Temperature Sensing inside Thermal Barrier Coatings using Phosphor Thermometry*, IET & ISA 60th International Instrumentation Symposium, London, UK, 2014 [8].

9. Yáñez González, Á., Skinner, S., Beyrau, F., Heyes, A.L., *Optical Thermal History Sensing via Oxidation of Divalent Rare Earth Ion Based Phosphors Synthesized by the Sol-Gel Process*, Proceedings of the 13th UK Heat Transfer Conference, London, UK, 2013 [9].

NOMENCLATURE

APS – Atmospheric Plasma Spray

BAL – $Ba_{0.75}Al_{11}O_{17.25}$

BAM – $BaMgAl_{10}O_{17}$

BR – Beever-Ross

CCD – Charge-Coupled Device

CTE – Coefficient of Thermal Expansion

CVD – Chemical Vapour Deposition

DTA – Differential Thermal Analysis

EBPVD – Electron Beam Physical Vapour Deposition

ECCP – European Climate Change Programme

EDS – Energy Dispersive x-ray Spectroscopy

emf – electromotive force

EPD – Electrophoretic deposition

ESM – Exponential Series Method

ESR – Electron Spin Resonance

ICDD – International Centre for Diffraction Data

KJMA – Kolmogorov-Johnson-Mehl-Avrami

MEM – Maximum Entropy Method

MOS – Metal Oxide Semiconductor

PDP – Plasma Display Panel

PIV – Particle Image Velocimetry

PLD – Pulsed Laser Deposition

PMT – Photomultiplier tube

PVD – Physical Vapour Deposition

REACH – Regulation on Registration, Evaluation, Authorisation and Restriction of Chemicals

SAE – $SrAl_{14}O_{25}$

SCS – Sensor Coating Systems Ltd.

SEM – Scanning Electron Microscope

SOFC – Solid Oxide Fuel Cells

SSZ – Scandia-stabilised Zirconia

SVHC – Substances of Very High Concern

TBC – Thermal Barrier Coating

TGA – Thermogravimetric Analysis

VUV – Vacuum Ultraviolet

XANES – X-Ray Absorption Near Edge Structure

XPS – X-ray Photoelectron Spectroscopy

XRD – X-Ray Diffraction

YAG – $Y_3Al_5O_{12}$

YSZ – Y_2O_3-stabilised ZrO_2

ρ – Intensity ratio

ACKNOWLEDEMENTS

back home (María, Mary, Juan Carlos, Carlos, Pablo and many others) because your support and confidence have made this work possible.

I owe a big thank you to Lidia, who has been the pillar that held me in the difficult moments. Thank you for your patience and being always there to take care of me.

Finally, I would like to express my deepest gratitude to my family, who supported me to begin this adventure and were always eager to help.

CONTENTS

LIST OF FIGURES

LIST OF TABLES

1. INTRODUCTION

1.1. The importance of temperature in gas turbines

Gas turbines have been in continual development since the early 1900s and have found applications in various fields, which include power generation, shaft power and vehicle propulsion. In each of these fields the design criteria of the gas turbine may be different, but it is always a common objective to achieve the maximum efficiency. This has become even more important in recent years as greenhouse gas emission and energy efficiency policies have been implemented such as the European Climate Change Programme (ECCP).

Despite the increased use of renewable sources of energy, gas turbines are going to continue to be an important source of power generation in the next few decades due to the flexibility of their operation, which makes them a backup technology for variable renewable energy sources. New capacity of gas-fired plants is also planned to be installed in the next few decades according to predictions in the UK [10] and in the European Union [11]. Additionally, the jet engine market will continue to grow in the foreseeable future as emerging economies demand more air transport and low-cost carriers expand.
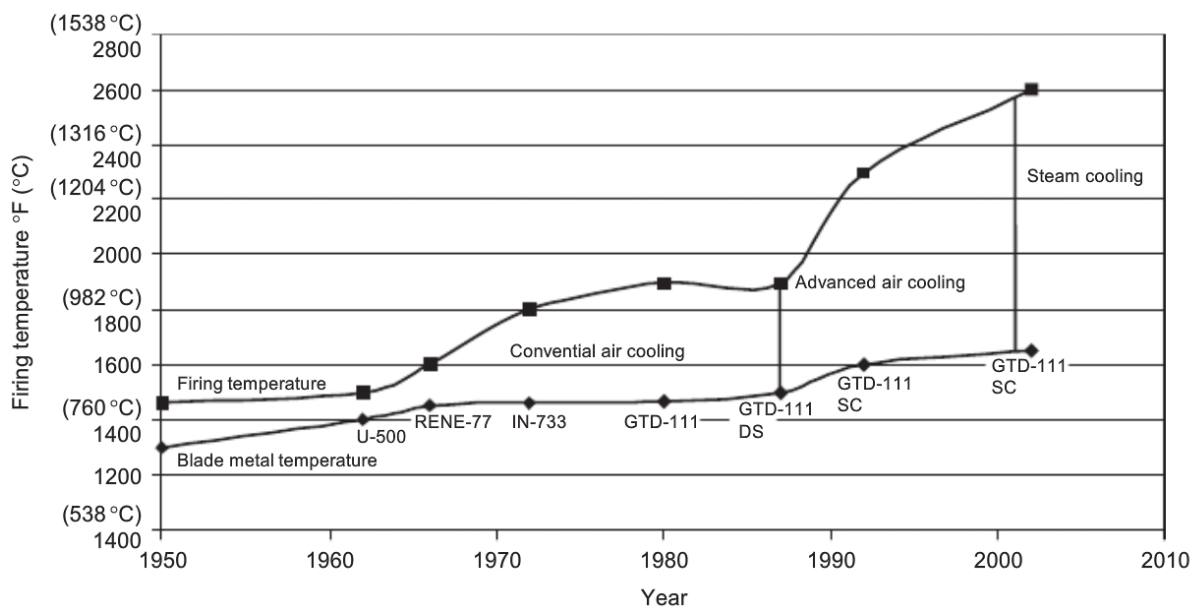
Figure 1.1. Evolution of the metal and firing temperatures in gas turbines over the past 50 years. Reproduced from [12].

Simple cycle gas turbine efficiency has increased from about 15 % for the first available designs to more than 45 % [12]. Although many design improvements have contributed to

this increase, the simultaneous increase in the pressure ratio and firing (or turbine inlet) temperature has played a predominant role. For example, an increase of 56 °C in the firing temperature raises efficiency by approximately 2 - 4 % [12], and every percentage increase in efficiency can save up to $200,000 in fuel every year for a simple-cycle 40 MW gas turbine [13].

The firing temperature has been the principal factor to limit efficiency due to the survivability of the metallic components in the first stage of the turbine. The turbine blades in this first stage are exposed to the most severe conditions of stress, temperature and corrosion; and this makes the design of their constituent materials a great challenge. The development of new alloys (such as U-500, IN-733, GTD-111 [14] in Figure 1.1) with higher temperature capabilities and corrosion resistance permitted the increase of the blade metal temperature over the years, as indicated in the figure. Additionally, the implementation of complex air and steam cooling systems in combination with protective coatings creates a temperature gradient from the gases to the metallic components that has permitted a progressive increase of the firing temperature while maintaining the metallic components at an acceptable temperature. This can be observed in Figure 1.1 by the progressive separation between the blade metal temperature and the firing temperature.

The protective coatings, also known as thermal barrier coatings (TBCs), were first introduced in the 1950s and are now widely used in the gas turbine industry. They consist normally of two layers: a bond coat (typically a platinum aluminide or a MCrAlY alloy), which protects the metal from oxidation and corrosion; and a ceramic top layer (normally made of 7 wt.% Y_2O_3-stabilized ZrO_2 or 7YSZ), which maintains a temperature gradient from the gas to the metal due to the low thermal conductivity of the ceramic material. This temperature difference could be greater than 100 °C when used in combination with internal cooling systems [15, 16]. The degradation and failure of TBCs is affected by several factors such as oxidation of the bond coat, thermal cycling stresses, creep, sintering and phase instabilities of the ceramic layer [17], all of which are dependent on the temperature experienced. However, the main cause of TBC failure is related to the temperature at the interface between the bond coat and the ceramic layer, such that an increase of 51 °C of that temperature reduces by a factor of six the life of the coating [18].

Monitoring the turbine temperature is therefore important to maximise the efficiency while maintaining the lifetime of the components. For example, the measurement of the exhaust gas

temperature is useful to avoid overheating of the turbine elements and is normally measured using thermocouples [12]. The measurement of the inlet temperature of the turbine would be important too because it provides more accurate information about the performance of the turbine, but it is complicated to measure it directly using intrusive methods such as thermocouples. This is because any broken piece of equipment upstream can cause severe damage when it passes through the turbine blades [12]. Manufacturers are also interested in obtaining profiles of the maximum temperatures experienced during operation by some of the turbine components, such as turbine blades or nozzle guide vanes. These temperature maps would be useful to detect hot spots and can serve as an input to develop or validate numerical models.

The harsh environment and extreme conditions present in gas turbines make temperature measurements very challenging. In the following sections a brief review of the main available methods used to measure temperatures in gas turbines is provided.

1.2. On-line temperature measurements

On-line temperature measurements provide real time information about temperature while the system is in operation, which is useful to control performance and for condition monitoring systems. In the following sections on-line temperature measurement techniques are briefly discussed.

1.2.1. Thermocouples

Thermocouples are temperature sensors based on the Seebeck effect, by which an electromotive force (emf) is generated in a conductor when it experiences a temperature gradient. As indicated in Figure 1.2, thermocouples generally consist of two wires made of distinct materials in contact at one end (measuring junction) and connected to a voltmeter at the other end so that the generated emf can be measured. Because the emf depends on the temperature at both ends of the conductors, the temperature at a reference junction must be known in order to accurately obtain the absolute temperature at the measurement junction. In such cases the temperature at the reference junction is controlled and copper wires are used to connect the reference junction to the thermocouple reader. However, thermocouples are normally connected directly to the instrument and a correction is applied for the cold junction temperature.
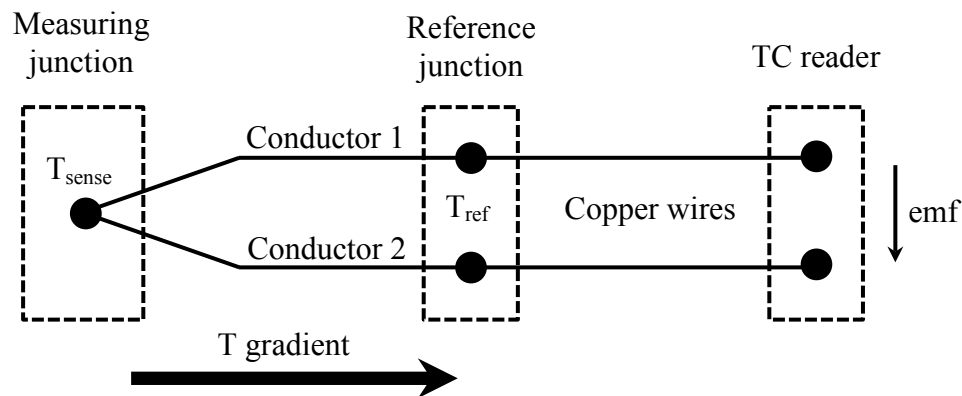
Figure 1.2. Scheme of the typical configuration of a thermocouple measuring a point temperature (T_{sense}) and connected through a reference junction (T_{ref}) to a reader.

Thermocouples are widely used in industry and their constituent materials and electrical output standardised. They are generally inexpensive and can be used in a wide range of temperatures from -250 °C to 2600 °C. K-type (nickel-chromium vs nickel-aluminium) is the most common thermocouple used for general purpose applications up to 1100 °C, and the measurement uncertainty can be as low as 0.4 %. The N-type thermocouple (nickel-chromium-silicon vs nickel-silicon-magnesium) shows an improved performance compared to other thermocouples. It has a superior oxidation resistance, improved repeatability in the temperature range where K-type thermocouples present hysteresis induced by magnetic or structural inhomogeneities and does not suffer from long-term drifts associated with exposure to high temperatures. Therefore, it can be used to higher temperatures (~ 1280 °C) than K-type. Other thermocouples, based on platinum-rhodium alloys (types R, S and B), can measure higher temperature ranges up to 1600 °C but they have lower sensitivity and are more expensive. Even higher temperatures up to 2600 °C can be measured by tungsten-rhenium thermocouples, but there are no officially recognised standards for this type of thermocouple [19].

There are some disadvantages associated with the use of thermocouples. They are intrusive, which means that their environment is modified during the measurement. For example, sub-surface thermocouples embedded in a hole perturb the surrounding temperature field due to the different thermal properties of the thermocouple compared to the component in which they are embedded. As a result, the temperature recorded by the thermocouple can deviate several degrees from the real undisturbed surface temperature [20]. Numerical models can be used to study this deviation [21, 22]. Furthermore, the exact location of the thermocouple

junction is difficult to know exactly and small errors in its location can lead to large measurement errors, especially when thermal gradients exist across the component.

Thermocouples can be mounted directly on the surface of the component, for example platinum based thermocouples can be deposited as thin films by sputtering on the surface of the blades [20]. In this case they similarly affect the local temperature due to conduction across the wires (fin effects), which can lead to large measurement errors [23]. The installation of this type of thermocouples is complex and costly due to the equipment necessary for the thin film deposition. Additionally, errors arise from differences in the generated emf between standard thermocouple tables and the deposited films, which is due to differences between the properties of the deposited film and the bulk material [20].

Finally, thermocouples provide point measurements so multiple sensors are required to obtain surface temperature maps. This further increases the complexity and cost of the set-up necessary to obtain temperature profiles on gas turbine components.

1.2.2. Pyrometers

Pyrometers are optical devices used to carry out on-line surface temperature measurements. They collect, in a given wavelength range, the electromagnetic radiation emitted by a body at temperatures above 0 K, and then produce an electrical output proportional to the irradiance. This irradiance is wavelength and temperature dependent according to Planck's law:

$$E(\lambda, T) = \varepsilon(\lambda, T) \frac{2hc^2}{\lambda^5} \frac{1}{e^{\frac{hc}{\lambda k_B T}} - 1}$$
(1.1)

Where E is the spectral radiance (W·m^{-3}), ε the spectral emissivity, h the Planck's constant (J·s), c the speed of light (m·s^{-1}), k_B the Boltzmann's constant (J·K^{-1}), λ the wavelength (m) and T the absolute temperature (K).

Pyrometers are non-intrusive and thus they do not affect the environment where the temperature measurement is performed. They offer a fast measurement response and there is no theoretical limit to the maximum sensing temperature. Pyrometers are therefore suitable to perform blade temperature measurements in the first stages of the turbine but present some challenges [24]. They need optical access to the components, which requires additional design considerations for gas turbine manufacturers. In addition, the environment in the first stages is such that pyrometers are subjected to multiple sources of uncertainty. These include: secondary radiation reflected from other elements such as nozzle guide vanes and the

combustor; selective absorption of radiation by the combustion gases; emission from these gases and presence of soot, particles or flames in the optical path [24].

Furthermore, as shown in Equation (1.1), the emissivity of the emitting surface at a particular wavelength and temperature must be known in order to correctly calculate the temperature. This emissivity has a value between 0 (non-radiative surface) and 1 (black body) which depends on the material, chemistry, oxidation, surface roughness and contamination [24]. The accurate evaluation of the emissivity is considered one of the main sources of uncertainty in gas turbine applications and it has been investigated for different alloys and TBCs using single-wavelength pyrometers [25, 26]. Two-colour or ratio pyrometers are devised to elude this problem by collecting the radiance from two narrow regions of the spectrum and calculating the signal ratio. When this ratio is calculated, and assuming the surface behaves as a grey body (constant emissivity at all wavelengths), the emissivity cancels out (see Equation (1.1)) and therefore the temperature can be calculated without evaluating the emissivity. However, many materials do not behave like grey bodies and therefore there is a systematic error in the measurement. Multi-colour pyrometers use three or more signals at different wavelengths to calculate both temperature and emissivity by means of numerical fitting algorithms [27].

The measurement of temperatures on the surface of TBCs has the additional difficulty of overcoming the transparency of the ceramic coating in the visible range of wavelengths, which could result in radiation from inside the coating being detected instead. Long-wavelength pyrometers, whose observation wavelength is in the infrared, can be used when measurement of the surface temperature of the TBC is required.

1.2.3. Resistive Thermal Detectors

Resistive thermal detectors (RTD) are sensors based on the temperature dependence of the electrical resistivity of materials. They normally consist of wired metal, generally platinum, through which a constant current is supplied. By measuring the voltage drop and thus the resistivity, the temperature of the sensor can be inferred. They exhibit the best uncertainty in temperature measurements, which could be as low as ± 0.01 °C [12]. They are more accurate and stable than thermocouples, and the required set-up is simpler as there is no need for reference junction compensation. However they are also intrusive. Additionally, the maximum measurable temperature is only about 1000 °C, they are more expensive, larger and their response is slower than thermocouples. Furthermore, they generate heat because of the

electric current flowing through the circuit. When this heat is not correctly dissipated, the RTD temperature raises with respect to the surroundings thus resulting in a measurement error.

1.2.4. Thermographic phosphors

Thermographic phosphors generally consist of a ceramic host material, such as $Y_3Al_5O_{12}$ (YAG) or $BaMgAL_{10}O_{17}$ (BAM), which is doped with small quantities of an optically active element, generally a rare earth (Dy, Eu, Sm) or transition metal ion (Mn, Cr). By addition of this dopant, an otherwise transparent material in the visible range becomes absorbent and emits luminescence when irradiated with a suitable light source. Normally the light source is a UV or visible laser or LED and the phosphorescence emission is in the visible range, which makes it suitable for common detectors such as cameras and photomultiplier tubes. The optical properties of the emitted luminescence, such as the emission spectrum and the lifetime decay of the intensity, change with temperature and can be used to perform temperature measurements. These two variations lead to the two main thermographic phosphor techniques namely lifetime decay and intensity ratio. These have been used extensively and detailed analysis of their practical application can be found in the literature [28-34]

Scientific research in the field of thermographic phosphors has been very active in the past 30 years [28-30, 35, 36] due to the potential advantages of thermographic phosphors over other techniques. Amongst these advantages is their high melting points and chemical stability that permit survivability in harsh environments such as those present in a gas turbine. Measurements are normally performed by observing the lifetime of the decay or the relative changes in the intensity of two emission lines. This results in the insensitivity of the measurement to contamination of the optical path, which is an advantage when compared to pyrometry. The possibility of obtaining temperature maps and not only point information is also an advantage over thermocouples and pyrometers. Finally, by selecting the right phosphor it is possible to vary the observation wavelength and thus filter out background and light reflected from other components or emitted by flames. On the downside, the technique might be considered intrusive as the phosphors are normally applied in thin films that can influence the heat flux around them. The luminescence intensity decreases with temperature and therefore it becomes more difficult to detect when the blackbody radiation becomes more intense. This limits the maximum temperature measurable with a particular phosphor.

Moreover, for some phosphors the emission can also be sensitive to pressure and oxygen concentration [37].

Thermographic phosphors were first used in a combustion environment as early as 1987 [38], although the maximum sensed temperature then was only about 315 °C. Since then, their use has been reported in many applications such as on rotating blades with temperatures up to 1000 °C [39], to study film cooling in a combustor with temperatures up to 600 °C [40], in a jet engine afterburner with temperatures up to 600 °C [41] and in HCCI engine cylinder walls [42].

Temperature measurements using thermographic phosphors can also be performed on the TBCs of a gas turbine, which is important to evaluate the lifetime of these protective coatings. Because the ceramic layer of the TBC is normally made of YSZ, which is a common thermographic phosphor host, this layer can be directly doped with a rare earth ion to obtain a luminescent sensor [43]. The production of a phosphor-based temperature sensor in a standard TBC was successfully demonstrated in [44, 45]. Later, TBC sensors also found application in non-destructive self-evaluation of erosion, corrosion and ageing [46-50]. TBC sensors have been recently applied and used to measure temperatures in a Rolls-Royce Viper engine on nozzle guide vanes, the combustor liner and rotating blades [51, 52] with a precision comparable to that of thermocouples. In such an application, the presence of a large thermal gradient across the TBC sensor due to internal cooling mechanisms needs to be considered as it may affect the accuracy of the luminescent measurement [53, 54]. Because of the transparency of the TBC, the total emitted phosphorescence is composed of signals coming from different depths within the coating, each of which is at a different temperature. Therefore, the measurement of the overall signal provides a temperature reading which is at an effective depth within the coating. This temperature can significantly differ from the surface temperature given the large thermal gradient in the order of 1 °C/μm that is normally present in gas turbines. Theoretical calculation of potential errors introduced by this effect has been made in [54] and the experimental validation of these results has been addressed by the author and co-workers [2] (further details can be found in section 6.2).

Although thermographic phosphors are normally used for surface temperature measurements in the form of a thin film, they have recently been successfully applied in simultaneous temperature and velocity measurements in gas flows [55-59]. In this type of measurement the phosphors are seeded in the flow in powder form similarly to normal Particle Image

Velocimetry (PIV). The excitation light that is scattered by the phosphor particles is used to measure velocity (PIV), and the excitation light that is absorbed by the phosphor and re-emitted in the form of phosphorescence is used to measure temperature.

1.3. Off-line temperature measurements

Although on-line temperature measurements during operation are desirable, often optical access or use of intrusive instrumentation is not possible or inconvenient while the engine is running. In that case off-line temperature measurements can be used instead, in which the maximum temperatures of operation are recorded and analysed at room temperature at a later time. These sensors are thus called thermal history sensors because they are based on irreversible changes undergone by the material caused by thermal exposure, which is composed of both temperature and duration of the exposure.

1.3.1. Temperature sensitive paints

Temperature sensitive paints or thermal paints are temperature sensors formed of various metallic compounds (cobalt, lead, magnesium, etc.) mixed with a binder and a solvent [60, 61], which can be applied on complex surfaces such as turbine blades, nozzle guide vanes and combustors. At high temperatures, the metallic components undergo chemical reactions that permanently change their colour. Thermal paints show either single colour or multiple colour changes in a determined temperature range, and these colour changes are dependent both on the maximum temperature reached and on the time over which the temperature is maintained [61]. The temperature or temperatures at which the paint changes colour are calibrated for a specific exposure time (see example in Figure 1.3) and this calibration is used later to draw the isothermal lines on the surface of a painted component.

Thermal paints commercially available from Rolls-Royce are divided in two groups [62]: low temperature paints present four or less colour changes in the range from 120 °C to 590 °C and high temperature paints have at least five colour changes in the range from 500 °C to 1300 °C. These paints are normally calibrated for exposure times from 3 to 60 minutes [20, 63], although the best results are obtained for exposure times of 5 to 10 minutes since longer exposures lead to colour changes happening at lower temperatures and therefore reduce the dynamic range of the paint.
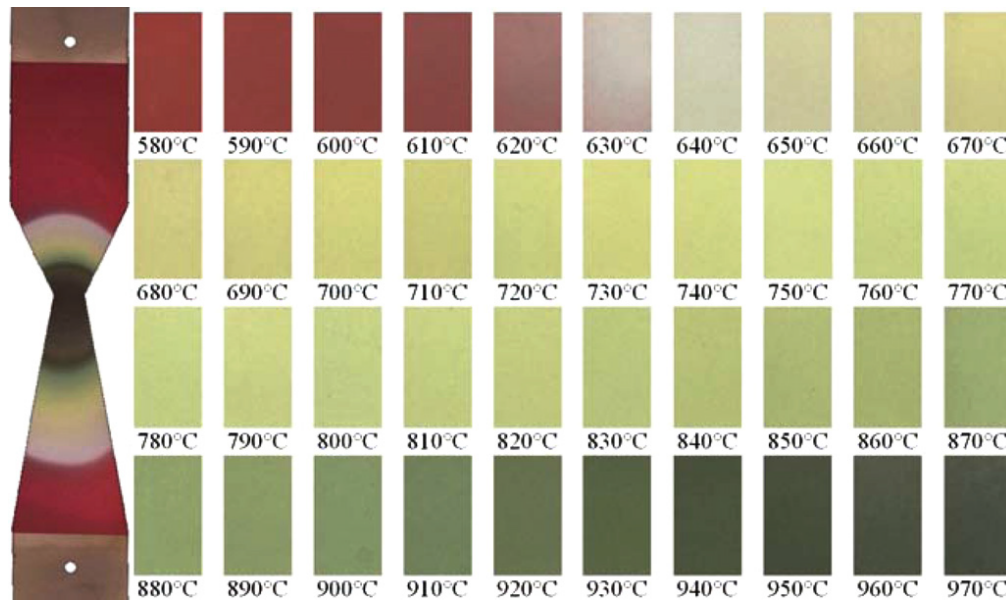
Figure 1.3. Example of the colour changes in a butterfly sample (left) and in coupons treated at 10 °C steps (right) painted with Rolls-Royce paint TP96. Reproduced from [64].

The practical implementation of thermal paints presents some difficulties. The application of the paint on the component, normally sprayed onto the surface using a spray gun, needs to be careful to obtain an even surface whose reflectance spectra permits valid visual interpretation of the colour. Additionally, the thickness should be kept below a few microns so that the paint does not interfere with the heat flux of the component. However, if the deposited layer is too thin the paint might be eroded for long exposure times losing information of the temperature in a particular area of the surface.

The interpretation of the colour changes requires the skills of an experienced operator which is time consuming and increases the cost of the technique. Further, the interpretation of the isothermals by an operator is essentially a subjective measurement and therefore might be prone to systematic errors induced by the ambient lighting conditions and illumination of the sample [65]. This is especially important in the cases when the colour changes are very subtle such as in the light to dark green transition in Figure 1.3. An additional drawback associated with the requirement of an operator visual interpretation is the need to remove the components from the engine for inspection under carefully controlled conditions of illumination. This is especially costly if the engine is operated for a limited period of time, based on the exposure time calibration of the paint, during which no other tests can be performed simultaneously.

As mentioned earlier, the number of colour changes is limited which directly implies low resolution. For example temperature cannot be distinguished in the range from 680 °C to 780 °C in Figure 1.3. To improve the resolution in rotating components such as blades, a different paint can be applied to each of them and the results of all the blades can be combined to obtain one temperature map [64]. However, this cannot be done on static components unless axial symmetry is assumed.

The automation of the process is being investigated with the purpose of overcoming the subjectivity and poor resolution of the manual mode as well as making the digitisation of the results possible. First models based on the human vision (Red-Green-Blue - RGB) [65] and later those that separate the colour information from the intensity of the light (Hue-Lightness-Saturation - HLS) [64] permit identification of colour changes and also interpretation of the evolution of the colour itself. Temperature information between isothermals can then be retrieved by comparison with the colours of previously calibrated samples, although this method exhibits a resolution which is at best 10 °C [64] and largely increase the complexity and cost of the process.

The toxicity of thermal paints is also problematic. The Regulation on *Registration, Evaluation, Authorisation and Restriction of Chemicals* (REACH [66]) introduced by the European Union in 2007 has a direct impact on the use of thermal paints. This regulation, which aims to protect human health and the environment, regularly updates a list with Substances of Very High Concern (SVHC) whose use is subjected to authorisation by the European Chemicals Agency. Included in this list are some substances present in thermal paints, such as cobalt, nickel and lead compounds and therefore safe alternatives must be sought.

1.3.2. Off-line thermographic phosphors

Thermographic phosphors have been used in on-line temperature measurements for many years but were first proposed as thermal history sensors by Feist et al. [67] in 2007. Off-line measurements using thermographic phosphors are based on permanent changes in the optical properties of the phosphors caused by the exposure of the material to high temperatures. These optical properties can be examined in-situ, at room temperature and using the same methods as for on-line temperature measurements. This is advantageous when compared to thermal paints since the measurement is objective (does not rely on the subjective observation of colour changes by an operator) and unaffected by ambient conditions such as illumination

and type of light source used. Temperature information obtained is continuous across the component (as opposed to discrete colour changes of thermal paints) and therefore the resolution is improved, there is no need to dismantle the components to perform the measurement, and the chemicals used are not restricted by the REACH regulation.

The changes in optical properties that lead to the possibility of measuring temperatures arise from structural modifications in the phosphor caused by different mechanisms namely amorphous to crystalline transformation, oxidation of the dopant and thermally driven diffusion [63].

The amorphous to crystalline mechanism is based on the crystallisation of an initially amorphous phosphor that occurs when it is exposed to high temperatures. Amorphous phosphors show low luminescent efficiency and are characterised by broadband emission spectra. This is because the environments of the dopant ions differ from each other. However, when the phosphor crystallises, the dopants occupy specific sites in the highly ordered structure and show efficient luminescence, narrow emission bands and increased lifetime decay [63, 68]. These changes are progressive with temperature and can be used for temperature measurements up to 1000 °C as shown for Y_2SiO_5:Tb phosphor powder [68].

The oxidation mechanism relies on the change of coordination state of divalent dopant ions (generally europium) upon heating at high temperatures. The ion changes its coordination state as it oxidises and the phosphorescent emission changes accordingly. By examining the evolution of the emission spectra with oxidation of the ion a temperature measurement can be performed. The oxidation of Eu^{2+} to Eu^{3+} has been previously reported as being a suitable candidate for temperature history sensing up to 1300 °C in different host materials such as $BaMgAl_{10}O_{17}$ (BAM) and $SrAl_{14}O_{25}$ (SAE) [63, 69].

Finally, the thermally driven diffusion is related to the temperature and time dependent diffusion of a dopant ion in an undoped host. Impurities are known to affect the optical properties of the material in which they are introduced and can act as sensitizers (improve the luminescence efficiency and/or increase the lifetime) or quenchers (reduce the luminescence efficiency and/or the lifetime). Particularly, transition metal ions such as Fe, Ni and Co strongly affect the luminescence of already doped materials and would be suitable candidates for the concept. However this mechanism has not been yet practically demonstrated.

In the previous paragraphs, the temperature dependent optical properties of the various phosphors mentioned were reported for powder samples. However, it is desirable to apply these phosphors as coatings on the surfaces of components so as to obtain useful temperature profiles. Two main procedures can be distinguished here: thermal history paints and thermal history coatings. The concept of thermal history paints is very similar to the temperature indicating paints discussed in the previous section. They consist of a suspension of the appropriate phosphor powder in a high temperature binder, which can be applied as a coating in the same manner as common paints, for example using a spray gun. The use of a binder presents some limitations since it might not withstand the harsh environments present in gas turbines and be eroded from the surface on which it is applied. The binder can also interact with the phosphor at high temperatures modifying the composition of the phosphor or altering the mechanism of change of the phosphor. For example, when the amorphous to crystalline mechanism is employed the binder inhibits the crystallisation process, which was demonstrated in Y_2SiO_5:Tb paints where the lifetime decay measurements were shorter compared with the powder [70]. In the case of the oxidation mechanism the binder is likely to prevent the oxidation of the dopant thus affecting the temperature measurement. The binder is also responsible for the attenuation of the phosphorescence emitted which can be attributed either to the absorption of the excitation energy or the emitted light. However, successful temperature measurements up to 800 °C have been reported using a europium based phosphor in a high temperature binder [71] with precision better than 10 °C.

On the other hand, thermal history coatings present an alternative to avoid the use of a binder. These coatings can be deposited by using a conventional method employed for TBCs such as Atmospheric Plasma Spray (APS) or Electron Beam Physical Vapour Deposition (EBPVD). Although these processes are more complex than the application of a simple paint, these coatings normally resist for longer in harsh environments and do not present any interference from the use of a binder. YAG/YSZ:Dy APS coatings have been applied in a Rolls-Royce Viper engine combustion liner, in which preliminary measurements up to about 700 °C were performed [70]. Also YAG:Ln APS coatings have been tested in a butterfly sample in the temperature range from 400 °C to 900 °C [71]. Finally, sol-gel dip-coated samples of YSZ:Sm have been reported to have potential for thermal history measurements up to approximately 700 °C.

All the thermal paints and coatings reported so far are based on the amorphous to crystalline transformation mechanism and are capable of measuring temperatures up to only 900 °C. This is because of the complete crystallisation of the employed phosphors above that temperature which stops measurable changes in the phosphorescent emission. The oxidation mechanism studied in this thesis should not suffer from this limitation as it is based on a different physical principle and might be useful for higher temperature measurements. Additionally, as it is based on an intensity ratio, it is straightforward to obtain accurate surface data, for example with a simple two-camera set-up or a single camera and an image doubler. It should be noted, however, that with intensity based techniques it is important to correct for background radiation and this can be achieved by recording a background and subtracting it from each of the subsequently recorded images. This method is advantageous when compared to high speed CCD cameras necessary in the lifetime decay method, which present limited temporal resolution and sampling rate [36].

1.3.3. Other history sensors

Several methods based on different physical principles have been developed to measure off-line temperatures. These sensors are generally intrusive, require modification of the components in which they are located and provide point information, and therefore find little practical application. Some of these methods are briefly described in the following paragraphs.

Metallurgical temperature sensors are basically metallic pieces that can be introduced in the component of interest and change properties such as hardness, magnetism and phase composition upon thermal exposure [72]. Feroplug sensors are made of duplex stainless steel and measurements are based on a decreased magnetism due to phase change. They can measure temperatures between 400 °C and 600 °C after long exposure times normally thousands of hours. Sigmaplug is a similar sensor aimed to extend the measurable temperatures up to 900 °C by measuring the Curie temperature of stainless steel, which is dependent on the exposure temperature. Templugs permit temperature measurements from 90 °C to 850 °C by determining the permanent changes in hardness after exposure to high temperatures. These feroplug sensors have been used on internal combustion engines and gas turbines and are currently under development by Vernolab SGS. The main disadvantages of these metallurgical sensors are that they are intrusive, they retrieve point information, the

engine components need to be modified in order to place the sensor and measurements need to be done under laboratory conditions with specialised equipment.

Crystal temperature sensors are made of diamond or SiC. These sensors are irradiated with neutrons that induce defects so that the crystal lattice expands. After exposure to high temperature the defects are eliminated and the lattice parameter decreases. This lattice parameter, which can be examined using X-Ray Diffraction (XRD), depends on the time and temperature of exposure. This sensor, commercialized by LG Tech-Link Inc., covers a temperature range from 150 °C to 1450 °C with an uncertainty of ± 6 °C. Exposure times can vary from 1 minute up to about 2400 hours.

Glass-ceramic arrays are a type of sensors investigated by Fair et al. [73] which are based on phase transformation materials. Glass-ceramics are alkali, alkaline-earth or transition metal alumina-silicates obtained by quenching the molten components to temperatures close to room temperature. The resultant glass sequentially crystallises upon heating and as a consequence of the formation of crystallites, its optical properties change. By calibration of the transmittance of the glass for different exposure temperatures and times, arrays of sensors can be used as fingerprints to interrogate the temperature. Experimental measurements up to 900 °C with resolution of about 50 °C are reported [73].

A thermal history sensor based on changes in electrical resistance across two electrodes was patented by Yokota et al. [74]. The sensor consists of a pair of electrodes, a diffusion layer and an electrically conductive metal. When the sensor is heated, the conductive metal diffuses across the diffusive layer and after a certain time the resistance abruptly changes. The time necessary for this change to happen depends on the temperature. This sensor provides only one discrete change in resistance, can be only used to obtain point measurements and is intrusive. Examples are provided for sensors capable of measuring temperatures from 400 °C to 900 °C [74].

1.4. Coating deposition techniques

It is evident that the development of thermographic phosphors as thermal history sensors is bound to their potential to be deposited as films on the surfaces of the different components. This depositing process is not trivial since each phosphor has its own requirements as their functionality is based on various physical principles. Also the coatings need to survive in a harsh environment involving high pressures and temperatures, thermal shock and high speed

gases. Many processes exist that can be used to deposit ceramic materials onto metallic substrates and extensive literature can be found about each of them. In the following sections the coating deposition techniques more relevant to thermal history sensors are briefly reviewed.

Firstly, the thermal spraying processes are described, which involve the transfer of droplets of the depositing material at high temperatures. The following two processes, in which the vapour of the material is deposited, involve an atom-by-atom transfer to the substrate. The last four techniques are often considered as thick film depositing methods and involve the use of a solution or paste that must be dried and sintered after depositing.

1.4.1. Thermal spraying

In the thermal spraying processes the ceramic powder is heated to high temperatures so that the particles become molten or semi-molten. These particles are then propelled towards the substrate where they are deposited as lamellae, solidify and form a thick coating by accumulation. The material can be heated in different ways for example with a combustion flame or a wire arc, although the use of a plasma jet generated with an electric arc and an inert gas is the most common method. Plasma spraying therefore permits control of the atmosphere and it can be performed in air, in an inert gas atmosphere or a medium vacuum.

Thermal spraying is an economic and versatile coating method. However, porosity might be an issue due to the way the particles are deposited. The thickness of the coating is difficult to control and poor surface finish is normally obtained. Further, the coating might oxidise during deposition possibly leading to corrosion problems. Finally, deposition is restricted to line of sight, so that closed shapes cannot be coated.

Atmospheric plasma spraying (APS) is widely used to deposit thermal barrier coatings on annular surfaces of gas turbines but is not extended to blades or nozzle guide vanes [75]. This is due to their porosity, surface finish, low erosion resistance and poor mechanical compliance.

1.4.2. Physical Vapour Deposition (PVD)

Physical vapour deposition techniques are based on the evaporation of the target material (normally in the solid state) followed by the transport to the substrate and the condensation of the vapour to form a film. There are three PVD processes: evaporation, ion platting and sputtering [76].

The evaporation processes differ in the way that the material is heated to obtain the vapour, and this could be achieved for example by an electron beam or a pulsed laser beam [76]. In electron beam physical vapour deposition (EBPVD) the atoms of the target are evaporated in a vacuum chamber by the action of an electron beam. The vapour is then transported in the line of sight and condensed on the substrate. This is one of the industry standard methods to deposit YSZ thermal barrier coatings in moving elements of advanced gas turbines. In pulsed laser deposition (PLD) the solid target is ablated by a focused laser beam. The evaporated material further absorbs energy from the laser and expands away from the target until it is finally deposited on the substrate. The fast heating caused by the laser beam permits rapid and simultaneous evaporation of all the components of the target material, which maintains the stoichiometry and is a major advantage of this method. In evaporation processes, the properties of the film can be controlled by different means such as the distance of the target to the substrate, the substrate temperature and the gas atmosphere (or vacuum) of the chamber. Limitations of the method include small size of the deposited film, complexity of the laser system and delivery of the beam and low energy conversion efficiency.

The ion-platting process is similar to evaporation processes but the vapour is partially ionised by passing it through a glow discharge. In this procedure the substrate is biased to a high negative potential and a gas (generally argon) is introduced in the chamber. The aim of this ionisation is for the gas ions to collide with the substrate, subsequently removing part of the deposited material. This results in a constant process of deposit and removal of material which improves the adhesion and the purity of the film. However, the deposition rate is substantially reduced.

Sputtering processes use ionised gas ions (normally argon) to bombard the target and remove groups of atoms which then vaporise and deposit on the substrate. This method offers the lowest deposition rates of the three PVD methods mentioned and it is not widely used in industrial applications.

PVD processes are superior to other techniques in that almost any material (except some polymers) can be deposited. They offer good control of the microstructure, purity and surface finish. The substrate temperature can be controlled and excellent bonding can be achieved. On the downside there is the complexity of the equipment and the higher cost derived.

1.4.3. Chemical Vapour Deposition (CVD)

Chemical vapour deposition comprises a series of methods in which a vapour enters a reactor where it is then deposited on a substrate by means of a chemical reaction which occurs near or on the substrate [76]. There are many possible chemical reactions such as thermal decomposition, reduction and exchange. Complex computational methods are routinely employed to calculate the thermodynamic conditions favourable for a particular reaction, although the design of a particular deposition normally results in an iterative process. The gas flow dynamics are an important factor that affects the deposition conditions of the film, and three different CVD processes can be distinguished depending on the atmosphere pressure range: atmospheric pressure, low pressure and ultrahigh vacuum. The way in which the reaction is initiated and maintained can be controlled by using heat, photons, electrons or ions. The use of photon, electron or ion beams further allows limitation in the area of deposition or deposition of a selected phase, microstructure or chemical composition. This is called selective deposition and is a major advantage of CVD processes. The microstructure of the film is controlled by many factors which influence each other such as temperature, substrate, gas flows and presence of impurities. Some theories are available to explain the film growth although for specific details the reader is referred to some of the available literature [76, 77].

Because CVD processes are based on a gas precursor, they offer the possibility to uniformly coat components with complex shapes and holes, as opposed to line of sight deposition of PVD processes. CVD processes also permit careful control of the materials deposited so that high purity coatings can be obtained. CVD processes present some disadvantages. The main one is that precursors should be volatile at room temperature and it is sometimes difficult to find a suitable precursor for a particular element and they can be very expensive. Furthermore, some precursors or products of CVD reactions can be hazardous. Finally, most CVD processes involve a high temperature for the substrate, which limits the type of substrates that can be used.

Some of the applications of CVD include, amongst others, functional layers in the microelectronics industry (passivation layers, diffusion barriers, oxidation barriers), internal coating of optical fibres to obtain a correct refractive index profile and wear-resistant coatings of TiC, TiN and A_2O_3 on cutting-tools [76].

1.4.4. Sol-gel methods

Sol-gel methods consist of the formation of a liquid solution that contains all the precursors and which is then deposited onto a substrate where it forms a solid film after evaporation of the solvent and condensation reaction of the precursors. The two main procedures to deposit the solution on the substrate are dip-coating and spin-coating. Sol-gel processes are rather complex and a detailed explanation of the reactions involved is beyond of the scope of this thesis. An in depth study of sol-gel can be found in Brinker et al. [78] and here only the basics of the process is briefly explained.

The precursor materials for sol-gel processes are inorganic or metal organic compounds which are hydrolysed by dissolving in water or alcohol. This solution then undergoes condensation reactions to form inorganic polymers which ultimately form a gel. By further treatment of the gel, such as sintering, the desired material structure can be obtained.

In dip-coating [78, 79], the substrate is normally immersed in the solution and then withdrawn vertically at a constant speed. When the substrate leaves the liquid bath, the solution forms a boundary layer with the surface, where gravitational draining and evaporation of the solvent and condensation reactions of the precursors cause the deposition of the precursors. The drying and gelation processes occur almost simultaneously unlike in bulk sol-gel processes. The microstructure of the deposited film is affected by the physical and chemical properties of the precursors, rates of evaporation and condensation, withdrawal speed and capillarity effects.

In spin-coating, the liquid solution is deposited on top of a spinning substrate. The liquid then spreads radially due to centrifugal forces and excess liquid is expelled in the edges as droplets. Evaporation of the solvent can occur over the whole process. The viscosity of the solution and the angular velocity at which the substrate rotates are the main parameters used to control the film thickness.

Sol-gel deposition processes are simple to apply and inexpensive. They permit the deposition of thin and thick films in complex surfaces with axial and radial symmetry and materials in the amorphous state can be easily deposited. The main disadvantages of sol-gel deposition techniques are the fragility of the films due to appearance of cracks during the drying and sintering processes. The sintering process itself might impose a limitation in the type of substrate that can be used if the temperature needed is too high. The requirement for some symmetry in the substrate in the dip-coating and spin-coating methods is also a limitation.

Sol-gel coatings were initially used in optical applications to obtain reflective or coloured coatings. Other applications include ferroelectric, superconducting and protective films. Finally, porous films in which the volume, size and surface area of the pores can be controlled have been obtained by sol-gel [78].

1.4.5. Electrophoretic deposition (EPD)

Electrophoretic deposition is a technique based on electrophoresis, i.e. the movement of particles suspended in a fluid due to application of an external DC electric field. These particles are attracted to the electrode of opposite charge (the substrate) on which they deposit forming a film. The exact mechanism by which the deposit is formed is not completely understood [80]. Further drying and sintering is normally performed to obtain the desired microstructure.

The factors that permit control of the EPD deposition are those related to the suspension and those related to the process itself [80]. Parameters of the first group include viscosity and dielectric constant of the liquid, size and zeta potential of the particles and conductivity and stability of the suspension. Parameters related to the process are deposition time, voltage applied, concentration of particles and conductivity of the substrate [80].

The deposition rate and thickness of the film depend on the voltage or current applied. At constant voltage, the electrical resistance increases as the coating forms. Thus the current and the deposition rate decrease with time. However, if a constant current is maintained across the fluid solution the deposition rate remains constant. Aqueous solutions are preferred as water has a high dielectric constant. However, when high electric fields are applied electrolysis of water can occur and reduce the quality of the film. In these cases organic solvents such as alcohols and ketones are employed instead.

Advantages of EPD are simplicity and versatility, high deposition rates, reduced presence of organics in the green body, possibility to coat complex shapes and good control of microstructure and thickness. A limitation of EPD, when compared to other methods based on colloidal suspensions such as sol-gel, is the restriction in the use of water based solutions when high voltages are applied. Another issue is the requirement of a conductive substrate, although recently the possibility of deposition on non-conductive substrates is being developed [80].

EPD has been used to deposit layers of luminescent materials, superconductors, layered ceramics and solid oxide fuel cells [80].

1.4.6. Screen printing

The process of screen printing consists of the transference of an ink through a screen mesh and the deposition of that ink onto a substrate, as depicted in Figure 1.4. The ink is forced through the mesh by the action of a moving squeegee that advances along the substrate. When the squeegee moves on and releases the pressure, the screen separates from the substrate and the ink is deposited on it. Normally, a baking process is necessary after the deposition to eliminate undesired components of the ink and to sinter the ceramic film.
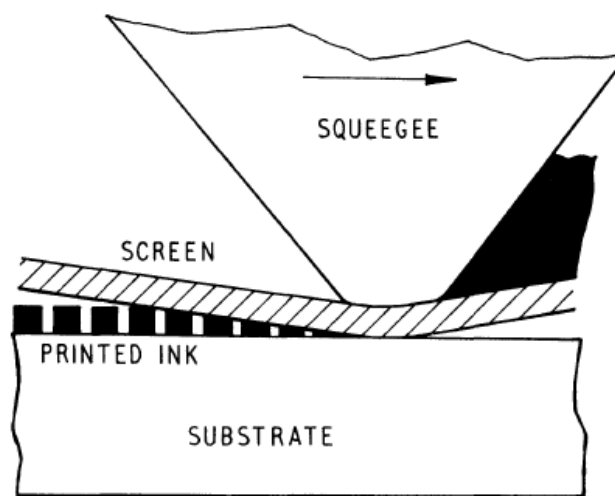
Figure 1.4. A schematic of the screen printing process. Reproduced from [81].

Several factors influence the completion of the ink deposition and the final coating thickness obtained [81-83]. The rheological properties of the ink are fundamental because the ink should flow easily through the mesh but remain on the substrate without flowing laterally. These properties are restricted by the ink composition and the amount of solids present. Other elements that affect the process are related to the configuration of the screen (screen tension, orientation and mesh density) and the printer itself (squeegee force, hardness and contact angle).

The screen printing method is used in many manufacturing processes such as for electronic applications. Recently, the method has been of great interest in the manufacture of solid oxide fuel cells (SOFC), where YSZ electrolytes are deposited as thin films [82, 83]. Other reported applications of screen printing are related to the use of YAG:Ce in the manufacture of LEDs [84, 85] and the use of phosphor-based electroluminescent devices [86]. The screen printing

method has a low cost and is simple to apply. Custom patterns can be easily printed by simply changing the mesh and multiple layers can be deposited on the same substrate. However, the film structure and thickness are difficult to control, and fully dense films are normally difficult to achieve.

1.4.7. Tape casting

In the tape casting process, an ink similar to that of screen printing is deposited on a moving tape made of polymer. The thickness of the deposited layer, which can vary between 10 – 1000 μm [87], is controlled by a doctor blade and multilayer films can be obtained by using multiple inks and blades. As the tape moves, the ink dries and the product is rolled to constitute the green tape. Industrial tape casting machines exist that can achieve casting speeds as high as 0.15 m/min [77]. The green tape can be applied on the surface of components and then heated to eliminate components of the ink and sinter the ceramic material.

Tape casting can be used in many applications, for example the manufacture of ceramic substrates with highly controlled thickness for the microelectronic industry [88], piezoelectric ceramics for actuators [89], and SOFC components [87].

1.5. Objectives and outline of the thesis

Temperature measurements in gas turbines are highly desirable both for performance and maintenance. There are a multitude of methods available to retrieve temperature information, revealing the importance of the field. On-line temperature methods such as thermocouples and pyrometers are well established and standardised, and the use of thermographic phosphors for on-line surface temperature measurements has been a field of active research for the past 20 years. However, these on-line methods are sometimes difficult to implement and alternative off-line temperature measurements are used. Off-line surface temperature measurements in gas turbines are currently restricted to thermal paints, which have demonstrated several limitations. Other physical thermal history sensors are highly intrusive and offer point information only. The use of thermographic phosphors as thermal history sensors was first proposed by Feist et al. [67] in 2007, and the potential application of phosphors as coatings or paints has been investigated since then. Most of the research developed on this topic has focused on the amorphous to crystalline mechanism, which so far

has been successful up to temperatures of about 900 °C. The current work investigates the oxidation mechanism and the main objectives are:

- To investigate in detail the oxidation concept of Eu^{2+} doped phosphors, and in particular BAM:Eu which has been reported previously to be sensitive to temperatures up to 1300 °C. This includes a thorough characterisation of the degradation mechanisms experienced by this phosphor in order to identify the applications and temperature ranges in which it might be suitable for history sensing.

- Correlation of the degradation of the phosphor to some optical properties that can be used as a measurand that offers advantageous attributes in terms of precision, accuracy and resolution compared to conventional thermal paints.

- To further investigate physical properties of the phosphor relevant to identifying a suitable coating deposition technique and to investigate potential problems related to its practical application as an optical sensor coating.

The thesis includes (in chapter 2) a theoretical description of the principles involved in phosphorescence processes that lead to the possibility of temperature measurements both on-line and off-line. It also includes a brief explanation of the main techniques used to measure temperatures using thermographic phosphors and a review of the theoretical model of propagation of light through phosphor layers that explains inaccuracies in temperature measurements due to thermal gradients across TBCs. In chapter 3 a thorough review of the phosphor BAM:Eu is addressed with the objective of creating a reference that can be used to explain the changes observed in the phosphor after exposure at high temperatures during this project. Chapter 4 encompasses a detailed description of the instrumentation and material characterisation techniques used during this work. Chapter 5 includes a thorough investigation of physical and optical properties of the BAM:Eu phosphor powder. An exhaustive characterisation of the optical properties of the phosphor after thermal degradation is performed and the influence of several different parameters in this degradation is investigated. In chapter 6 the manufacture of a sensor coating is investigated and practical issues are identified. The effect of thermal gradients on measurement accuracy is further investigated.

2. FUNDAMENTALS OF LUMINESCENCE

2.1. Physics of thermographic phosphors

Photoluminescence of thermographic phosphors is caused by the absorption of light that is then re-emitted at a different wavelength. Phosphors are normally transparent inorganic crystalline materials doped with small quantities of rare earth or transition metal ions. These added impurities are responsible for the photoluminescence process. The excitation of the phosphor is achieved by lasers or diodes which normally emit in the UV, where the absorption of phosphors is more efficient. However, excitation can also be achieved at longer wavelengths within the visible region of the spectrum. The excitation source promotes electrons of the dopant ions to higher energy states. When the excitation ceases, these electrons relax to the ground state via two competitive processes (radiative and non-radiative), which results in the emission of light as shown in Figure 2.1. When the optical properties of the emitted light are temperature dependent, these materials are called thermographic phosphors.
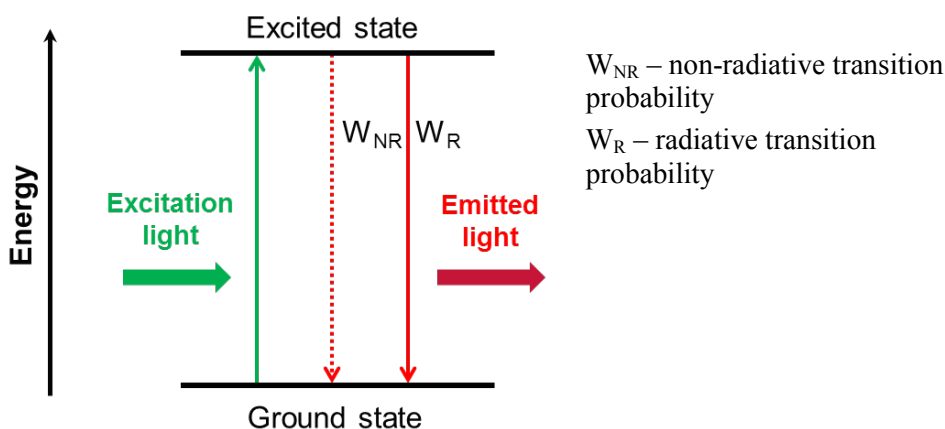
Figure 2.1. Schematic of the luminescent process between the ground and excited states of an optically active dopant.

The following sections provide the quantum mechanical basis for the understanding of the different processes leading to this photoluminescence. The dependence of the luminescence on temperature, which is the basis for temperature measurements using thermographic phosphors, is also discussed. An overview of the two main techniques used to perform temperature measurements with thermographic phosphors, i.e. lifetime decay and intensity ratio, is introduced. Finally, a model of the propagation of light through phosphor layers will

be introduced. This model is useful to predict inaccuracies when the temperature measurements are performed in situations in which a thermal gradient exists across a phosphor coating.

2.1.1. The Schrödinger equation and energy levels

The energy levels of ions in a vibrating crystalline environment can be calculated by solving the Schrödinger equation:

$$\mathcal{H}\Psi = E\Psi \tag{2.1}$$

where H is the Hamiltonian of the system, E the energy eigenvalues and Ψ the wavefunctions. The several terms in the Hamiltonian describe different interactions that affect the electrons and can be written as [90]:

$$\mathcal{H} = \sum_i \left(-\frac{\boldsymbol{p}_i^2}{2m} + V'(r_i) \right) + \sum_{i>j} \left(\frac{e^2}{4\pi\varepsilon_0 r_{ij}} \right) + \sum_i \zeta(r_i)\boldsymbol{l}_i\boldsymbol{s}_i$$
$$+ \frac{1}{4\pi\varepsilon_0} \sum_i \sum_l \frac{Z_l e^2}{|\boldsymbol{R}_l - \boldsymbol{r}_i|} + V_I(\boldsymbol{R}_l) + \sum_l \frac{\boldsymbol{P}_l^2}{2M_l} \tag{2.2}$$

Where $\boldsymbol{p}$ is the operator for linear momentum, m the mass of an electron, V' the potential energy caused by the central field of the nucleus and the inner electrons, r_i the radial distance of an electron, e the charge of an electron, ζ the spin-orbit coupling function and $\boldsymbol{l}_i$ and $\boldsymbol{s}_i$ are the operators for the angular and spin momentum of the electrons. $\boldsymbol{R}_l$ is the position, Z_l the atomic number and M_l the mass of the neighbouring (l) ions. V_I is the inter-ion potential energy and $\boldsymbol{P}_l$ the operator for linear momentum of the neighbouring ions.

The first three terms represent the free-ion Hamiltonian. The first of these terms embodies the interactions (kinetic energy and Coulomb) of the outer electrons with the nucleus, the second term is the Coulomb interaction between the outer electrons themselves and the third term is the spin-orbit coupling.

The fourth term includes the effect of considering the ion as part of a crystal structure and it is called the crystal field Hamiltonian. The ligand ions in the crystal are thus represented by point charges.

The last two terms further consider the effect of lattice vibrations and represent the potential and the kinetic energy of the lattice ions. The consideration of these lattice vibrations introduces difficulty in the Schrödinger equation due to the coupling between the motion of

the electrons and the vibrations in the lattice. The *Born-Oppenheimer* (or *adiabatic*) approximation, which assumes that the electronic state of the central atom is not changed by the lattice vibrations because the electronic motion is much faster, simplifies the consideration of the lattice vibrations in the Schrödinger equation and permits decoupling the electronic states of the atom from the lattice vibrations. This approximation, which is only valid for non-degenerate electronic states, will be considered later when the electronic transitions are explained.

The solutions of the Schrödinger equation are pairs of eigenfunctions (Ψ_i) and eigenvalues (E_i). According to the Born interpretation [91], the square modulus of the eigenfunction or wave function ($|\Psi_i|^2$) can be related to the probability distribution of the electron being in a determined region in space, and it is actually called the probability density. In one-electron atoms the wavefunctions describe the dynamics of the electron in the ion, i.e. the atomic orbitals. Each of these atomic orbitals has a discrete energy defined by E_i and the electrons in these orbitals are defined by a series of unique quantum numbers: n, l, m_l, m_s. "n" is the principal quantum number, which takes positive integer values and defines the energy of the orbital ($E_i(n)$). "l" represents the orbital angular momentum and takes values: $l = 0, 1, 2, ..., (n-1)$. "m_l" is the z-component of the angular momentum with values of $m_l = l, (l-1), ..., -(l-1), -l$. "$m_s$" represents the z-component of the spin angular momentum (s) and takes values of $\pm \frac{1}{2}$. s does not define the state of the electron because it can only take the value $\frac{1}{2}$.

An alternative representation of the orbitals considers the total angular momentum $\boldsymbol{j = l + s}$. This angular momentum and its z-component are characterised by the quantum numbers j and m_j. j takes values $l \pm \frac{1}{2}$ and m_j values of $j, (j-1), ..., -(j-1), -j$. For further details on quantum numbers, the reader is referred to [90-92].

When multi-electron atoms are considered, the *Pauli Exclusion Principle* applies and no two electrons in an atom can occupy identical states (or have all the same quantum numbers). The different orbitals are occupied by electrons following the *Aufbau principle* [91] and now the states of the electrons depend on how the individual orbital angular momenta and spin momenta of all the electrons add together. These multi-electron states can be defined by a set of total quantum numbers: L, S, M_L and M_S; or alternatively L, S, J and M_J.

L is the total orbital angular momentum quantum number and takes values $L = 0, 1, 2, 3, ...$ (or S, P, D, F, …). M_L distinguishes the multiple orientations of L and takes the values $M_L = L, L - 1, ..., -L$.

S is the total spin quantum number and takes non-negative integer or half integer values. The value $2S + 1$ is called the multiplicity and it accounts for the pairing of the electrons in the same orbital (the relative orientation of their spins). For example, in the case of two electrons, if their spins are paired they cancel each other and the net spin is zero. This is called a singlet. On the other hand, if the two spin momenta add together, the net spin is nonzero and it is called a triplet. M_S follows similar rules as M_L.

J is the total angular momentum quantum number that represents the spin-orbit coupling and has a non-negative integer or half integer value. M_J can again be calculated using the same procedure as for M_S and M_L.
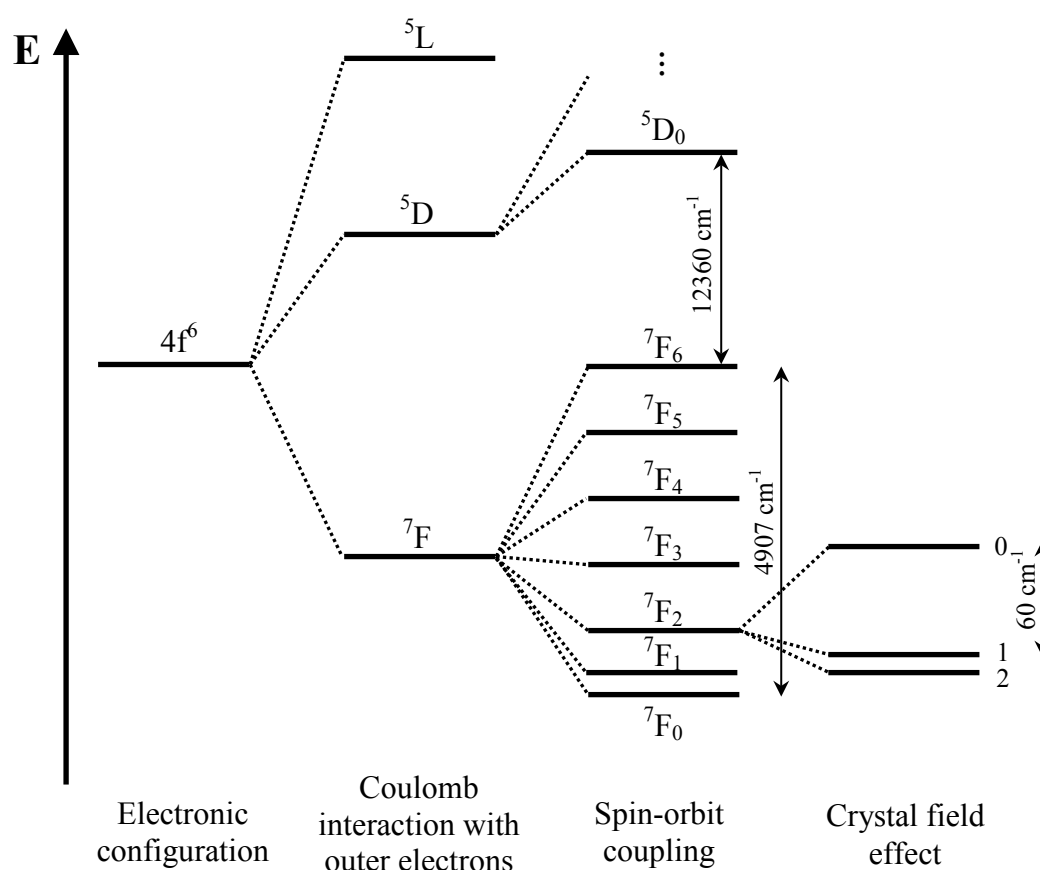
Figure 2.2. A scheme of the splitting of the 4f energy levels of Eu^{3+} in LaCl$_3$. Data obtained from [93].

In order to obtain the actual values of these total quantum numbers the individual values of each electron have to be coupled. This is done by using the *Clebsch-Gordan* series [91]. For example, for two electrons:

$$L = l_1 + l_2, l_1 + l_2 - 1, ..., |l_1 - l_2| \qquad (2.3)$$

$$S = s_1 + s_2, s_1 + s_2 - 1, ..., |s_1 - s_2| \qquad (2.4)$$

The total angular momentum quantum number can be obtained using the *Clebsch-Gordan* series if the *Russell-Saunders* approximation is considered [90, 91], i.e. the spin-orbit coupling is weak. *J* can be expressed then as:

$$J = L + S, L + S - 1, ..., |L - S| \qquad (2.5)$$

The energy levels of the outer electrons in a free atom can be classified by the term symbols. These symbols are of the form $^{2S+1}L_J$ where *L*, *S* and *J* are the total quantum numbers explained before. These symbols, which include information about the splitting of the energy levels as shown in Figure 2.2 for Eu^{3+} in $LaCl_3$, are normally used in spectroscopy for identification of electronic transitions related to absorption or emission of photons.

2.1.2. Electronic transitions and the configurational coordinate model

Luminescence originates from electronic transitions in an atom. The process of luminescence in ions interacting with a vibrating lattice can be explained using the configurational coordinate model shown in Figure 2.3. This model is explained in detail in [90] and only the main aspects relevant to the understanding of the absorption and emission processes are explained here.

The model considers the optically active ion as a linear harmonic oscillator vibrating into the lattice. By adopting the *Born-Oppenheimer* approximation mentioned earlier, the eigenstates of the atom can be separated into electronic and vibrational coordinates by:

$$\psi_a(\boldsymbol{r}_i, Q_0^a)\chi_a(Q) \qquad (2.6)$$

Where Ψ_a is the wave function for the static lattice, χ_a is a vibrational wave function of the configurational coordinate *Q* and *a* indicates a particular electronic state. This configurational coordinate (*Q*) represents the distance from the optical centre to the complex of ions surrounding it. *Q* simplifies the many normal modes of vibration present in the lattice to a single mode of vibration (*breathing mode*) with frequency ω. The parabolas in Figure 2.3 represent the potential energy ($^1/_2 KX^2$) of the ground (*g*) and excited (*e*) states of the ion. The

horizontal lines represent discrete energy levels due to lattice vibrations $\left(E_i = \left(i + \frac{1}{2}\right)\hbar\omega\right)$. Each of these energy levels has a probability density distribution $\chi_i(R_l)$, where R_l has the same meaning as in Equation (2.2).
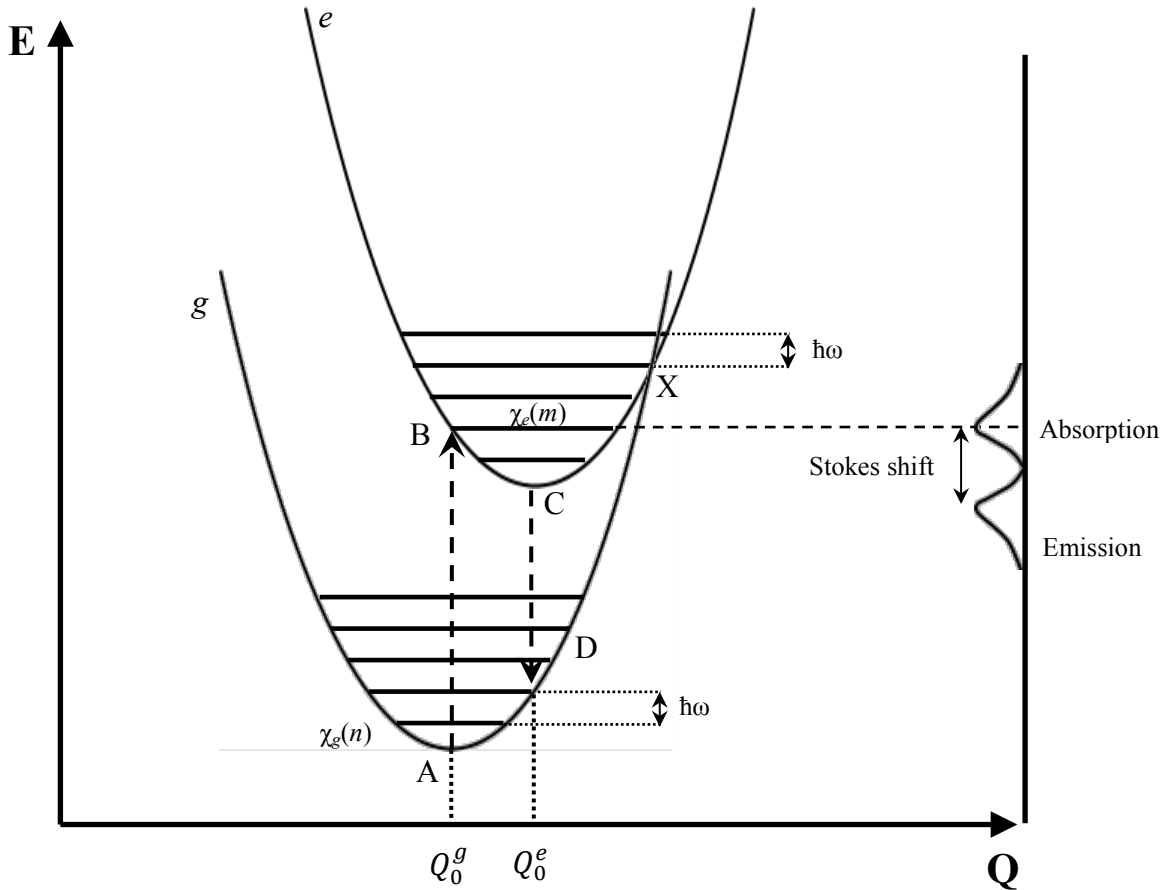
Figure 2.3. Configurational coordinate model for the ground and excited states in a single harmonic oscillator.

The absorption of a photon is represented by a vertical line from the equilibrium point of the ground state (A) to the m energy level of the excited state (B). The quantum mechanical basis for this is that the probability for the transition depends on the overlap between the vibrational wave functions on each energy level (χ_i). These wave functions have their maxima close to the parabola and therefore the maximum transition probability occurs for the m energy level in the excited state.

When the electron is in the excited state B the probability to relax emitting light is low compared to the non-radiative process. The electron therefore relaxes to the equilibrium point of the excited state (C) by interacting with the vibrating lattice (phonon emission).

In point C, the probability of the radiative transition to the ground level depends again on the overlap between wave functions. The transition can be illustrated by a vertical line from C to D and it is mediated by the emission of a photon. The energy of this photon is generally lower than that of the absorbed photon and the emission occurs at a longer wavelength. This energy difference between absorption and emission is known as *Stokes shift*. Finally, the electron decays to point A with the emission of vibrational energy.

The distance $Q_0^e - Q_0^g$ represents the electron-lattice coupling or electron-phonon interaction. When the coupling is weak, this distance is close to zero and there is no displacement of the ion in the excited state. The absorption and emission transitions occur from and to the equilibrium points of the ground and excited states. The absorption and emission spectra consist in this case of a single line called zero-phonon line (there is no relaxation B-C or D-A). If the coupling is larger, vibrational sidebands appear in the spectrum and, because there are more than the single *breathing-mode* considered in the model, these sidebands appear as broad bands. The shape of these broad bands is not symmetrical for small values of the distance $Q_0^e - Q_0^g$ but becomes approximately Gaussian for larger values. This explains the finite width of the peaks observed in the emission spectra of thermographic phosphors even though the electron-phonon coupling is small.

2.1.3. Electronic configuration of rare earths and transition metal ions

Phosphors are essentially crystalline materials which are doped with an optically active ion. These optically active ions are mainly rare earths or transition metal ions, and the particular electronic configuration of these elements makes them emit light in the visible region for a determined period of time after the excitation has ceased.

2.1.3.1. *Rare earths*

Rare earths or lanthanide elements comprise all the elements in the fifth period of the periodic table from cerium (Ce) to ytterbium (Yb). These elements adopt the form of trivalent or divalent ions in solid materials and present an unfilled 4f shell shielded by the 5s and 5p outer shells. Therefore, the crystal field effect on the 4f electrons, which are responsible for the radiative transitions, is weak. The free ion energy levels can then be considered to determine electronic transitions and their main features would remain unchanged for different crystal environments since the variations of the energy levels due to the crystal field effect are at most in the order of few hundred cm^{-1} [92]. These energy levels were determined by Dieke

and co-workers for rare earths in $LaCl_3$ and are collected in the so-called *Dieke diagram* shown in Figure 2.4 [90, 92].
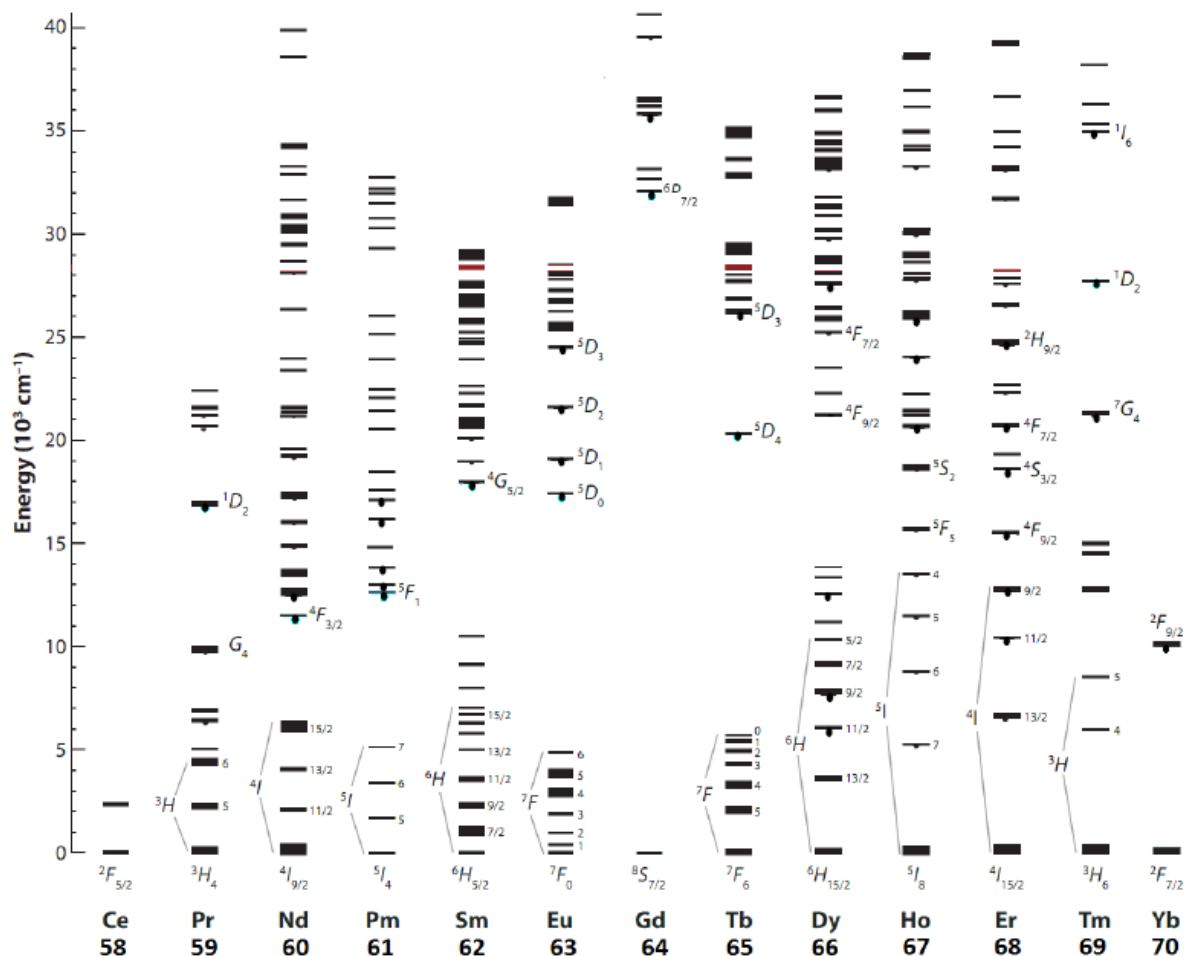
Figure 2.4. Energy levels of trivalent rare earth ions in LaCl₃, adapted from [94]. Phosphorescence emitting levels are indicated by semi-circular markers.

Emission of light in trivalent rare earth ions occurs from transitions between 4f energy levels with a large energy gap that cannot be bridged by emission of phonons, such as the $^5D_0 \rightarrow {}^7F_2$ transition responsible for the characteristic 611 nm emission of Eu^{3+}. Electronic transitions in rare earths that lead to luminescence are mainly due to electric dipole or magnetic dipole interactions [92]. Electric dipole f-f transitions are parity-forbidden in free ions but become partially allowed by mixing of orbitals due to an odd crystal field component. Therefore the intensity of these transitions depends on the site symmetry of the host lattice and the selection rules applicable to the particular transitions. Because of this forbidden character of the transitions, the lifetime of these ions is normally in the order of milliseconds. On the other hand, magnetic dipole transitions are not affected by the site symmetry because they are parity-allowed.

The emission spectrum of rare earths is usually formed of narrow bands at wavelengths that are nearly constant independently of the host. However, for divalent ions the next highest energy levels $4f^{n-1}5d$ may lay at similar energies as the 4f configuration and participate in the luminescent process. These levels interact strongly with the crystal lattice and therefore the crystal field effect cannot be neglected. The emission spectrum of these divalent ions consists of broad bands and the emission wavelength highly depends on the crystal environment. This is the case of Eu^{2+}, which emits a broad band in the blue, green or yellow region of the spectrum depending on the host in which it is embedded.

2.1.3.2. *Transition metal ions*

The transition metal ions relevant to phosphors include elements in the fourth period of the periodic table from scandium (Sc) to zinc (Zn). Transition metal ions have an unfilled 3d shell whose electrons are responsible for the radiative transitions. This is an outer shell with a strong crystal field interaction, and therefore the energy of the levels involved in radiative transitions depends both on the electronic configuration of the ion ($3d^n$) and the crystal field strength. The *Tanabe-Sugano* diagrams [92] show the dependence of energy levels against the crystal field energy for the different $3d^n$ (n=2…8) configurations in an octahedral crystal field.

These diagrams permit analysis of the emission spectra of transition metal ions in different host materials and demonstrate that the ions with emission features in the visible range of the spectrum are those with the $3d^3$ and $3d^5$ configurations. A consequence of this is that the only transition metal ions used in commercial phosphors are Cr^{3+} and Mn^{4+}, which have the $3d^3$ configuration, and Mn^{2+} and Fe^{3+}, with the $3d^5$ configuration.

More details on the energy levels (including the *Tanabe-Sugano* diagrams) and emission spectra of these dopants in different hosts can be found in [92] and references therein.

2.1.4. Selection rules

The selection rules determine whether a dipole transition between two energy levels is allowed or forbidden, and they arise from the fact that the total angular momentum must be conserved when a radiative transition occurs. Because a photon has a spin of 1, when a photon is absorbed or emitted the transition of the electron must compensate the change in angular momentum.

The quantum mechanical basis for the selection rules is related to the probability of radiative transitions between different electronic states, which depends on the wave functions of these

states. The probability of a transition can be calculated using matrix elements [90, 92] although this is not necessary in order to determine the selection rules. Symmetries of the wave functions and matrix element operators permit one to determine if a transition probability is zero (forbidden) or non-zero (allowed) although in practice these rules are less strict due to spin-orbit coupling and crystal field effects. Therefore partially allowed transitions exist that are responsible for the radiative transitions of rare earths. Further details can be found in the literature [90, 92].

Transition probabilities are normally represented by the absorption cross-section (σ, inverse of the absorption probability) and the radiative lifetime (τ, inverse of the spontaneous emission probability). Therefore the selection rules are important in determining how fast the emission of light is.

For the free atom characterised by the total quantum numbers S, L and J the selection rules for the electric and magnetic-dipole transitions are [92]:

$$\Delta S = 0, \Delta L = 0, \pm 1$$

$$\Delta J = 0, \pm 1 \ (J = 0 \rightarrow J = 0, \text{not allowed})$$

(2.7)

The first rule (spin selection rule) states that the total spin does not change. The total orbital momentum rule determines that allowed transitions occur between states with different parity to compensate for the angular momentum of the photon. When the spin-orbit coupling is considered, these rules relax and only the ΔJ rule applies.

In rare earths, transitions between states in the 4f shell are parity-forbidden according to these rules, but become partially allowed for ions in crystals due to the crystal field effect. These transitions are also spin-forbidden and therefore show slow lifetime decay (in the order of milliseconds). On the other hand, transitions between the $4f^{n-1}5d$ state of some divalent ions to 4f states are parity-allowed and the decay is in the order of microseconds.

The transitions between the 3d states of transition metal ions are also parity-forbidden but become partially allowed due to spin-orbit coupling and crystal field effects. Therefore emission from transition metals is slow too (in the order of milliseconds).

2.1.5. Non-radiative transitions and temperature dependence

In the previous sections transitions between electronic states were discussed and explained using the configurational coordinate diagram. In that model, non-radiative transitions

occurred between energy levels separated by small energy gaps that could be bridged by emission of one phonon while for larger energy gaps radiative transitions occurred. However, these large energy gaps can also be bridged in non-radiative ways.

Radiative and non-radiative processes compete with each other affecting the luminescence. If a transition between two energy levels is considered as in Figure 2.1, de-excitation from the excited state has a probability rate:

$$W_{e \to g} = (W_R + W_{NR}) \tag{2.8}$$

where W_R and W_{NR} are the radiative and non-radiative transition probabilities. If the excited state has a population density of N_e electrons per unit volume, the rate of depopulation can be expressed as:

$$\frac{dN_e}{dt} = -(W_R + W_{NR}) \cdot N_e \tag{2.9}$$

The solution of this equation gives the number of electrons in the excited state as a function of time. If the intensity of the emission is assumed to be proportional to the number of electrons that relax in a radiative way, it can be calculated by:

$$I(t) = W_R N_{e0} e^{-(W_R + W_{NR})t} \tag{2.10}$$

The decay time constant (τ), which plays an important role in temperature measurements, is defined as:

$$\tau = \frac{1}{W_R + W_{NR}} \tag{2.11}$$

In the previous equations, the radiative rate of relaxation (W_R) is independent of temperature. However, the non-radiative transition probability depends on the temperature, which results in the quenching of the emission at high temperatures and the reduction of the lifetime decay. This last effect is the basis for the on-line temperature measurements using the lifetime decay method. The non-radiative transitions include emission of multiple phonons, cross-over relaxation or relaxation through a third energy level laying at similar energies. In the case of off-line temperature measurements, changes in the environment such as variations in the number of defects affect the non-radiative probability and thus the lifetime of the emission.

2.1.5.1. Multi-phonon emission

When the energy gap between two states is larger than the total energy of a single phonon, emission of more than one phonon is necessary to bridge the gap non-radiatively. For rare earth ions the probability of emission of multiple phonons is temperature dependent and can be described by [90]:

$$W_{NR}^p = W_{NR}^p(T = 0) \left(1 - exp\left(\frac{E_p}{k_B T}\right) \right)^{-p} \tag{2.12}$$

where E_p is the energy of the individual phonon, p the number of phonons involved, k_B is the Boltzmann constant and T the absolute temperature. From equation (2.12) it can be deduced that multi-phonon emission probability remains relatively constant at low temperatures but drastically increases at higher temperatures. In addition, this emission probability depends inversely on the number of phonons emitted, which explains why large energy gaps that involve larger number of phonons are more difficult to bridge by multi-phonon emission. The phonon energies of host materials used in phosphor applications are low (for example 650 cm^{-1} for YSZ [95]) so that many phonons become necessary to bridge the large energy gaps of rare earths ions and phosphors present high luminescence.

2.1.5.2. Crossover relaxation

In the configurational coordinate model in Figure 2.3, the energy level m in the excited state (point B) lies at energy below the cross-over point (X). This is the case for weak electron-lattice coupling. When the coupling is larger, point B might lay at higher energies than X. In this case electrons excited to point B start to relax to lower energy levels by emitting phonons. When the electron reaches the energy of the cross-over point the two states (ground and excited) mix and the electron "crosses" to a highly excited level of the ground state. Then it relaxes by emission of phonons to the equilibrium point of the ground state without any emission of light.

This cross-over relaxation can still happen when point B has lower energy than the cross-over point due to thermal activation. The probability of the transition from point B to point X is given by:

$$P_{B \to X} = s \cdot e^{-\frac{\Delta E}{k_B T}} \tag{2.13}$$

where s is a frequency factor [92], ΔE is the energy gap between the points B and X, k_B the Boltzmann constant and T the absolute temperature. For sufficiently high temperatures, electrons can populate vibrational levels above the cross-over point leading to non-radiative relaxation processes and the quenching of the luminescence.

2.1.5.3. Charge transfer state (CTS) and $4f^{n-1}5d^1$ states

In some cases a third electronic state is found at the same energy as the 4f and 3d energy levels of rare earths and transition metals, which participates in the luminescence process. For rare earths these energy levels are the charge-transfer state (CTS) and $4f^{n-1}5d^1$ levels. The CTS involves excitation of electrons in a neighbouring ion, which are then transferred into a 4f orbital, and $4f^{n-1}5d^1$ levels involve excitation of a 4f electron into a 5d orbital. These processes result in broad band absorption at around 300 nm and can also lead to direct luminescence from these states (for example 5d$\rightarrow$4f emission in Eu^{2+}) [92]. CTS transitions are found for the excitation of Eu^{3+} and f-d transitions for Pr^{3+} and Tb^{3+}. CTS are also present in transition metal ions but they are not as well understood as for rare earths [92].

2.1.5.4. Defects

The host lattice in real applications presents defects, such as intercalated water molecules and oxygen vacancies. These defects not only disturb the crystal field around the dopant ions but can also act as killer centres of the excitation energy therefore reducing the probability of the radiative transitions. Since defects normally have high energy phonons, they offer a non-radiative path for relaxation of the excitation energy. This excitation energy can be transferred from the rare earth ion to a defect and then rapidly released by multi-phonon relaxation. A higher concentration of defects is present at the surface of the crystal lattice. Here, different phonon modes are available since ions may interact with neighbouring impurity elements, which favours non-radiative relaxation.

In the presence of defects the lifetime decay of phosphors becomes faster (small value of the lifetime decay) as the non-radiative decay probability increases. This is especially relevant in thermal history phosphors in which the concentration of defects might vary before and after heat treatment due to evaporation of water, burning of organic compounds or oxygen absorption or adsorption. This elimination of defects results generally in an increase of the lifetime decay (slower lifetime decay) with heat treatment temperature.

2.1.6. Energy transfer
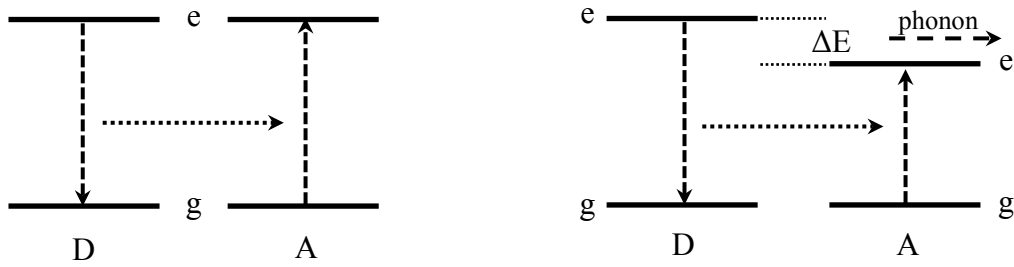
Figure 2.5. Energy transfer between donor (D) and acceptor (A) in the cases where the resonance condition is satisfied between excited (e) and ground (g) energy levels (left) and where the energy transfer is assisted by emission of a phonon of energy ΔE.

Energy transfer between unlike or identical luminescence centres can occur when they are located at a sufficiently short distance so that they can interact with each other. The mechanisms involved in the energy transfer between a donor (D) and an acceptor (A) are explained by Dexter's theory of resonant energy transfer [92, 96]. According to this theory energy transfer can occur when the energy difference between ground and excited states of D and A are equal (see Figure 2.5 left). This condition can also be regarded as the spectral overlap between the emission spectrum of D and the absorption spectrum of A, so that no energy transfer will occur if there is no spectral overlap between D and A.

In addition to the spectral overlap a certain interaction between D and A must exist. This interaction can be an electric multipolar interaction, in which the energy transfer probability is dependent on the distance (R) between D and A. This dependence varies with R^{-6}, R^{-8} and R^{-10} for dipole-dipole, dipole-quadrupole and quadrupole-quadrupole transitions respectively. Effective energy exchange is observed for allowed transitions between ions separated about 30 Å [96]. The probability of the electric multipolar interaction will become low if the transitions involved are not allowed and, in this case, exchange interactions may take place. These interactions are effective when the donor and acceptor are located sufficiently close to each other (less than 8 Å [96]), so that both wave functions overlap. For this type of interactions the distance dependence is exponential and the transition probability is not dependent on the type of optical transitions involved.

If the resonance condition is not completely satisfied and there is a small energy mismatch between the energy levels of D and A, as shown in Figure 2.5 right, a phonon-assisted energy

transfer might occur [92]. Here, the spectral overlap is low and the energy difference between energy levels of D and A is balanced by the emission or absorption of one or more phonons.

In practice, energy transfer can be used to increase the emission efficiency of some phosphors, which is called sensitisation of luminescence. The donor, also named sensitizer, effectively absorbs the excitation energy which is then transferred to the acceptor or activator which emits light. While sensitisation causes an increase in the emission intensity, if a similar process occurs in which the acceptor ion releases the energy in a non-radiative way (or light emission from this ion is undesirable) luminescence is quenched. In this case the acceptors are called luminescence killers or quenchers.

Furthermore, luminescence from phosphors is normally decreased when the concentration of the dopant ion is increased above a certain value. This process, known as concentration quenching, is thought to be caused by one of these mechanisms: the excitation energy is lost due to cross-over relaxation between dopant ions, the migration of excitation energy between activator ions increases with concentration so that the probability of reaching a luminescence killer is higher or activator ions become paired and changed to a quenching centre [90, 92]. However, in some phosphors the concentration can be increased to 100 % substitution of ions without any concentration quenching effect. This has been reported for example in $Tb_xLa_{1-x}P_5O_{14}$ [92].

Non-radiative energy transfer can be observed in the optical properties of the phosphor. For example energy transfer is evidenced if emission from the acceptor is observed when only the donor is selectively excited. Furthermore, in accordance with Equation (2.11) the non-radiative energy transfer from D to A makes the lifetime decay of the donor faster. However, the particular behaviour of the decay of the intensity depends on the energy transfer mechanisms between D and A involved in the process. A further discussion on this can be found for example in [90, 96].

2.2. Propagation of light through phosphor layers

The propagation of light through phosphor layers is of great importance to understand the functioning of phosphor coatings and has direct implications on the accuracy achievable in surface temperature measurements. When the excitation light enters a phosphor layer it is scattered multiple times by the phosphor particles before it is absorbed, and the same happens to the emitted light before it exits the phosphor layer.

Several methods can be applied to study the behaviour of the light within the phosphor layer, for example the Kubelka-Munk's theory, the Johnson method and the Monte Carlo method [92]. The Kubelka-Munk's model, which will be reviewed in the following section, simply considers the phosphor layer as a continuous optical medium and requires only two optical constants to characterise it: the scattering and absorption coefficients. Due to its relative simplicity, this theory has been used to develop a theoretical model that can predict the propagation of excitation and emission light across phosphor coatings. This model can be extended to predict the effect that thermal gradients across a phosphor coating have in the accuracy of a temperature measurement using the lifetime decay method [54, 95]. This effect in the accuracy is a consequence of the light coming from different regions within the coating which are at different temperatures due to the existing thermal gradient. The Kubelka-Munk's theory and the model developed to predict the propagation of light across phosphor coatings are introduced in the following sections. This model will be experimentally validated in different thermal gradient conditions and applied to the intensity ratio method in section 6.2.

2.2.1. Kubelka-Munk's model
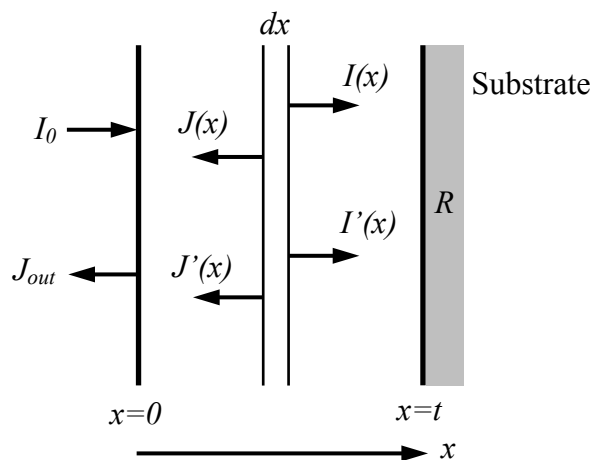
Figure 2.6. A schematic of the Kubelka-Munk's theory applied to a phosphorescent coating of thickness *t* deposited on a substrate with reflectivity *R*. Primes represent the phosphorescence emission light.

The Kubelka-Munk's model is a one dimensional model in which the light is considered to travel perpendicular to the coating surface, as depicted in Figure 2.6. The light entering the coating (I_0) is scattered and can travel in the positive or negative *x* direction, which is denoted by *I(x)* and *J(x)* respectively. The light propagating inside the coating layer can be scattered, absorbed or transmitted, which is described by the differential equations:

$$\frac{dI(x)}{dx} = -(k+s)I(x) + sJ(x) \tag{2.14}$$

$$\frac{dJ(x)}{dx} = (k+s)J(x) - sI(x) \tag{2.15}$$

These equations can be generalised for the case that incident light is diffuse and scattering of light occurs in all directions inside the phosphor layer by defining new coefficients $K = 2k$ and $S = 2s$ [92]. The solutions to the previous differential equations, in which the new coefficients are considered, are:

$$I(x) = A(1-\beta)e^{\alpha x} + B(1+\beta)e^{-\alpha x} \tag{2.16}$$

$$J(x) = A(1+\beta)e^{\alpha x} + B(1-\beta)e^{-\alpha x} \tag{2.17}$$

These equations, in which $\alpha = \sqrt{K(K+2S)}$ and $\beta = \sqrt{K/(K+2S)}$, describe the propagation of the excitation light across the phosphor coating. The constants A and B can be calculated using the boundary conditions $I(0) = I_0$ and $J(t) = R \cdot I(t)$, where t is the total thickness of the phosphor layer and R the reflection coefficient of the phosphor-substrate interface. If the phosphorescence is considered to be generated in both positive and negative x direction, the propagation of the emission light is governed by these equations:

$$\frac{dI'(x)}{dx} = -(K'+S')I'(x) + S'J'(x) + qK(Ae^{\alpha x} + Be^{-\alpha x}) \tag{2.18}$$

$$\frac{dJ'(x)}{dx} = (K'+S')J'(x) - S'I'(x) - qK(Ae^{\alpha x} + Be^{-\alpha x}) \tag{2.19}$$

In these equations q is the quantum efficiency of the phosphor and the prime symbol refers to the properties of the phosphor layer at the emission wavelength. The solutions for these equations, which represent the propagation of the emission light within the phosphor layer, are:

$$I'(x) = \frac{qKA}{\beta'}\frac{\alpha\beta' - \alpha'}{\alpha^2 - \alpha'^2}e^{\alpha x} - \frac{qKB}{\beta'}\frac{\alpha\beta' + \alpha'}{\alpha^2 - \alpha'^2}e^{-\alpha x} + A'(1-\beta')e^{\alpha' x}$$
$$+ B'(1+\beta')e^{-\alpha' x} \tag{2.20}$$

$$J'(x) = -\frac{qKA}{\beta'}\frac{\alpha\beta' + \alpha'}{\alpha^2 - \alpha'^2}e^{\alpha x} + \frac{qKB}{\beta'}\frac{\alpha\beta' - \alpha'}{\alpha^2 - \alpha'^2}e^{-\alpha x} + A'(1+\beta')e^{\alpha' x}$$
$$+ B'(1-\beta')e^{-\alpha' x} \tag{2.21}$$

The new constants A' and B' can be calculated with the boundary conditions $I'(0) = 0$ and $J'(t) = R \cdot I'(t)$.

2.2.2. KM model under thermal gradients

The Kubelka-Munk's model is useful to predict the phosphorescence intensities expected from a phosphor coating. Recently, the model has been employed to reconstruct the luminescence decay signal obtained from a phosphor coating under a thermal gradient [54]. In such a case, the phosphorescence decay emitted at the surface is a combination of the decays from different depths within the coating, each of which has a different lifetime because they are at different temperatures. Therefore, the overall decay is multi-exponential and the value of the lifetime decay measured at the surface corresponds to a temperature at a certain depth within the coating. The model in [54] assigns a depth to the phosphorescence signal which depends on the coating material, thermal gradient and the total coating thickness.

The model breaks down the whole coating into discrete layers and calculates the contribution of each layer to the total signal emission by considering that only the particular layer of study is phosphorescent, and the rest of the coating simply scatters or absorbs the light. If the contributions of each individual layer are added up the total emission intensity of a fully phosphorescent coating is obtained.

When a thermal gradient is considered, each of the layers emits light with a different decay rate because they are at different temperatures. If the lifetime decay calibration curve for the material is known from experiments and the model is used to calculate the total intensity emitted (which is considered to be the area under the decay curve), the individual decay curve of each layer can be computed. By adding up the decay curve from each layer the total signal emitted by the coating can be generated. The lifetime decay of this signal, which is multi-exponential, can then be calculated. When this lifetime decay is converted to temperature using the calibration curve, it has a value that corresponds to a temperature at a certain depth within the coating.

By using this model, the inaccuracies in the temperature measurements related to the presence of a thermal gradient across a phosphor coating can be predicted, which is useful during the design phase of as phosphorescent sensor. Although the validation of the model has been extensively discussed in [95] for single and dual layer YSZ coatings deposited by APS and EBPVD methods, no experimental results under a controlled thermal gradient are available for comparison with the theoretical model. This experimental validation of the model under

thermal gradients will be addressed later in this work and the results will be used to predict inaccuracies in a phosphorescent sensor that uses the intensity ratio technique rather than the lifetime decay method.

3. STATE OF THE ART OF BaMgAl$_{10}$O$_{17}$:Eu

Europium-doped barium magnesium aluminate (BaMgAl$_{10}$O$_{17}$:Eu^{2+} or BAM:Eu^{2+}) is a highly efficient blue phosphor first developed in 1974 for its use as a blue emitter in fluorescent lamps [97, 98]. Since then, it has been widely used in the lighting industry (see for example [99, 100] and references therein), with particular interest for the manufacture of plasma display panels (PDP) due to its high quantum efficiency and brightness. However, a problem arises related to the manufacturing processes of fluorescent lamps and PDPs, in which the phosphor is heated at temperatures in excess of 500 °C in air. This baking process results in a reduction of the emission efficiency and a change in the colour coordinates which is undesirable for lighting applications. Investigation of this thermal degradation has been the focus of great research effort in the past 20 years, which is reflected in the many publications available on this topic (see Table 3.1 at the end of the chapter).

Recently, this phosphor has found a potential application as a thermal history sensor based on the degradation process undergone at high temperatures. However, most of the previous research on this phosphor was designed to optimise it for lighting purposes and this needs to be carefully considered when extrapolating the results for the application of the phosphor as a thermal history sensor. A collection of the most relevant literature available about this material, which includes a description of its physical and optical properties, proposed degradation mechanisms and manufacturing methods, is provided in this chapter.

3.1. Crystalline structure and Eu sites

BaMgAl$_{10}$O$_{17}$ (BAM), sometimes referred to as BaMg$_2$Al$_{16}$O$_{27}$ [101], crystallizes in the *β*-alumina structure corresponding to the P6$_3$/*mmc* crystallographic group [102]. This structure, shown in Figure 3.1, consists of dense layers called spinel blocks alternated along the *c* direction by the less packed conduction layer (also called mirror plane). Spinel blocks contain oxygen, aluminium and magnesium ions, while the conduction layer is formed by barium and oxygen ions. The structure of the phosphor, with its conduction layer, favours the diffusion of cations [103], which plays an important role in the degradation mechanism of BAM:Eu^{2+}.

BAM:Eu^{2+} is synthesised under the assumption of a one-to-one substitution of Ba ions, which are located in the Beevers-Ross (BR) position, by Eu ions. However, more than one site is actually possible for Eu^{2+} ions into the BAM structure according to the literature. Although three sites are commonly cited, there is no agreement about the actual locations of these sites.
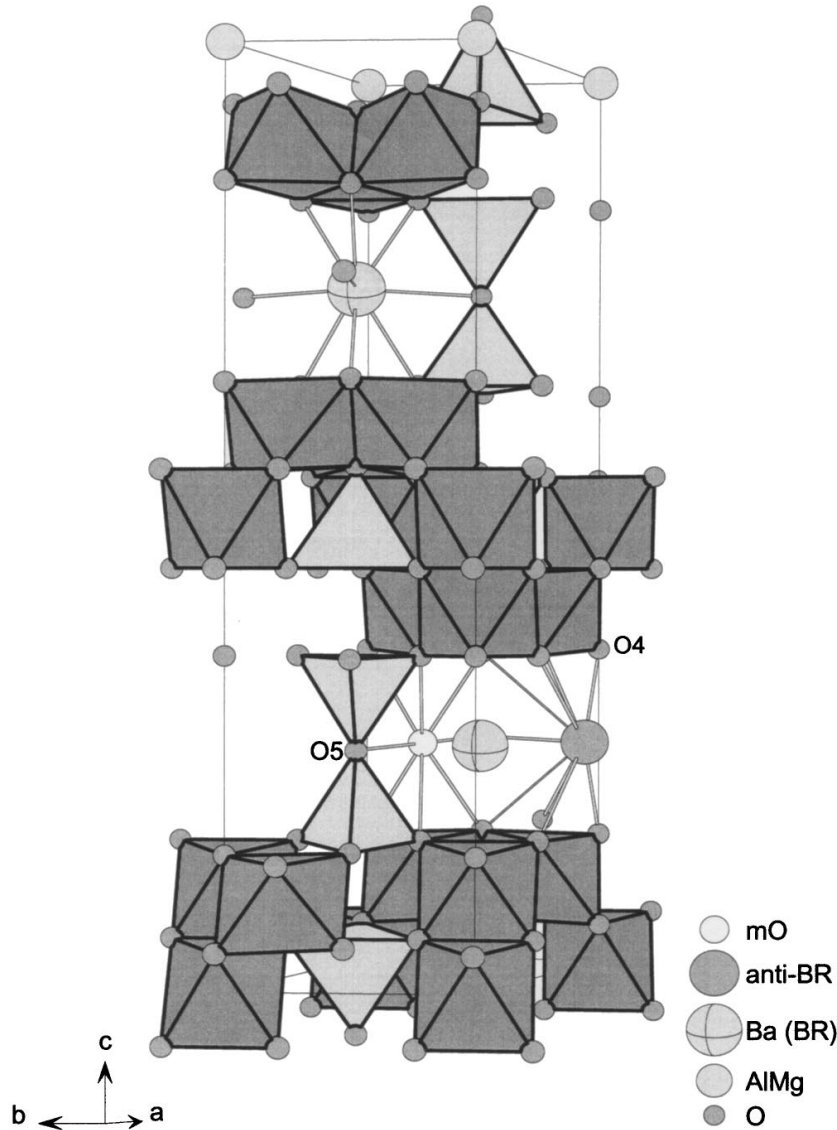
Figure 3.1. BAM crystallographic structure, reproduced from [102].

Ellens et al. [104] identified two or three possible sites for Eu^{2+} in the BAM structure based on spectroscopic studies on BAM:Sm^{2+} and the similarities between the Sm^{2+} and Eu^{2+} ions. Boolchand et al. [102] reported three possible sites for Eu^{2+} ions using ^{151}Eu Mössbauer spectroscopy. These sites were the Beevers-Ross (BR), anti-Beevers-Ross (aBR) and mid-oxygen (mO) sites (see Figure 3.1), and all three sites have a similar occupancy of about 20-30 %. Pike et al. [105] argued that occupancy of the third site is almost negligible in

BAM:Eu^{2+} and it is related to the presence of the $Ba_{0.75}Al_{11}O_{17.25}$ (BAL) phase. This BAL phase, which also crystallises in the β-alumina structure, forms a solid solution with BAM and modifies the optical properties and thermal resistance of the phosphor. A different study by Lambert et al. [106], based on synchrotron diffraction, suggested as the three possible sites for Eu^{2+} ion the near BR, the near mid-oxygen and the near O(5) sites, with an occupancy of 75 %, 14 % and 11 % respectively. The multiple locations of the dopant are responsible for the particular luminescence characteristics of the phosphor, and in particular might be responsible for the broad emission band characteristic of this phosphor as will be explained later. The thermal degradation might also affect each site differently as reported by Zhu et al. [107]. In this study the authors stated that the aBR site is more thermally stable than the BR site, which is located in a place where it is easier for the cation to move.

There is very little reference to the location of the europium ion after oxidation. Boolchand et al. [102] reported the presence of this ion even in fresh samples and provided evidence of the appearance of a new trivalent site after oxidation. However they do not allocate this site in the BAM structure. Wu and Cormack [108] numerically studied the formation of defects in the BAM structure due to the introduction of the dopant ion. The authors concluded that trivalent europium is thermodynamically more stable when substituting an aluminium ion in the spinel block, but the ion would need to migrate after oxidation from the original location in the conduction layer.

3.2. Phosphor degradation mechanism

The degradation of BAM:Eu^{2+} has been extensively studied for its use in fluorescent lamps and PDPs. In the manufacture of fluorescent lamps and PDPs the phosphor is heated in air at temperatures of about 700 °C and 500 °C respectively [99], which results in a decrease of blue light emission from the phosphor. Furthermore, during service the phosphor is excited using a Xe plasma discharge that generates vacuum ultraviolet (VUV) light [105]. This excitation also results in the reduction of luminous efficiency and a colour shift of the broad band emission. However, for its application as a thermal history phosphor the degradation under VUV irradiation [109, 110] is not relevant.

One of the first studies to investigate the mechanisms of degradation of BAM:Eu after baking in air is reported in [99]. The authors concluded that the decrease in emission was due to oxidation of Eu^{2+} to Eu^{3+}, which resulted also in the formation of a second phase

EuMgAl$_{11}$O$_{19}$ (magneto-plumbite). Observation of the second phase was made by XRD analysis and it was observed at annealing temperatures above 800 °C. They also reported that the luminance remained above 80 % of that of the untreated phosphor when the heat treatment was in N$_2$ atmosphere. Kim et al. [111] also reported the presence of the magneto-plumbite phase and calculated the mass fraction of this phase based on XRD and neutron data by Rietveld refinement. The amount of this phase was up to 12 % after treatment at 1200 °C for 1 hour (slow cool down). Shon et al. [112] studied the degradation of the luminance for samples treated at 500 °C for various times. They concluded that oxidation of Eu^{2+} was in this case a minor cause of degradation and suggested changes in the local environment of Eu^{2+} as the main cause of deterioration. They based this assumption in the uncorrelated decrease between Eu^{2+} concentration and emission intensity. Furthermore, they detected Eu in the trivalent state using X-Ray Absorption Near Edge Structure (XANES) even in untreated samples. Yamada et al. [113] proposed a different degradation mechanism for temperatures below and above 900 °C based on observations of the unit cell volume and its relation to the content of Eu^{2+} in the host lattice. Up to 900 °C, they proposed that degradation was caused by the formation of lattice vacancies (Schottky defect) and oxidation of Eu^{2+}. Above 900 °C, degradation was caused by the appearance of the magneto-plumbite phase.

A later study by Bizarri and Moine [114] analysed samples baked at temperatures between 300 °C and 1000 °C for 150 minutes. The authors concluded that the degradation mechanism of BAM:Eu consists of three steps. Firstly, oxygen atoms from the air atmosphere are adsorbed on the phosphor surface and fill oxygen vacancies. This idea is supported by the reduction of surface traps observed in the thermoluminescence spectra. The second step consists in the diffusion of Eu^{2+} atoms through the conduction layer and towards the surface, which is favoured at high temperatures. Finally, there is an electronic transfer from the divalent europium to the adsorbed oxygen ions that results in the formation of Eu^{3+} ions, which are observed by the authors in the optical properties of the phosphor (emission, reflectance and excitation) and Electron Spin Resonance (ESR) spectra. This process is further supported by the negligible degradation observed by the authors in a non-oxidizing (Ar/H$_2$) atmosphere, which is also corroborated by other studies [115, 116].

Additionally, Lacanilao et al. [100] measured the concentration of the different ions from the surface to the bulk material by X-ray Photoelectron Spectroscopy (XPS). They concluded that Eu^{3+} is mainly formed at the surface (as Eu$_2$O$_3$), where the concentration of Eu^{2+} for baked

samples is close to zero. Because of the difference in concentrations, Eu^{3+} ions rapidly diffuse through the conduction layer to the bulk material and Eu^{2+} ions in the opposite direction so that these ions further oxidise when they reach the surface. At the same time, Ba^{2+} ions also diffuse to the bulk material to maintain the local charge equilibrium. This 2D cation diffusion in the conduction layer is supported by the high values of the cation mobility in β-alumina structures for Ba^{2+} and Sr^{2+}, the last one with almost the same ionic radius as Eu^{2+}.

Mishra et al. [117, 118] suggested that the presence of water might also contribute to the degradation of the BAM:Eu^{2+} emission. According to their findings, the water molecules enter the BAM:Eu^{2+} lattice and dissociate to OH^- and $(H_2O)H^+$ groups. The released protons are then responsible for the oxidation of the Eu^{2+} ions. The authors observed a decrease in emission intensity of BAM:Eu after humidification at only 450 °C, which was accompanied by a green shift of the emission broad band. They also accounted for an increase in the amount of Eu^{3+} ions by [151]Eu Mössbauer spectroscopy, although they could not detect any luminescence from these ions. They argued that Eu^{3+} ions are present even in fresh samples but their emission is undetectable.

Finally, some studies [119, 120] claim that migration of Eu^{2+} ions to the spinel block at high temperatures is also a cause of the thermal degradation of the phosphor intensity. This is observable when the phosphor is excited via the spinel block at 147 nm (see section 3.3.1) since it shows a new emission peak at 513 nm. However, when the phosphor is excited directly in the dopant by using 254 nm light, the Eu^{2+} migrated to the spinel block is not excited and more light is emitted at 445 nm.

3.3. Optical properties

The optical properties of BAM:Eu^{2+} are well-known due to its application as a blue emitter in the lighting industry. Here, a brief review of the excitation and emission properties of BAM:Eu is introduced as the starting point for its use as a thermographic phosphor. The evolution of these properties after baking at high temperatures is then explained in order to justify the election of this phosphor as a candidate for thermal history sensing.

3.3.1. Excitation

BAM:Eu^{2+} can be effectively excited using light in a wide range of wavelengths from about 120 nm to 400 nm, although the excitation mechanisms are different at each wavelength region. According to Howe et al. [110], excitation up to about 190 nm occurs via energy

transfer from the host (BAM) to the activator (Eu^{2+}). This can be observed in Figure 3.2, where the excitation and emission spectra of undoped BAM are illustrated. The emission of undoped BAM, centred at around 270 nm overlaps with the absorption of Eu^{2+} ions, and therefore energy can be effectively transferred to the dopant. Within the wavelength range up to 190 nm, excitation below 150 nm occurs via the spinel block, while excitation from 150 nm to 190 nm is related to absorption of energy by Ba-O groups.
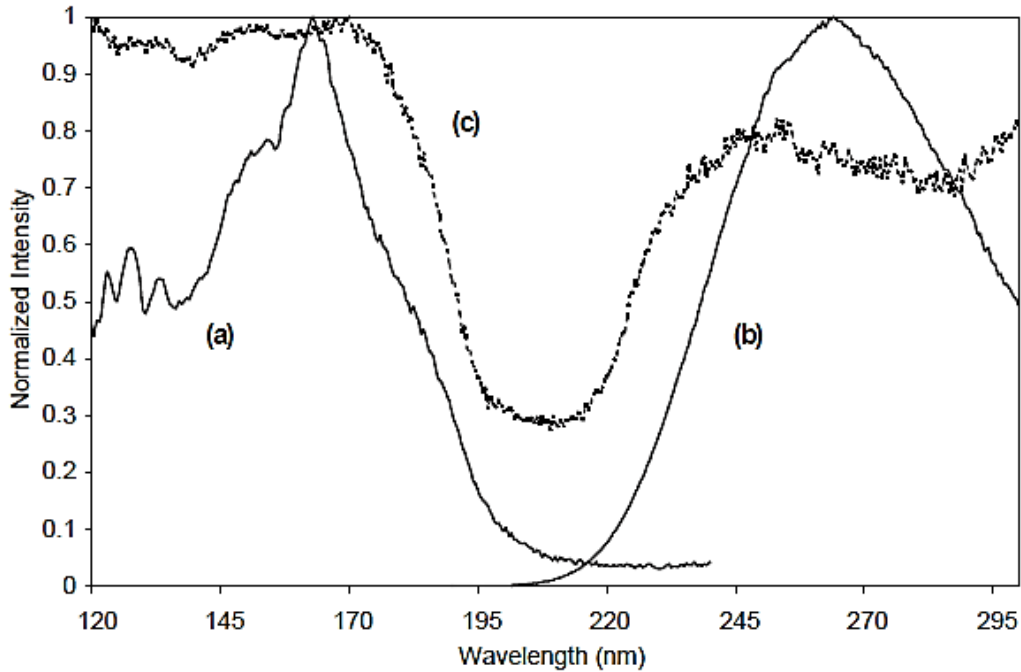
Figure 3.2. (a) Excitation (λ_{em}=260nm), (b) emission spectra (λ_{ex}=160nm) of BaMgAl$_{10}$O$_{17}$, and (c) the excitation spectrum of Ba$_{0.95}$MgAl$_{10}$O$_{17}$:Eu$_{0.05}$ (λ_{em}=450nm). Reproduced from [110].

Excitation at wavelengths above 220 nm occurs directly into the Eu^{2+} activator ions. Excitation of the phosphor is possible at wavelengths as long as 400 nm when the excitation efficiency drops to about 40 % of the maximum [121]. Mishra et al. [121] theoretically decomposed the experimental excitation spectrum of BAM:Eu in seven Gaussian peaks. Each of these peaks was related to one of the three theoretical sites occupied by Eu^{2+} ions in the BAM lattice. They discussed the possibility of exciting individual sites using excitation light of a particular wavelength, but this idea was not experimentally tested. A similar study was developed by Yoshida et al. [122].

The mechanism of excitation of Eu^{3+} ions in BAM is not discussed in the literature to the knowledge of the author. However, it can be speculated that direct excitation via CTS can be achieved by light at around 253 nm [92]. Additionally, excitation at different wavelengths can be expected by energy transfer from Eu^{2+} to Eu^{3+} ions. This energy transfer was revealed

during this work as absorption dips in the otherwise featureless emission spectra of BAM:Eu^{2+} (see spectra in Figure 5.4).

3.3.2. Emission

BAM:Eu^{2+} emits light in a featureless broad band centred at approximately 450 nm, as shown in Figure 3.3. This broad band is due to the partially allowed transitions from the $4f^65d^1$ to the $4f^7$ level of divalent europium ions, which are greatly affected by the crystal environment. These transitions result in a fast emission whose lifetime decay constant is normally reported to be around 1 µs [57, 63, 123-126]. The shape of the emission band is reported to be the same under 147 nm and 254 nm excitation [105]. In this work, it is further verified that this broad band remains invariable when the excitation wavelengths changes from 266 nm to 355 nm, as shown in Figure 3.3.
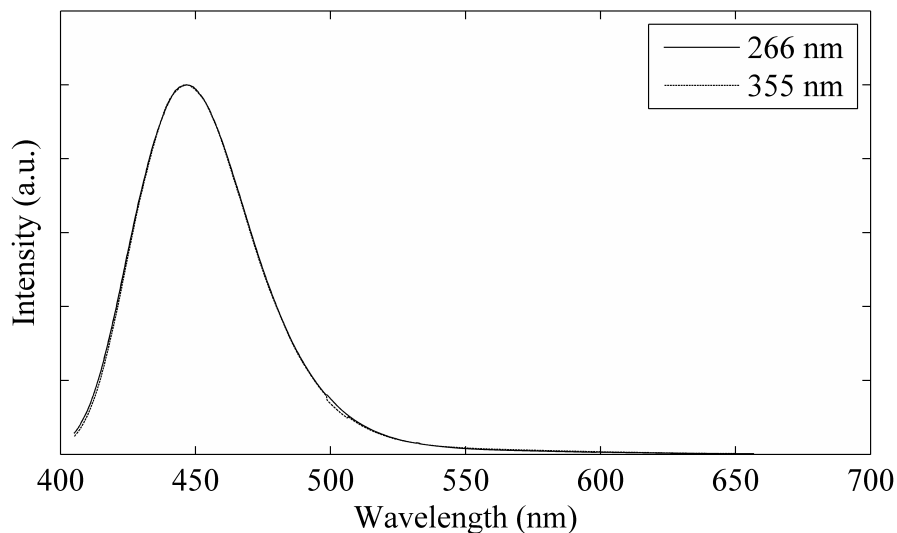
Figure 3.3. Emission spectra of commercial BAM:Eu^{2+} after excitation at 266 nm and 355 nm. The two curves overlap and cannot be distinguished.

The asymmetry of this broad band is as a result of the multiple site occupancy of Eu^{2+} ions in the crystal lattice, as reported by Mishra et al. [117]. They rejected the possibility of the asymmetry being caused by a weak electron-phonon coupling or reabsorption of the emission in the short wavelength range. On the contrary, they stated that the asymmetry of the emission band of BAM:Eu is due to the presence of multiple luminescence centres, in which the europium ions experience different crystal field strengths as a result of variations in their environment, and specially due to differences in the surrounding oxygen ions. According to their assumptions, the emission of each of the sites could be represented by a Gaussian function, with the broad band being the result of the superposition of the multiple curves.

Therefore, they successfully modelled the experimental spectra of BAM:Eu^{2+} samples with more than one area-normalised Gaussian. A good fit was obtained with two or more Gaussian curves, but the physical relevance of these multiple curves could not be confirmed by using this method. The various studies in section 3.1 suggest that more than three curves may not have any physical meaning.

The shape of the emission broad band is sensitive to variations in the stoichiometry of the host. As was discussed in section 3.1, Pike et al. [105] studied the solid solution formed by BAM and BAL phases. When this second phase is present, a green shift of the emission spectra is clearly observable and the tail of the broad band extends to the red part of the spectrum. Pike et al. [105] actually fitted three Gaussian curves for different compositions of the BAM-BAL (Ba$_{0.75}$Al$_{11}$O$_{17.25}$:Eu^{2+}) solid solution and related each peak to the emission of the different sites: BR site (448 nm), aBR site (475 nm) and a third site related to the formation of BAL (538 nm).
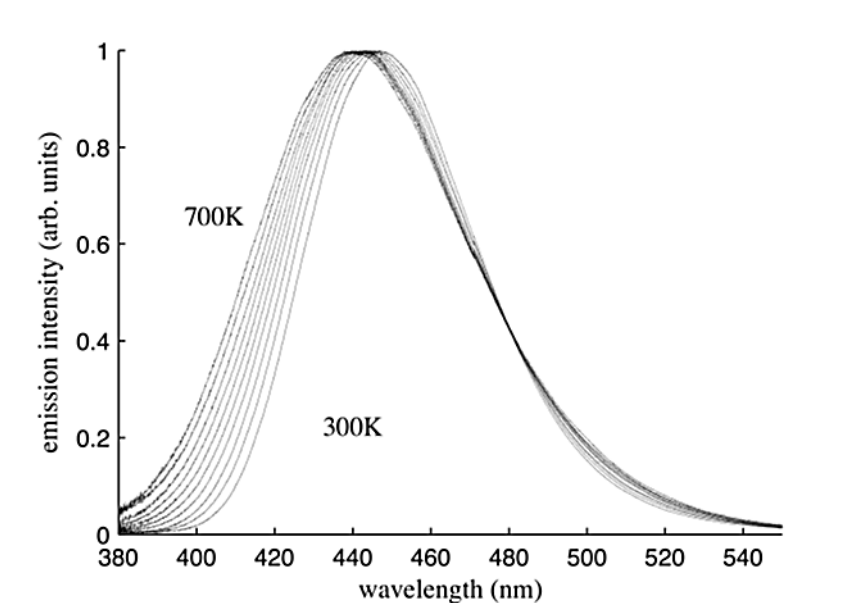
Figure 3.4. Normalised intensity of the BAM:Eu^{2+} emission with increasing temperatures in air and excited at 355 nm. Reproduced from [126].

The emission spectrum of BAM:Eu shifts and broadens towards the UV region when the temperature is increased, as depicted in Figure 3.4 [126], which can be used for on-line temperature mapping by applying an intensity ratio technique. This variation of the spectrum is thought to be caused by a change in the crystal field experienced by the dopant ions as the host lattice expands, which modifies the position of the 4f^{6}5d^1 levels. In addition to the change of the spectrum, the intensity of the emission is quenched when the temperature

increases, and at about 700 °C it decreases below 10 % of the intensity at room temperature [126]. The absolute intensity of the broad band emission of BAM:Eu^{2+} is also dependent on dopant concentration, and the maximum intensity is found when the concentration is about 11 mol % Eu [124].

3.3.3.   Permanent changes after heat treatment

The emission spectrum of BAM:Eu^{2+} depends on the temperature and atmosphere in which the material is heat treated. When BAM:Eu^{2+} is heated in air, oxidation of Eu^{2+} to Eu^{3+} occurs [99, 111, 112, 114]. This oxidation results in a decrease of the broad band emission intensity at 450 nm and the appearance of emission peaks from 550 nm to 750 nm, which are ascribed to the electronic transitions from the $^5D_0$ to the ^7F_J (J=0,1,2,3,4) electronic levels of Eu^{3+} [69, 114]. In contrast, if BAM:Eu^{2+} is heated in a reducing atmosphere, such as in a mixture of N_2/H_2, the intensity of the emission remains above 90 % of that of the untreated BAM:Eu^{2+}, even when the heat treatment is at temperatures of 1500 °C [116]. According to this study [116], heat treatment in N_2 atmosphere results in a reduction of emission intensity with increasing temperatures up to 1200 °C with a recovery of intensity (more than 100 % of the initial intensity) above this temperature. They suggest that this could be related to the effect of adsorbed oxygen and self-reduction of Eu^{3+}.

It is also reported that a red shift of the broad band emission occurs when BAM:Eu^{2+} is heat treated in air, while a blue shift of the emission spectrum occurs after heat treatment in a reducing atmosphere [115]. These shifts are explained in terms of variations in the crystal field strength acting on the Eu^{2+} ions due to changes in their environment. Oxygen vacancies are likely to be formed during the reduction heat treatment. Some oxygen atoms in the BAM lattice act as a link between two neighbouring spinel blocks and their removal weakens the bonding between the spinel blocks and therefore reduce the crystal field acting on the europium ions, which explains the blue shift of the spectrum [115]. The opposite would be true when the oxygen vacancies are filled during oxidation of the phosphor.

There are two features in the emission spectrum of BAM:Eu that appear after heat treatment of the material in air and are rarely reported in the literature. These are the appearance of an additional emission peak at 513 nm and a dip at approximately 465 nm in the broad band emission of BAM:Eu^{2+}.

The 513 nm emission peak, reported in [116, 119], is only observable when the phosphor is excited with light of 147 nm, as opposed to the 254 nm excitation light used in most of the

studies of BAM:Eu. This additional peak is thought to be related to the migration of Eu^{2+} ions from the conduction layer to the spinel block upon heating. Because the 147 nm excitation is absorbed by the spinel block, energy transfer to Eu^{2+} located in this region can occur and the emission peak at 513 nm is observed. However, when the 254 nm excitation is used, the Eu^{2+} located in the compact spinel block cannot absorb light and the emission peak is not visible.

The dip around 465 nm in the emission spectrum of BAM:Eu^{2+} was reported by Zych et al. [123] and also observed during the current research. Zych et al. [123] identified this dip as the $^7F_0 \rightarrow ^5D_2$ absorption of the residual Eu^{3+} present in BAM after vacuum-sintering a pressed pellet at 1750 °C for 5 h. This feature strongly suggests that excitation of Eu^{3+} ions occurs via energy transfer from Eu^{2+} ions, although additional excitation mechanisms cannot be excluded.

3.4. Manufacturing processes

There are several methods that can be used to manufacture BAM:Eu^{2+}, each of which presents some advantages and disadvantages. The preferred method for lighting application is the solid state reaction [99, 101]. This technique consists of mixing and firing the precursors (oxides and carbonates) and a small amount of flux (MgF_2, AlF_3 or LiF) at about 1500 °C – 1600 °C in a reducing atmosphere (95 % of N_2 / 5 % of H_2). By selecting the fluxes, the particle size and shape can be controlled, and therefore the luminescent properties of the phosphor changed [127]. Generally, particles with the shape of a hexagonal plate are obtained by this method, such as the commercial BAM:Eu^{2+} used in this work. Very high temperatures are necessary to obtain high crystallinity and phase purity, and the reducing atmosphere is necessary to obtain a dopant in the divalent state of oxidation (Eu^{2+}).

This phosphor has also been successfully manufactured by other methods. These include the sol-gel method [107, 128-131], in which the phosphor is synthesised from a liquid solution of the precursors which is then dried and sintered. The heat treatment temperature necessary for the calcination of the phosphor in this method is notably lower than in the solid state reaction, and it is reported to be of only 1400 °C. However the reducing atmosphere is still necessary to obtain the correct oxidation state of the europium ions. It is also reported that phosphors made by this method are brighter and more resistant to thermal degradation.

Another method is spray-pyrolysis [113, 132], by which hollow and dense spherical particles are obtained at heat treatment temperatures of 1400 °C. On the other hand, the combustion

synthesis method [133, 134] permits the production of the phosphor at very low temperatures (~ 500 °C) and short times (~ 5 min). Although this process is simple and inexpensive, the shape of the particles obtained is irregular and the particle size distribution broad. Furthermore, the luminescence emission is lower compared to a commercial phosphor manufactured by the solid state process (about 68 % [134]), and further heat treatment at high temperatures is necessary to achieve properties similar to commercial phosphors.

3.5. BAM:Eu thin films

To the author's knowledge, the first report about deposition of BAM:Eu phosphor in thin films is the work by Golego et al. [135], in which successful deposition of BAM:Eu^{2+} thin films on different substrates is achieved by the spray pyrolysis method. The thicknesses of the films varied between 1 μm and 10 μm. Successful deposition of the phosphor was achieved at temperatures above 300 °C and below 550 °C, but formation of crystallised BAM phase occurred only after annealing at high temperatures in excess of 1200 °C. Furthermore, after deposition only red luminescence from oxidised Eu^{3+} was observable and heat treatment in a reducing atmosphere (H$_2$/N$_2$) was necessary to obtain the blue broad band emission characteristic of BAM:Eu^{2+}. The substrates utilized in this work were: Corning 7059 glass, quartz, indium-tin oxide coated glass, single-crystalline silicon and aluminosilicate ceramic plates, which withstand the high temperatures necessary for the heat treatments.

A subsequent study on thin films of BAM:Eu is the one by Sohn et al. [136], in which films from 0.3 μm to 1.2 μm were deposited by pulsed laser deposition, a PVD method. The phosphor was successfully deposited on quartz glass substrates in a vacuum and in oxygen atmospheres with partial pressures from 50 to 200 mTorr. Best results in terms of phase purity and luminescence were obtained in the vacuum, while a second phase (Ba,Mg)Al$_2$Si$_2$O$_8$ was observed when the films were deposited in the presence of oxygen. This phase, which was thought to originate due to reaction with the substrate, showed an emission band at about 380 nm. Authors suggest a minimum value for the laser energy density that should be employed (> 2.3 J/cm^2) in order to obtain good phase purity, and they also suggest that a further heat treatment in a reducing atmosphere at 1200 °C for 2 h is useful in terms of luminescence emission efficiency.

The author is not aware of any other relevant work regarding thin or thick film deposition of the phosphor BAM:Eu and especially no attempt has been previously made to deposit this

material in a metallic substrate. It seems that technical difficulties to obtain the exact stoichiometry in the final product are the main limiting factor for PVD processes. Furthermore, the necessary annealing at high temperatures in a reducing atmosphere is a compromising factor for successful deposition on metallic substrates.

3.6. BAM:Eu as an on-line TP

The phosphor BAM:Eu has been mainly used as an on-line thermographic phosphor due to the spectral broadening that it experiences with increasing temperatures, which permits the definition of a temperature sensitive intensity ratio between two spectral lines. Additionally, its short lifetime decay (~ 1 μs) makes it suitable for combustion environments where contributions from background emission are high and short exposure times of the detection system desirable. Sarner et al. [125] investigated BAM:Eu amongst other blue emitting thermographic phosphors. They characterised a temperature sensitive intensity ratio between two spectral lines (centred at 400 nm and 456 nm) up to temperatures of 1150 K. Calibration of the lifetime decay was also performed, which showed sensitivity from approximately 700 K (~ 1 μs) to 1150 K (~ 10 ns). However the authors did not consider the effect of oxidation of the phosphor at high temperatures during the calibration of the curves. Further work by Linden et al. [137] studied the precision in 2D temperature measurements using this phosphor in the temperature range from 280 K to 470 K.

A new technique, known as thermographic Particle Image Velocimetry (PIV), has been developed at Imperial College based on the use of BAM:Eu [126]. This technique combines the temperature sensitive phosphorescence shown by thermographic phosphors with a conventional PIV technique that relies on the seeding of solid tracer particles. Therefore, it makes possible simultaneous 2D temperature and velocity measurements in turbulent flows by means of a single tracer and a relatively simple set-up [57]. The fast lifetime decay of the phosphor allows the technique to expand to high speed measurements in the kHz rate [58]. Additionally, BAM:Eu phosphor has been used to exemplify the characterisation of particles that can be used in this technique and their performance [59].

3.7. Summary of literature on BAM:Eu

Table 3.1. Summary of the literature about thermal degradation of BAM:Eu^{2+} and relevant findings

Author	Year	Manufacturing process	BAM composition	Excitation wavelength	Heat treatment	Degradation mechanism	Relevant findings
Oshio et al. [99]	1998	Solid state reaction (N$_2$/H$_2$)	10 % Eu	253.7 nm	500 °C – 1600 °C 1 h Air and N$_2$	Oxidation of Eu^{2+} to Eu^{3+} and formation of Eu(III)MgAl$_{11}$O$_{19}$	- ESR and XANES support the reduction of Eu^{2+} and increase of Eu^{3+} concentration.
Ellens et al. [104]	2001	-	-	-	-	-	- Two or three different sites identified in BAM:Sm at liquid helium temperature. Can be extrapolated to Eu due to the similar radius of Sm and Eu
Boolchand et al. [102]	2002	-	6, 12 and 20 % Eu	-	600 °C – 40 min 1000 °C – 6 and 12 h Air	-	- Identification of Eu^{2+} sites in BAM using Mössbauer spectroscopy: • Beevers-Ross (BR) • Anti-Beevers-Ross (aBR) • Mid-Oxygen (mO)
Sohn et al. [112]	2002	-	KX-501A, Kasei Optonix, Ltd.	147 nm	500 °C 1, 5 and 10 h Air	Local structure change in the surroundings of Eu^{2+} ions	- XANES support the reduction of Eu^{2+} and increase of Eu^{3+} concentration. - Decrease in Eu^{2+} concentration is not proportional to decrease in luminescence intensity for 1 h treatment.

Author	Year	Manufacturing process	BAM composition	Excitation wavelength	Heat treatment	Degradation mechanism	Relevant findings
Kim et al. [111]	2003	Solid state reaction (N_2/H_2)	2.25 wt. % Eu	254 nm	500 °C – 1400 °C – 1 h – Air / 700 °C – 1 h – N_2	Oxidation of Eu^{2+} to Eu^{3+} and formation of $Eu(III)MgAl_{11}O_{19}$	- EPR and XANES support the reduction of Eu^{2+} and increase of Eu^{3+} concentration.
Pike et al. [105]	2003	Solid state reaction (N_2/H_2)	10 % Eu BAM-BAL solid solution: $\left(1 - \frac{3}{11}x\right)BaO \cdot Mg_{1-x}Al_{10+(2/3)x}O_{16}$ x = 0, 0.51, 1	147 nm 254 nm	-	-	- Emission spectra of BAM under 147 and 254 nm are almost identical - Evaluates the evolution of emission spectra for BAM-BAL solid solution (there is a red shift when BAL is formed) - Three Eu^{2+} sites are identified: Beevers-Ross, anti-Beevers-Ross and a third site that is thought to be Eu^{2+}-O_{Ba} or Eu associated with Al^{3+} vacancies in the spinel block
Yamada et al. [113]	2004	Spray pyrolysis method (Ar/H_2)	$Ba_{0.90}Eu_{0.10}MgAl_{10}O_{17}$	335 nm	500 °C – 1300 °C 2 h Air	< 900 °C – Schottky defect and oxidation of Eu^{2+} > 900 °C – formation of $Eu(III)MgAl_{11}O_{19}$	- Spectrum peak shifts towards UV at 700 °C - Lattice strain released at 1100 °C
Zhang et al. [109]	2004	Solid state reaction (N_2/H_2)	$Ba_{0.90}Eu_{0.10}MgAl_{10}O_{17}$	147 nm 254 nm	500 °C 30 min and 30 h Air +VUV irradiation – 65 h	Baking – oxidation of Eu^{2+} VUV – damage on the surface of BAM host	- Emission intensity is more affected under 147 nm excitation than under 254 nm

Author	Year	Manufacturing process	BAM composition	Excitation wavelength	Heat treatment	Degradation mechanism	Relevant findings
Howe and Diaz [110]	2004	-	Undoped BAM 1 and 5 % Eu	147 nm 160 nm	500 °C 1 h Air +VUV irradiation – 1 h	Baking – Oxidation of Eu^{2+} to Eu^{3+} VUV – reduces excitation of BAM	Excitation: - <150 nm in the spinel block - 150 nm and 190 nm in the host (Ba-O groups in the cation layer) - >190 nm in activator Eu
Bizarri and Moine [114]	2005	-	7 % Eu	305 nm	300 °C – 1000 °C 150 min Air	Three-step mechanism: - Adsorption of O_2(g) in an oxygen vacancy - Diffusion of Eu^{2+} through the conduction layer - Electronic transfer from Eu^{2+} to O_2(g)	- Defects play a role in degradation, and the number of defects decrease with temperature - Treatment in Ar/H_2 affects emission intensity less than 5%
Mishra et al. [117]	2005	Solid state reaction (reducing conditions)	8 % and 12 % Eu	147 nm 250 nm	Humidification: 425 °C – 2 h +VUV irradiation – 1 h	Due to presence of H_2O: $2(Eu_{Ba}^{3+})' + 2(Ba_{Ba}^{2+} - -OH^-)^{\cdot} \leftrightarrows 2(Ba_{Ba}^{2+})^x + 2(Eu_{Ba}^{2+})^x + \frac{1}{2}O_2 \uparrow + \frac{1}{2}H_2O \uparrow$	- Eu^{3+} is present even in untreated samples but emission is not observable - Hydration of BAM causes degradation of luminescence intensity - Asymmetry of emission band is thought to be due to multiple luminescent centres

Author	Year	Manufacturing process	BAM composition	Excitation wavelength	Heat treatment	Degradation mechanism	Relevant findings
Wang and Zhang [119]	2005	Solid state reaction (N$_2$/H$_2$)	10 % Eu	147 nm 254 nm	500 °C – 1000 °C 1 h Air	- Oxidation of Eu^{2+} to Eu^{3+} - Migration of Eu^{2+} to spinel block	- No second phase was observed at 1000 °C - Migration of Eu^{2+} to the spinel block is observed in the emission as a distinct feature at 513 nm (observable only under 147 nm excitation)
Mishra et al. [118]	2006	-	-	-	-	Due to intercalated water molecules	- Theoretical investigation of thermodynamical stability of water molecules into BAM structure.
Yoshida et al. [122]	2007	Solid state reaction (N$_2$/H$_2$)	Ba$_{1-x}$Eu$_x$MgAl$_{10}$O$_{17}$ x=0 to 0.2	173 nm			- Experimental and theoretical investigation of absorption spectra - Absorption peaks are ascribed to absorption of ions in different sites
Zhang et al. [120]	2007	Solid state reaction (N$_2$/H$_2$)	10 % Eu	147 nm 254 nm	500 °C 1 h to 10 h Air	- Oxidation of Eu^{2+} to Eu^{3+} - Migration of Eu^{2+} to spinel block	- Different emission after heat treatment of the phosphor under excitation at 147 nm and 254 nm

Author	Year	Manufacturing process	BAM composition	Excitation wavelength	Heat treatment	Degradation mechanism	Relevant findings
Lambert et al. [106]	2008	Solid state reaction (Ar/H$_2$)	Ba$_{0.9}$Eu$_{0.1}$MgAl$_{10}$O$_{17}$	-	-	Migration of activator ion from the BR site	- Three sites (and estimated occupancy) identified for Eu^{2+} in BAM using synchrotron diffraction: • near-Beevers-Ross (nBR) – 75 % • near-mid-oxygen – 14 % • near-O(5) – 11 %
Zhu et al. [107]	2008	Sol-gel	1, 5, 10 and 18 % Eu	254 nm 310 nm	600 °C – 1400 °C 2 h Air and reducing atmosphere	Oxidation of Eu^{2+} to Eu^{3+}	- aBR site is thought to be more stable than BR against thermal degradation, but requires higher temperature and Eu concentration to be populated - BAM:Eu is more stable against thermal degradation if Eu concentration increases - Eu^{3+} reduction to Eu^{2+} achieved treating the phosphor in a reducing atmosphere (CO)
Wu et al. [138]	2008	Solid state reaction (N$_2$/H$_2$)	Ba$_{1-x}$Eu$_x$MgAl$_{10}$O$_{17}$ x=0 to 0.05	-	300 °C – 600 °C 0.5 h – 72 h Air 300 °C – 1100 °C 1 h Argon	Migration of Eu^{2+} ions and oxidation caused by oxygen	- Colour coordinates of BAM change after heat treatment from temperatures of 300 °C to 1100 °C

Author	Year	Manufacturing process	BAM composition	Excitation wavelength	Heat treatment	Degradation mechanism	Relevant findings
Liu et al. [128]	2009	Sol-gel	10 % Eu	254 nm	Manufacture: 1300 °C 4 h or 8 h N$_2$/H$_2$, N$_2$ and Air - Degradation 550 °C 1 h - Air		- Reduction of Eu^{3+} to Eu^{2+} in a non-reducing atmosphere explained by the model of charge compensation mechanism
Kim and Kang [115]	2010	Solid state reaction (Active carbon)	10 % Eu	147 nm	500 °C 1 h Air, active carbon, H$_2$/N$_2$ and N$_2$ +200 V discharge	In air: Oxidation of Eu^{2+} to Eu^{3+} In reducing conditions: Oxygen vacancies generated due to reduction of oxygen in the BAM structure	- Atmosphere was the major factor affecting degradation - Treatment in air: red shift of emission - Treatment in N$_2$ or N$_2$/H$_2$: blue shift of emission
Liu et al. [116]	2010	Solid state reaction (N$_2$/H$_2$)	10 % Eu	147 nm	500 °C – 1500 °C 1 h Air, N$_2$ and N$_2$/H$_2$	Lattice vacancies similar to Schottky defect brought by introduced oxygen ions	- Emission intensity degradation in air and N$_2$ (up to 1200°C) - No emission intensity degradation in N$_2$/H$_2$

Author	Year	Manufacturing process	BAM composition	Excitation wavelength	Heat treatment	Degradation mechanism	Relevant findings
Lacanilao et al. [100]	2013	Flux post-treatment of spray dried suspension	$Ba_{0.9}Eu_{0.1}MgAl_{10}O_{17}$	266 nm	600 °C Various times Air	2D diffusion of cations in the conduction layer: Ba, Eu^{2+} and Eu^{3+}	- Three sites (nBR, nmO and nO5) - nO5 site almost disappears after baking - Eu^{2+} concentration on the surface is negligible - Eu^{3+} concentration decreases with depth - Diffusion of Eu ions in the conduction layer - On cooling, oxidation stops at around 500°C

4. INSTRUMENTATION

In this chapter the instrumentation and techniques relevant to the development of this work are discussed. Firstly, the equipment necessary for the luminescence characterisation of thermographic phosphors is described. Then, the instrumentation employed to heat the multiple samples at high temperatures and under different gas atmospheres is explained in detail. Finally, the material characterisation techniques relevant to this work are briefly introduced.

4.1. Luminescence characterisation

The equipment employed for the optical characterisation of thermographic phosphors is described in this section. A typical set-up (Figure 4.1) consists of a light source which excites the phosphor; detection devices to collect the luminescence and transform it into an electric signal; and an analogue-to-digital converter that digitises the electric signal which is then stored and post-processed in a computer.
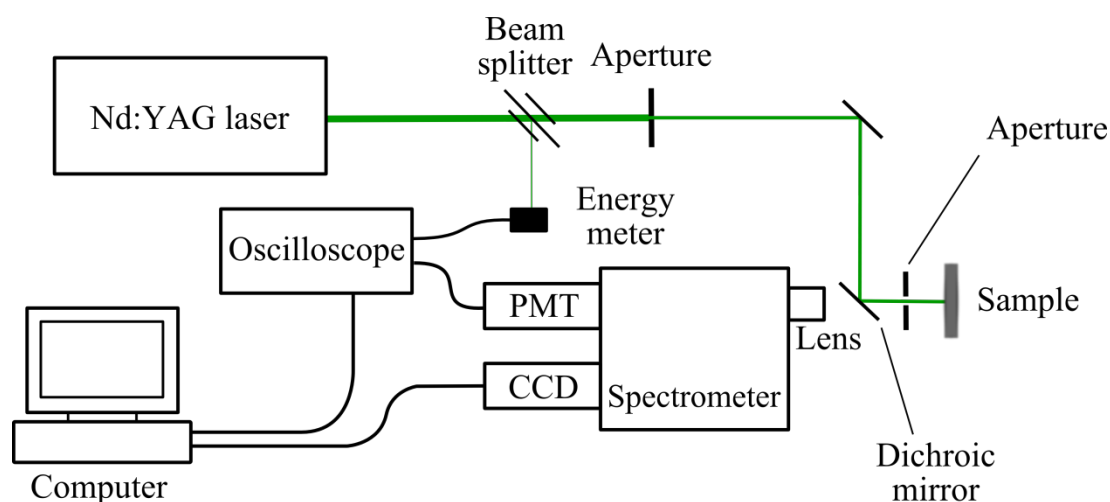
Figure 4.1. Typical set-up employed for luminescence characterisation in this work.

4.1.1. Excitation

The excitation of the thermographic phosphors employed in this work is achieved by using a pulsed Nd:YAG laser. This is a solid state laser which uses Nd^{3+} doped rods as the active medium. This medium is optically pumped by flash lamps and the amplification of light is achieved by building a population inversion as depicted in the four-level system in Figure 4.2. In this four-level system electrons are promoted to an excited state and then they quickly relax

to the $^4F_{3/2}$ level of Nd^{3+} where they stay for a relatively long time. At that point electrons decay to the $^4I_{11/2}$ level by emitting a photon at 1064 nm. The residence time in this $^4I_{11/2}$ level is short and electrons quickly relax to the ground state. It is therefore possible to build a population inversion between the two mentioned energy levels and light can be amplified at 1064 nm.
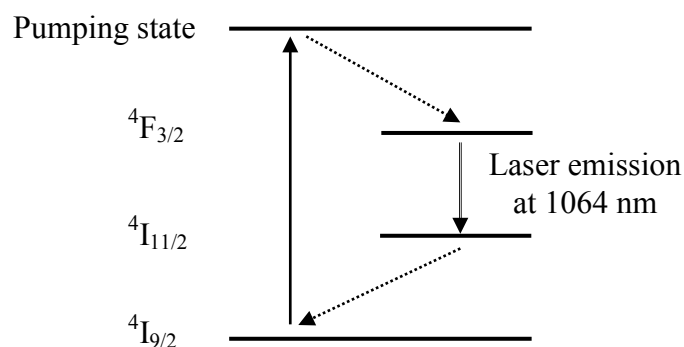
Figure 4.2. Population inversion and laser emission in the four-level system of Nd^{3+}.

Short pulses (<10 ns) of high intensity (tens of megawatts) can be obtained by Q-Switching the laser. A Q-Switch is a device that introduces high loss to prevent emission while the population inversion is built. A high voltage is sent to the so called Pockels cell inside the Q-Switch when the maximum population inversion is reached, which opens the Q-Switch and releases a short pulse of light. The high energy pulse can be frequency doubled by using non-linear crystals such as potassium dideuterium phosphate (KD*P), which results in emission at 532 nm. This light can be doubled again to obtain light at 266 nm or mixed with the fundamental wave to produce light at 355 nm. Frequency doubling is a non-linear process and therefore some energy is lost. Single pulses at 1064 nm present typically energies above 500 mJ, while maximum energies for the fourth harmonic (266 nm) are only around 50 mJ.

Two Nd:YAG lasers were used during this work: a Spectra-Physics Quanta-Ray GCR-150, at a repetition rate of 15 Hz; and a Spectra-Physics Quanta-Ray LAB-150, at a repetition rate of 10 Hz. Only the third and fourth harmonics (355 nm and 266 nm) were employed for the excitation of phosphors during this work.

The energy delivered to the samples by the laser was monitored using pyroelectric energy detectors (QE25SP-S-MB, Gentec or PEM-45K, Radiant Dyes). When needed, a previously calibrated energy monitor unit (Energy monitor V9, LaVision) permitted shot to shot measurements of the laser pulse energy. The fluence was calculated based on the laser beam spot diameter, which was controlled by a manually adjustable iris diaphragm.

4.1.2. Detection and acquisition

The phosphor samples analysed were either in powder form or as a deposited thin film. The spectroscopic and lifetime measurements were performed in 1-D with a resolution determined by the laser spot size. The following sections describe the detectors used for the collection of the luminescence emitted by the phosphors.

4.1.2.1. Spectrometer
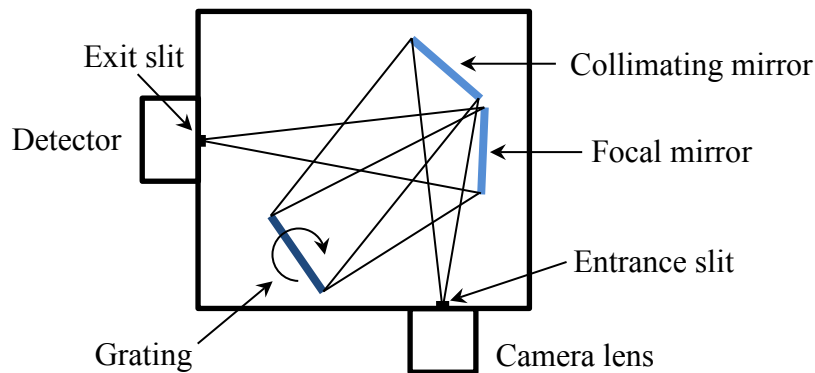
Figure 4.3. Scheme of the functioning of a Czerny-Turner spectrometer.

Two Czerny-Turner spectrometers were used during the present work, one employed for spectral analysis and the other used as a monochromator for lifetime decay analysis. This type of spectrometer consists of an entrance slit, two mirrors, a grating and an exit slit. The light source is directed and focused by an objective lens at the entrance slit, which allows control of the amount of input light in the system and affects the spectral resolution. Light in the spectrometer is then reflected and collimated by the first mirror (collimating mirror) onto the grating. This light is then diffracted by the grating and as a result a different reflection angle for different wavelengths is obtained. The diffraction angle is dependent on the grating groove density. Diffracted light is next collected by the second mirror (focal mirror) and focused at the exit slit. The width of the exit slit (w) and the dispersion of the grating (d) determine the wavelength range observed ($\Delta\lambda$):

$$\Delta\lambda = w \cdot d \qquad\qquad (4.1)$$

The rotation of the diffraction grating allows scanning of several ranges of wavelengths, and multiple detectors can be placed at the exit slit of the spectrometer to analyse the diffracted light in the desired way. The specifications and settings of the two spectrometers used during this work are collected in Table 4.1.

Table 4.1. Specifications of the two Czerny-Turner spectrometers used in this work.

Spectrometer	Acton SP-2300i, Princeton Instruments	Jarrell-Ash MonoSpec 18
Focal length (mm)	300	156
Aperture (f/)	4	3.8
Grating groove (g/mm)	300	1200
Collection optics	50 mm Nikon lens	50 mm Nikon lens
Entrance slit width (μm)	100	100
Spectral resolution (nm)	< 1	< 1
Exit slit width	-	Adjustable
Grating drive	Automated	Manual
Detector	CCD camera	PMT

For spectral studies, the 300 g/mm grating of the Acton SP-2300i permitted the coverage of a wavelength range of approximately 92 nm. Therefore multiple recordings at different positions of the grating were necessary to cover the range from the blue (445 nm) to the red (611 nm) emission of BAM:Eu. Up to five recordings were made to reconstruct the whole spectrum with central wavelengths at 450, 500, 550, 610 and 675 nm.

The Jarrell-Ash spectrometer, which was employed for lifetime decay analysis, was used as a monochromator. The manual adjustment of the exit slit width determined the wavelength range detected by the PMT, which can be estimated in each specific case by considering the dispersion given by the manufacturer (d = 4.5 nm/mm). Generally, an exit slit width of 200 μm was set so that the wavelength range observed was in the order of 1 nm.

4.1.2.2. CCD camera

Charge-Coupled Device (CCD) cameras are based on the photoelectric effect which converts the incident light photons into electrons that are then stored and sequentially transferred in a semiconductor [139]. The CCD sensor has a Metal Oxide Semiconductor (MOS) structure and the signal charge is accumulated and transferred in the semiconductor by the creation of potential wells in the metallic electrodes. There are multiple sensor types and operating principles, but here only interline transfer CCDs will be explained as this is the type of camera used in this project.
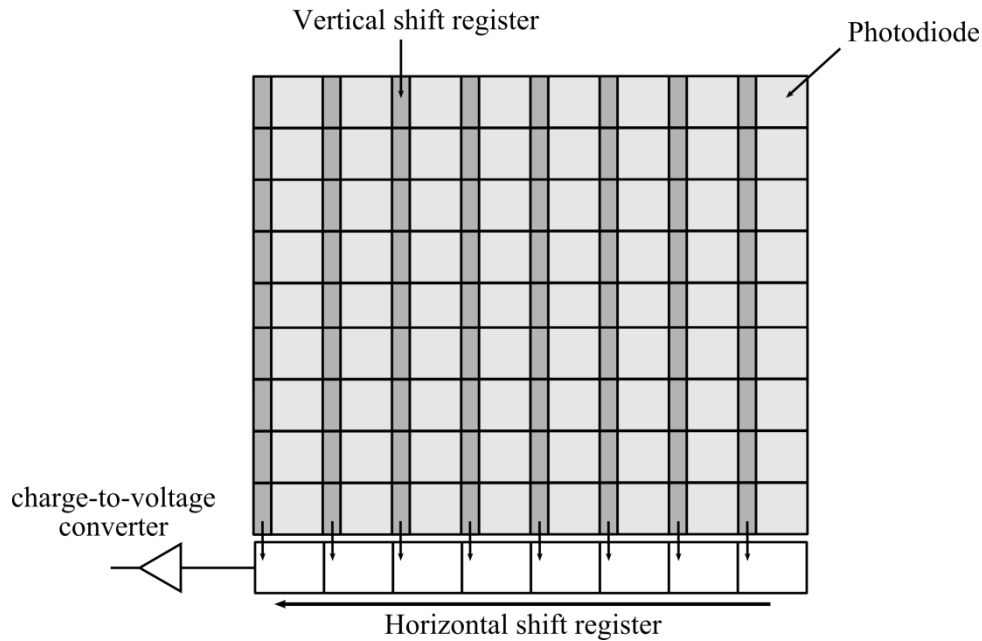
Figure 4.4. Structure of an interline transfer CCD array with an active photodiode, a masked vertical shift register and a horizontal shift register.

The interline transfer CCD is formed of an active area and a vertical shift register disposed parallel along the active area, as depicted in Figure 4.4. The signal produced by photoelectric effect in the active area is rapidly (typically < 1 µs) transferred to the vertical shift register through a transfer gate. This is done simultaneously for all the pixels. The charges are therefore separated from the active area which allows fast gating of the exposure time. Then the charge is sequentially transferred to the horizontal shift register for every line and later converted to a voltage proportional to the number of electrons. The readout time necessary to convert all the charges into an electric signal limits the maximum frequency of operation of the camera. The fact that the vertical shift register is physically placed parallel to the active area means that the latter needs to be necessarily smaller, which reduces the amount of light collected by the sensor. This interline transfer CCD camera uses micro lenses placed on each pixel to partially compensate that effect.

The interline transfer CCD camera (Imager Intense, LaVision) used in this work was attached to the exit slit of the spectrometer and recorded the light emitted by the samples studied. The sensor of the camera was formed of 1376x1040 pixels with a size of 6.45x6.45 µm each. The resolution of the sensor was 12 bit and the readout frequency at full frame was 10 Hz. Non-linearity of the sensor is specified to be of less than 1 %.The integration time was normally set to 1 ms so that the slowest emission from the phosphor material was completely recorded. The background was dynamically recorded and thus for every spectral image a background

image was recorded immediately after. A total of 150 images were recorded in a typical measurement, made of alternate spectral images and background images, so that the precision of the measurement could be assessed. Further post-processing of the 2-D images was necessary to obtain the actual emission spectra. It was also necessary to adjust the hardware binning of the camera in order to compensate for the differences in emission intensities between samples while keeping all the other parameters involved in the measurement constant. This was necessary to obtain sufficient light at low signal levels and to avoid saturation of the sensor when the emission intensity was too high. The horizontal binning, which affects the wavelength calibration of the sensor as will be explained in section 4.1.3.1, was kept constant so that the same wavelength calibration of the system was always valid. The vertical binning was varied according to the intensity of the light collected in order to keep the pixel counts well below the saturation limit and to maintain a good signal to noise ratio.

4.1.2.3. *Photomultiplier tube (PMT)*

Photomultiplier tubes (PMTs), similarly to CCDs, are also light detectors based on the photoelectric effect. Typically a PMT (Figure 4.5) is formed of a vacuum tube with an input window that permits the entrance of light. When the photons pass through the window they hit a photocathode that generates electrons by the photoelectric effect. The number of electrons generated per incident photon is known as the quantum efficiency (η). Later, a series of dynodes, which have a sequentially increased electric potential, accelerate the generated electrons and multiply them by means of secondary electron emission. The total gain (μ) achieved along the dynodes stage can be calculated by:

$$\mu = \alpha \cdot \prod \delta_i \qquad (4.2)$$

Where α is the collection efficiency and δ_i is the ratio of generated electrons to incident electrons in each dynode. After the last dynode, the electrons are collected by the anode which creates a measurable current that becomes the output of the PMT. The output current is normally amplified and then digitised by an oscilloscope before post-processing in a computer.
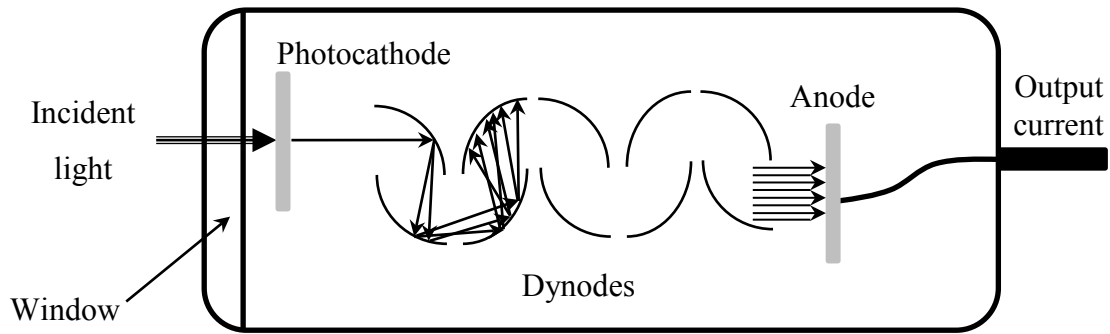
Figure 4.5. Schematic view of a PMT structure

The particular PMT must be matched to the specific application considering the characteristics of the light to be detected and the speed of the process [140]. PMTs mainly differ in the window and photocathode materials, type and arrangement of the dynodes and amplification of the output signal.

For the detection of phosphor decays in this work a side-on type PMT (R955HA, Hamamatsu) was used. It was connected to a high voltage power supply socket (C6270, Hamamatsu) and a wide bandwidth amplifier (C6438, Hamamatsu). The PMT showed peak sensitivity at 400 nm and spectral response up to 900 nm and was therefore suited to detect the light emitted by most thermographic phosphors.

The performance of the PMT system was studied with regards to linearity and saturation, which are crucial to obtain accurate lifetime decay measurements [141, 142]. The two main causes of non-linearity in PMTs are high light intensities incident on the photocathode, which can cause bleaching, and high electrical gains that lead to the development of space charge in the last stages of the dynodes and in the anode [142]. These two processes cause optical and electrical saturation of the PMT respectively, which negatively affects the accuracy of the lifetime decay measured for a particular phosphor [142]. This lifetime decay is directly related to the output signal of the PMT and thus if the PMT response is in the non-linear regime, a variation in the light intensity or in the gain setting changes the lifetime decay measured by the system.

Linearity was studied for the PMT set-up described previously, which was connected to a 1 MΩ load impedance oscilloscope. As given by the manufacturer, the maximum linear output voltage (2 % linearity) is typically 100 mV. The linearity of the system was therefore studied for signal peaks ranging from 50 mV to up to 3000 mV by measuring the lifetime

decay of the 445 nm emission of BAM:Eu. The excitation of the phosphor was kept constant accordingly to future experiments in which the light level was relatively low and no photocathode bleaching is expected. On the other hand, the gain of the PMT was gradually increased while keeping all other settings constant ("uncorrected" in Figure 4.6) to test dynode and anode saturation. The results in Figure 4.6 demonstrate that the operation of the PMT is non-linear since the lifetime decay increases at higher gains while the signal peak voltage becomes greater. This is in accordance with the saturation behaviour of the lifetime decay described in [142]. However, if the signal peak voltage is maintained at a relatively constant value by adjusting the camera lens aperture while the gain is increased (the amount of input light is reduced), the decay time remains constant ("corrected" in Figure 4.6). Saturation of the PMT can therefore be avoided by reducing the amount of light reaching the sensor.
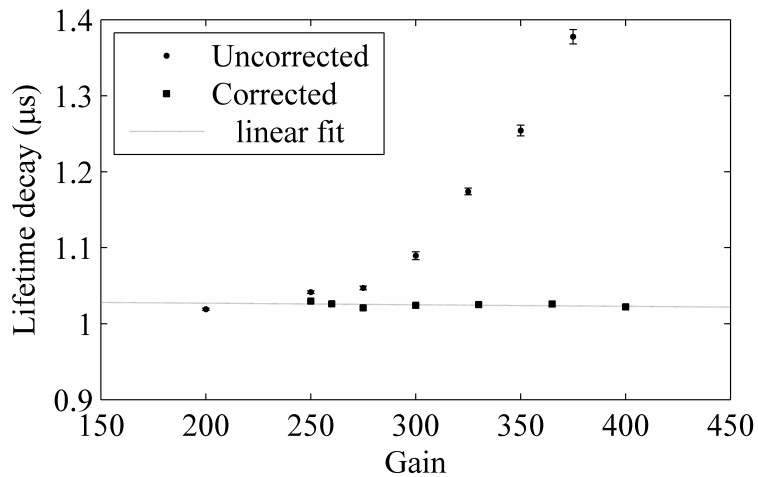
Figure 4.6. Lifetime decay of the 445 nm emission of BAM:Eu for different PMT gains. In the corrected signal the aperture of the camera lens aperture is adjusted so that the signal peak voltage is the same at all gains.

In this work, the PMT was operated in such a way that the signal peak voltage remained constant at low values. The signal intensity was adjusted by using the camera lens aperture and by modifying the gain settings. By doing this it was assured that no saturation occurred in the PMT at any time. Additionally, because the signal intensity remains constant, the vertical resolution of the oscilloscope can be kept constant too and full use of the bits available for digitisation can be made in all the measurements.
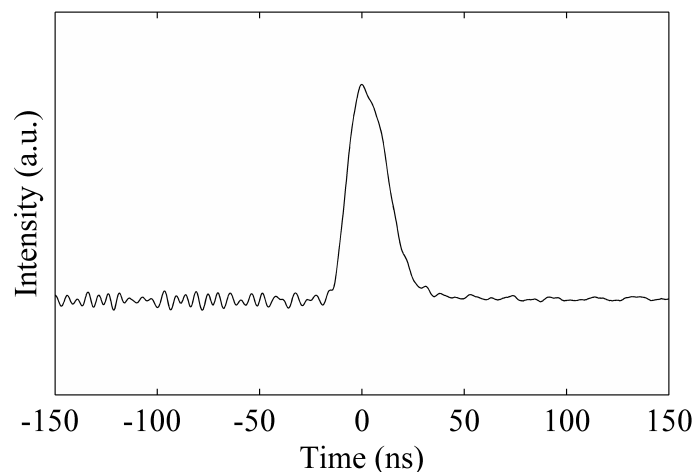
Figure 4.7. PMT system response recorded for a laser pulse input (7 ns). It shows that the fastest decay that can be measured by the system is of about 35 ns.

The response time is also an important feature of PMTs, which limits the fastest signal that can be measured by the system. Lifetime decays for thermographic phosphors can be as fast as a few nanoseconds and therefore PMTs need to have fast response times if those signals have to be recorded. The response time of the PMT is mainly limited by the so called electron transit time, i.e. the time necessary for the electrons to travel from the photocathode to the anode [140]. For the PMT used in this work this transit time is specified to be 22 ns. However, the electronics needed to amplify and digitise the signal also affect the response time and therefore it is expected that the minimum signal measurable be longer than 22 ns. The response time of the whole system described previously was experimentally measured by detecting the light of a short laser pulse (7 ns) as shown in Figure 4.7. The signal recorded presents a rise time of about 20 ns and a decay time of about 35 ns, which confirms that the set-up is suitable for the measurement of the lifetime of the phosphors used in this work (the minimum lifetime recorded is above 100 ns).

4.1.2.4. Oscilloscope

Oscilloscopes permit observation and digitisation of fast changing voltage signals. In this research the signal from the PMT was digitised by a digital oscilloscope (PicoScope 3205B, Pico Technology). This oscilloscope performs with an 8-bit vertical resolution and a maximum sampling rate of 500 MHz.

It has been previously reported that the vertical resolution of the oscilloscope can affect the value of the lifetime obtained in the measurement [95]. If the signal amplitude is too low the value of the calculated lifetime decay can drastically decrease. Therefore it is convenient to

maintain the signal amplitude close to the maximum vertical voltage of the oscilloscope. It was mentioned in the previous section that the PMT peak signal was kept at a relatively constant value to avoid non-linearity effects in the PMT. This was also useful to avoid uncertainty due to a low vertical resolution of the oscilloscope and to make use of its full dynamic range.

The sampling rate of the oscilloscope is a parameter that can also affect the value measured for the decay time since it determines how accurately the signal is digitised. If the number of samples per unit time is too low the signal recorded will not be accurate, but if it is too high the computing time will be unnecessarily increased. It has been previously estimated that the optimum sampling rate is 1500 samples per decay time [95]. In this research the sampling rate was adjusted to record at least 10 decay times in the decay curve and 32000 samples were taken (i.e. 3200 samples per decay time). The signal was then downsampled by a factor of 16 before post-processing to further reduce the computing time.

The signal was coherently averaged in order to improve the signal to noise ratio. Again a balance must be reached between the reduction in the noise level achieved and the total time required for the measurement. The noise level decreases as the number of single shot signals averaged increases. However, above a certain number of averages the noise reduction is marginal. This has been previously reported to occur between 10 and 20 single shot averages [143]. In this work, because the signal level was relatively low, 32 single shot decay curves were generally averaged unless otherwise stated. A total of 25 measurements were made to check the uncertainty of the measurement.

4.1.3. Data processing

The data recorded from the CCD camera and PMT need to be post-processed after acquisition before it can be converted to a temperature value, and the way in which these data are processed can greatly affect the uncertainty of the results obtained. The treatment of these data, which is quite different for the intensity ratio and the lifetime decay methods, is explained in the following sections. The intensity ratio method deals with 2-D images that are then converted to a 1-D spectrum from which the intensity ratio is calculated. The lifetime decay method analyses fast decay curves that are fitted by using three different numerical algorithms proposed in the literature. The performance of these three methods is compared in terms of precision and accuracy by using the data available from phosphors used in this work and the most suitable method is selected.

4.1.3.1. Spectroscopy and intensity ratio

The emission of BAM:Eu centred at 610 nm as recorded by the CCD camera is shown in Figure 4.8. In this image, the horizontal axis represents wavelength and the vertical axis simply records the emission intensity at a fixed wavelength located at different vertical positions on the sample. From this image, the emission spectrum can be extracted by performing a series of operations that include subtraction of the background, conversion to a 1-D spectral plot, assignment of a particular wavelength to each pixel and correction for the instrument intensity response.

A typical spectroscopy measurement consisted of 150 recorded images: 75 spectral images alternated with 75 background images. Each of the spectral images was background subtracted and then an average was obtained. After that, the 2-D image was converted into a spectral line by vertically averaging the 20 % of the pixels in the centre of the image as indicated by the dashed lines in Figure 4.8.
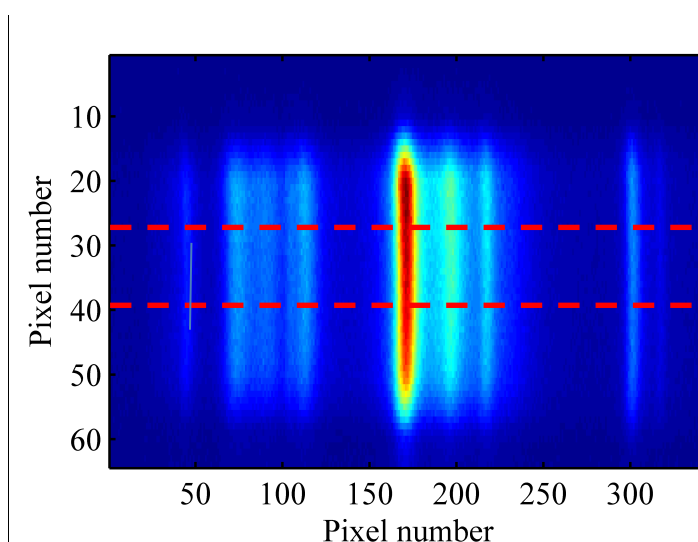
Figure 4.8. 2-D raw image from the CCD camera of a BAM:Eu sample spectrum centred at 610 nm. Dashed lines delimitate the central pixels that are used to obtain the 1-D spectrum.

The horizontal axis of the 1-D spectrum obtained was then assigned a wavelength according to a calibration performed by using the narrow emission lines of a mercury lamp. The wavelength calibration was carried out independently for each position of the grating of the spectrometer, which permitted observation of multiple portions along the visible region of the spectrum (with measurements centred at 450, 500, 550, 610 and 675 nm). An example of the narrow lines used for the calibration of the emission centred at 610 nm is shown in Figure 4.9. The calibration was performed by assigning the peak wavelengths to a particular pixel and then considering a linear dispersion of the spectrometer.
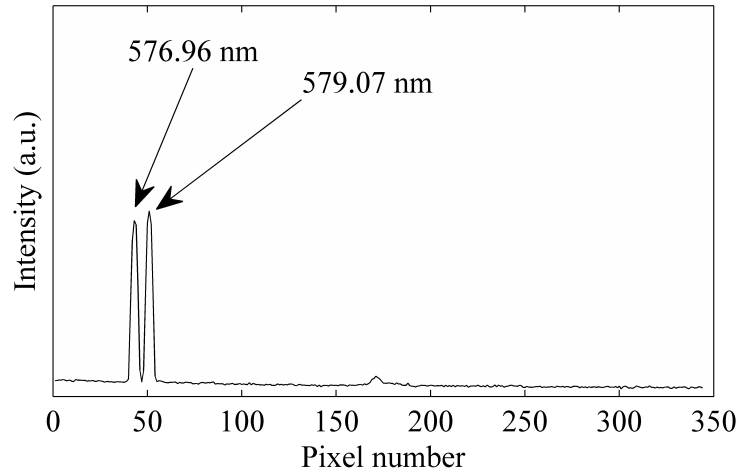
Figure 4.9. Narrow emission lines of a mercury lamp used for wavelength calibration of the spectrum centred at 610 nm.

The last step consisted of the intensity correction for the wavelength dependent response of the system. The response of the spectrometer, like many other optical instruments, is wavelength dependent and therefore it was necessary to calibrate the intensity response of the system in order to obtain the real shape of the spectra. Only relative calibration of intensities was performed during this work. This was done by using the known emission spectrum of a tungsten halogen lamp (LS-1, Ocean Optics) placed in the same spot where the analysed sample was located during the measurement. The instrument response curve was calculated by dividing the theoretical spectrum of the lamp (TL_t) by its measured spectrum (TL_m). The real spectra of the samples could then be calculated by simply multiplying the recorded spectral intensities by the instrument response curve as:

$$I_{real}(\lambda) = I_m(\lambda) \cdot \frac{TL_t(\lambda)}{TL_m(\lambda)} \tag{4.3}$$

The theoretical or actual spectrum of the tungsten halogen lamp is certified by the manufacturer and provided in a data sheet. The impossibility to modify the lamp configuration (such as voltage applied) makes it a reliable light source, and it was found that the uncertainty introduced by this calibration in the calculated intensity ratio was negligible compared to typical experimental uncertainties.

The intensity ratio between different regions of the spectra was calculated from these spectra in a similar way as would be done by a dual-camera system using spectral bandpass filters. However, in order to calculate the intensity ratio the 75 spectral images were not averaged so that single-shot statistics could be calculated. Therefore, each of the 75 images was

background subtracted and then the same wavelength and intensity corrections were performed as for the averaged spectra. Once the 75 individual spectra were obtained the two areas below the curve were integrated over a certain wavelength range which simulates the FWHM of a bandpass filter. These integrated intensities were calculated for each of the single images and then the statistics were computed. It was further checked that the intensity ratio obtained by calculating the average intensities of the 75 single-shot spectra was the same as the one obtained by using the intensity from the averaged spectrum of the 75 images. The intensity ratio (ρ) was calculated by averaging the intensities of each spectral line and dividing them:

$$\rho = \frac{\sum I_{1,i}/n}{\sum I_{2,j}/n} = \frac{I_1}{I_2} \tag{4.4}$$

Where $I_{1,i}$ and $I_{2,j}$ are the intensities of each image at the two spectral lines respectively, $n = 75$ and I_1 and I_2 are the mean of the intensities calculated for each spectral line. On the other hand, the standard deviation of the measurement was calculated by propagation of uncertainty and is given by:

$$\sigma_{IR} = \rho \cdot \sqrt{\left(\frac{\sigma_1}{I_1}\right)^2 + \left(\frac{\sigma_2}{I_2}\right)^2} \tag{4.5}$$

where I_1 and I_2 are the mean of the intensities calculated for each spectral line, σ_1 and σ_2 are the standard deviations of these intensities and ρ is the intensity ratio calculated in Equation (4.4).

Comparison of absolute intensities between different samples was possible if the power of the laser was maintained constant. However, the uncertainty in the measurement of the intensity was estimated to be of about 8 % after successive measurement of the same sample under constant experimental conditions. This was mainly due shot to shot fluctuations of the laser fluence and variations in the illumination of the sample as a result of the slightly different position occupied by the sample after it was removed and relocated.

4.1.3.2. Lifetime decay

In the lifetime decay method the discrete data recorded by the oscilloscope during the decay of the phosphor emission is normally fitted to a single exponential equation by using the non-

linear least squares Levenberg-Marquardt algorithm. However, the decay observed for many phosphors is not always single-exponential and other fitting algorithms might be more suitable in those cases. In the following sections, some of these algorithms are described and tested on data acquired during the development of this work. At the end, a conclusion is made about the use of these methods and the most suitable one is selected which will be used in the present project.

Single-exponential

As it was previously stated, many phosphors show a decay of the emission that is exponential or nearly exponential, and therefore the most common means of fitting the lifetime decay is by using a single exponential equation of the form:

$$I(t) = I_b + I_0 e^{-\frac{t}{\tau}} \tag{4.6}$$

Where I is the intensity at a time t and the constants I_b, I_0 and τ are the background offset, initial intensity and lifetime decay constant respectively. Occasionally the fit can be performed by first calculating and subtracting the background offset I_b, and then using only two variables in the Levenberg-Marquardt fitting routine. However, in the present work the fit was performed by including the three variables simultaneously in the fitting routine since no significant difference was observed between the two methods.

A frequent concern in the application of this method is the observation window that should be considered in the fitting routine, i.e. the portion of the data that is actually used. The initial point of the data considered for the fitting is relevant since the recorded decay presents in some cases a fast initial response followed by a slower exponential decay. There is disagreement about the origin of this effect as it has been related to stray laser light collected by the PMT but also to a fast fluorescence process of the material that precedes the phosphorescence emission. In either case this fast initial decay has an effect in the calculated lifetime decay and the inclusion or exclusion of the first section of the decay needs to be carefully considered.

The length of the observation window, and therefore the last point of the data incorporated to the fit, is related to the amount of data necessary to accurately estimate the lifetime decay. An observation window too short compromises the precision of the measurement while if it is too long the tail of the signal will be formed of background noise only.

A well-established approach to define the observation window is an iterative algorithm proposed by Brubach et al. [144]. In this algorithm the observation window is iteratively adjusted to a length which is proportional to the previously calculated lifetime decay. This is done by using two constants c_1 and c_2 that define the beginning and the end of the data that is used as input of the fitting algorithm as a function of the lifetime decay (see Figure 4.10). This algorithm was envisaged to adapt a single-exponential model to fit multi-exponential decays and can be used to deal with the issues related to initial fast decay mentioned previously. The values adopted and recommended by the authors for the constants c_1 and c_2 are 1 and 4 respectively [144] but they indicate that these values should be reconsidered for every particular phosphor application.
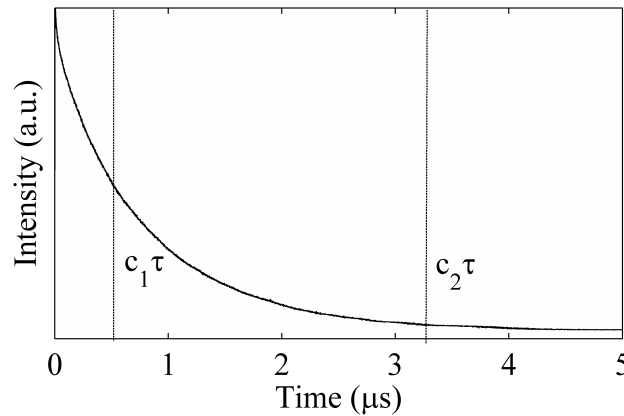
Figure 4.10. Observation window defined on a decay curve using the constants c_1 and c_2 as explained in [144].

In the present work, the 611 nm emission of BAM:Eu^{3+} was used to study the best value for these parameters. 25 decay curves, each of which consisted of 32 coherently averaged single shot decays, were recorded for a sample of BAM:Eu commercial powder heat treated at 1000 °C for 20 minutes. These decay curves were fitted to the single exponential shown in Equation (4.6) using different values of c_1 and c_2, which varied from 0 to 1.5 and 3 to 15 respectively. The single-exponential lifetime decays were calculated for each combination of the defined parameters and the results are shown in Figure 4.11.
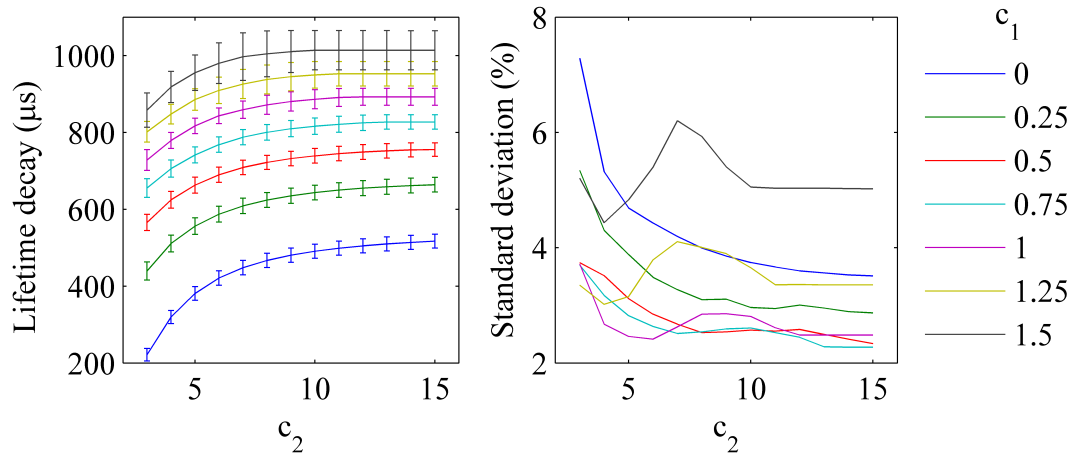
Figure 4.11. Measured lifetime decay and its estimated standard deviation for the 611 nm emission line of BAM:Eu heat treated at 1000 °C for 20 minutes calculated using multiple values of the algorithm parameters c_1 and c_2.

These results reflect the great effect that the fitting parameters have in the absolute value and precision of the calculated lifetime decay. In terms of c_1, high values above 1 imply large uncertainties because the part of the signal with the highest signal to noise ratio is excluded (i.e. the first part of the signal). The values of $c_1 = 0$ and $c_1 = 0.25$ result in a notably low estimated lifetime decay which yields a high relative standard deviation. This occurs because the initial point of the observation window is moved towards shorter times and therefore a larger portion of the fast initial component of the decay is included in the fit, which makes the overall estimated decay shorter. The best results in terms of precision are thus obtained for values of c_1 between 0.5 and 1. The second parameter, which determines the last point of the observation window, has an effect in the absolute value of the calculated lifetime decay when this parameter is below around 9. When c_2 decreases the value of the lifetime decay also diminishes. Here the reason is that the end point of the observation window is moved towards shorter times, which discards a portion of the slow decay in favour of the fast initial component. For values above 9 the effect is negligible because the intensity of the decay is already extinguished and an increase of the observation window only adds background noise. According to these considerations, the values that provide the best precision in the results for this particular phosphor are $c_1 = 0.5$ and $c_2 = 10$. This was also true for other samples analysed during this work (YAG:Dy and YSZ:Dy), and therefore this parameters were adopted unless otherwise stated.
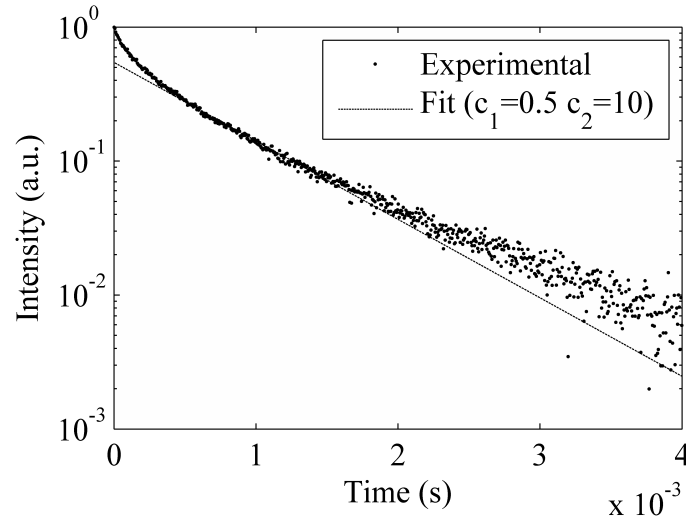
Figure 4.12. Single-exponential fit of an experimental decay curve of BAM:Eu heat treated at 1000 °C for 20 minutes. The fit used the parameter values $c_1 = 0.5$ and $c_2 = 10$. The actual decay curve is clearly multi-exponential and the fit is only accurate in the defined observation window.

The great variability of the results with the fitting parameters is a consequence of the signal being not single-exponential as shown in Figure 4.12. The single exponential fit therefore fails to accurately represent the decay and only resembles the actual decay in a small range, which in Figure 4.12 spans from 0.5 ms to approximately 2 ms. At the beginning and at the tail of the decay the fit does not follow the curve. This can be quantified by the coefficient of determination (R^2) which in this case is only 0.9285.

In this case the best parameters are considered those that provide the most precise measurement although the curve is not properly fitted. This means that the parameters must be kept constant throughout measurements to assure reproducibility of the results. The case of BAM:Eu, whose decay is multi-exponential possibly due to complex energy transfer mechanisms, can be extended to other thermal history phosphors whose emission is affected by the development of surface and bulk defects upon degradation and energy transfer mechanisms between traps and other dopants.

Bi-exponential

Due to the multi-exponential nature of the decays observed during this work, a bi-exponential function was used to improve the fitting, which was of the form:

$$I(t) = I_b + I_1 e^{-\frac{t}{\tau_1}} + I_2 e^{-\frac{t}{\tau_2}} \tag{4.7}$$

Similarly to the single exponential equation, I is the intensity at a time t, I_b is the background offset, I_1 and I_2 are intensity constants and τ_1 and τ_2 are the lifetime decay constants. The fit

was also performed using a Levenberg-Marquardt algorithm with 5 fitting variables. The experimental decay curves used for analysis were the same used in the single-exponential section but in this case the whole curve was considered into the fit (the observation window included all the data).

The results of the bi-exponential fit indicate that the curve is formed of a rapid decay of about 130 μs, which fits the experimental data in the initial moments, and a slower decay of about 780 μs, which is representative at later times. This fit reproduces the experimental decay more accurately than the single exponential decay as can be visually evaluated in Figure 4.13 for one of the 25 decays used in the study. This evaluation is further supported by the value of R^2 which is now increased to 0.9982. Although the quality of the fit is better when the bi-exponential fit is used, the precision in the estimation of any of the lifetime decays is not improved and therefore the potential temperature measurement precision would not be better. Additionally, the algorithm is more elaborate and the computing time higher. Furthermore, the sensitivity with temperature of the two lifetime decays must be checked since normally only the slow decay is sensitive. This is true in the case of BAM:Eu, where the fast decay is not significantly sensitive with temperature and therefore cannot be used as a measurand.
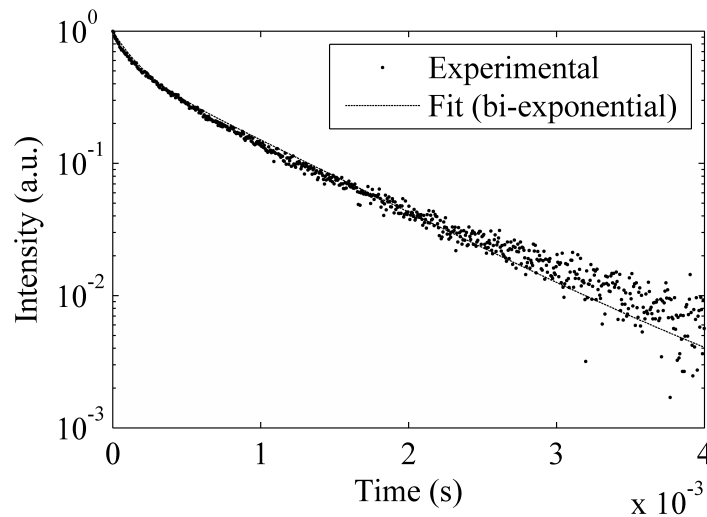
Figure 4.13. Bi-exponential fit of an experimental decay curve of BAM:Eu heat treated at 1000 °C for 20 minutes. The bi-exponential model provides a better fit of the curve than the single-exponential method.

The slow decay, on the other hand, shows a similar sensitivity to the lifetime decay calculated by the single-exponential fit with parameter values of $c_1 = 0.5$ and $c_2 = 10$. This is because

the observation window of the single-exponential fit begins sufficiently late so that the fast decay no longer affects the signal.

The similarity between a bi-exponential fit and a single exponential fit with $c_1 > 0$ has been further tested with the emission decay of the on-line phosphor YSZ:Dy filtered at 592 nm. The decay curves of a coating sample of this phosphor were recorded at different temperatures while the sample was cooling down from high temperatures and a calibration curve was obtained. This calibration curve was dependent on the type of fit applied to the experimental data as represented in Figure 4.14. The single exponential fit that considers the data from the beginning of the decay ($c_1 = 0$) has a significantly faster lifetime decay at all temperatures, as expected from previous results. When c_1 increases, the curve moves up and progressively approaches the calibration curve obtained by the slow lifetime constant of the bi-exponential fit. This means that the fast decay at the beginning of the curve is ignored and only the slow decay is considered. This is important in practical applications where the initial fast decay of the curve might differ from the calibration to the actual measurement due to external factors such as laser reflections. Variations on the fast initial decay were observed by the author in the YSZ:Dy sample that affected the uncertainty of the measurement by up to 2 %. Therefore, either a bi-exponential fit or a single exponential fit with $c_1 > 0$ are recommended.
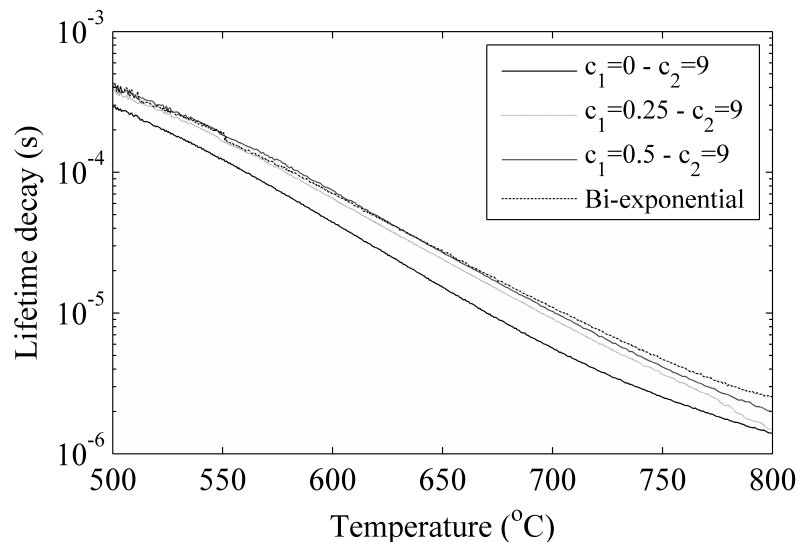
Figure 4.14. Evolution of the calibration curve of YSZ:Dy with different fitting algorithms. As c_1 increases in the single exponential fit, the calibration curve approaches the one obtained with the slow decay of the bi-exponential fit.

Exponential Series Method (ESM)

A multiple exponential analysis can be performed to the whole decay curve by considering a model of the decay of the form:

$$I(t) = I_b + \sum_{i=1}^{n} I_i e^{-\frac{t}{\tau_i}} \tag{4.8}$$

where I_b is the baseline offset, t is the time, n is the number of exponential terms, I_i is the amplitude of exponential i and τ_i is the lifetime decay of exponential i. The application of these spectral methods to a thermographic phosphor (Mg_4FGeO_6:Mn) has been recently reported for the first time in [145]. As it is explained in that work, the application of spectral methods is based on the consideration of the intensity as a Laplace integral:

$$I(t) = \int_0^{\infty} \alpha(\tau) e^{-\frac{t}{\tau}} d\tau \tag{4.9}$$

where the amplitudes I_i are considered a continuous distribution $\alpha(\tau)$. Spectral methods then determine an approximate discrete distribution $\alpha(\tau_i)$ for a series of τ_i with i=1, …, n by minimizing the functional:

$$\Phi = \left\| I(t) - \int_0^{\infty} \alpha(\tau) e^{-\frac{t}{\tau}} d\tau \right\|^2 + \lambda\psi\big(\alpha(\tau)\big) \tag{4.10}$$

Here λ is a regularization parameter and ψ is a regularization functional. In that work [145] two types of methods are reviewed: the maximum entropy method (MEM) and the exponential series method (ESM). The MEM requires the definition of a regularization functional, which is based on probability theory. On the other hand, in the ESM this functional is equal to zero, and therefore the ESM results in a simple least-squares method that consists in minimizing the functional:

$$\Phi = \left\| I(t) - \sum_{i=1}^{n} I_i e^{-\frac{t}{\tau_i}} \right\|^2 \tag{4.11}$$

Due to the relative simplicity of this method and similarity of results with the MEM, it was implemented to calculate the multiple exponential components of the BAM:Eu decay curves analysed in the previous sections. The results of the ESM algorithm applied to these data are shown in Figure 4.15 (left) for two of the 25 decay curves of the set (green and red). According to the results of the ESM, these decay curves consist of 5 exponential components in the range from 10^{-5} to 10^{-2} s. However, the lifetime decay values are quite different for the

two curves, which ultimately results in poor precision in the estimation of the lifetime decay. It is thought that the low SNR of the signal emitted by BAM:Eu at 611 nm is the reason why the results obtained with this method have a high variability.
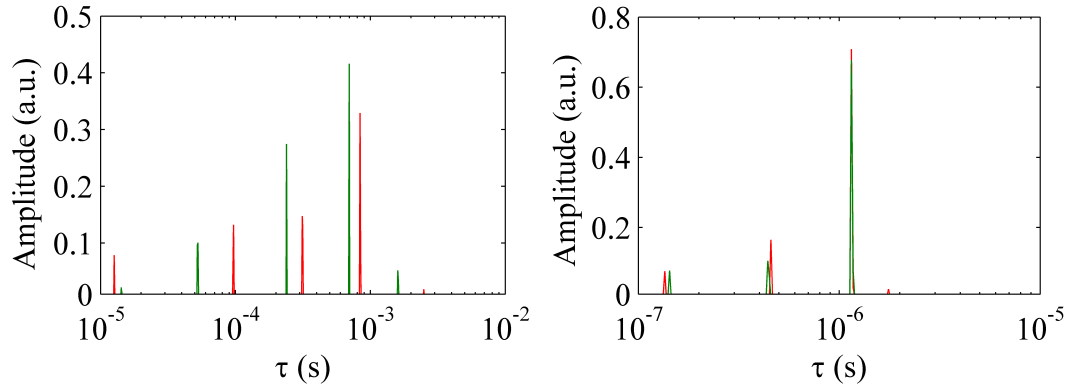
Figure 4.15. Spectral distribution of the lifetime decays calculated for two different decay curves (green and red) recorded in repeated measurements from the 611 nm emission of BAM:Eu (left) and from the 445 nm emission of BAM:Eu (right).

This was tested by applying the method to the brighter emission of BAM:Eu at 445 nm, which had a SNR of about one order of magnitude higher than the emission at 611 nm. The decay curves of this emission were fitted by the ESM and the results are shown in Figure 4.15 (right). This emission is formed of three distinct exponential decays in the range 10^{-7} - 10^{-5} s. However, in this case the results for different curves (green and red) are very similar and the precision of the results was comparable to those obtained by the single exponential method. This points out that SNR is a major factor that affects the precision of this method.

Concluding remarks

Three fitting algorithms, namely single-exponential, bi-exponential and exponential series method (ESM), have been tested on 25 decay curves recorded from the emission at 611 nm of a heat treated BAM:Eu sample. Due to the non-exponential characteristics of these decays, the single-exponential algorithm failed to accurately fit the shape of the curve, which makes the actual value calculated to be highly dependent on the fitting parameters. However, this method obtained positive results in terms of precision.

The bi-exponential algorithm improves the fitting of the curve but the precision of the lifetime decay calculation is not improved with respect to the single-exponential algorithm. Furthermore, a single-exponential algorithm that rejects the first part of the decay curve

exhibits a lifetime decay that is almost equivalent to the slow lifetime decay of the bi-exponential fit.

Finally, a method recently introduced to phosphor thermometry has also been tested, which is based in the spectral decomposition of the decay curve. The ESM permits identification of the multiple exponentials that compose the decay curve, but the fitting routine seems highly sensitive to the noise of the signal and the precision of the results is not comparable to the other two methods.

It can be thus concluded that the single exponential algorithm, in which the parameter $c_1 > 0$, offers the best balance between calculation time/complexity and precision in the measurement of the lifetime decay. This algorithm provides a similar result to the double-exponential algorithm but is much simpler in terms of computing. This approach, where $c_1 = 0.5$ and $c_2 = 10$, is followed in the rest of the thesis unless otherwise stated.

4.2. Isothermal heat treatment

The thermal history of the samples studied in this work was mainly investigated after heat treatment in air, and a box furnace was used for this purpose. Eventually, a controlled atmosphere was necessary for manufacture of coatings or to study specific heat treatment conditions. In these cases the sample was placed inside a quartz tube located in a tube furnace through which the necessary gasses flowed.

4.2.1. Heat treatment in air

Heat treatments in an air atmosphere were performed in a box furnace (UAF 16/5, Lenton) with a maximum continuous operating temperature of 1550 °C. The furnace was adapted with an optical access port that is normally used for on-line phosphor calibration. In this work, an alumina tube was placed at this port which was used to insert and remove samples from inside the furnace at high temperatures without damaging the ceramic components of the furnace by thermal shock. In order to heat treat the samples, the furnace was set to the desired temperature and allowed to reach thermal equilibrium. At that point the sample was slid inside the alumina tube until it reached the centre of the furnace. An N-type thermocouple was located in contact with the sample to continuously monitor the temperature. The heat treatment timer was started once the temperature reached 98 % of the objective temperature, which normally occurred in 3 - 4 minutes. When the heat treatment was finished, the sample

was quickly removed from the tube and allowed to cool down in air, which normally took about 2 - 3 minutes.

4.2.2. Heat treatment in a controlled atmosphere
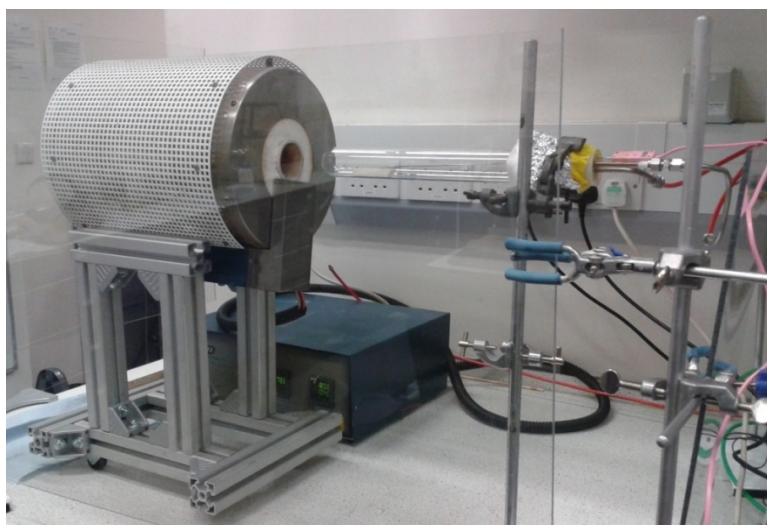
Figure 4.16. Image of the furnace set-up for the heat treatment of samples in a controlled gas atmosphere.

When the heat treatments for history measurements required a controlled atmosphere, the samples were heat treated in a tube furnace (Elite TSH12/50/300) with a maximum continuous operating temperature of 1150 °C. The sample was placed inside an overhanging quartz tube closed at one end. At the other side, a drilled silicon rubber stopper permitted the flow of gases through steel pipes, so that the atmosphere inside the tube was closed. An N-type thermocouple was also passed through the silicon stopper and placed in contact with the sample to continuously monitor the temperature. The furnace was mounted in a metallic structure, as shown in Figure 4.16, which allowed horizontal displacement. The quartz tube could then be located concentrically within the furnace during the heat treatment, and the furnace could be moved away when the treatment was finished so that the sample rapidly cooled down.

The current of gases was managed by a set of mass flow controllers (Fideris) that permitted the flow of multiple gases simultaneously. The gases employed during this research were air, oxygen, nitrogen/argon and hydrogen. The mass flow controllers were calibrated when necessary in order to obtain the appropriate mixtures required for each specific application.

4.3. Material characterisation

The characterisation of some of the samples studied during this work was necessary to complement the luminescence analysis and to characterise the deposited coatings and identify structural changes. Characterisation of the particle size and shape was possible by scanning electron microscopy, and phase identification was performed by conventional X-Ray Diffraction.

4.3.1. Scanning Electron Microscope (SEM)

A Scanning Electron Microscope (SEM) is a type of microscope that uses an electron beam in the keV range to obtain images of the surface of objects with resolutions of up to 1 nm. The use of electrons instead of photons in the visible region (optical microscope) is justified by the dependence of the beam diffraction on the wavelength. This beam diffraction limits the resolution of the image and therefore more energetic beams (lower wavelength) permit to image smaller objects. The electrons from the beam impact onto the sample and there they can undergo various transformations which result in the generation of different signals that are collected by multiple detectors. Three of these signals were of use in this work. Firstly, secondary electrons that are generated from inelastic scattering. The intensity of these secondary electrons is related to the atomic number of the elements in the sample and they generate an image with information about the composition of the sample. Secondly, back-scattered electrons result from elastic scattering. Their intensity is related to the angle of scattering and therefore to the topography of the sample. Finally, characteristic x-rays arise from the radiative transitions in the K, L and M shells of the excited atom after interaction with the electrons in the beam. These x-rays are characteristic of each element in the periodic table and they act as a fingerprint that can be calibrated and used to quantitatively analyse the composition of the sample. This technique, named Energy-Dispersive x-ray Spectroscopy (EDX or EDS), gives information about the composition in one point of the sample rather than an image map of the composition. A more detailed explanation of the functioning and structure of SEM is out of the scope of this work and the reader is referred to some of the literature available [146, 147].

The SEM used in this work (S-3400N, Hitachi) has a specified maximum resolution of 3 nm for scattered electrons and 4 nm for back-scattered electrons at an accelerating voltage of 30 kV. For EDS analysis, no specifications were available from the manufacturer. However, a default reference spectra for all the elements is included in the system so semi-quantitative

EDS analysis could be performed [148]. The uncertainty of this type of analysis is not as good as a standard quantitative analysis, which can be at best about 2 %, but it is still sufficient to estimate the composition of the sample and to identify phases [148].

The quality of the SEM images obtained and the EDS analysis depend on the correct preparation of the sample to be analysed. The preparation of the coating samples for cross section analysis was crucial in order to obtain a flat surface characteristic of the coating. The samples were mounted in a black phenolic resin (Conducto-Mount, MetPrep) in a mounting press (CitoPress-1, Struers). This resin wraps the coating and facilitates the following processes of grinding and polishing. Since the resin is conductive, it also facilitates the SEM analysis by reducing the charging effects. The sample surfaces were ground using silicon carbide paper from a grit size of 400 to 2500, and finally polished using a monocrystalline diamond suspension (down to 3 µm). BAM:Eu is a non-conductive ceramic and charging problems were important during SEM analysis. Large areas appeared completely white in the image due to electrical charge accumulation. A gold layer of a few atoms was plasma sputtered on the surface of the sample to reduce the charging effects although this layer affected the results of the EDS.

On the other hand, powder samples were prepared by depositing a few drops of a suspension of the particles in isopropyl alcohol on an aluminium stage so that they could dry. A thin layer of gold was deposited by sputtering to avoid charging of the particles when considered necessary.

4.3.2. X-Ray Diffraction (XRD)

XRD is a material characterisation technique which is based on the elastic scattering of x-ray radiation directed to the sample of interest. This technique is based on the Bragg's law, which is schematically represented in Figure 4.17. Incident x-ray radiation is scattered by the atoms in the lattice planes separated a regular distance d. The scattered waves will interfere constructively when the path difference between the two waves ($2d \cdot \sin\theta$) is an integer number of the wavelength (λ), where θ is the scattering angle. When these scattered waves interact constructively, a strong intensity peak is obtained at that angle in the diffraction pattern.
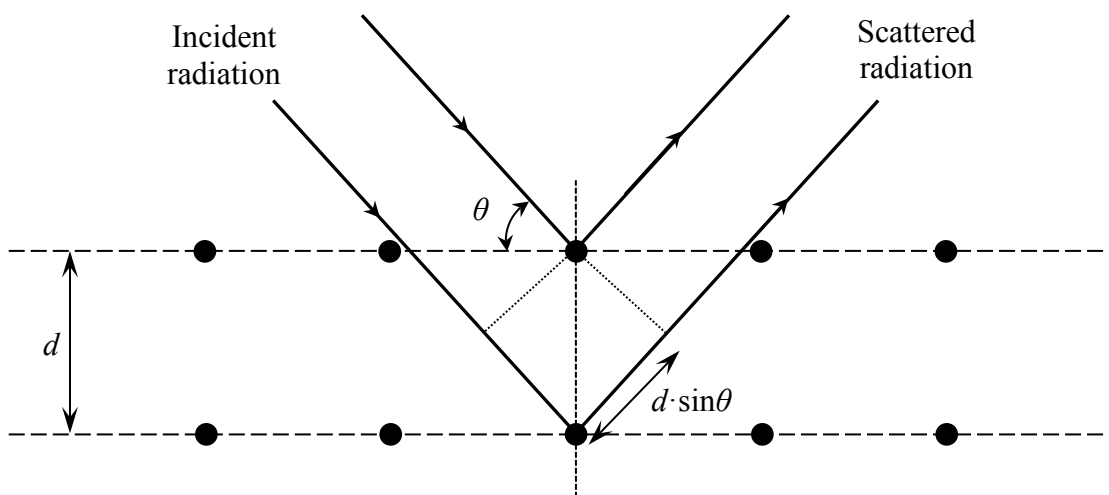
Figure 4.17. Constructive interference of two radiation beams according to Bragg's law.

X-ray diffractometers generally consist of an x-ray source, a sample holder and a detector that collects the scattered x-rays. The source and the detector rotate around the sample so that a series of 2θ angles are scanned. The sample remains static in the case of powders because the random orientation of the powder grains guarantees that all the crystallographic planes will be detected. However, the sample spins when coatings are analysed so that preferential orientation of the grains in the coatings can be avoided and all crystallographic planes detected. The machine used in the present work (D2 Phaser, Bruker) uses CuK_α radiation (1.5418 Å) and permits the scanning 2θ angles from 5 ° to 90 °.

The scattered radiation is collected by the detector and a diffraction pattern constructed. A typical x-ray diffraction pattern is formed of a series of peaks related to the scattering angle. Each of these peaks belongs to a certain d-spacing in the crystal structure and the whole pattern can be used as a fingerprint and compared to a reference for material identification. Identification and quantification of several phases present in a sample is also possible. The crystallite size of the powder samples can be estimated using Scherrer's equation [149, 150], or Williamson-Hall plots [151, 152] when lattice strain effects are considered. However, the use of XRD for crystallite size determination is restricted to sizes of less than approximately 200 nm, which was exceeded by the fully crystalline powder used in this project. Therefore XRD analysis was only used for identification purposes.

5. MATERIAL INVESTIGATION

This chapter describes the investigation of the physical and optical properties of the thermographic phosphor BAM:Eu and how they change at high temperatures. The aim is to understand the mechanism by which oxidation of the dopant ion occurs and to relate the subsequent structural changes to the observed optical properties of the phosphor so that a suitable measurand can be defined and calibrated against past exposure temperature. Some of the results presented in this chapter have been published in references [1, 3].

The first section describes the characterisation of the phosphor powder used in this work. It first includes details about the composition and particle size and shape. Then thermal analysis of the powder is performed, which includes dilatometry and simultaneous thermogravimetric analysis and differential thermal analysis (TGA-DTA). These are useful to detect any physical or chemical processes that may occur to the powder at high temperatures, such as phase changes. Dilatometry is also used to determine the coefficient of thermal expansion, which is not available in the literature and is important for coating applications. Finally the optical properties of the phosphor that can be used for thermometry are identified and suitable measurands defined.

The second section of the chapter is a detailed calibration of the measurands defined in the previous section against heat treatment temperature. Several factors that affect the sensitivity and accuracy of these measurements are investigated namely the exposure time, excitation fluence, cooling down time of the samples, composition of the heat treatment atmosphere, dopant concentration and particle size. Finally the possibility to reuse the sensor is explored in detail at two different ranges of temperatures.

The last section includes a summary of the relevant findings about the oxidation mechanism that can be related to degradation mechanisms proposed in the literature. The exceptional measurement capabilities that make BAM:Eu a potential candidate for thermal history coatings are also briefly summarized.

5.1. Powder characterisation

5.1.1. Physical composition

The BAM:Eu phosphor used during this work for characterisation was, unless otherwise stated, a commercial powder purchased from Phosphor Technology (KEMK63 UF-P1). Specific details about this powder, such as manufacture process and dopant content, are not readily available from the manufacturer. Therefore the physical properties of the powder were investigated by the material characterisation techniques available in this research.

The powder was observed using SEM (see Figure 5.1), which shows irregular-shaped particles with a wide size distribution from sub-micron up to about 4 μm. This is in accordance with a manufacturing process via a solid state reaction followed by milling of the powder to obtain a finer particle size.

5 μm
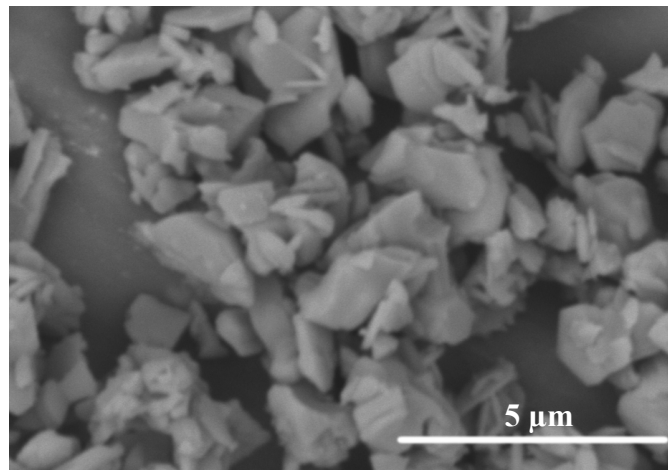
Figure 5.1. SEM image of BAM:Eu commercial powder (KEMK UF-P1, Phosphor Technology).

The europium content is known to be greater than 1 % (only information provided by the manufacturer). However, it is reported in the literature that a content close to about $x = 0.09$ mol of europium ($Eu_xBa_{1-x}MgAl_{10}O_{17}$) provides the highest quantum efficiency [124], therefore a similar concentration would be expected in the current sample. Semi-quantitative EDS measurements were performed on the powder sample in order to estimate the europium content. Measurements were performed in two different areas and three different positions on each area, so that 6 independent measurement values were obtained. The results, which are summarised in Table 5.1, confirm a europium content with an average value of 0.086 (standard deviation: 0.013) which is close to the theoretical optimum. These results can also be used to estimate the uncertainty of the semi-quantitative EDS measurements performed with the current equipment, which is of approximately 15 %.

Table 5.1. Europium content (x in $Eu_xBa_{1-x}MgAl_{10}O_{17}$) according to EDS measurements in two different regions of a commercial BAM:Eu powder sample.

Europium content (x)	Area 1	Area 2
Site 1	0.087	0.083
Site 2	0.101	0.074
Site 3	0.103	0.067

5.1.2. Thermal analysis

The commercial BAM:Eu powder was analysed at high temperatures to identify physical or chemical processes that affect the material structure or composition. Dilatometry and TGA-DTA analyses of BAM:Eu have not been previously reported in the literature and therefore can improve understanding of the oxidation mechanism of the phosphor. The results of these analyses will be useful not only in the study of thermal history sensing capabilities of the phosphor but also when considering the development of a sensor coating.

5.1.2.1. Dilatometry

Dilatometry is a thermal technique which allows measurement of the expansion or shrinkage of materials exposed to a predetermined temperature program under controlled conditions. Dilatometry can be used to characterise solids, powders and liquids and provides information such as the coefficient of thermal expansion (CTE), phase transitions, sintering temperature and softening points.

In the present work a horizontal pushrod dilatometer (DIL 402 E, Netzsch) under air atmosphere was used. In this type of dilatometers the sample is placed in a holder that is located inside a movable furnace. A pushrod is placed in contact with the sample so that any change in size is transmitted via the rod to a transducer that records the linear displacement. A temperature program is then set to the furnace and the displacement recorded against temperature. This displacement is due to the expansion of both the pushrod and the sample, and therefore the contribution from the displacement of the pushrod must be corrected. This can be done by recording a correction curve when the same program runs without any sample.

The sample consisted of a cylindrical pellet of pressed powder (isostatically pressed at 300 Pa) of 16.2 mm of length and 8 mm in diameter. The sample was placed in the dilatometer under an air atmosphere and heated at a rate of 10 °C/min from room temperature to 1700 °C. Melting of the sample was avoided by selecting a maximum temperature of

1700 °C. The melting point of BAM:Eu is reported in the literature to be of about 1900 °C [125]. However, during the present work a powder sample melted at temperatures of only 1800 °C and therefore a safe maximum temperature of 1700 °C was selected for the test.
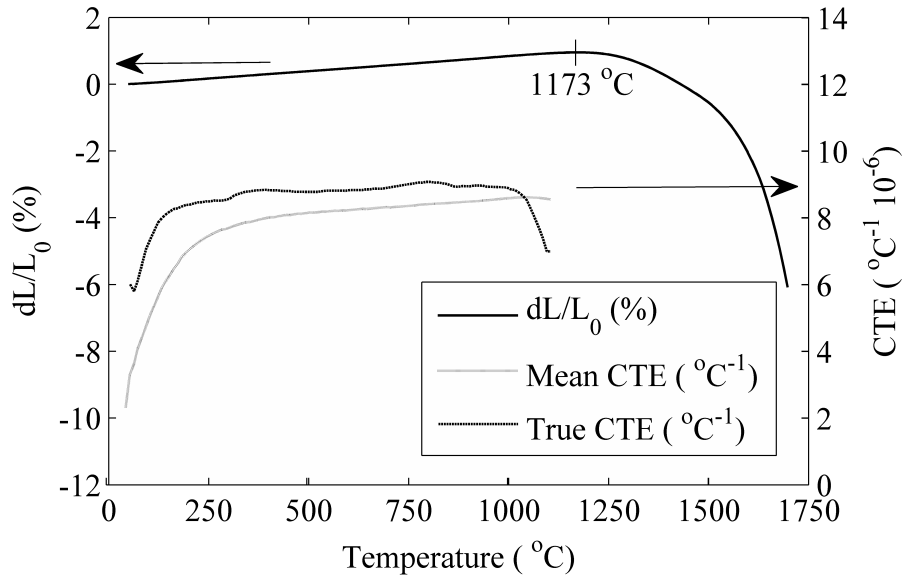
Figure 5.2. Dilatometry curve and calculated coefficient of thermal expansion (CTE) of the BAM:Eu powder.

The dilatometry curve obtained after correction of the pushrod contribution is shown in Figure 5.2. This curve represents the percentage of linear thermal expansion as a function of temperature. The expansion of the sample is nearly linear with temperature up to approximately 1173 °C, which is the temperature at which the sintering of the material begins. The fact that there is no change of slope that can be seen in the curve indicates that no phase transformation or compositional change occurs in that temperature range that is observable with this technique. The sintering rate is low for temperatures below 1500 °C and increases at higher temperatures. The highest rate seems to be achieved at temperatures around 1700 °C, although the exact temperature could not be determined since the test was stopped at 1700 °C.

From the recorded curve of linear expansion the CTE can be calculated, although different definitions of this coefficient are available in the literature. In the present work, the mean and true CTEs are calculated, which are additionally plotted in Figure 5.2. The mean CTE is defined by [153]:

$$\alpha_m = \frac{1}{L_0}\frac{(L_2 - L_1)}{(T_2 - T_1)} \qquad (5.1)$$

where L_0 is the length of the sample at a reference temperature T_0. The mean CTE therefore represents the average expansion over the temperature range from T_1 to T_2. The definition of this CTE requires reporting all temperatures T_0, T_1 and T_2, although normally T_0 and T_1 are the same so that the lower limit of the range is used as the reference. This is the procedure followed to calculate the values in Figure 5.2. In this figure, the mean CTE rapidly increases from $2.3 \cdot 10^{-6}$ °C^{-1} at 50 °C to $7.7 \cdot 10^{-6}$ °C^{-1} at 300 °C and then remains relatively constant and increases to only $8.5 \cdot 10^{-6}$ °C^{-1} at 1100 °C.

An alternative definition of the CTE, which is based on the slope of the linear expansion curve dL/dT and uses the initial length of the sample L_0 as a reference, is given by:

$$\alpha_t = \frac{1}{L_0} \frac{dL}{dT} \tag{5.2}$$

This is the true CTE which is slightly higher than the mean CTE in Figure 5.2. This is due to the slight curvature of the linear expansion curve. The true CTE has a similar trend to the mean CTE and remains relatively constant from 300 °C to 1100 °C, with values between $8.5 \cdot 10^{-6}$ °C^{-1} and $9 \cdot 10^{-6}$ °C^{-1}.

The values of the CTE of BAM:Eu calculated at different temperatures are compared to CTE values of other relevant materials in Table 5.2. These materials will be important when considering the application of BAM as a thin film. Inconel 625 is representative of a possible metallic substrate. YSZ, scandia-stabilised zirconia (SSZ) and Al_2O_3 are ceramic materials that can be used as interlayers between the metallic substrate and the BAM coating to improve the CTE mismatch and avoid diffusion of elements from the substrate (see section 6.1.2.2). No information about how these CTEs were calculated is reported in the referred studies and the true CTE of BAM is used for comparison in Table 5.2.

Table 5.2. CTE values for various materials for comparison with BAM:Eu.

Material	α (10^{-6} °C^{-1}) (at 100 °C)	α (10^{-6} °C^{-1}) (at 1000 °C)	Reference
Inconel 625	12.8	16.2	Material datasheet
8% YSZ	7.6	10.9	[154], [155]
8% SSZ	-	10.4	[155]
Al_2O_3	-	7.5	[156]
BAM:Eu (α_t)	7.0	8.9	This work

These data indicate that the CTE mismatch between BAM and a metallic substrate is higher than that for standard YSZ coatings, while it is better than that for Al_2O_3. Therefore, an interlayer of YSZ or SSZ would be beneficial in terms of CTE mismatch.

5.1.2.2. TGA-DTA

Simultaneous thermogravimetric analysis (TGA) and differential thermal analysis (DTA) is a thermal technique that provides information about composition and structural changes upon heating. TGA continuously measures the mass of a sample as a function of temperature so that mass loss or gain can be related to physical or chemical phenomena. DTA continuously records the temperature difference between a sample and an inert reference while a constant heat flow is simultaneously applied to both of them. The temperature difference is plotted against absolute temperature so that endothermic or exothermic reactions in the sample can be detected. These reactions provide information about many physical and chemical processes and some of them are summarised in Table 5.3.

The particular features of a DTA curve are highly dependent on the experimental configuration [157]. The heating rate affects the temperature at which reactions occur such that higher heating rates displace the reaction to higher temperatures. The sample and the crucible play an important role in the shape of the DTA curve since changes in the mass, heat capacity and heat conductivity can modify the features of the curve. The atmosphere is another factor of importance since it can induce or prevent reactions in the sample.

Table 5.3. Physical and chemical phenomena responsible for temperature differences in DTA, adapted from [157].

Physical		Chemical	
Adsorption	Exothermic	Oxidation	Exothermic
Desorption	Endothermic	Reduction	Endothermic
Crystallisation	Exothermic	Chemisorption	Exothermic
Melting	Endothermic	Solid state reaction	Endo/Exothermic
Vaporization	Endothermic	Desolvation	Endothermic
Sublimation	Endothermic		

Efforts have been made to standardise TGA-DTA measurements, but the many factors involved in the process that modify the obtained curve make it necessary to reference the particular experimental set-up and equipment employed. Therefore, comparison of curves

from different experiments is often difficult and results of reaction temperatures must be carefully considered.

In the present study the BAM:Eu powder sample was analysed in a simultaneous TGA-DTA instrument (STA 449F1 Jupiter, Netzsch). The aim of this test was to identify possible phase changes in the material as reported in the literature, as well as identifying any other structural changes that might be relevant to understand the degradation process. Tests were carried out both under air atmosphere and argon atmosphere (60 ml/min). The heating rate was 10 °C/min and the experiment covered the temperature range from room temperature to 1600 °C. The curves were corrected for systematic errors derived from the crucible (alumina) and reference sample by calculating a calibration curve without any sample. The initial amount of powder was 67.2 mg and 94.5 mg in the air and argon tests respectively.
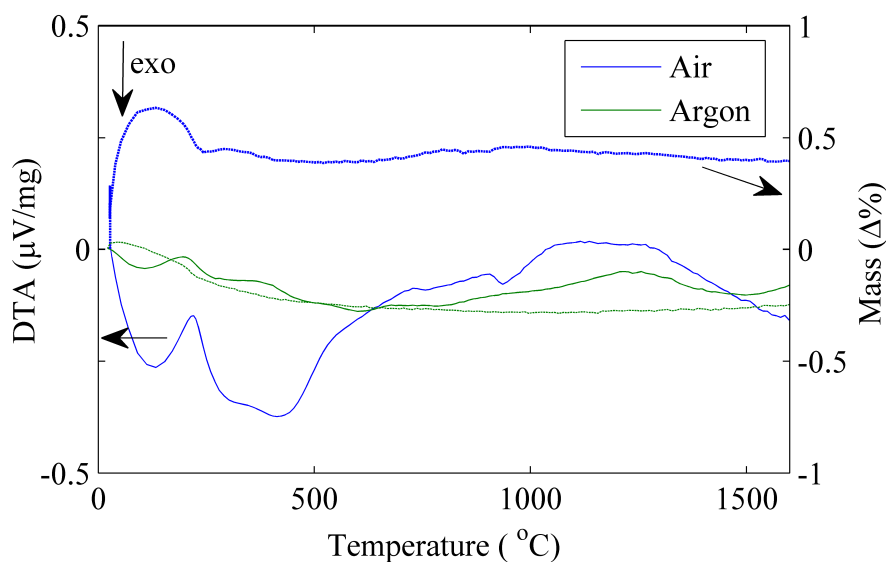
Figure 5.3. TGA-DTA curves of the BAM:Eu powder sample under air (blue) and argon (green) atmospheres. Solid and dashed lines represent DTA and TGA curves respectively.

TGA-DTA curves for the two tests are shown in Figure 5.3. DTA (solid lines) read on the left axes and TGA (dashed lines) on the right axes. The test in air (blue lines) presents a high mass gain of about 0.63 % while heating up to 130 °C that might be due to adsorption of oxygen since it is accompanied by an exothermic reaction. At that temperature the mass starts to stabilise and an endothermic reaction peak begins. This peak maximum is located at 220 °C and the mass reduces by approximately 0.2 % at about 250 °C. This can be ascribed to evaporation of water from the sample. No significant changes in the mass of the sample are identified at higher temperatures. However, an exothermic reaction extends from room

temperature to approximately 1030 °C which is thought to be caused by oxidation of the europium ion. Above 1250 °C a new exothermic reaction appears which extends up to the maximum test temperature of 1600 °C. This coincides with the sintering process of the powder as depicted previously in Figure 5.2.

In the test with argon (green lines), no significant mass increase can be observed at the initial test temperatures, which supports the idea that the mass gain in an air atmosphere was caused by adsorption of oxygen. On the contrary, a continuous mass loss which reaches a maximum of 0.25 % at approximately 600 °C is observed. This mass loss is more pronounced at 200 °C, which corresponds with the dehydration process also observed in the DTA peak. Additionally, the oxidation reaction observed up to 1030 °C is still present, although it is much weaker. An explanation for this could be that the sample adsorbs oxygen before it is placed in the crucible or alternatively oxygen is trapped in the voids within the powder inside the crucible. Later, this oxygen leads to an oxidation reaction of the dopant ion in the powder, but due to the low availability of oxygen the magnitude of this oxidation is small. In this test in argon, the exothermic peak that was previously related to sintering of the powder is also observed and peaks at 1500 °C.

TGA-DTA analysis provides further evidence to understand the mechanism by which the phosphor oxidises. It is clear from this analysis that adsorption of oxygen at low temperatures and a continuous oxidation from room temperature to approximately 1030 °C occur and are responsible for the changes observed in luminescence. It also suggests that presence of a certain amount of oxygen is necessary for the phosphor to be used as a thermometer, and this will be investigated in detail in section 5.2.5. Additionally, no other structural changes are observed by this analysis that could affect the measuring capabilities of the phosphor such as phase change or crystallisation.

5.1.3. Optical properties

The optical properties of BAM:Eu phosphor after heat treatment in air are discussed in this section in order to identify suitable measurands to perform temperature measurements. Firstly, the emission spectrum is studied and an intensity ratio (ρ) is defined, which will be used throughout this work. Secondly, the temporal emission properties are investigated in different regions of the spectral range and discussed in detail.

5.1.3.1. Emission spectra and intensity ratio

The emission spectrum of BAM:Eu after heat treatment in air includes features from the emission of the europium ions in the divalent and trivalent states. The broad band emission peaking at approximately 445 nm, which is due to the partially allowed $4f^65d^1 \rightarrow 4f^7$ transition as indicated in Figure 5.4, shows a decreased intensity after heat treatment. On the other hand, transitions due to emission from Eu^{3+} that extend from 575 nm to 720 nm appear after heat treatment at high temperatures, as shown in Figure 5.4. The $^5D_0 \rightarrow {}^7F_0$ transition shows weak intensity as expected from the selection rules [90]. The $^5D_0 \rightarrow {}^7F_1$ is an allowed magnetic dipole transition and therefore its emission intensity is insensitive to the site symmetry [90]. All other transitions are electric dipole transitions and therefore their intensity is greatly affected by the site symmetry. The $^5D_0 \rightarrow {}^7F_2$ and $^5D_0 \rightarrow {}^7F_4$ transitions show higher intensities than the $^5D_0 \rightarrow {}^7F_3$ transition, in accordance with the selection rules for electric dipole transitions.
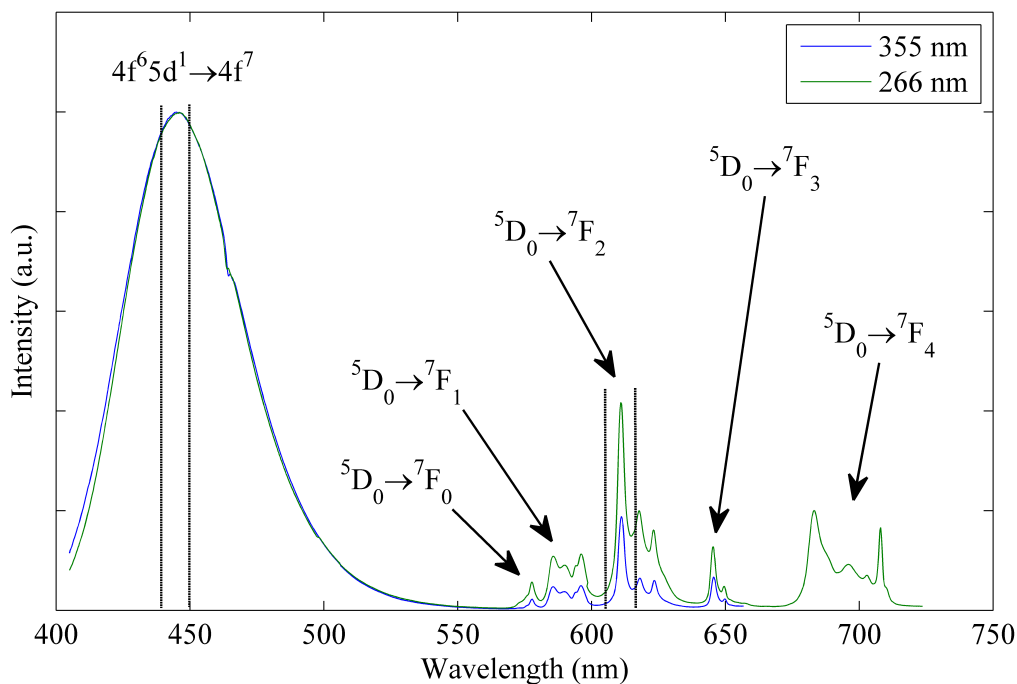
Figure 5.4. Normalised emission spectra of BAM:Eu after heat treatment in air after excitation with 266 nm and 355 nm light. The energy levels from which emission proceeds are indicated by arrows, and the area of the spectrum integrated to calculate the intensity ratio is delimited by vertical dashed lines.

The emission spectrum is in good agreement with previously reported data [63]. Excitation is possible with 266 nm and 355 nm light, and both emission spectra have nearly the same shape (at least up to 660 nm, since emission spectra were not recorded at higher wavelengths for the

355 nm excitation). The overall intensity of the emission after excitation with 266 nm light is higher than the intensity of the emission recorded after excitation with 355 nm, which is expected from the excitation spectrum of BAM:Eu. Additionally, the relative intensity of the Eu^{3+} peaks with respect to the Eu^{2+} broad band is also higher when the 266 nm excitation is used. This is thought to be related to direct excitation of Eu^{3+} ions in the CTS level which is not achieved by 355 nm light [92]. With 355 nm light, direct excitation of Eu^{3+} ions is not efficient, and therefore energy transfer from divalent europium ions must occur in order to observe emission from trivalent ions. This energy transfer might occur via different mechanisms as described in section 2.1.6. Spectral overlap of the emission of Eu^{2+} ions and absorption of Eu^{3+} ions occurs at 466 nm, and reabsorption of emitted light can be observed in the broadband emission at this wavelength where a dip in the emission spectrum is visible. However, this small absorption seems insufficient to explain all the emission intensity observed from trivalent ions, and thus phonon-assisted energy transfer is likely to occur simultaneously.

When the phosphor is illuminated with light at 532 nm only emission from Eu^{3+} ions is observed, which indicates that no up-conversion processes occur that can derive emission from Eu^{2+}. The intensity of the emission after excitation with 532 nm was not quantitatively compared to spectra obtained at 266 nm and 355 nm due to the impossibility of using this excitation for intensity ratio measurements.

The relative intensities of the emissions of Eu^{2+} and Eu^{3+} ions change with temperature and a ratio of these intensities was reported to be sensitive to temperatures up to 1300 °C [63, 69]. Temperature was measured by defining a ratio between the Eu^{3+} emission peak at around 611 nm, which increases with temperature, and the broad band emission of Eu^{2+} centred at 445 nm, which decreases with temperature. In the present work a similar ratio between these two intensities is also used. The intensities to calculate the ratio are integrated over a range of 10 nm centred at 445 nm and 611 nm as indicated in Figure 5.4 by the vertical dashed lines. This ratio is employed throughout this thesis unless otherwise stated. The definition of the ratio might be further optimised in practical applications by careful selection of bandpass filters, but this optimisation step was not performed in this work.

5.1.3.2. *Transient response and lifetime decay*
The lifetime decay of the BAM:Eu emission is normally reported in the literature to be of around 1 μs [57, 63, 123-126]. Slower lifetime decays in the order of 100 μs have been

reported too [116, 124], although these studies did not indicate the wavelengths of observation. Due to the multiple available locations for the europium ions and the possibility of these ions to be in the divalent or trivalent state of oxidation, the transient characteristics of the emission from BAM:Eu are thus expected to be the result of multiple interactions and have different behaviours at different wavelengths, which may explain the disagreement amongst the reported results. Furthermore, the decay of the signal is unlikely to be single exponential, which might also affect the results depending on the algorithm used to fit the experimental data.
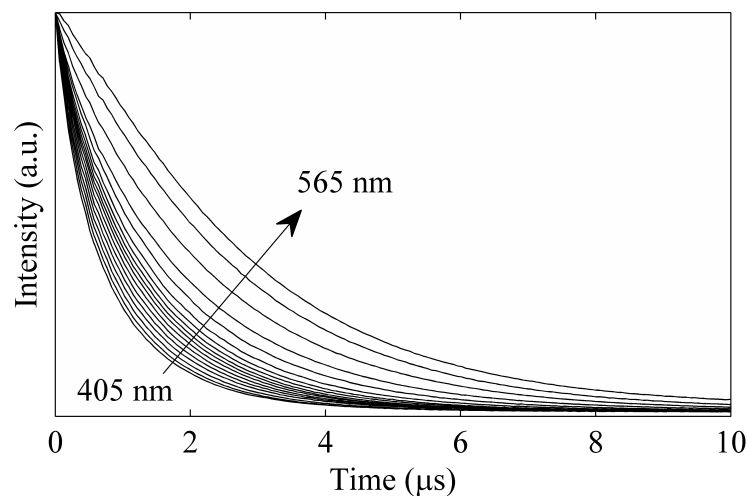
Figure 5.5. Normalised decay curves of the BAM:Eu^{2+} emission measured at room temperature and at different wavelengths from 405 nm to 565 nm in 10 nm increments.

In order to clarify this, the emission of BAM:Eu was filtered using the Jarrel-Ash spectrometer as a monochromator with a spectral resolution of less than 1 nm and the decay of the emission recorded at different wavelengths in the range 405 - 565 nm. The decay of these emission intensities, plotted in Figure 5.5, presents a lifetime in the order of microseconds and becomes clearly slower at longer wavelengths. It is hypothesised that the different emission decays are the result of the europium ions being located in different sites in the crystal lattice and therefore experiencing different environments.

The lifetime of the decay curves in Figure 5.5 was calculated by using the three fitting methods discussed in section 4.1.3.2, and results are shown in Figure 5.6. The decay of emissions below 530 nm is multi-exponential. The multi-exponential fit detects three different exponential components, from which the slowest one is in the order of 1 μs. The other two components are fast and their lifetime decays are of about 500 ns and 130 ns. The bi-

exponential fit also provides a slow decay in the order of 1 µs and a faster decay of about 270 ns, which is nearly the average of the two fast decays provided by the multi-exponential method. The single-exponential fit measures a lifetime decay which is slightly lower than that of the slow lifetime decay measured by the other two methods. This is a consequence of the effect of the fast initial decay on the fitting routine, as explained in section 4.1.3.2. Above 530 nm, however, the decay becomes single-exponential and all three methods converge to the same value of the lifetime decay. This implies that the 2nd (and 3rd) exponential fitted by the bi-exponential (and multi-exponential) method become zero, and therefore are not plotted in the figure.
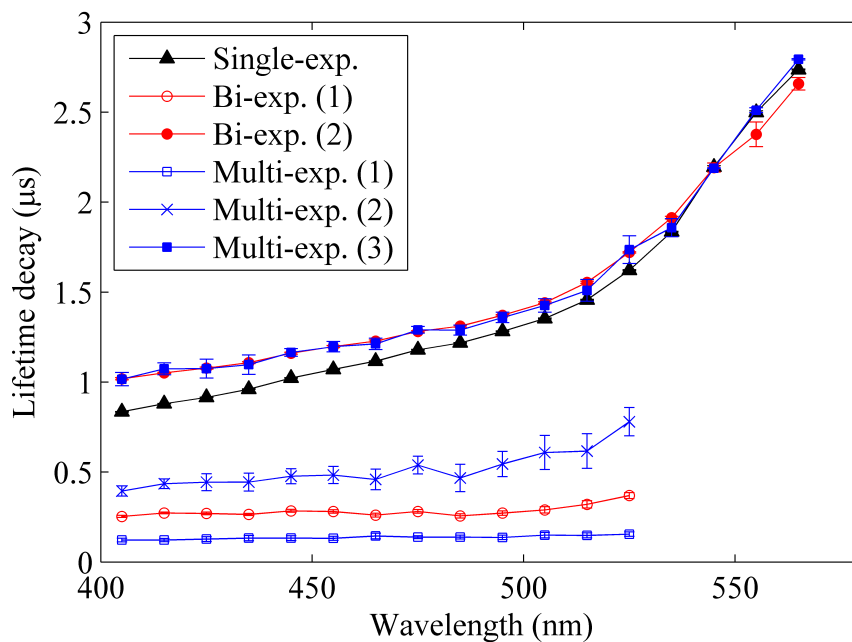
Figure 5.6. Lifetime decays of the BAM:Eu^{2+} emission calculated using the single-exponential (c_1 = 0.5 − c_2 = 10), bi-exponential and multiple-exponential methods in the wavelength range 405 - 565 nm.

A single-exponential algorithm is therefore preferred to fit the decay of the broad band emission since it is simpler, almost unaffected by the multi-exponential characteristics of the decay and the precision obtained is the best of the three methods. The use of the lifetime decay as a measurand of temperature is subjected to the observation wavelength since the lifetime decay changes significantly from one side of the spectrum to the other (lifetime decay increases by a factor of 3 from 405 nm to 565 nm). It was previously reported that the lifetime decay at 445 nm decreases with temperature [63] and could be used to measure temperature. However, detection of the decay of the Eu^{3+} emission was not possible due to the low intensity of the emission. In this work, the decay of the Eu^{3+} emission is also detected after

heat treatment of the phosphor and investigated as a potential measurand of the temperature. This lifetime decay is expected to be the same at all wavelengths since emission occurs from the same energy level, although this could not be experimentally checked due to the low intensity of this emission at wavelengths others than the 611 nm peak. A single-exponential fit was also used for this emission due to the better precision of the method.

5.2. Thermal history sensing

In this section, the optical properties of BAM:Eu after exposure to high temperatures are related to the temperature in order to use the phosphor as a thermal history sensor. The two measurands (intensity ratio and lifetime decay) defined in the previous section are calibrated against temperature and the influence of several factors on the precision, accuracy and sensitivity of the measurement is investigated.

5.2.1. Calibration with temperature

Powder samples of the phosphor BAM:Eu were heat treated in a range of temperatures from 700 °C to 1200 °C. Temperature was measured using an N-type thermocouple as indicated in section 4.2.1. The standard calibration uncertainty specified for this type of thermocouple is 0.75 %, which at 1200 °C implies an uncertainty of approximately ±10 °C. The uncertainty due to radiation and conduction was minimised by using a thin wire thermocouple (1 mm in diameter) placed inside the phosphor powder. The uncertainty related to variations in the location of the thermocouple relative to the powder was less than ±1 °C. The drift of the thermocouple, which can be of about 4 °C after 1000 h of exposure at 1000 °C [158], was not significant as the thermocouple was used for a much shorter amount of time.

Moreover, the uncertainty in the temperature measurement does not affect the uncertainty of the phosphor measurement, but rather the calibration data used to interpret it. The uncertainty on the temperatures measured with the thermocouple can be improved at a later stage and would result in an improved calibration curve of the phosphor, but would not directly affect the performance of the phosphor as a thermometer since in theory the phosphor could be calibrated using an alternative temperature standard.

In this section all samples were heat treated in air for 20 minutes (the effect of the exposure time will be discussed in section 5.2.2). After heat treatment, the optical properties of the samples were interrogated by using excitation at 266 nm. This same excitation was used for

all the results presented in this chapter unless otherwise stated. The intensity ratio and the lifetime decay of both Eu^{2+} and Eu^{3+} emissions were calibrated against temperature.
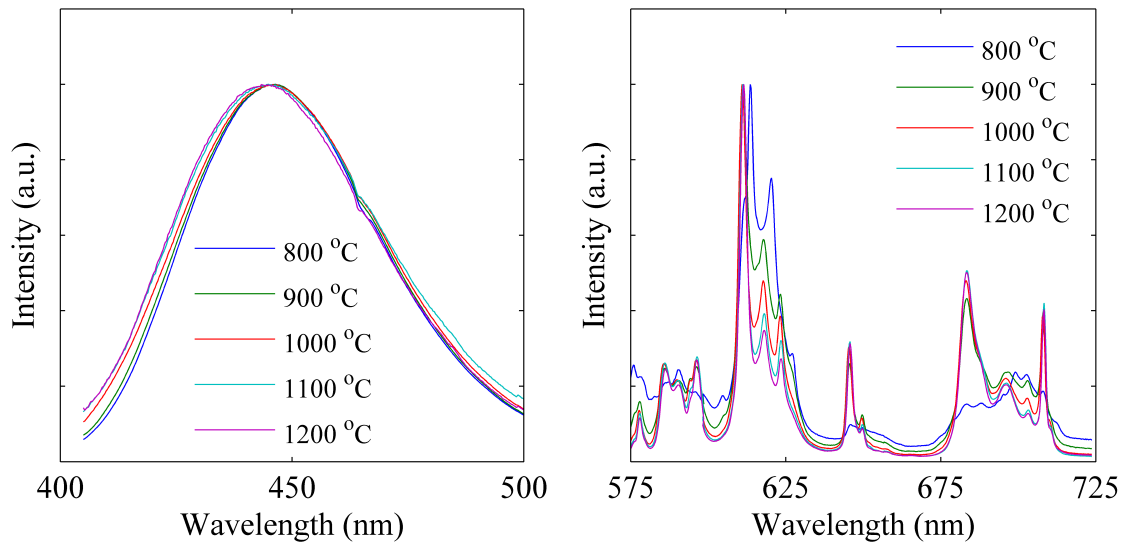
Figure 5.7. Emission spectra of BAM:Eu samples heat treated at different temperatures and normalised to the peaks at 445 nm (left) and 611 nm (right).

The normalised emission spectra of BAM:Eu samples after heat treatment are shown in Figure 5.7. The Eu^{2+} emission broadband and the Eu^{3+} emission peaks are normalised to the peaks at 445 nm and 611 nm respectively. Although the intensity of the broad band emission drastically decreases with temperature (see Figure 5.8), the shape is not significantly changed after heat treatment. There is, however, a blue shift of the spectra with increasing temperatures, which amounts a maximum of 3 nm for the sample heat treated at 1200 °C. This shift, which is contrary to the red shift reported in [115] that occurred after heat treatment in air (see section 3.3.3), indicates that the environment around Eu^{2+} ions slightly changes. It is likely that an expansion of the crystal lattice, similar to that which occurs in the on-line process, decreases the crystal field acting on the Eu^{2+} ion and increases the energy of the lowest excited energy level, which results in a shift of the spectrum to shorter wavelengths. The lattice expansion after heat treatment in air was previously reported in [113], and it can be explained by the distortion caused by Eu^{3+} ions incorporated into the spinel block. After heat treatment, a small dip appears at 466 nm in the otherwise featureless broad band, which is due to the $^{7}F_{0} \rightarrow {}^{5}D_{2}$ absorption of Eu^{3+} ions.
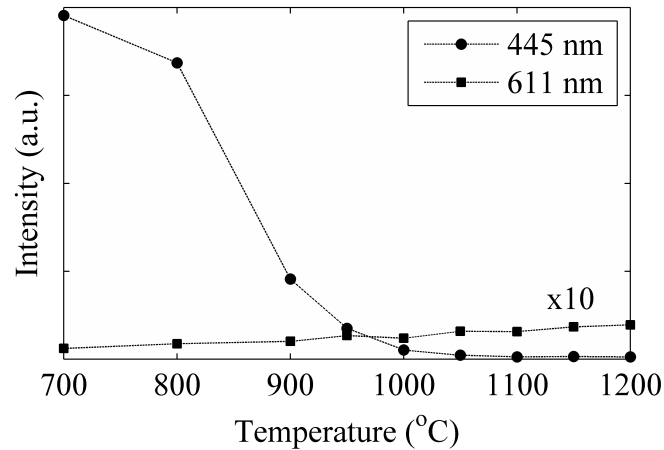
Figure 5.8. The variation of the absolute intensity with heat treatment temperature of the two integrated emissions at 445 nm and 611 nm. Emission at 611 nm is multiplied by a factor of 10 to improve visibility.

The absolute intensity of the emission spectra of the Eu^{3+} ions slightly increases with temperature due to the continuous oxidation of divalent ions into the trivalent state as shown in Figure 5.8. At 800 °C the intensity is very low and the peaks are broad. The spectrum is similar to the emission spectra of phosphors that are not fully crystalline. This suggests that the ions occupy various sites in the lattice with different crystal environments, and it might be illustrative of a process of migration experienced by the Eu^{3+} ions after oxidation. This is further supported by the findings of Boolchand et al. [102] who identified two different sites in the lattice for Eu^{3+} ions before and after heat treatment in air.

Above 800 °C, Eu^{3+} emission peaks are narrow and intense, which indicates that the ions occupy a fixed location in the lattice at these temperatures. Only a decrease of the relative intensity of the peaks at 618 nm and 623.5 nm occurs at temperatures above 800 °C. The hypersensitive emission of Eu^{3+} around the peak at 611 nm is reported in detail in [159] in a Y_2O_3 host. Here, peaks at 617 nm and 626 nm are associated with a phase (monoclinic) different to the one responsible of the 611 nm peak (cubic). Extrapolation of this interpretation might further support the notion that two sites are available for Eu^{3+} ions in BAM, each of which experiences a different symmetry and emits peaks at slightly different wavelengths.
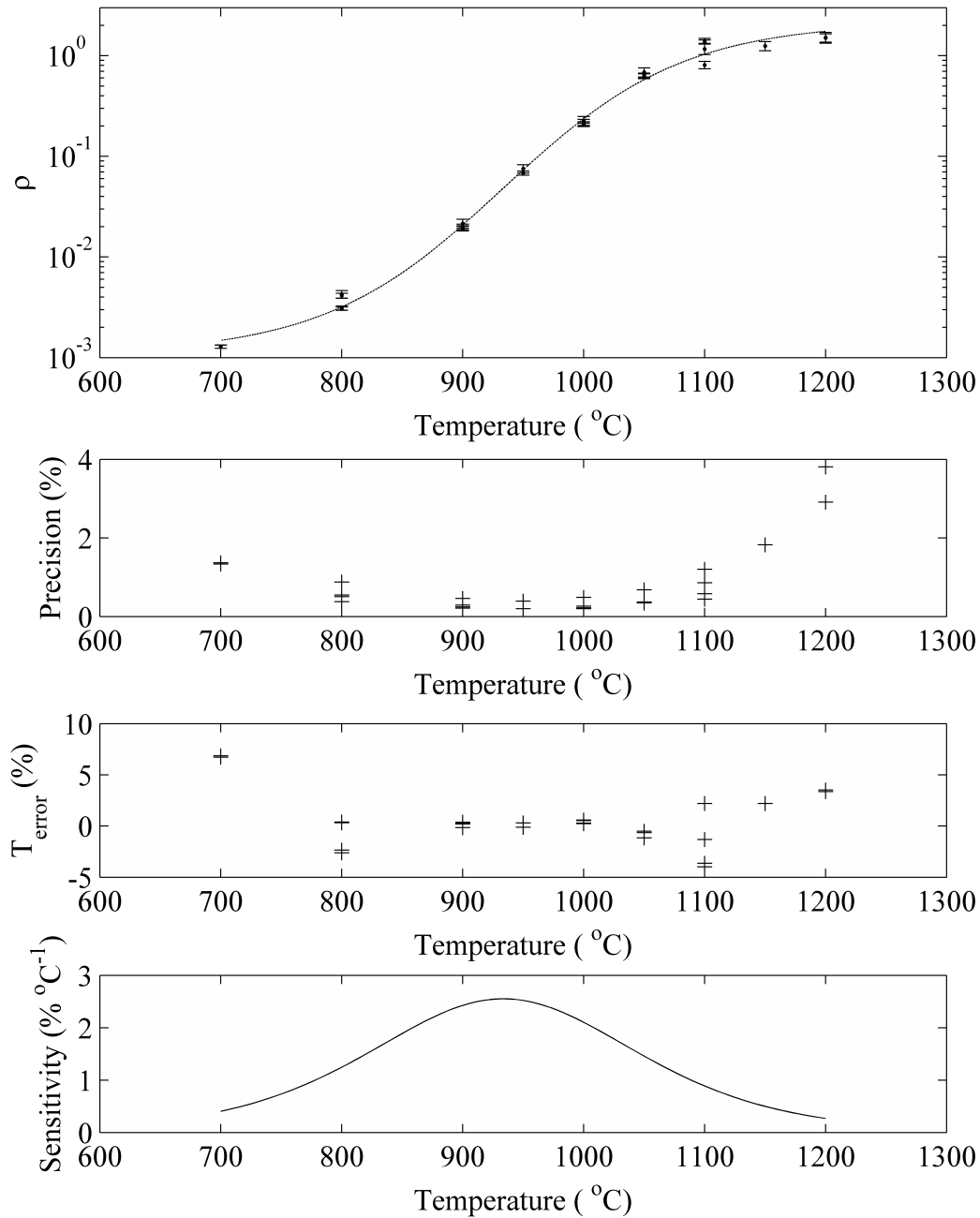
Figure 5.9. Intensity ratio of BAM:Eu (excitation at 266 nm) after heat treatment in the temperature range from 700 °C to 1200 °C for 20 minutes and fit of the experimental data using a logistic function (top). The precision of the measurement (second graph), the temperature error between the model and the experimental data (third graph) and the relative sensitivity (bottom) are also shown.

Analysis of ρ as a measurand of temperature is shown in Figure 5.9. This figure includes 27 data points obtained from several samples heat treated at the same temperature as well as various measurements of the same samples, which permits checking of the repeatability of the measurement. In the top graph of Figure 5.9, ρ increases continuously and monotonically in

the whole temperature range over three orders of magnitude. The experimental data is fitted to a model by using a logistic function with four parameters as indicated in Equation (5.3).

$$\ln(\rho) = a_1 + \frac{a_2}{1 + e^{-a_3[T(°C)-a_4]}}$$
(5.3)

Parameters a_1 and a_2 define the lower and upper asymptotes, a_3 establishes the growth rate and a_4, which is in units of °C, corresponds to the temperature of maximum growth, i.e. the temperature of maximum sensitivity. The parameter fitting retrieves the following values: $a_1 = -6.83$, $a_2 = 7.59$, $a_3 = 0.0135$ and $a_4 = 934$. The R^2 value of the fitting is 0.996, which indicates a very good agreement between the model and the experimental data.

The precision of the measurement, indicated in the second graph of Figure 5.9, is evaluated based on the 75 single-shot spectra recorded, as explained in section 4.1.3.1. Precision is better than 1 % in the temperature range from 800 °C to 1100 °C, which is directly related to the high sensitivity of ρ at these temperatures. The relative sensitivity, plotted in the bottom graph of Figure 5.9, is higher than 1 %·°C⁻¹ in the whole range from 800 °C to 1100 °C (with a maximum sensitivity of 2.5 %·°C⁻¹ at 934 °C), while it decreases at lower and higher temperatures.

The repeatability of the measurement is estimated by comparing the experimental data to the model described by Equation (5.3). The temperature error with respect to the model, depicted in the third graph of Figure 5.9, is typically below 2.5 %, and it is only higher at the extreme values of 700 °C and 1200 °C where the fitting curve deviates from the experimental data in the area where the curve flattens. An unusual effect is observed for samples heat treated at a temperature of 1100 °C, which is not observed in any other sample and is illustrated in Figure 5.10. The intensity ratio measured shortly after heat treatment of the sample is about 20 – 30 % higher than the intensity ratio measured a few days later. This intensity ratio does not decrease further at later times. This behaviour was not observed on samples heat treated at other temperatures, which showed a constant ρ independently of the moment of the measurement. The cause of this behaviour is not known and further study is necessary to determine it.
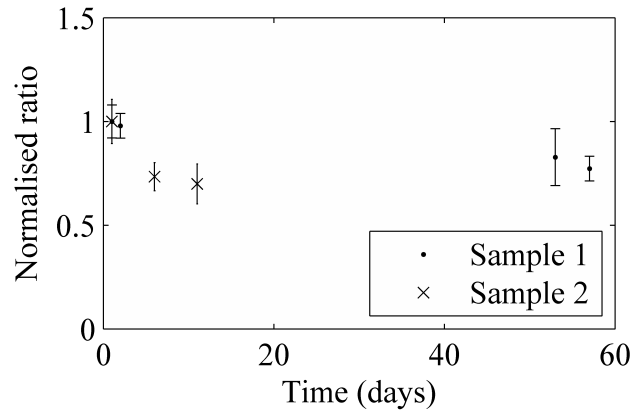
Figure 5.10. Normalised intensity ratio of two samples heat treated at 1100 °C plotted against the time at which the measurement was performed after the heat treatment.

The lifetime decay was also measured for samples heat treated in the temperature range from 700 °C to 1200 °C, both for the broad band emission and the peak at 611 nm.

The lifetime decay of the broad band emission was analysed at single wavelengths in the range from 405 nm to 565 nm by selectively filtering the light with a monochromator (see section 4.1.2.1), and the results are shown in Figure 5.11 left. The lifetime decay was calculated by using a single-exponential fit with parameters $c_1 = 0.5$ and $c_2 = 10$. The lifetime decay across the entire spectrum shows small variation with temperature and has a value that remains nearly constant at around 1 µs. A drastic reduction of the lifetime decay of fresh samples occurs after heat treatment only for wavelengths above 520 nm, where the lifetime drops from a value above 2 µs down to 1 µs. This could be interpreted as complete disappearance of emission from one of the sites occupied by Eu^{2+} ions. In this wavelength range emission from a site with low occupancy is reported by most authors [102, 104-107, 117], although there is disagreement about the exact location of this site in the crystal lattice.

The lifetime decay centred at the peak of the emission broad band (445 nm) was analysed in more detail and it is plotted in the right graph of Figure 5.11. The lifetime decay initially increases from 700 °C to 800 °C and then decreases continuously up to 1100 °C. At this temperature an inflexion point occurs and the lifetime decay increases again. These results are not in accordance with those reported in [63], where the lifetime decay at 450 nm had a value of about 1.2 µs that remained unchanged up to 1000 °C. At this temperature the lifetime decay drastically decreased down to 0.4 µs at 1100 °C. This drastic decrease is not observed in the current experiments even though the system is fast enough to detect such lifetime

decay. A new increase of the lifetime decay at higher temperatures similar to those observed in the current case was also observed in [63].

The sensitivity of the lifetime decay measured at 445 nm is small, about 0.15 %·°C^{-1} in the steepest part of the curve (~ 950 °C). The precision of the temperature measurement in this region is of about 0.1 % which indicates the possibility to use the lifetime decay as a measurand in this range. However, the low sensitivity of this method and the wavelength dependence of the decay make it very susceptible to systematic errors and therefore this lifetime decay will not be used further as a measurand.
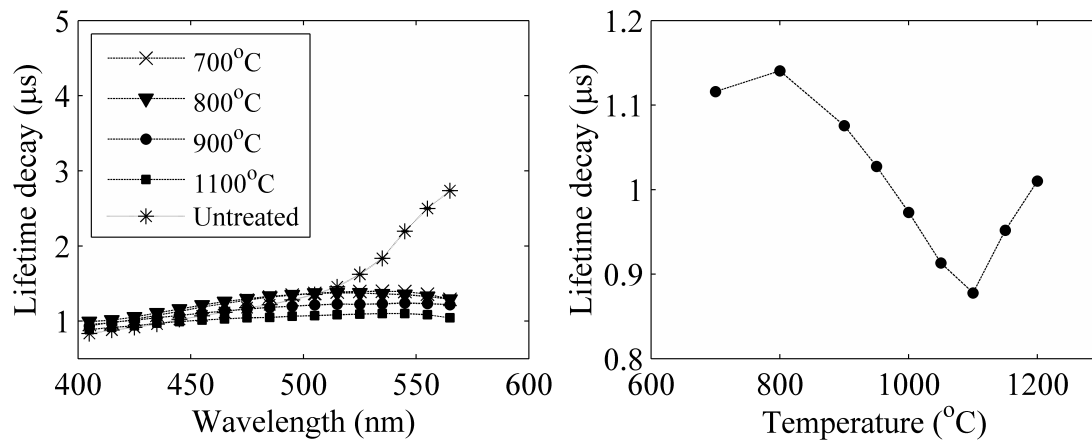
Figure 5.11. Lifetime decay at different temperatures and wavelengths of the broad band emission of Eu^{2+} (left). Lifetime decay of the broad band peak of Eu^{2+} at 445 nm versus the heat treatment temperature (right). Excitation in both graphs is at 266 nm.

The lifetime decay of the Eu^{3+} emission was also analysed in the same temperature range from 700 °C to 1200 °C and monitored at 611 nm. Figure 5.12 shows four calibration curves of this lifetime decay obtained by fitting the decays with a single-exponential fit. In these four curves the parameter c_1 is varied from 0 to 0.75 while c_2 is kept constant at 10. All the curves show a similar trend but they shift towards higher values of the lifetime decay when the parameter c_1 increases. The lifetime decay continuously increases from 700 °C to 1100 °C, when it decreases again. The sensitivity at 1050 °C is of about 0.4 %·°C^{-1} with a precision of about 0.5 %. The precision is significantly lower for the curve with highest value of c_1, and the sensitivity at temperatures below 950 °C is best when the parameter c_1 is 0.25 or 0.5. Therefore, in accordance with the discussion in section 4.1.3.2, the curve with $c_1 = 0.5$ is selected as a possible measurand of the temperature for further investigation.
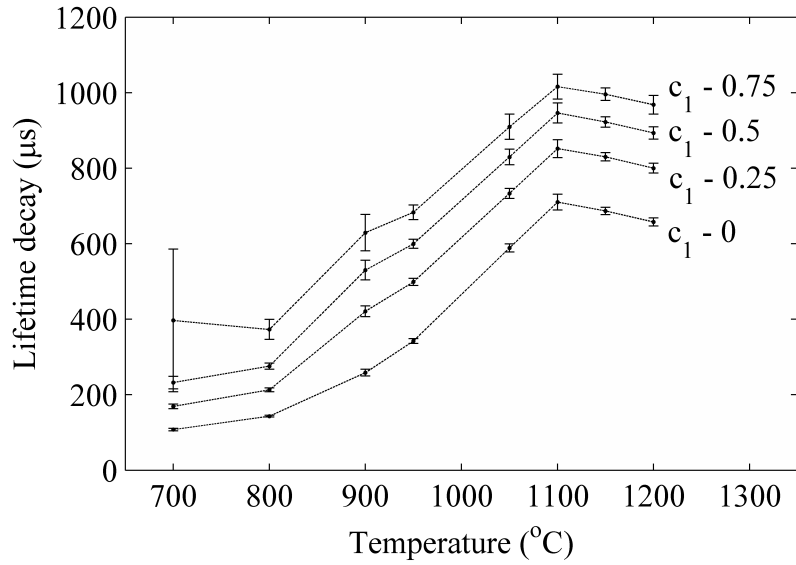
Figure 5.12. Lifetime decay of the Eu^{3+} emission at 611 nm (excitation at 266 nm) after heat treatment at temperatures from 700 °C to 1200 °C. The fitting parameter c_1 is varied from 0 to 0.75.

In Figure 5.11 and Figure 5.12, the inclination of the curve changes at 1100 °C for both emissions at 445 nm and 611 nm. This suggests that a structural change might be happening at that temperature. It is interesting to note that it is at this same temperature that the intensity ratio showed a drift over time as explained in the previous section. It is speculated that formation of a second phase may cause this change in trend of the lifetime decay, similarly to that which occurs in the phosphor YAG:Eu [95]. In the crystallisation of this phosphor, formation of the second phase YAP occurs at 900 °C, which is accompanied by a change in the behaviour of the lifetime decay. In the present study, phase transformation could not be observed in any of the thermal analysis performed in section 5.1.2. Additional XRD measurements on the samples heat treated at 1100 °C did not show any additional peaks from a second phase. Furthermore, the emission spectra of samples heat treated at this temperature did not show any changes compared to lower temperatures, which indicates that the crystal field of the ions in the bulk material is not affected. Therefore, this effect might be associated with changes on the surface of the material that modify the distribution or nature of defects thus affecting only the lifetime decay of the emission. Some authors [100] suggest that Eu_2O_3 is formed on the surface of BAM:Eu particles when oxidation occurs and then Eu^{3+} ions diffuse towards the bulk material. If this is true, the small amount of Eu_2O_3 formed would not be detected with the resolution of thermal or XRD analysis. Interestingly, Eu_2O_3 undergoes a phase transformation from cubic to monoclinic at approximately 1100 °C [160], which could

explain changes on the surface of the material and therefore on the trend of the lifetime decay. However, this hypothesis needs to be confirmed by further investigations, which is out of the scope of this work.

5.2.2. Calibration with exposure time

The oxidation process undergone by the phosphor during exposure at high temperatures, which is the basis for the temperature measurement, is dependent not only on the temperature experienced but also on the duration of that exposure. Until now, all the samples analysed were heat treated for 20 minutes, which is a reasonable time compared to standard thermal paints (see section 1.3.1). In this section, BAM:Eu samples heat treated for various times and temperatures are investigated and the influence of the exposure time on the measurement accuracy and sensitivity is discussed.

BAM:Eu powder samples were heat treated in air in the temperature range from 800 °C to 1200 °C, with exposure times of 5, 10, 20, 40, 60 and 120 minutes. The optical properties of the samples were then interrogated at room temperature. Overall, the effect of the exposure time on the emission spectra is the same as that observed for the temperature, i.e. the broad band around 445 nm decreases for longer exposure times while the emission features of Eu^{3+} increase their intensity. Therefore, it could be suggested that the effect of exposure time in the oxidation of the phosphor is somehow equivalent to the temperature. The broad band emission centred at 445 nm shows a decrease of intensity with the exposure time but the shape remains constant at all exposure times. The emission features of Eu^{3+}, however, present some changes with exposure time. This Eu^{3+} emission, normalised to the peak at 611 nm, is shown in Figure 5.13 for samples heat treated at 800 °C, 900 °C, 1100 °C and 1200 °C.

The evolution of the Eu^{3+} emission is comparable to the changes experienced with temperature as discussed in section 5.2.1, which further supports the similarity between the effects of time and temperature on the oxidation of the phosphor. At 800 °C (Figure 5.13 (a)) the peaks of the spectra have low intensity and are broad. This suggests that the ions are experiencing multiple crystal fields. In particular, the peak with the highest intensity is located at 613.5 nm for short exposure times. When the exposure time increases the intensity of this peak progressively reduces and the intensity of the peak at 611.5 nm continuously rises up to at least 120 minutes. This indicates that europium ions move while the heat treatment is maintained at this temperature for long times. Also emission from transitions less sensitive to

the crystal environment of the ion, between 575 - 600 nm, around 650 nm and in the range 675 – 710 nm, resolve into more intense peaks at longer exposure times.
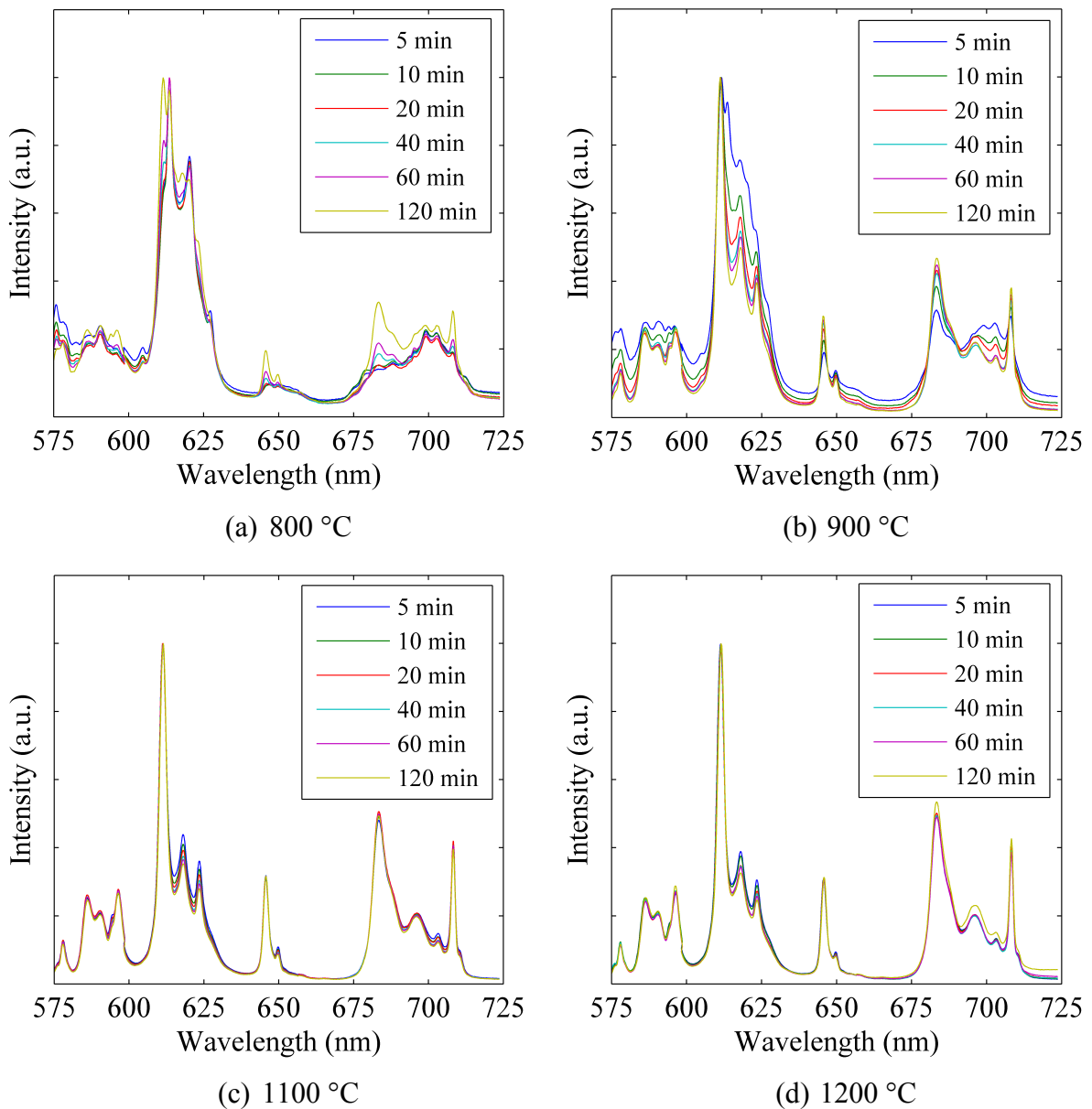
Figure 5.13. Emission spectra of Eu^{3+} ions of samples heat treated at (a) 800 °C, (b) 900 °C, (c) 1100 °C and (d) 1200 °C for exposure times ranging from 5 to 120 minutes. The spectra are normalised to the peak at 611 nm.

At 900 °C (Figure 5.13 (b)) and 5 minutes of exposure, the spectrum shows a structure very similar to that of the sample heated at 800 °C for 120 minutes. The two peaks at 611.5 nm and 613.5 nm have nearly the same intensity and the emission around 611 nm is broad. The peaks develop to a nearly constant shape after 10 minutes of heat treatment. After that time only small reduction of the intensity of the peaks at 618 nm and 623.5 nm occurs, similar to what was reported in section 5.2.1 for increasing temperatures above 900 °C.

At temperatures above 900 °C (Figure 5.13 (c) and (d)), the changes of the spectral features with exposure time are negligible (including spectra at 1000 °C not shown in Figure 5.13), although oxidation of ions is still occurring as indicated by the relative change of intensity of Eu^{2+} and Eu^{3+} emissions. This points to a fixed location of the ions regardless of the duration of the exposure at this temperature, which suggests that movement of the ions probably requires an activation energy that is achieved at temperatures between 800 °C and 900 °C.
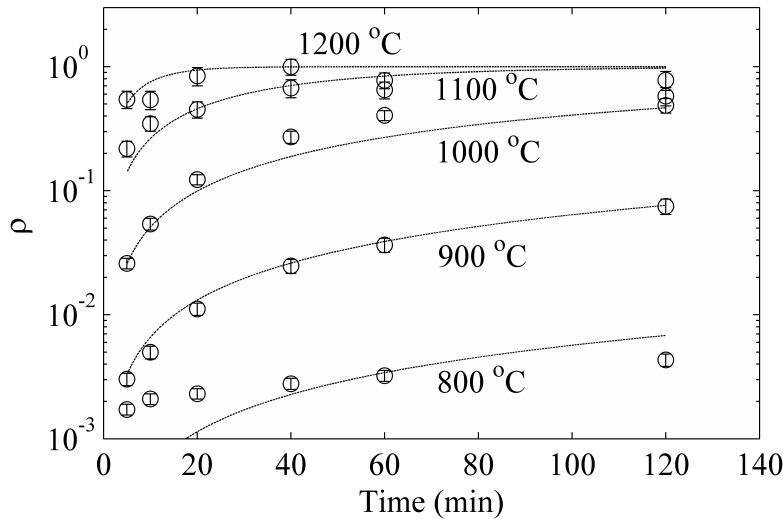
Figure 5.14. ρ versus exposure time for samples heat treated at temperatures in the range 800 - 1200 °C. The data is fitted to the KJMA theory.

The effect of the exposure time on ρ[1] is investigated for all the heat treated samples and the results are shown in Figure 5.14. The normalised intensity ratio increases monotonically with time except at 1200 °C, where ρ decreases slightly for samples heat treated for more than 40 minutes. The normalised intensity ratio seems to saturate at high temperatures as the heat treatment duration increases. This behaviour is however not observed in samples heat treated at the lowest temperature of 800 °C. Saturation of ρ, and thus of the oxidation, might be explained by the mechanisms proposed by Bizarri and Moine [114], which is further supported by the spectra in Figure 5.13 and investigations of the effect of the atmosphere in section 5.2.5. This model includes three steps: adsorption of oxygen molecules on the surface of the phosphor, diffusion of europium ions through the bulk phosphor towards the surface and oxidation of europium when it reacts with the adsorbed oxygen. The oxidation process may be limited by the amount of oxygen adsorbed, which determines the number of Eu^{3+} ions

---

[1] ρ is the intensity ratio

that can be generated. Additionally, the increase in concentration of Eu^{3+} ions may reduce the diffusion rate thus slowing down the oxidation process.

Interpretation of the experimental data has been attempted by means of the Kolmogorov-Johnson-Mehl-Avrami (KJMA) theory, which is widely applied to most types of transformations, such as crystallisation, chemical reaction, phase changes, and oxidation processes [161-164]. This law is expressed by the following equation:

$$y = 1 - exp(-kt^n) \qquad (5.4)$$

where k is the growth rate, t is the time and n is the Avrami exponent. The growth rate is generally dependent on the thermodynamic temperature following an Arrhenius expression:

$$k(T) = A\,exp\left(-\frac{E_a}{k_B T}\right) \qquad (5.5)$$

Where A is a pre-exponential constant, E_a is the activation energy and k_B is the Boltzmann constant.

The curves fitted to the normalised intensity ratio based on the model described by Equations (5.4) and (5.5) are shown in Figure 5.14. All the experimental data is fitted by using only the two parameters A and E_a, and the R^2 value of the fit is of 0.88. The numerical model agrees well with the experimental data for an Avrami exponent of 1, except for the lowest temperature of 800 °C. At this temperature, the experimental data does not conform to the KJMA theory, which suggests that a different process is occurring at this temperature, or simply that the temperature is too low to achieve complete transformation and thus the model should be modified to account for this effect.

As it was mentioned before, samples heat treated at 1200 °C seem to recover part of their emission intensity at 445 nm for exposures longer than 40 minutes, and thus ρ decreases slightly. This recovery of intensity was previously reported in [69] but an explanation was not provided. There are two physical effects observed at this temperature that could be related to this decrease in ρ.

The first possible effect is the appearance of a new phase, $EuMgAl_{11}O_{19}$ [99], which is only observed by XRD measurements in samples heat treated at 1200 °C for sufficiently long times (see Figure 5.15). Although this second phase might be present at lower temperatures, it could not be detected with the resolution of the technique. However, the possibility to detect this phase in samples heat treated at 1200 °C and long exposure times points to an increase of the

concentration of the phase at high temperatures that could affect the optical properties of the phosphor. However, Kim et al. [111] observed formation of this phase with a continuous decrease of the Eu^{2+} emission and a continuous increase of the Eu^{3+} emission up to 1400 °C, which contradicts this hypothesis.
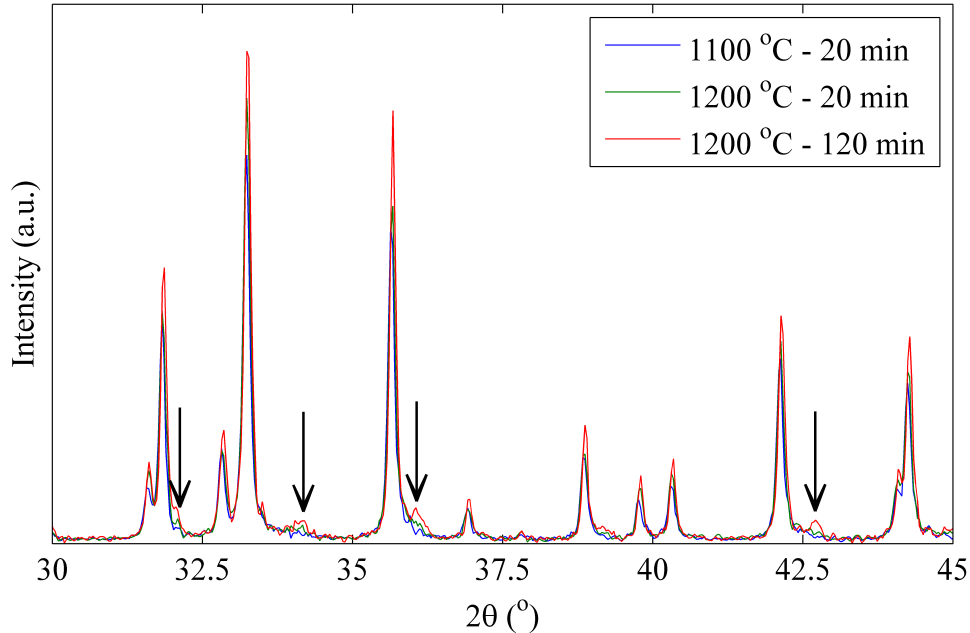
Figure 5.15. XRD pattern of BAM:Eu samples heat treated at 1100 °C for 20 minutes and 1200 °C for 20 and 120 minutes. The appearance of peaks that belong to the phase $EuAl_{12}O_{19}$ is indicated by arrows.

The second effect is the sintering of the particles. The sintering process begins at a temperature slightly below 1200 °C according to the dilatometry analysis in section 5.1.2.1. Although the sintering rate would be slow at 1200 °C, after a sufficiently long exposure of more than 40 minutes the increase of particle size and formation of necks between particles could significantly affect the optical properties of the phosphor. In particular, the increase of particle size increases the light absorption, reduces the scattering and decreases the specific surface area which diminishes the number of surface defects and therefore of luminescence quenchers. Furthermore, increase of the particle size has been reported to be responsible for an increase in the 445 nm emission of BAM:Eu in [132]. Further investigation is still necessary to prove this hypothesis.

The use of the KJMA theory to fit the experimental data in the temperature range from 900 °C to 1200 °C makes it possible to determine the temperature from ρ and knowledge of the exposure time. At temperatures below 900 °C, temperature can still be measured but would

require additional calibration data. Furthermore, the data in Figure 5.14 suggest that the uncertainty of the measurement at a selected temperature can be improved by adjusting the exposure time. For high temperatures, exposure times of less than 20 minutes seem more adequate, while lower temperatures can be more precisely measured with longer exposure times.

The lifetime decay of the emission at 611 nm was also investigated with regards to the exposure time. Figure 5.16 shows the lifetime decay of the samples heat treated at the indicated temperatures and times. The variation of the lifetime decay with exposure time is similar to that of ρ, and it continuously increases for longer exposure times and temperatures up to 1100 °C. At this temperature the lifetime decay shows small variation with exposure time and remains relatively constant from 10 to 60 minutes of exposure. Above that time the lifetime decay starts to decrease. At 1200 °C the lifetime decay continuously decreases with exposure time. The explanation for the decrease of the lifetime decay at temperatures above 1100 °C has been discussed in section 5.2.1.
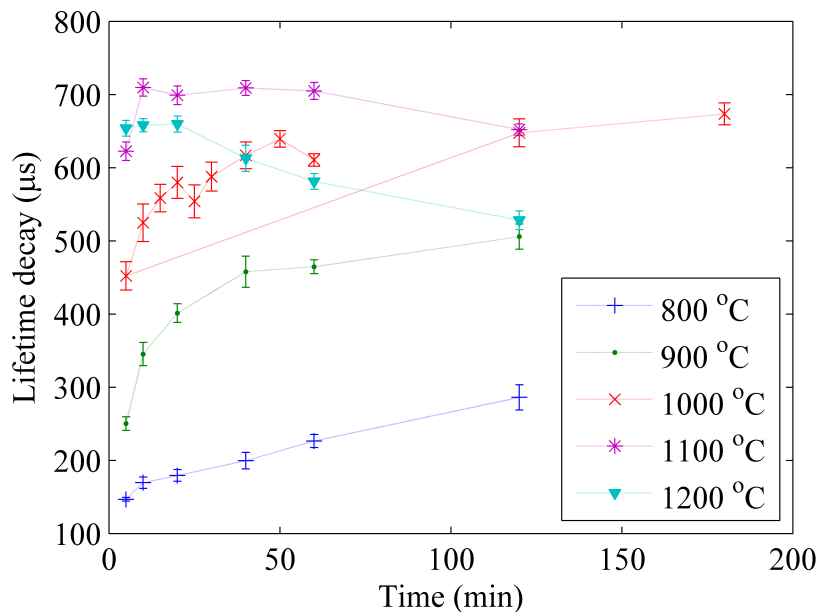
Figure 5.16. Lifetime decay versus exposure time of samples heat treated at temperatures in the range 800 - 1200 °C.

Since the lifetime decay at 611 nm presents a variation with time and temperature similar to that of the intensity ratio, it could potentially be used to measure temperatures. However, the curve does not change monotonically above 1100 °C. Since the same lifetime decay can refer to two different temperatures, it is necessary to evaluate which side of the calibration curve should be used in the measurement. The method can thus be used simultaneously with the

intensity ratio to obtain two independent temperature readings in the same location, which would help to improve the accuracy of the measurement.

5.2.3. Effect of excitation fluence

The amount of energy used to excite a phosphor plays an important role in the radiant efficiency of that phosphor. As the energy density increases, the luminescence intensity of the phosphor increases accordingly up to a certain point at which the quantum efficiency of the phosphor starts to decrease. This effect, which is known as saturation, might be caused by several reasons.
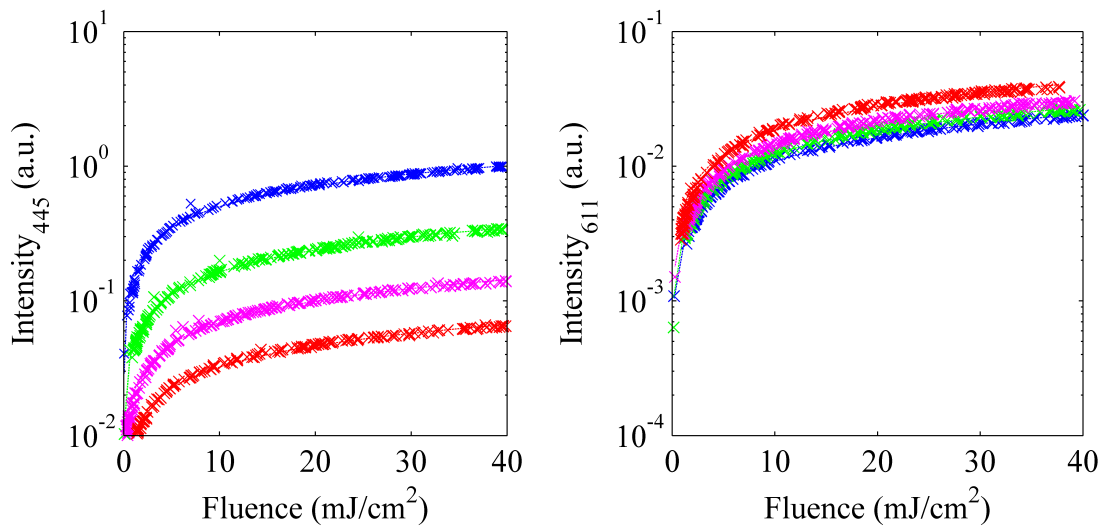
Figure 5.17. Experimental saturation curves of BAM:Eu samples heat treated at 900 °C (blue), 950 °C (green), 1000 °C (pink) and 1050 °C (red) in air.

A possible interpretation is that an increase of the excitation energy leads to an increase of the phosphor temperature and thus to thermal quenching [165]. However, some phosphors with a high quenching temperature show saturation even at low temperatures. An alternative explanation is thus that saturation occurs when all the activator ions are excited and the emitted light reaches a maximum. This is called activator ground state depletion. However, saturation is usually found at lower excitation densities than would be expected by this mechanism, which is explained by the presence of high order recombination processes between excited activator ions and Auger-type electrons in the phosphor host lattice [165]. Non-radiative energy transfer between an excited-state of the activator and an exciton reduces the quantum efficiency of the phosphor leading to saturation.

The saturation of the Eu^{2+} emission of BAM:Eu has been previously reported in [126], but the Eu^{3+} emission was not then investigated. In this work, the saturation of both emissions was

investigated in samples heat treated at 900 °C, 950 °C, 1000 °C and 1050 °C for 20 minutes. The samples were illuminated normally while the beam diameter was set to a fixed value of 4 mm. The energy of the laser pulse and the intensity emitted by the phosphor were recorded simultaneously by using an energy monitor as described in section 4.1.1. The emission intensity, as calculated to compute the intensity ratio, could then be related to the excitation fluence defined as the total energy divided by the area of the laser beam (J/cm^2). In Figure 5.17 the intensities of the emissions at 445 nm (left) and 611 nm (right) are plotted versus the laser fluence for the samples studied. The results of the 445 nm emission are comparable to those reported in [126], in which the emission intensity followed a linear behaviour at low excitation densities of less than 2 mJ/cm^2. Above that value, the slope of the curve decreases until it reaches again a constant value above approximately 10 mJ/cm^2. This behaviour is analogous for the 611 nm emission intensity in Figure 5.17.
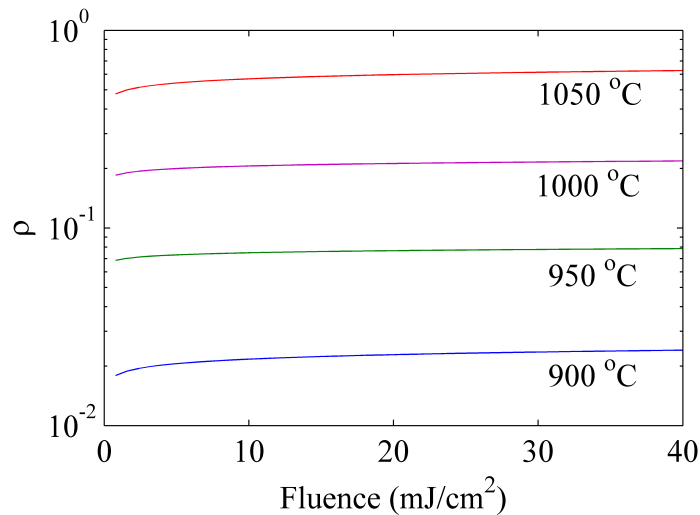
Figure 5.18. Calculated ρ of BAM:Eu samples heat treated at 900 °C (blue), 950 °C (green), 1000 °C (pink) and 1050 °C (red) in air at various excitation fluences.

The experimental data in Figure 5.17 is fitted to an exponential function of the form $I(x) = ax^b$, where a and b are fitting parameters and x is the laser fluence (mJ/cm^2). The fitted functions are then used to calculate ρ over the range of fluences, and the results are shown in Figure 5.18. Although ρ remains nearly constant for all samples, and especially above the saturation limit of 10 mJ/cm^2, a minor increase with excitation fluence can be observed. This increase in ρ is probably related to variations in the penetration depth of the excitation laser light through the phosphor powder layer and differences between the scattering and absorption coefficients at the two evaluated emission wavelengths. In any case, a change in the excitation fluence from 10 mJ/cm^2 to 40 mJ/cm^2 results in a maximum temperature

variation which is in all cases of less than 1 %. In practical applications such a large variation in the excitation fluence is unlikely and therefore ρ can be considered unaffected by the excitation energy fluctuations.
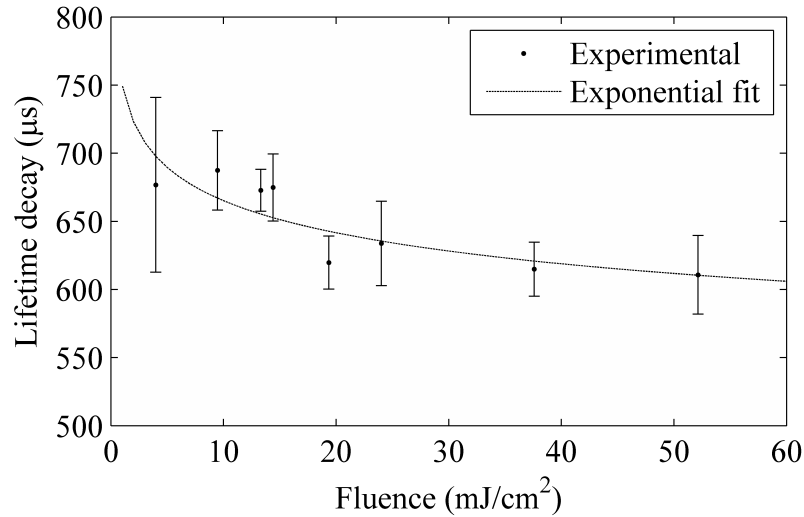
Figure 5.19. Lifetime decay versus excitation fluence of a BAM:Eu sample after heat treatment at 1000 °C in air. Fitting parameters are $c_1 = 0.5$ and $c_2 = 10$.

The influence of the excitation fluence is also investigated on the lifetime decay of the emission at 611 nm. Saturation effects might also cause variations on the lifetime decay of the phosphor due to complex energy transfer mechanisms. It is known that a rise in the excitation energy causes a decrease of the lifetime decay when recombination processes occur in the activator [165] and it has been experimentally evaluated for Mg_4FGeO_6:Mn [166]. The variation of the lifetime decay with excitation fluence is investigated for a BAM:Eu sample heat treated at 1000 °C for 20 minutes. The results in Figure 5.19 indicate that the lifetime decay decreases with excitation fluence as expected from the theory. The maximum variation of the lifetime decay from a fluence of 4 mJ/cm^2 to 50 mJ/cm^2 results in a measured temperature difference of approximately 40 °C, which is of about 4 %. The effect of energy is therefore significant in the lifetime decay method and careful control of the excitation energy is necessary to avoid systematic errors. The high variability of the results that would be introduced by fluctuations of the excitation fluence is one of the main limitations for the use of the lifetime decay method with BAM:Eu phosphor.

5.2.4. Effect of cooling down time

The influence of the time required for the sample to cool down after the heat treatment is terminated is important for practical applications in which the components might remain at high temperatures for long times. In section 5.2.2 the effect that extending the heat treatment time has on ρ was investigated. A long cooling down time can be regarded as an additional exposure time at temperatures that are below the set temperature of the heat treatment. Therefore, ρ is expected to increase as the cooling down time increases, which is quantified in this section.
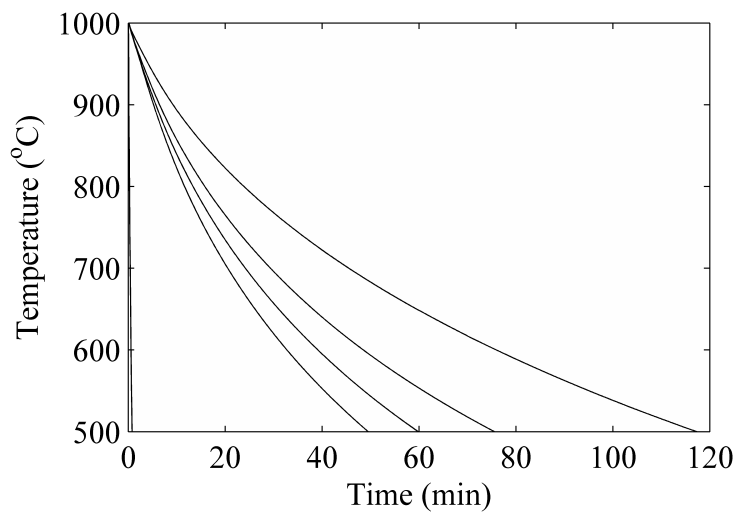
Figure 5.20. Cooling curves of the samples cooled down at different rates with an initial temperature of 1000 °C as measured by an N-type thermocouple.

The study of the effect of the cooling down time is performed in samples heat treated at 1000 °C for 20 minutes that are then cooled inside the heat treatment furnace while ambient air is flushed at four different flow rates that control the cooling rate of the sample. The limit case is when no cooling air is introduced and the sample cools down at the slowest possible rate of the system. The temperature is continuously monitored by an N-type thermocouple, and the recorded cooling down curves are plotted in Figure 5.20. The samples are considered to have cooled down when they reach 500 °C since this is the temperature at which BAM:Eu stops its degradation [167]. The optical properties of the heat treated samples are then investigated at room temperature and compared to those of a sample cooled down in air at room temperature, which is the normal procedure followed to cool down the samples in this work. The samples that are quenched in air rapidly cool down in less than 3 minutes as depicted by the nearly vertical curve in Figure 5.20.

The definition of a suitable measurand of the cooling down time needs careful consideration if samples under different cooling conditions are to be compared. Although the use of the time required for the sample to reach 500 °C can be a suitable estimate of the cooling down time for the curves in Figure 5.20, where the cooling down rate is nearly constant, it might not be representative of a more discontinuous process. For example, the sample might reduce its temperature rapidly at the beginning and then remain at moderate temperatures above 500 °C for a relatively long time. In such a case the "cooling down time" would be long but the actual exposure to high temperatures would be small and the additional oxidation induced in the phosphor marginal.

Therefore, a suitable estimate of the cooling down time can be based on the thermal load, which is a measure of the area under the cooling down curve. In this work this estimate is defined as the equivalent time necessary to obtain the same area under the curve if the sample remained at the initial temperature and the cooling down was an instantaneous process. Therefore, the cooling down time is regarded as an extra exposure at the heat treatment temperature whose duration depends on the cooling conditions.
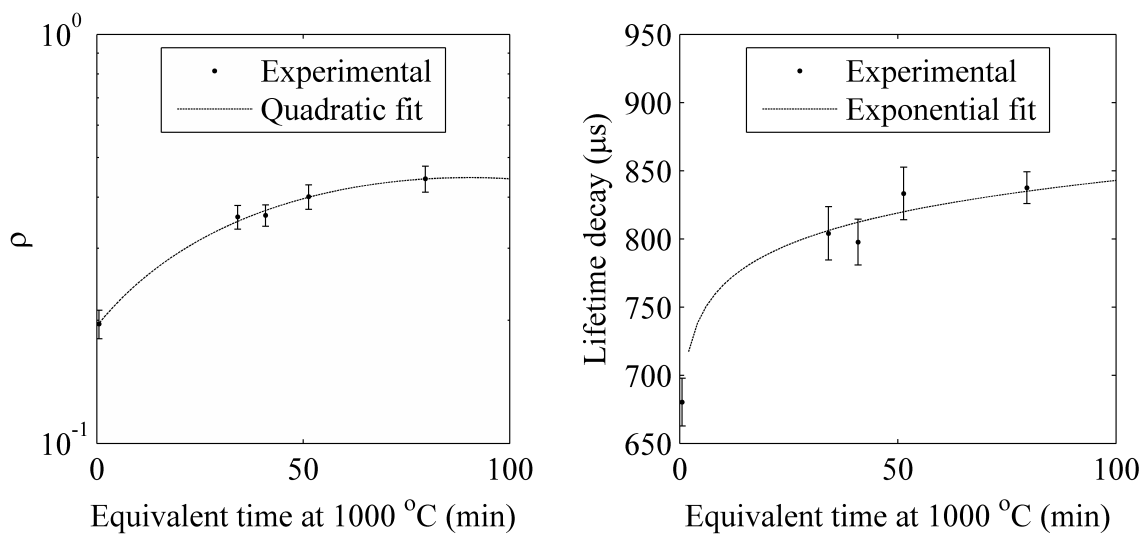
Figure 5.21. ρ (left) and lifetime decay (right) versus equivalent time at 1000 °C as a measurand of the cooling down time.

According to this definition of the cooling down time, ρ and the lifetime decay of each heat treated sample is calculated and plotted against the equivalent time at 1000 °C in Figure 5.21. Both ρ and the lifetime decay increase as the cooling down time increases, which is already expected as the overall heat treatment time is slightly higher. This increase is however not

comparable to that of Figure 5.14 and Figure 5.16 since the equivalent time at 1000 °C is only an estimate of the thermal load and not a real time. If the cooling down time is not accounted for, a systematic error would be introduced and the maximum temperatures measured would be overestimated. The maximum temperature error introduced when the cooling down takes longer than one hour can be estimated from the plots in Figure 5.21, and it is of about 40 °C (4 %) for the intensity ratio technique and 65 °C (6.5 %) if the lifetime decay method is used. This error is relatively small given the large differences in cooling down times between the extreme cases (from 2 minutes to 2 hours) and can be acknowledged and calibrated for prior to the measurement thus reducing any systematic errors.

5.2.5. Effect of atmosphere

The understanding of the influence that the gas atmosphere composition plays on the oxidation of BAM:Eu is essential to perform temperature measurements with this phosphor. Until now all the samples have been heat treated in air at ambient pressure. However, the conditions in the turbine of a gas turbine can be significantly different: the compression ratio can be as high as 45:1 and 20 % of the air compressed is actually consumed during the combustion [168].

The degradation of BAM:Eu is known to be related to the oxidation of the europium ion, which in many studies is associated to the presence of oxygen in the gas bath. On the contrary, when the phosphor is heated in a neutral or slightly reducing atmosphere the degradation process is attenuated or completely inhibited. However, no specific study has been made that considers the sensitivity of the oxidation of BAM:Eu to the oxygen concentration. This would be helpful to quantify the effect of atmosphere composition variations on the temperature measurements derived from the oxidation of the phosphor. This is especially relevant in the study of temperatures in gas turbines where the distribution of oxygen can be heterogeneous in different areas of the combustor and first stages of the turbine.

The effect of the atmosphere is studied on samples heat treated at 1000 °C for 20 minutes in a controlled atmosphere, by using the set-up described in section 4.2.2. The atmosphere composition was adjusted by mixing flows of air, nitrogen and oxygen in the required proportions to obtain oxygen partial pressures that varied from approximately 0.02 bar to 0.31 bar (the partial pressure of oxygen in air at ambient pressure is of about 0.21 bar). The optical properties of the heat treated samples were interrogated at room temperature and the

intensity ratio calculated for these samples is shown in Figure 5.22. A fit is performed to the experimental data that will be discussed later. A control sample was heat treated under a commercial mixture of 2 % oxygen and 98 % nitrogen for comparison with the in-house gas mixture, and the results showed good agreement.
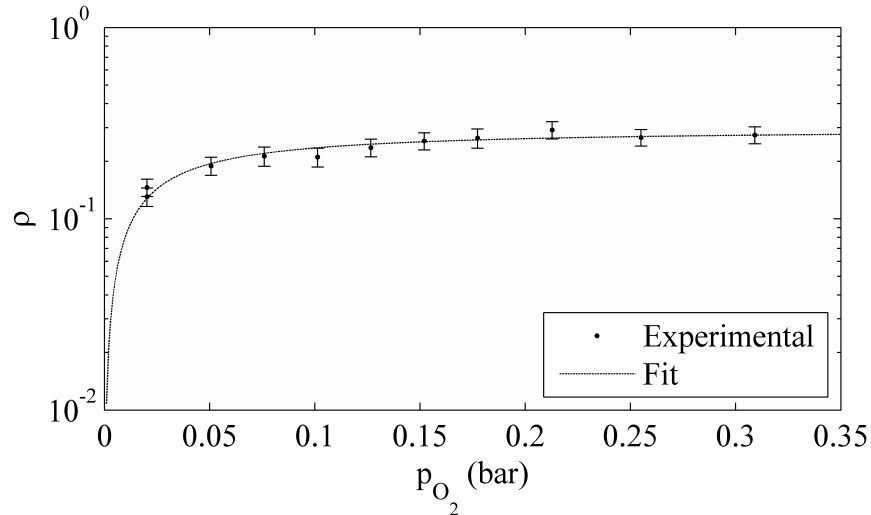
Figure 5.22. ρ versus oxygen partial pressure of BAM:Eu samples heat treated at 1000 °C for 20 minutes.

The intensity ratio shown in Figure 5.22 increases at low oxygen concentrations below approximately 0.1 bar. However, for partial pressures above 0.1 bar ρ remains nearly constant and the conversion to temperature gives a maximum variation of less than 2 %, which is within the limits of repeatability of the current measurement. When the oxygen partial pressure drops below 0.1 bar the temperatures are underestimated, the temperature measurement error at 0.02 bar being of about 4 %.

This behaviour can be explained by the degradation model proposed by Bizarri and Moine [114]. In this three-step model of the degradation of BAM:Eu, the first step consisted of the adsorption of oxygen atoms from the atmosphere into oxygen vacancies on the surface of the phosphor. They simulated this mechanism by using the Langmuir theory of adsorption of gases. In the present study this theory is also applied by considering a constant temperature and a variable oxygen partial pressure (whereas in their case the pressure was constant and the temperature variable). The Langmuir isotherm can then be expressed as:

$$N = \frac{N_0 k p_{O_2}}{1 + k p_{O_2}}$$

(5.6)

where N is the number of adsorbed molecules, N_0 is the total number of vacancies that can be filled, k is a constant and p_{o2} is the oxygen partial pressure. If the initial number of europium ions in the trivalent state is considered negligible, the amount of Eu^{2+} and Eu^{3+} ions after a certain heat treatment at a constant temperature can be obtained by:

$$N_{Eu^{2+}} = N_{Eu} - \alpha \frac{N_0 k p_{O_2}}{1 + k p_{O_2}} \tag{5.7}$$

$$N_{Eu^{3+}} = \alpha \frac{N_0 k p_{O_2}}{1 + k p_{O_2}} \tag{5.8}$$

Here, $N_{Eu^{2+}}$, $N_{Eu^{3+}}$ are respectively the number of Eu^{2+} and Eu^{3+} ions in the phosphor, N_{Eu} the total number of europium ions and α a constant that quantifies the ratio of conversion from Eu^{2+} to Eu^{3+} to the total number of oxygen atoms adsorbed. If the intensity emitted by each of these ions is considered to be proportional to the number of ions and the intensity ratio calculated by dividing both emission intensities, the following expression can be deduced for ρ which depends on the oxygen partial pressure and two constants K_1 and K_2:

$$\rho \propto \frac{N_{Eu^{3+}}}{N_{Eu^{2+}}} = \frac{K_1 p_{O_2}}{1 + K_2 p_{O_2}} \tag{5.9}$$

This equation has the same form as Equation (5.6) and the fit shows good agreement with the experimental data in Figure 5.22 ($R^2 = 0.93$). These results support the hypothesis by Bizarri and Moine that the first step in the degradation of BAM:Eu is the adsorption of oxygen atoms. They also demonstrate that saturation of the adsorption occurs at relatively low oxygen partial pressure (0.1 bar) and further increase of this pressure would have little effect on the measured ρ and therefore on the sensed temperature. This is especially advantageous in gas turbines where the partial pressure of oxygen is well above the threshold of 0.1 bar.

5.2.6. Effect of dopant concentration

The effect of the dopant concentration is normally studied in phosphors to seek the optimum quantum efficiency. This has been studied in BAM:Eu and it is commonly reported to be close to 0.09 mol of Eu [124] (approximately 10 % wt. of Eu) as discussed in section 3.3.2. It is however reported by Zhu et al. [107] that BAM:Eu is more resistant to oxidation if the europium content increases. According to the results from sections 5.2.1 and 5.2.2, the oxidation of BAM:Eu is associated to a continuous process governed by temperature and time. Increased resistance to degradation by modification of the dopant concentration would

slow down this process, which would imply that the sensor can be tuned to be sensitive at higher temperatures. This is opposite to the effect obtained when the exposure time is increased (see section 5.2.2). In order to test this hypothesis BAM:Eu samples were manufactured by the sol-gel method with dopant concentrations of 5 %, 10 % and 15 % of europium, and the optical properties after heat treatment in air were investigated.

5.2.6.1. Sample preparation
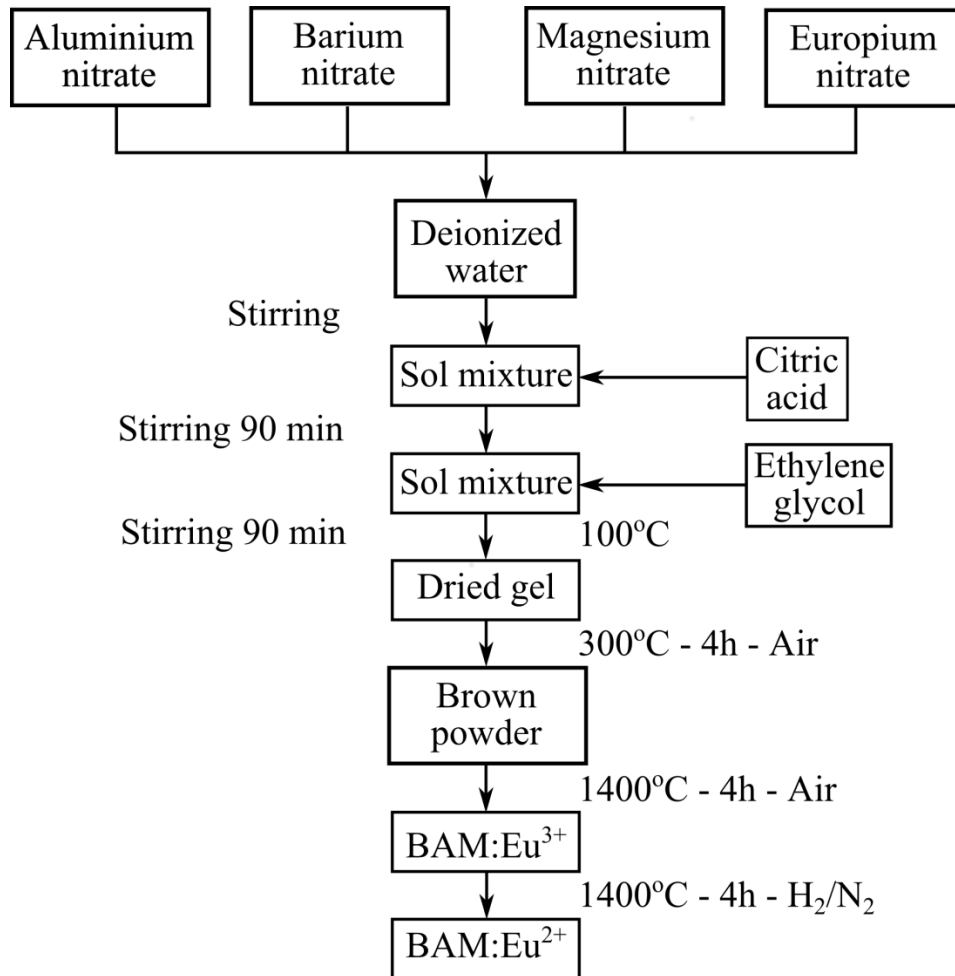
Figure 5.23. Description of the sol-gel process followed to produce the BAM:Eu samples with different dopant concentrations.

The BAM:Eu samples were prepared by the sol-gel method following the procedure previously described in [129, 130] and depicted in Figure 5.23. Aluminium nitrate nonahydrate (Alfa Aesar; No. 12360, 98%), barium nitrate (Alfa Aesar; No. 30481, 99.95%), magnesium nitrate hydrate (Alfa Aesar, No. 10799, 99.999%) and europium(III) nitrate hydrate (Alfa Aesar, No. 11296, 99.99%) were used as the precursors. These precursors were dissolved in deionized water and then a mass of citric acid (which acted as the chelating

agent) equal to the weight of all the metal precursors was added. The mixture was stirred for 90 minutes before 5 ml of ethylene glycol (Alfa Aesar, No. 44529) was added to the solution as the polymerizing agent. Next, the solution was heated at 100 °C and stirred for 3 hours until a dried gel was obtained. This product was further dried in a furnace at 300 °C for 90 minutes. The resulting brown product was then ground thoroughly in order to reduce the presence of agglomerates and not as a means of reducing the particle size (the effect of particle size reduction is studied in section 5.2.7). The powder obtained heat treated at 1400 °C for 4 hours in air. At that point BAM:Eu^{3+} was obtained and a heat treatment in a reducing atmosphere was necessary to reduce the europium to the divalent state. This was done at 1400 °C for 4 hours in an atmosphere that contained 5 % of H_2 and 95 % of N_2.
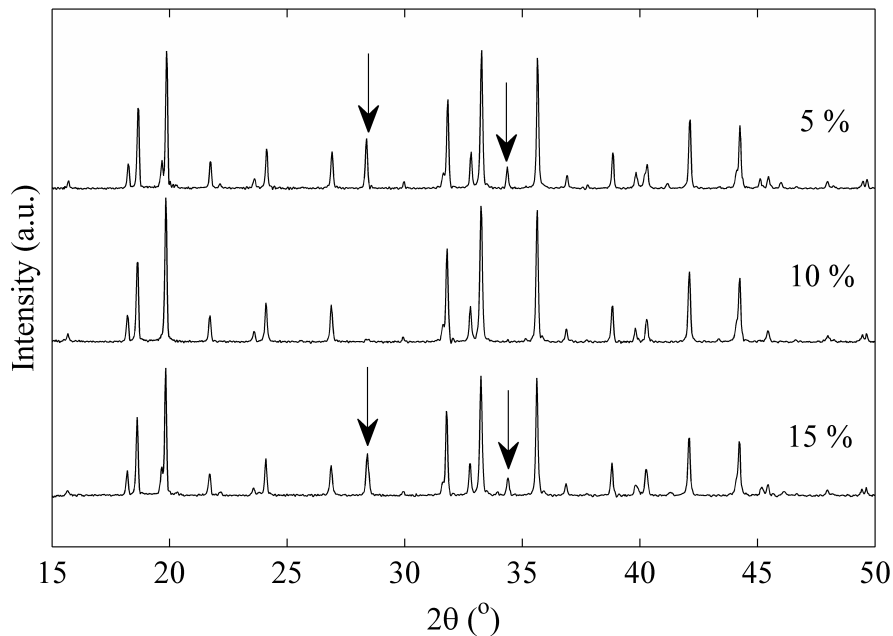
Figure 5.24. XRD diffraction patterns of the BAM:Eu samples manufactured by the sol-gel process. The arrows indicate the peaks of the second phase BaAl$_2$O$_4$ observed in the samples with 5 % and 15 % Eu content.

The as-synthesized samples were examined by XRD to confirm that the BAM phase was obtained and the obtained patterns are shown in Figure 5.24. The sample with 10 % Eu shows BAM as the single phase whereas for samples with 5 % and 15 % Eu the presence of a second phase is observed. This phase, which is identified as $BaAl_2O_4$ (BAL), has been previously reported to form a solid solution with the BAM phase [105] and its presence might be due to slight deviations of the stoichiometry. According to the XRD measurement the concentration of this second phase is only of about 6 - 7 % in the two mentioned samples, and therefore the effect on the optical properties of this second phase is expected to be negligible according to

the investigations of Pike et al. [105]. This is confirmed by the recorded emission spectra of the three BAM:Eu samples shown in Figure 5.25, which exhibits identically broad band emission for all three samples. The presence of the BAL phase, which would be reflected in a broader peak extending to longer wavelengths, is not observed. Emission spectra in Figure 5.25 further confirm that the reduction of the europium ion is complete since no emission features from Eu^{3+} are visible in the spectra. However, there is an unknown emission at around 700 nm whose origin has not been identified and it is likely related to the presence of an impurity ion. The influence of this emission on ρ is not significant since it is far from the 611 nm emission from Eu^{3+} and its intensity remains constant after heat treatment in air.
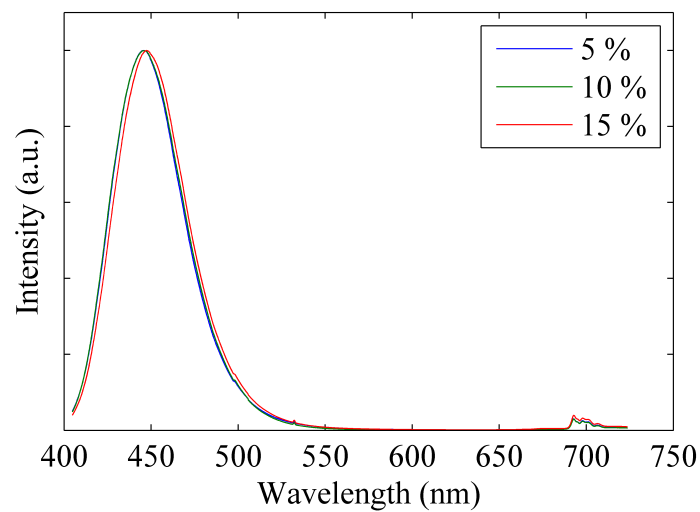
Figure 5.25. Normalised emission spectra of the as-synthesized BAM:Eu samples with different dopant concentrations. See text for further discussion.

5.2.6.2. Results

The three sets of BAM:Eu samples with 5 %, 10 % and 15 % Eu content were heat treated in air for 20 minutes in the temperature range from 800 °C to 1400 °C. The optical properties of the samples were then measured at room temperature. The intensity ratio of these samples was calculated and a calibration curve obtained for each of the dopant concentrations.

The calibration curves depicted in Figure 5.26 can be divided in three regions. Below 1000 °C the intensity ratio of the samples with 5 % and 10 % europium slightly increases with temperature, which indicates that these samples undergo some oxidation at these temperatures. The sample with 15 % europium shows an intensity ratio that remains nearly constant and then slightly decreases at 1000 °C. This can be explained because the degradation of the phosphor is very low and the 611 nm emission intensity is almost

negligible, which introduces uncertainty in the calculation of ρ and is responsible for the fluctuations of its value.
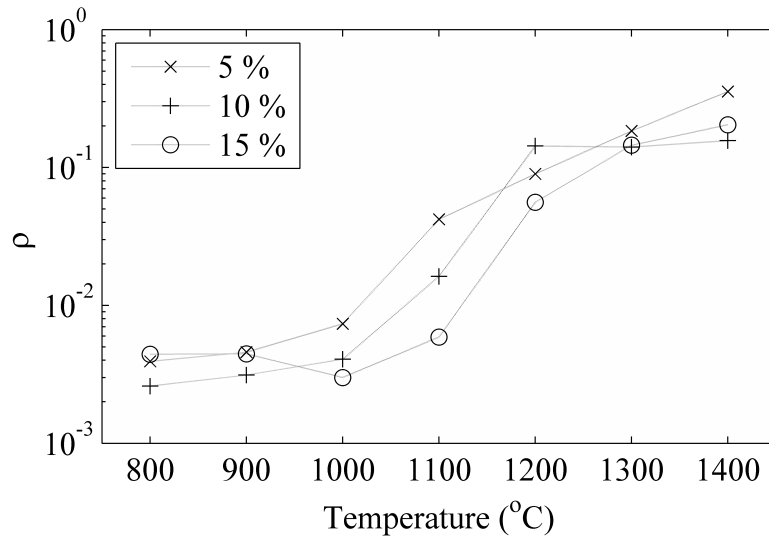
Figure 5.26. ρ versus temperature of the BAM:Eu samples with different Eu content after heat treatment in air.

The second region extends from 1000 °C to 1200 °C. Here ρ continuously increases with temperature with a marked sensitivity. It is worth noting that the curves of the samples with 5 %, 10 % and 15 % are shifted from left to right. This indicates that the same level of oxidation is reached at higher temperatures for the samples with a higher dopant concentration, which proves the hypothesis that a higher dopant concentration increases the resistance to thermal oxidation of BAM:Eu. Furthermore, the curve of the sample with 5 % europium starts to show saturation of the oxidation at 1200 °C, which is in agreement with that sample suffering the highest degradation.
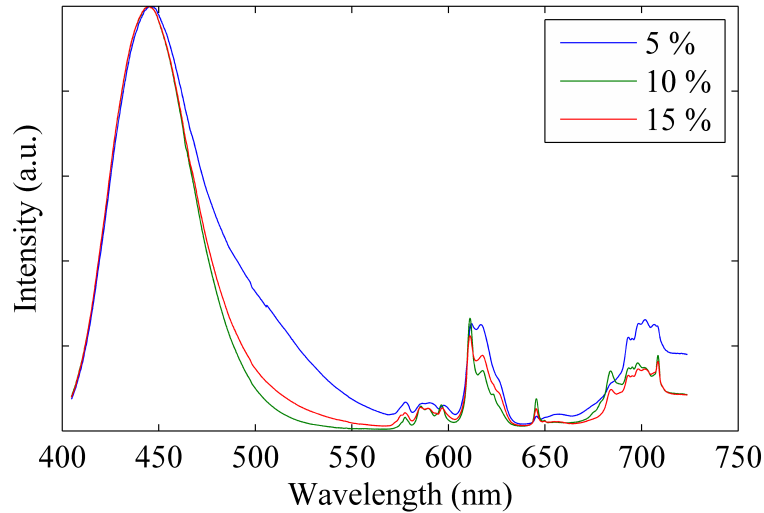
Figure 5.27. Normalised emission spectra of sol-gel samples heat treated in air at 1300 °C for 20 minutes. The sample with 5 % Eu shows an extended broad band towards the green due to appearance of the BAL phase.

The third region, above 1200 °C, requires careful consideration and analysis of the individual emission spectrum of each sample. The intensity ratio of the sample with 5 % europium should remain constant as saturation of the degradation occurs. However, ρ increases further. This tendency is ascribed to the appearance of emission from the BAL phase [105] at high temperatures as indicated by the emission spectra shown in Figure 5.27 for the sample heat treated at 1300 °C. The emission of these samples shows a broad band that extends to longer wavelengths, which in turn reduces the absolute intensity of the peak at 445 nm. The decrease of this intensity leads to an increase of the calculated ρ. Therefore, the variation in composition affects the optical properties of this sample at high temperatures, which could be studied further to extend the measuring capabilities of the phosphor. The other two samples in Figure 5.27 show a distinct broad band which belongs to emission only from the BAM phase. The intensity ratio of both these samples follows the expected trend. It saturates for the sample with 10 % europium and the sample with 15 % europium starts to show some saturation at 1300 °C and 1400 °C but ρ still increases at these temperatures.
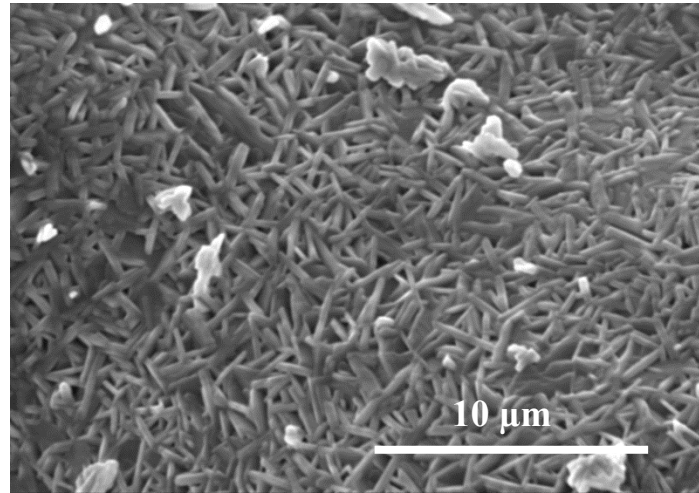
Figure 5.28. SEM image of the sol-gel sample with 5 % of europium.

The results presented in Figure 5.26 confirm the hypothesis that variations in the europium content can be used to increase or reduce the temperature range in which the sensor is more sensitive. These results are only qualitatively valid and the absolute value of ρ cannot be compared with that of commercial BAM:Eu. The reasons for this are related to the sol-gel manufacturing process, from which rod-like small particles (Figure 5.28) are obtained as opposed to the irregular shape of commercial BAM:Eu particles obtained by solid state reaction. Furthermore, the manufacturing temperature of the sol-gel phosphor of only 1400 °C is small compared to the temperatures used in the solid state method which are in excess of 1600 °C. Therefore, the level of crystallinity achieved in the sol-gel samples used in this study is probably lower than in the commercial BAM:Eu, which can also affect the resistance to thermal degradation.

5.2.7. Effect of particle size

The influence of the phosphor particle size on the temperature calibration of the sensor is investigated in this section. This effect is important because one of the steps in the oxidation process of the phosphor is the adsorption of oxygen on the surface.

In section 5.2.2 the possibility that a change in the particle size might affect the optical properties of the phosphor in such a way that ρ would increase when the particle size decreases was also discussed. If this hypothesis is true, ρ would increase when the particle size decreases, both as a result of a higher oxidation promoted by a high specific surface area and the change in the optical properties of the phosphor. Separation of the contributions of these two effects is complicated and was not possible during the present study, in which only the overall effect of the reduction of particle size was tested.
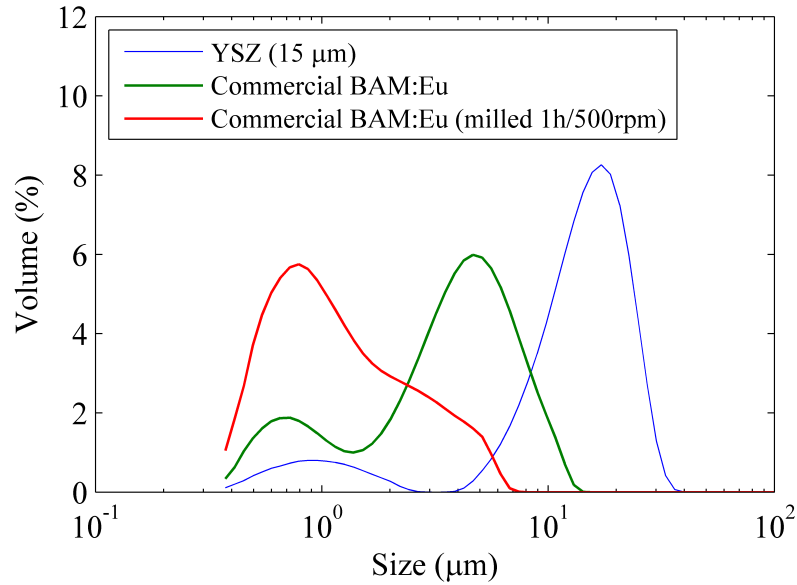
Figure 5.29. Particle size distribution (in volume) of the BAM:Eu powder before and after the ball milling process. Reference YSZ powder is also included for comparison.

A batch of commercial BAM:Eu powder was ball-milled (PM100, Retsch) at 500 rpm for 1 hour in order to reduce the particle size. The milling media used was YSZ balls of 5 mm in diameter. The particle size of the milled powder was then analysed and compared with that of the commercial BAM:Eu using a laser diffraction particle size analyser (LS230, Beckman). The particle size distributions in volume (%) were compared to a standard sample of YSZ spherical particles of 15 µm in diameter to test the accuracy and are shown in Figure 5.29.
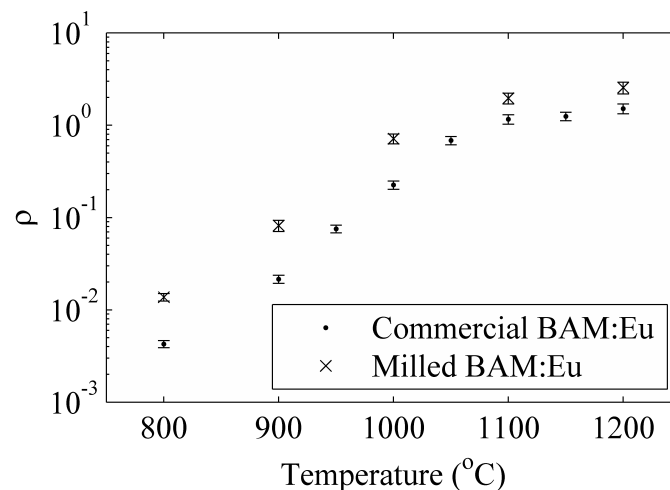
Figure 5.30. Comparison of ρ at different heat treatment temperatures for BAM:Eu powders with and without ball milling.

In Figure 5.29 a systematic error in the measurement of particle size is observed since the results of the 15 µm powder are shifted towards a slightly higher value of 17.2 µm. This

systematic error is significant and therefore quantitative evaluation of the results is not carried out. However, qualitative analysis of the results confirms a significant reduction of the particle size after ball milling (about 5 times for the median particle size). Furthermore, the particle size distribution becomes much broader, which is probably due to the different reduction achieved for different particles caused by a too short milling time.

The ball milled powder sample was then split up in several smaller samples that were heat treated in air in the temperature range from 800 °C to 1200 °C for 20 minutes. The optical properties of the samples were measured at room temperature. Figure 5.30 shows ρ calculated for these samples together with the calibration curve of the commercial powder for comparison. The intensity ratio of the ball milled powder follows the same trend as the commercial powder but the absolute value of ρ is higher. This supports the hypothesis that a smaller particle size increases ρ. In order to quantify independently the influence of the two effects mentioned earlier the samples should be milled after the heat treatment, which was not possible during the present study. The variation of ρ with the particle size has implications for the development of a sensor coating. The fact that the oxidation of the phosphor is dependent on the specific surface area available for the adsorption of oxygen implies that open porosity in a coating would play an important role in the sensing capabilities of the sensor. More importantly, because the area exposed to the gas would be small (low porosity) in a coating compared to the powder, it is likely that the coating would oxidise more slowly and thus be able to measure higher temperatures. This would however require careful control over the porosity of the coating to guarantee repeatability on the measurement.

5.2.8. Sensor reusability

The possibility to reset the sensor is a feature that arises given the nature of the physical process by which the temperature measurement is performed. The oxidation of europium ions can be reversed by means of a heat treatment in a reducing atmosphere, which is clear from the processes employed to manufacture the phosphor. These processes use as the starting materials Eu_2O_3 or $Eu(NO_3)_3$, in which europium ions are in the trivalent state of oxidation. Exposure to high temperatures in a reducing atmosphere during the synthesis of the phosphor induces the change of Eu^{3+} into Eu^{2+}. A similar heat treatment could be used to reset the sensor. However, these heat treatments involve temperatures in excess of 1400 °C, which is of little practical application if the phosphor is applied on metallic components that would melt at those temperatures.

In the following section, the resetting of the sensor after heat treatment at temperatures from 800 °C to 1100 °C was attempted by using relatively low temperatures of 800 °C, 900 °C and 1000 °C. After that, a higher resetting temperature of 1150 °C was employed to reset samples heat treated at 1100 °C and the results compared with those obtained at lower temperatures.

5.2.8.1. Low temperature resetting

In order to test the potential to reset the sensor at low temperatures four sets of 12 samples were prepared. The samples in each set were heat treated for 20 minutes in air at the temperatures of 800 °C, 900 °C, 1000 °C and 1100 °C respectively (initial heat treatment temperature). After that, each set was divided in three groups of four and all the samples within each group were heat treated for 2 hours at a selected reset temperature (800 °C, 900 °C or 1000 °C) in an atmosphere containing 5 % of H_2 and 95 % of N_2. Finally, the four samples that formed each of the referred groups were heat treated for 20 minutes in air at the temperatures of 800 °C, 900 °C, 1000 °C and 1100 °C (final heat treatment temperature). At the end, a total of 48 samples were obtained, and every sample had a different combination of initial heat treatment temperature, resetting temperature and final heat treatment temperature as indicated in Table 5.4. For the sake of clarity the top middle cell of the table will be explained. In this cell, each of the four samples was initially heat treated at 800 °C, as indicated on the left. Then, all the samples were reset at 900 °C as indicated above. Finally, each of the four samples was heat treated at a different temperature from 800 °C to 1100 °C.

Table 5.4. Combination of initial, reset and final heat treatment temperatures of the 48 samples used in the low temperature resetting study.

Final heat treatment temperature (°C)		Reset temperature (°C)					
		800		900		1000	
Initial heat treatment temperature (°C)	800	800	900	800	900	800	900
		1000	1100	1000	1100	1000	1100
	900	800	900	800	900	800	900
		1000	1100	1000	1100	1000	1100
	1000	800	900	800	900	800	900
		1000	1100	1000	1100	1000	1100
	1100	800	900	800	900	800	900
		1000	1100	1000	1100	1000	1100
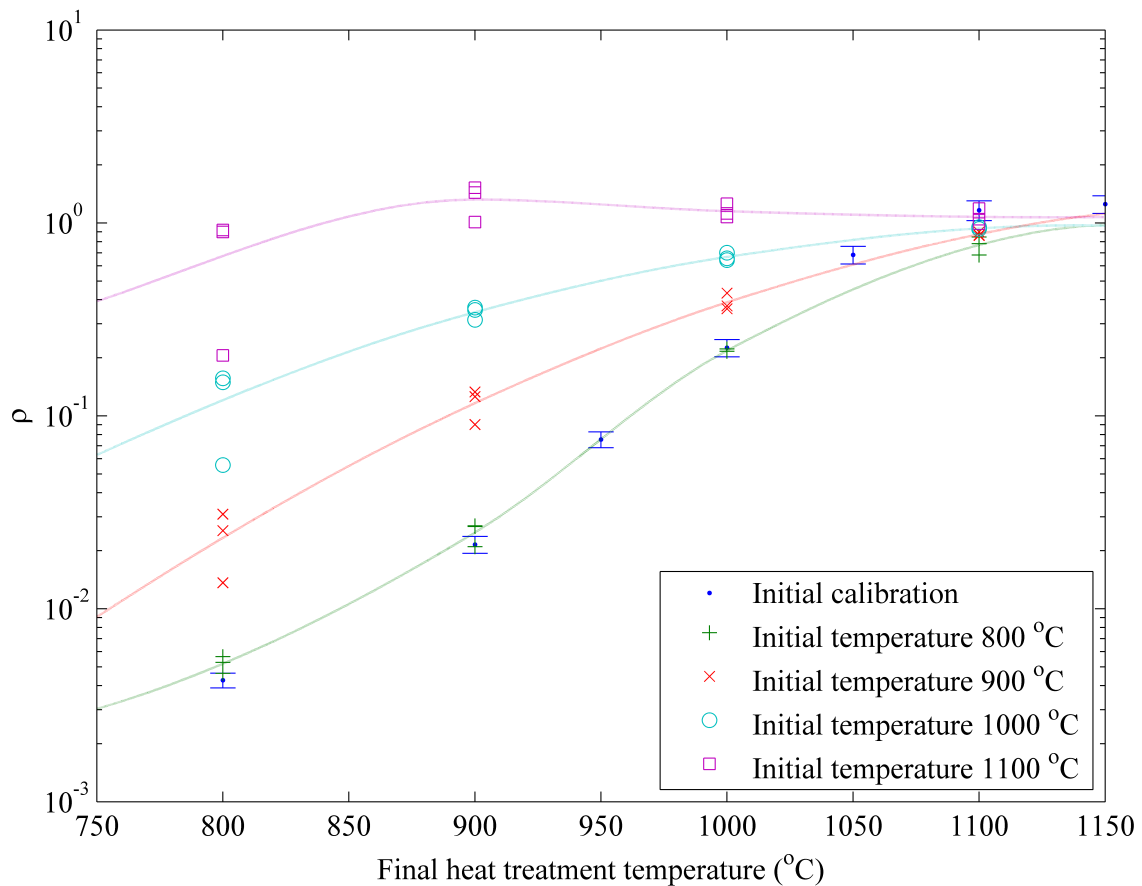
Figure 5.31. ρ of samples heat treated in the temperature range from 800 °C to 1100 °C after being reset at various temperatures. The initial temperature at which each set of samples was heat treated is indicated. The initial calibration of ρ versus temperature is also included for comparison and the dashed lines are to help the eye. See text for further discussion.

The intensity ratio of all the samples was calculated and the results plotted against the final heat treatment temperature in Figure 5.31. The intensity ratio calibration curve of the commercial powder is included for comparison. Figure 5.31 shows that samples heat treated after the resetting process provide four different calibration curves, which depend only on the initial heat treatment temperature. This suggests that the initial heat treatment temperature is the main factor that affects successive calibrations of the sensor. In general, all sets of three samples with the same initial and final heat treatment temperature provide the same value of ρ independently of the temperature at which they were reset. It is worth noting, however, that some samples reset at the highest temperature of 1000 °C, and especially those that are finally heat treated at the lowest temperature of 800 °C, present a slightly lower ρ than those samples reset at lower temperatures.
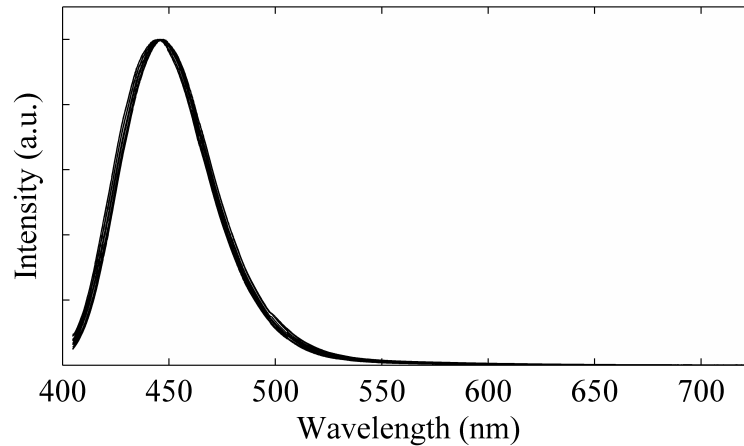
Figure 5.32. Normalised emission spectra of 12 samples after resetting at the various temperatures. What appears to be a thick line is the result of the overlapping of the 12 lines due to the shift of the curves (maximum shift of 3 nm).

The emission spectra of all reset samples in Figure 5.32 show only the emission broad band centred at 445 nm from Eu^{2+} ions, independently of the resetting temperature. Although emission from Eu^{3+} ions is not observed, complete recovery of the initial state of the phosphor is not achieved, as demonstrated by the higher ρ obtained after a second heat treatment of reset samples. An explanation for this could be related to the mobility of europium ions. According to [102], europium ions in the trivalent state occupy a new site within the lattice structure, which is also supported by the evolution of the emission spectra in Figure 5.13. It is therefore hypothesised that heating in a reducing atmosphere at low temperatures might induce the reduction of europium ions to the divalent state, but it is not sufficient for most of them to return to their original location in the lattice. This is further supported by the slightly reduced emission intensity of the samples after the heat treatment, although this reduction was not quantified. After a second heat treatment, the intensity ratio obtained is higher due to the residual effect of the previous oxidation.

Due to the incomplete resetting of the samples, the reusability of the sensor is associated to the initial heat treatment temperature. Samples heat treated initially at 1100 °C show a value of ρ after a second heat treatment which is in all cases close to the initial value of approximately 1. Therefore, these samples cannot be used for temperature measurements after resetting at low temperatures. Samples initially exposed to heat treatments at 900 °C and 1000 °C demonstrate some sensitivity to temperature after the resetting process. This sensitivity is higher for samples initially heated at the lowest temperature of 900 °C. This means that reuse of these samples is subjected to knowledge of the initial exposure

temperature. Finally, samples initially annealed at 800 °C are successfully reset at all temperatures and provide a calibration curve similar to that of commercial BAM:Eu.

In summary, complete recovery of previously heat treated samples cannot be achieved by annealing in a reducing atmosphere at temperatures equal or below 1000 °C. However, measurements can still be performed if the initial temperature of exposure is below 1100 °C and the second measurement is calibrated based on the initial heat treatment temperature.

5.2.8.2. *Medium temperature resetting*

The possibility to reset the phosphor at a higher temperature of 1150 °C is investigated in this section. According to the results in section 5.2.8.1, the temperature of the initial heat treatment is the main factor that limits the possibility to reuse the sensor. Therefore, only a sample initially heat treated at the maximum temperature of 1100 °C in air for 20 minutes was used for this study. This sample was then exposed to the resetting process which was now performed at a temperature of 1150 °C. The conditions of the resetting process are similar to those reported in section 5.2.8.1.

After the resetting process, the sample was split in two and each new sample was heat treated at temperatures of 900 °C and 1000 °C. At this point the optical properties of the samples were interrogated at room temperature and the intensity ratio calculated. Figure 5.33 shows these intensity ratios (*Reset x1*) together with the calibration curve of BAM:Eu. It must be noted that in this case results are obtained by exciting the phosphor with 355 nm light, which is qualitatively equivalent to excitation at 266 nm in terms of temperature sensing. The intensity ratio of these samples shows good agreement with the initial calibration of the phosphor, with a measurement repeatability of 2.5 % for the sample heat treated at 1000 °C. This result is clearly different to that obtained after resetting at lower temperatures and almost complete recovery of the phosphor is likely obtained after heat treatment at 1150 °C.
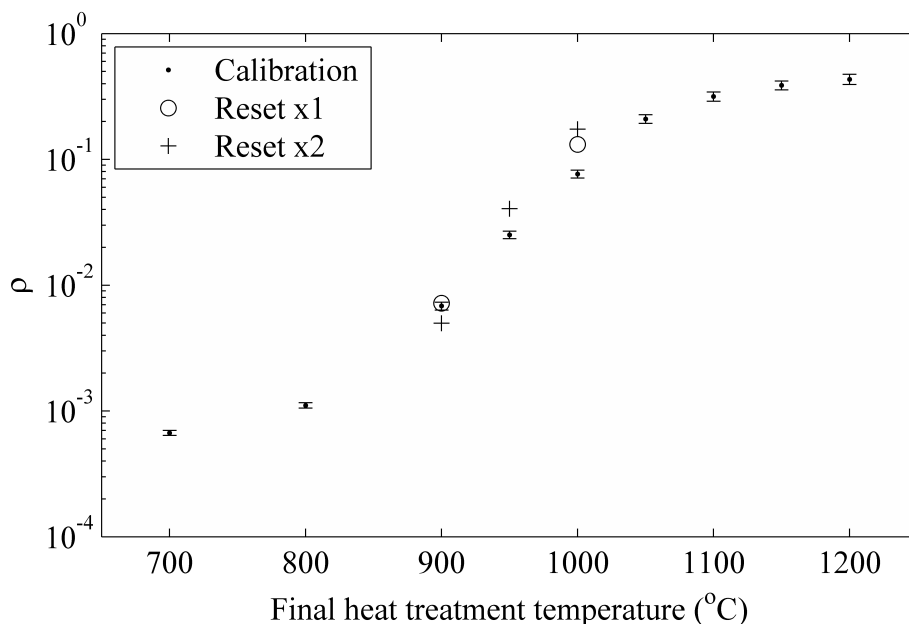
Figure 5.33. ρ of samples after two successive resetting processes at 1150 °C. The excitation wavelength used in this test is 355 nm.

The process was then repeated to confirm the results and the two samples were reset under the same conditions at 1150 °C. At that point the sample previously heated at 1000 °C was split up in two and the three remaining samples were heat treated at 900 °C, 950 °C and 1000 °C. The intensity ratio of the three samples was then calculated and is plotted in Figure 5.33 and labelled "*Reset x2*". The intensity ratio of these doubly-reset samples shows similar sensitivity to temperature compared to commercial powder. The sample heat treated at 1000 °C, however, overestimates the temperature by approximately 4 %.

5.3. Conclusions

The oxidation of commercial BAM:Eu in air has been investigated in detail and the combination of results obtained in the present study and from the literature have provided insight in the nature and mechanisms of the process. Thermal analysis showed that the main structure of the phosphor remains constant upon heating up to 1600 °C. DTA analysis and emission spectra of samples heat treated up to 1200 °C revealed that oxidation of Eu^{2+} occurs in air and Eu^{3+} is formed as a result of this oxidation. Emission spectra showed that the environment of the Eu^{2+} ions remained nearly constant independently of the temperature, except possibly a small expansion of the host lattice. The environment around Eu^{3+} ions was observed to change up to 900 °C, which was related to the movement of the oxidised ions to a

new location in the lattice structure [102]. Above 900 °C no further changes in the emission spectra of Eu^{3+} ions were detected apart from an increase of the absolute intensity.

The oxidation of the phosphor is, according to experimental observations, a continuous process dependent on the temperature and time of exposure, which can be explained by a three-step oxidation mechanism proposed by Bizarri and Moine [114]. The first step is the adsorption of oxygen on the phosphor surface. This was investigated and the experimental results agreed with a simple Langmuir isotherm model, which pointed out to a saturation of the adsorption at oxygen partial pressures below 0.1 bar. The second step, which consists of the diffusion of europium ions through the BAM conduction layer, was measured by Lacanilao et al. [100] and was used in this study to explain the existence of a maximum level of oxidation achievable by the phosphor. This maximum level of oxidation limits the maximum temperatures measurable by the phosphor. The third step is the oxidation of Eu^{2+} when these ions are in close proximity with oxygen atoms. This is evidenced by the change of the emission spectra of heat treated samples.

The change of the optical properties after oxidation of BAM:Eu was reliably used as an indication of the past temperature. The intensity ratio between the emission lines of Eu^{2+} and Eu^{3+} and the lifetime decay measured at 611 nm were used as measurands of the temperature. The intensity ratio showed great sensitivity to temperature in the range from 700 °C to 1200 °C, while lifetime decay only up to 1100 °C. A precision typically better than 1 % can be achieved with the intensity ratio and the lifetime decay methods. A negligible influence of the excitation fluence was observed on the intensity ratio method. However, the excitation fluence had a noticeable effect on the lifetime decay method, which is considered the main limitation to the use of this measurand. The effect of the duration of the exposure was investigated by means of the KJMA theory in order to decouple it from the effect of temperature. Experimental data agrees well with this theory at temperatures above 900 °C, and thus the theory can be used for calibration purposes. Below this temperature, a different mechanism is likely to occur and additional calibration data is necessary to account for the effect of time exposure, possibly in the form of look-up tables.

The effect of a slow cooling down time was also investigated and resulted in a small overestimation of the temperatures which can be accounted for by calibration. The use of the sensor in variable gas atmospheres was investigated related to the role of oxygen in the oxidation mechanism of the phosphor. A minimum threshold for the oxygen partial pressure

of 0.1 bar was found above which no influence on the measurement was observed. This behaviour reveals especially relevant to gas turbine applications where the oxygen partial pressure is well above that threshold, and therefore the measurement would be unaffected by local variations on the gas composition. Increase of the dopant concentration proved effective to raise the range of temperatures that can be sensed by the phosphor due to a higher resistance to oxidation. The oxidation of the phosphor also showed dependence on the particle size, which has implications for the application of the sensor as a coating where porosity would be an important factor.

The possibility to reuse the sensor by heat treatment under a reducing atmosphere was investigated. Limited reusability after heat treatment at temperatures below 1000 °C was achieved. At these temperatures, the sensitivity of the sensor after the resetting heat treatment was dependent on the initial sensed temperature. At higher temperatures of 1150 °C the sensor showed similar sensitivity to the temperature even after multiple resetting heat treatments.

6. COATING DEVELOPMENT

This chapter covers the aspects related to the development of a thermal history sensor coating and in particular the application of BAM:Eu on the surface of metallic components. As reviewed in section 3.5, the deposition of this phosphor on a metallic substrate has not been addressed before and only a limited number of studies investigated the deposition of this phosphor as a thin film on ceramic substrates. The complex stoichiometry, high sintering temperature and the oxidation of the phosphor during deposition in air are the main issues that make its deposition a challenging process.

In the first section of this chapter two methods to deposit BAM:Eu on a metallic alloy are investigated for the first time. Firstly, an air sprayed paint made of a mixture of the phosphor and an aqueous binder is deposited and the structure examined after heat treatment in air. Secondly, screen printed coatings are tested after heat treatment in air and their thermal history capabilities studied. The feasibility of using BAM:Eu as a sensor coating is demonstrated in these tests, and potential issues that can affect accuracy during the measurement identified and solutions provided.

The second section describes the investigation of the effect of thermal gradients on the measurement accuracy of phosphorescent coatings. The theoretical model previously described in section 2.2.2 is validated by experiments developed on a thermal gradient test rig owned by Sensor Coating Systems Ltd. (SCS). Based on the experimental results, the on-line lifetime decay model is adapted so that systematic errors in the off-line intensity ratio method with BAM:Eu can be estimated.

6.1. BAM:Eu sensor coatings

6.1.1. Paints

Embedding the phosphor powder in a binder and spraying it onto the surface of the substrate is a simple method of preparation of a sensor coating. Based on previous results the possibility of using a paint made with BAM:Eu depends mainly on two factors: the permeability to oxygen of the binder and the chemical reactions that may occur between the binder and the phosphor. Some paints such as those of Zyp Coatings Inc. are known to have an open porosity of 40 – 60 % [169] and therefore should permit oxidation of the phosphor. In

this section the sensing capabilities of a BAM:Eu paint coated by SCS was investigated at high temperatures.

6.1.1.1. Coating production

The painted samples were made available by SCS. The powder and the binder (IP66, Indestructible Paint Ltd.) were combined with the right proportion of water and then thoroughly mixed. The suspension was then sprayed by using a gravity-fed air spray gun onto the surface of Inconel 625 10x10x1 mm tiles to obtain a thickness of approximately 35 μm. The samples were then cured in a furnace at temperatures of about 200 °C. At that point the samples were examined by SEM and the image of the surface is shown in Figure 6.1. In the image, the particles of BAM:Eu are clearly seen embedded by the binder which also has small cracks due to the evaporation of water during the curing process.
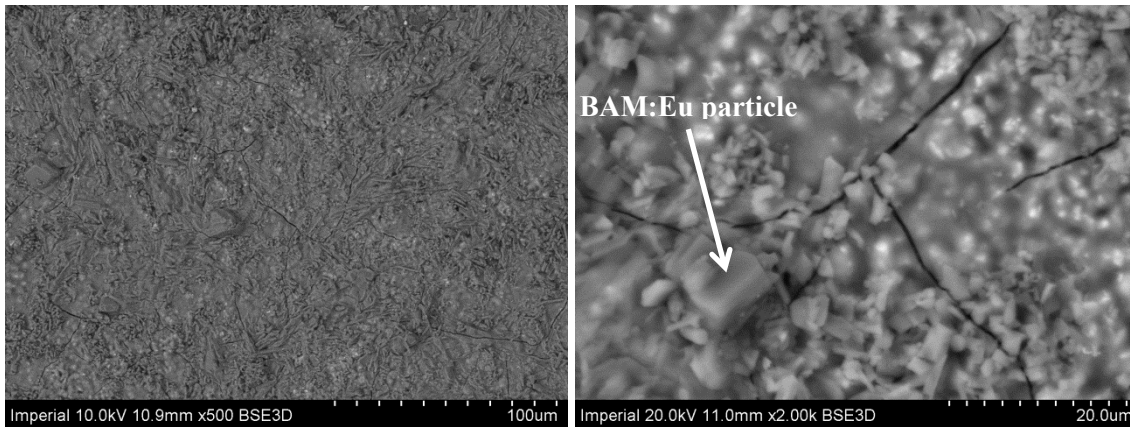
Figure 6.1. SEM images of the surface of the BAM:Eu painted samples.
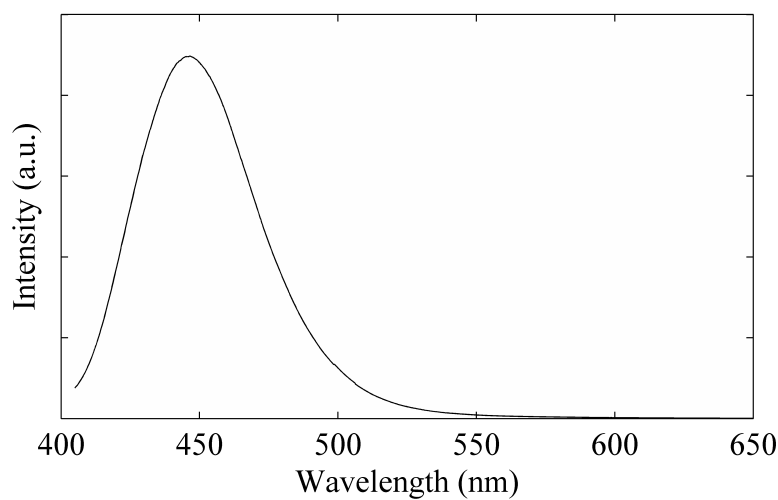
Figure 6.2. Normalised emission spectrum of an as-deposited painted sample of BAM:Eu.

The phosphorescent emission from BAM:Eu^{2+} was confirmed by spectroscopy as depicted in Figure 6.2. No other emission apart from that of BAM:Eu^{2+} is observed in these samples. In Figure 6.3 the diffraction patterns of a painted sample indicate the presence of a crystalline material after deposition. BAM:Eu is identified by using International Centre for Diffraction Data (ICDD) reference patterns as the main phase. However, several additional peaks are present that cannot be identified to any reference material and are ascribed to the binder. XRD peaks from the metallic substrate are not observed in these samples.

SEM, XRD and spectroscopy analysis therefore confirm the successful manufacture of the painted samples and the possibility to obtain sufficient luminescent signal from the as-deposited phosphor.
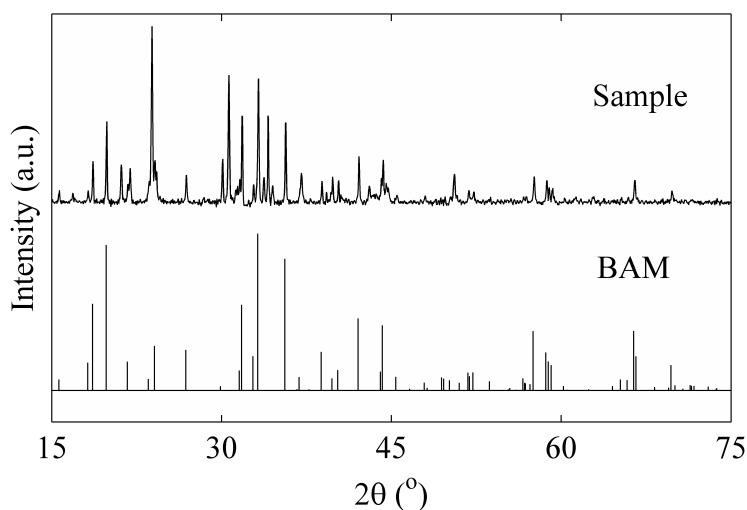
Figure 6.3. Diffraction patterns of the BAM:Eu paint sample and the ICDD reference pattern of the BAM phase.

6.1.1.2. Results

A painted sample was heat treated in air for 20 minutes at 1000 °C and its optical properties interrogated at room temperature afterwards. The phosphorescent emission from BAM:Eu was difficult to detect after the heat treatment and the only emission observed was from the 445 nm peak when a high excitation fluence was used. The SEM image of the surface of the paint, in Figure 6.4, indicates that multiple structural changes occurred due to the heat treatment. First of all the binder becomes glassy and large craters of about 0.3 mm in diameter are visible on the surface. The edge of one of these craters is visible on the bottom-right corner of Figure 6.4 left. Most of the BAM:Eu particles are no longer observed and instead flat clusters appear on the surface, some of which seem to have actually separated from the surface leaving cavities (see Figure 6.4 right).
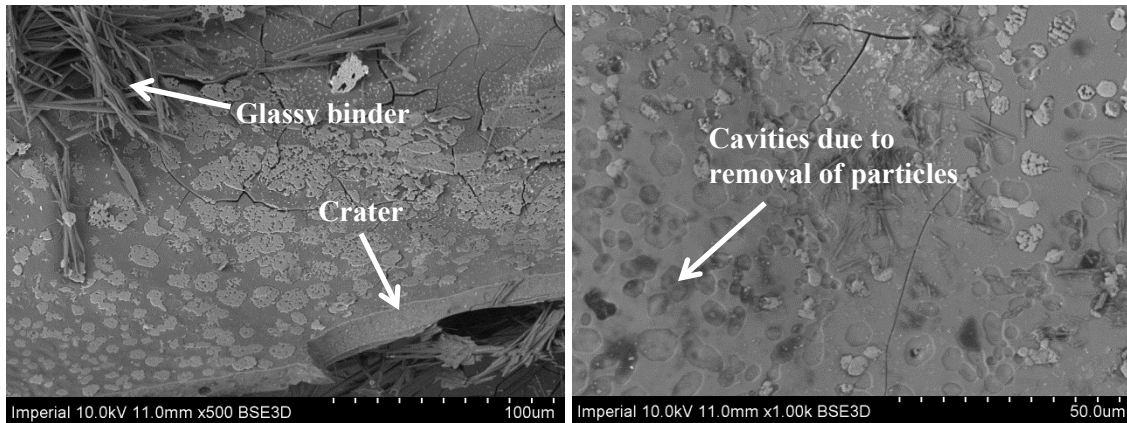
Figure 6.4. SEM images of a painted sample after heat treatment in air at 1000 °C for 20 minutes.

X-ray diffraction patterns shown in Figure 6.5 confirm the appearance of an amorphous phase, which is thought to be due to the transformation of the binder. This is supported by the disappearance of the peaks present in the untreated sample that were ascribed to the binder. The diffraction peaks of BAM:Eu are still present but their intensity is very low compared to that of the untreated sample, which indicates that the phosphor has undergone some reaction. This is consistent with the low phosphorescent emission observed from the heat treated sample and the SEM images. Finally, the peaks from the metallic substrate are clearly observed in the heat treated sample, and their intensity is higher than those of the peaks of BAM:Eu.
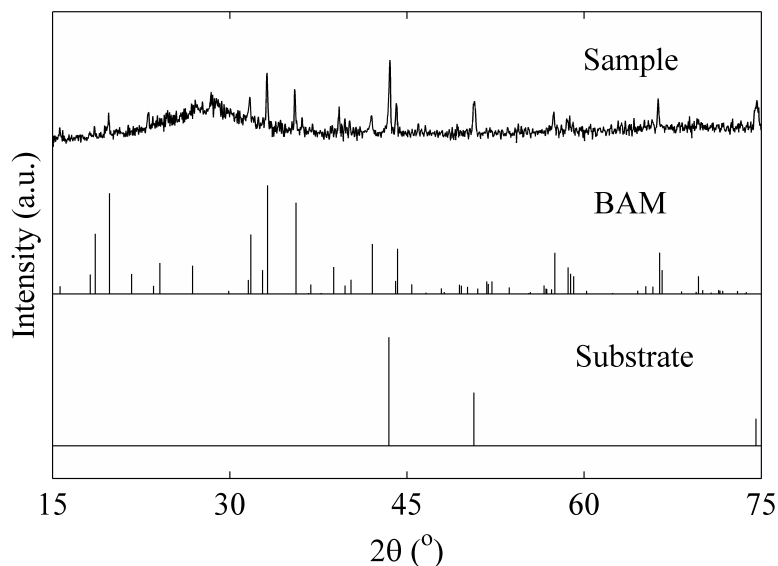
Figure 6.5. Diffraction patterns recorded for a paint sample heat treated in air at 1000 °C for 20 minutes. The ICDD reference patterns of the BAM phase and the substrate are also shown.

From the previous results, it can be deduced that the use of a binder is problematic due to chemical reaction between the binder and the phosphor, which annihilates the phosphorescent emission. The exact composition of the binder is not known from the manufacturer, but it is based on a potassium silicate compound. The use of an aluminium oxide-based binder, such as LRC from Zyp Coatings Inc., might be a suitable alternative. This type of binder was however not available during this work and could not be tested.

6.1.2. Screen printed coatings

The screen printing method was another deposition technique employed to manufacture some of the coatings in this work chosen due to its low cost and simplicity compared to other deposition methods. The screen printing method permits the coating of multiple substrates in a relatively short time with great flexibility in the composition, structure and thickness. These coatings were used to validate the application of the phosphor as a sensor coating and identify the potential problems derived from the heat treatment of the phosphor in the form of a coating on a metallic substrate.

6.1.2.1. Coating production

The first step of the screen printing method is the preparation of the ink which will then be printed onto the substrate. In this work, general guidelines were followed, which were generously provided by Enrique Ruiz-Trejo, an expert on advanced ceramics for electrochemical devices from the Department of Earth Science & Engineering, based on his experience in the manufacture of inks of similar ceramic materials.

The BAM:Eu ink was prepared by following the process described in Figure 6.6. The powder (referred to as solid) was first ball milled in a planetary ball mill (Retsch PM100) at 500 rpm for 1 hour using YSZ balls (5 mm in diameter) as the milling media. The dispersant (Hypermer KD15) was then added to the powder with ethanol in a quantity of 2.5 mg/m^2 of solid. At that point the mixture was left to dry and then ground. The solvent (Terpineol) was measured separately and placed in the final ink container. The amount of solvent needed is that which makes the ink to be composed of 75 wt % of solid. More solvent could be added later as required to give to the ink an adequate viscosity for printing. In the manufacture of BAM:Eu ink in this work addition of up to 1 ml was normally necessary. The amount of binder (ECN7, Hercules) was measured to be 2 wt % of solid and it was then added to the solvent while stirring. The solid and the dispersant, which were mixed and ground, were then

slowly added to the container with the solvent and the binder while continuously stirring. It is at this point, if the mixture becomes too thick, when additional solvent could be added.

After all the components were completely mixed, the ink was placed in an ultrasonic bath for 20 minutes to break down agglomerates. If lumps were still present, which was generally the case during this work, the ink was then passed through a triple roll mill for 20 minutes to homogenise it.

Once the ink was prepared, it was stored under refrigeration to avoid evaporation of the solvent. The other ink used during the present work, that of SSZ, was already prepared following the same procedure and optimised for deposition by screen printing. The relative composition of solid, solvent, dispersant and binder are unknown to the author.
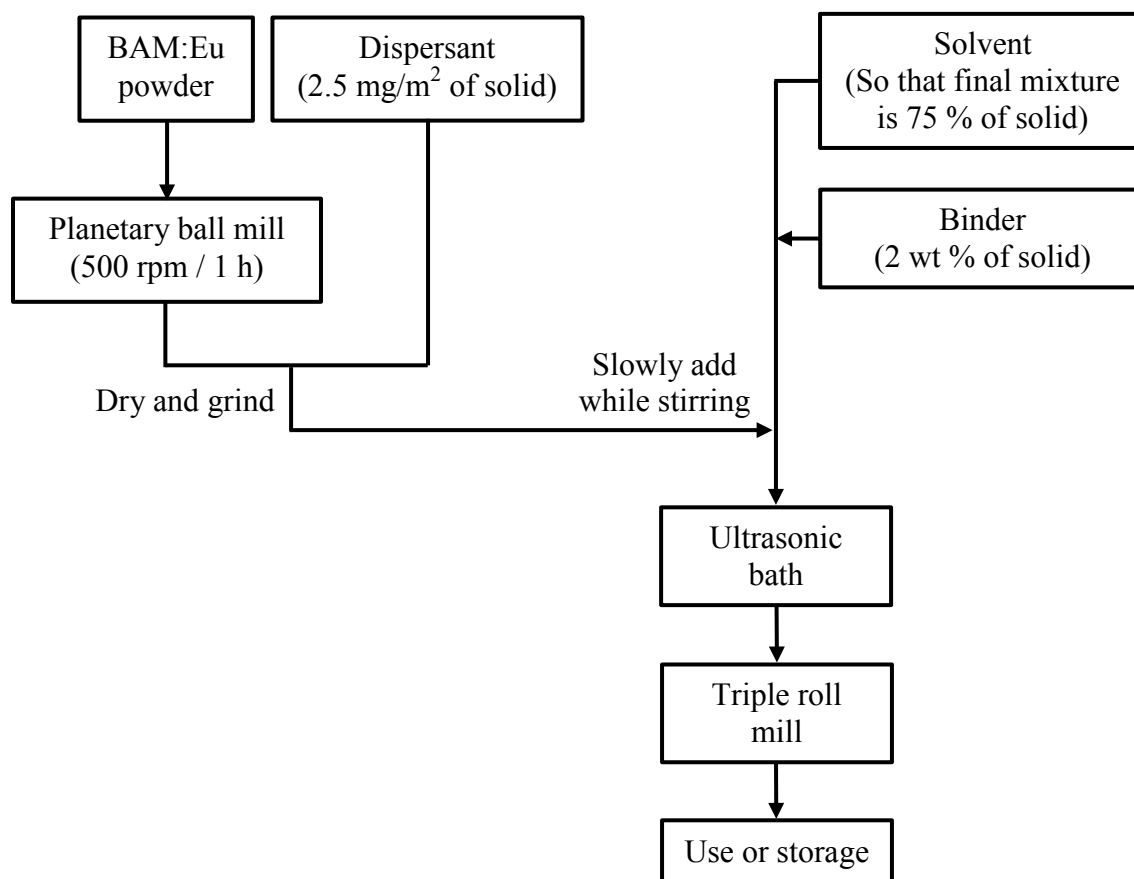
Figure 6.6. Description of the process followed to prepare the BAM:Eu ink used in the screen printing.

The printing was performed in a bench top printer (Benchmark, SigmaPrint). The screen used (8 x 10 325 45° 5m E04 EXP, MCI Precision) had an open squared area of 20 x 20 mm. The ink, which was at room temperature before printing, was deposited at the edge of the square

and then the squeegee performed the operation of printing. The substrate samples were Inconel 625 10x10x1 mm tiles. After the printing was done, the coated sample was placed in an air furnace at 100 °C for several hours until the ink was dried. At this point a new layer of ink could be deposited to obtain a thicker coating of the same or a different material. The sample was always dried in the air furnace immediately after a new layer was deposited.

After the samples were completely dried, a sintering process at high temperature (1150 °C) was performed to eliminate the organic compounds and improve the adhesion of the ceramic particles. In order to avoid thermal damage in the BAM:Eu particles, this heat treatment was performed in a reducing atmosphere which consisted of 10 % of H_2 and 90 % of N_2. The heating up and cooling down rates were always kept at 3 °C/min to avoid cracks and delamination, and the dwell time was set to 2 hours.

The surface of the coatings was observed by SEM after the heat treatment as shown in Figure 6.7. The BAM:Eu particles appeared as a stack of powder and did not present any sign of sintering. This is due to the relatively low temperatures of the heat treatment compared to the sintering temperature of the material as determined in the dilatometry tests in section 5.1.2.1. In order to reduce the sintering temperature of BAM:Eu and improve the adhesion of the particles three potential sintering aids were tested. Three compounds which are normally used as sintering aids, ZnO, NiO and Co_3O_4, were thoroughly mixed with the BAM:Eu powder in a proportion of 1 wt %. The mixture was pressed to form a pellet of 5 mm in diameter which was then heated at 1150 °C. However, no significant improvement in the sintering of the powder was observed with any of the mixtures due to the too low temperature used in the heat treatment, and the use of sintering aids was not further implemented in the manufacture of the coatings.
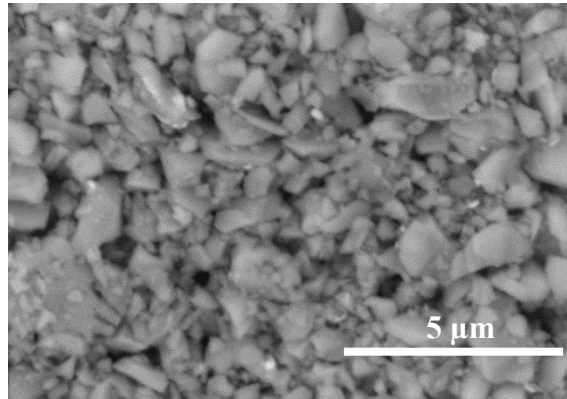
Figure 6.7. Surface image of a BAM:Eu screen printed single layer coating after heat treatment at 1150 °C for 2 hours in a reducing atmosphere. The particles do not show any signs of sintering.

The most simple coating manufactured consisted of a single layer of BAM:Eu deposited by a single pass of the squeegee. The cross section of this coating after the sintering process is shown in Figure 6.8, which indicates that the thickness achieved by a single pass is in the order of 15 to 20 µm. A darker area between the BAM:Eu particles and the substrate is visible in the image and it is speculated that it is caused by chemical reaction between the material of the substrate and the BAM:Eu at the interface or diffusion of elements.
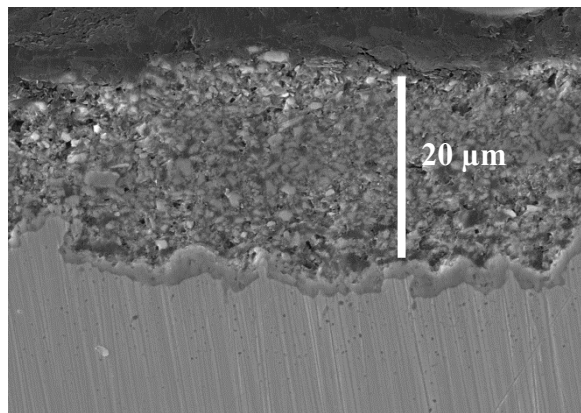
Figure 6.8. SEM cross-section of a single layer BAM:Eu screen printed coating.

The diffraction patterns of a single-layer sample prepared by this method are shown in Figure 6.9. The patterns are mainly identified with the BAM phase, which confirms that the phosphor did not react with the substrate. Low intensity peaks that are related to the cubic phase of the Inconel substrate are also identified with peaks at 43.6 °, 50.8 ° and 74.6 °.
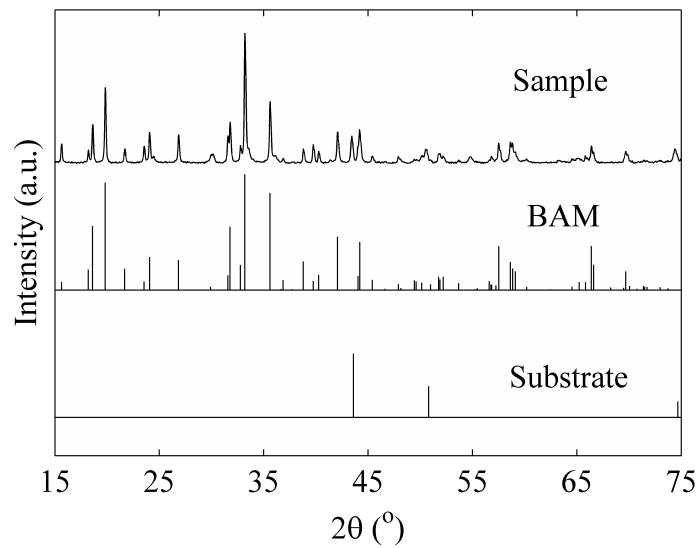
Figure 6.9. Diffraction patterns of a single-layer screen printed samples and ICDD reference patterns of the BAM phase and the substrate alloy.

A dual layer coating was envisaged which consisted of a first layer (interlayer) of SSZ and a top layer of BAM:Eu. The purpose of this coating was to avoid diffusion of elements from the metallic substrate into the phosphor layer, and the use of SSZ was justified by the availability of a suitable ink and the similarity of this material with the TBC standard YSZ. The potential use of SSZ replacing YSZ in standard TBCs has actually been studied due to its higher resistance to vanadate-sulphate corrosion [170]. A detailed discussion on the diffusion of elements from the substrate will be presented in section 6.1.2.2. The cross section of this dual-layer coating after the sintering process is shown in Figure 6.10 (left). The layer of BAM:Eu has a thickness of about 12 μm, while the interlayer of SSZ is of only 2 μm. The smaller thickness of this BAM:Eu layer with respect to the single layer coating can be explained by differences in the content of solvent of the ink, which was prepared in a different batch. On the other hand, the thickness of only 2 μm of the SSZ layer was expected for the ink used, as was observed for other samples prepared with that ink [171]. The thin interlayer of SSZ should not be confused with the interface present in the single layer coating as confirmed by the more detailed image in Figure 6.10 (right). In this image the particles of SSZ are clearly seen between the BAM:Eu and the substrate. These particles are likely to have undergone some sintering during the manufacture of the coating as the temperature at which the maximum sintering rate is reported for SSZ particles is of approximately 1190 °C [172].
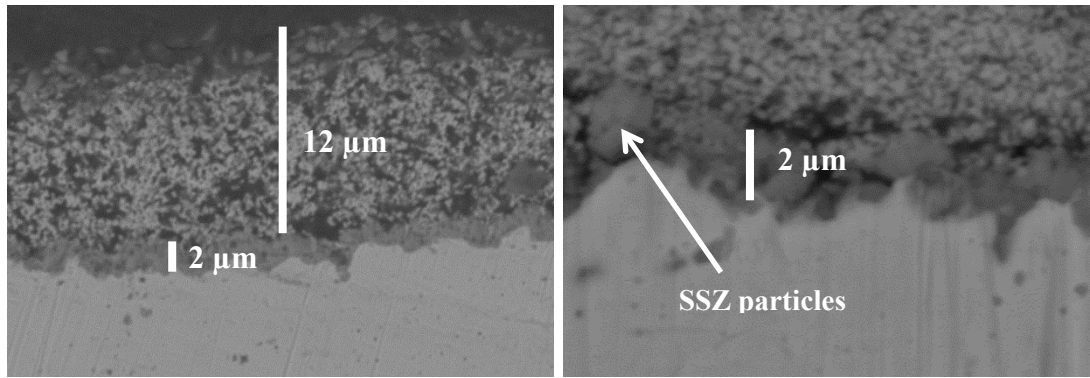
Figure 6.10. SEM cross-section of a dual layer (SSZ + BAM:Eu) screen printed coating (left) and a closer view of the SSZ interlayer (right).

The diffraction patterns of the dual-layer sample are shown in Figure 6.11. The presence of BAM:Eu as the main phase is confirmed while small peaks that belong to the interlayer (SSZ) and the substrate are also identified. From the XRD results, no reaction between SSZ and BAM:Eu can be detected and the composition of the phosphor layer remains unaffected by the interlayer.
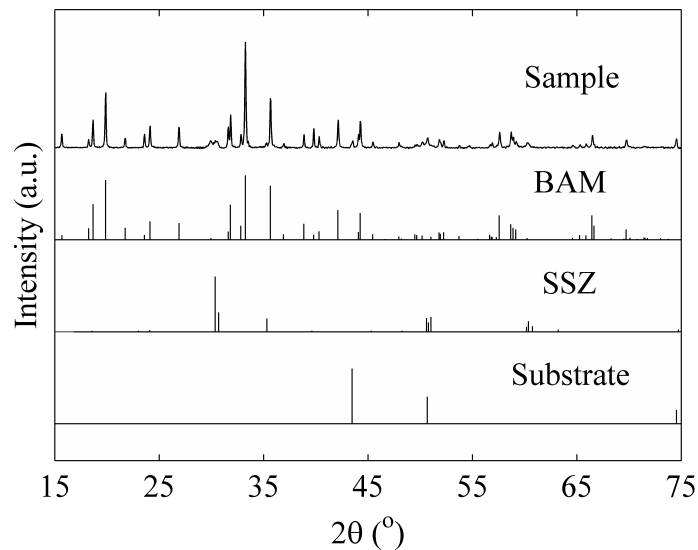
Figure 6.11. Diffraction patterns of a dual-layer screen printed sample and ICDD reference peaks of BAM, SSZ and the substrate alloy.

The normalised emission spectra of both single and dual-layer coatings recorded after the sintering process are shown in Figure 6.12. The main emission broad band centred at 445 nm, which corresponds to BAM:Eu^{2+}, is observed in the two samples and they both have identical width, which indicates that no other phase that affects the luminescence is present in the material. In the single-layer coated sample an additional emission peak arises at 513 nm which is not present in the dual-layer sample. It is hypothesized that this peak is due to the

presence of manganese that has diffused from the substrate, as this emission spectrum is similar to that of BAM:Eu,Mn [101, 173]. This will be further discussed in section 6.1.2.2.
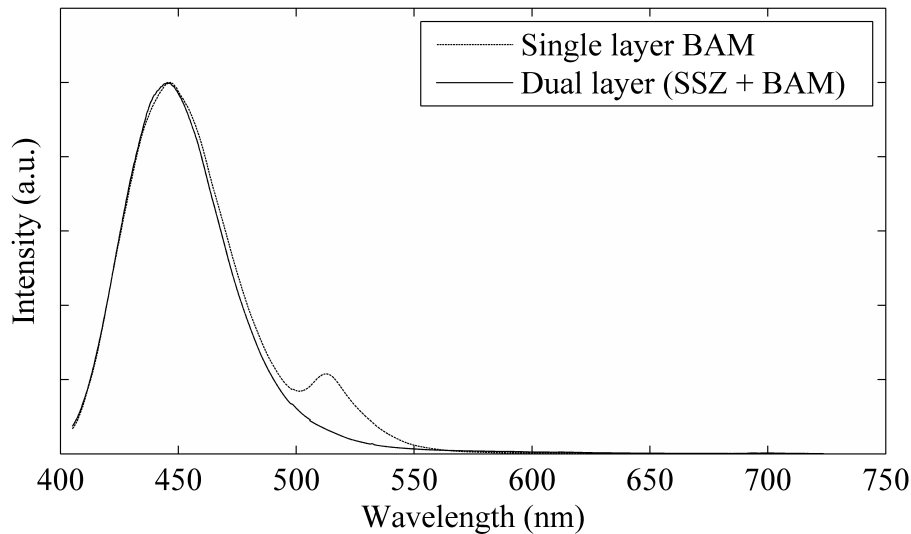
Figure 6.12 Normalised emission spectra of the single and dual-layer screen printed coatings.

6.1.2.2. Results

A set of single-layer samples were heat treated in air for 20 minutes at temperatures of 800 °C, 900 °C, 1000 °C and 1100 °C. The optical properties of these samples were investigated after the heat treatment and the recorded emission spectra are shown in Figure 6.13. The characteristic emission from BAM:Eu after heat treatment is present in these spectra, with the broad band centred at 445 nm and the multiple emission peaks above 570 nm. The peak at 513 nm, which was first remarked in Figure 6.12, can also be observed in these samples after heat treatment in air and the intensity of this peak increases with temperature relative to the broad band emission. An additional broad band is visible which extends from about 640 nm to at least 720 nm. This broad band exhibits a large intensity compared to the Eu^{3+} emission and its origin is believed to be related to the oxidation of manganese from Mn^{2+} to Mn^{4+}. According to [92] the luminescence from Mn^{4+} extends from 620 nm to 700 nm in various host materials and consists of several broad lines that originate from electronic transitions aided by lattice vibration. However, other transition metals present in the substrate can contribute to this broad band emission. For example Cr^{3+} emits in several host materials in the region between 680 nm and 720 nm [86, 92, 174, 175] and Fe^{3+} at wavelengths longer than 680 nm [92, 176].
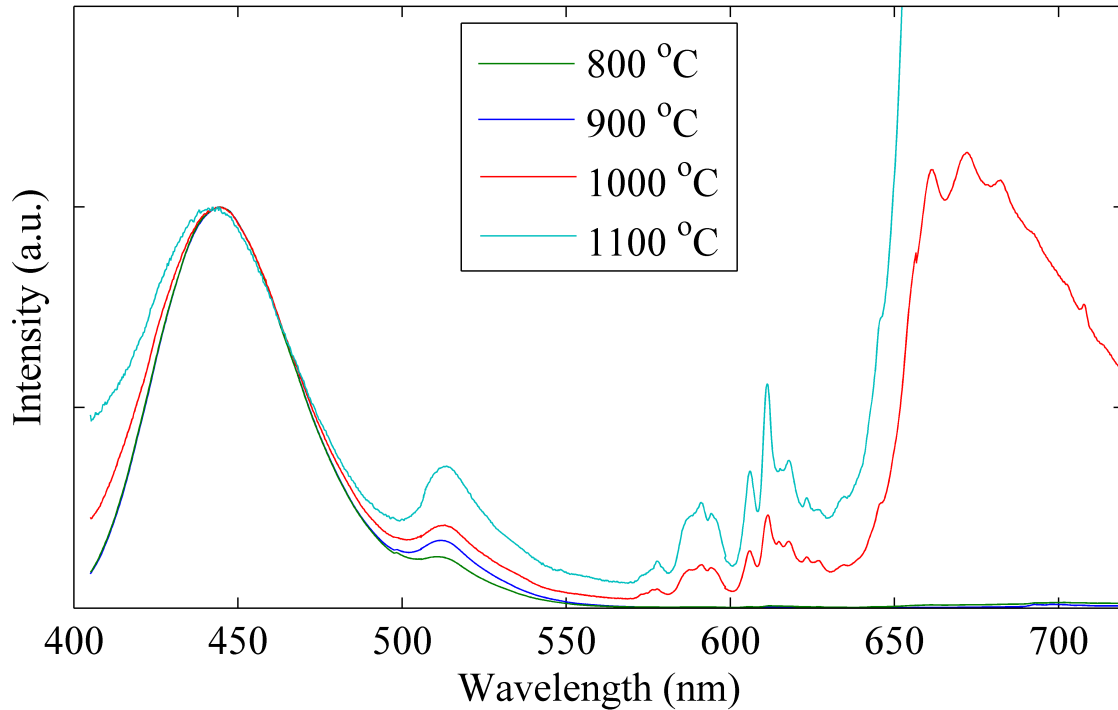
Figure 6.13. Normalised emission spectra of single-layer coatings after heat treatment in air for 20 minutes at the indicated temperatures.

The elemental composition of the coating layer was investigated by SEM EDS on a cross section of a single-layer coating sample heat treated in air at 1100 °C for 20 minutes. The EDS spectrum was recorded at 13 different locations across the coating as indicated by the black dots in Figure 6.14 (left). The results from the measurement were normalised to the content of aluminium which is considered to remain constant in the BAM:Eu spinel block (Mn is known to substitute for Mg [173]) and are shown in the graph in Figure 6.14 (right). The amount of Ba oscillates around 1 mol across the coating and it is only slightly higher in the proximity of the substrate. The amount of Mg is lower than expected for BAM:Eu, and it remains relatively constant throughout the thickness of the coating at 0.8 mol. This could be explained by the substitution of Mg ions in the spinel block by transition metal ions such as Mn, as reported in [173], Cr^{3+} or Fe^{3+}, all of which have similar ionic radii [177]. The presence of these transition metal ions is confirmed by the EDS analysis. The Cr ion is detected at all locations across the coating layer with a content of approximately 0.13 mol. This concentration shows a steep gradient near the substrate where it increases to almost 0.7 mol, which is indicative of the presence of diffusion of this element from the substrate. Mn and Fe are only detected close to the substrate where the concentration is approximately 0.15 mol. Far from the substrate these two elements are not detected possibly due to a smaller

diffusion speed. The Eu content is constant across the whole thickness of the coating at approximately 0.13 mol. It is only near the substrate that Eu is not detected which is consistent with the increase in Ba content and indicates a possible depletion zone of the dopant in favour of Ba.
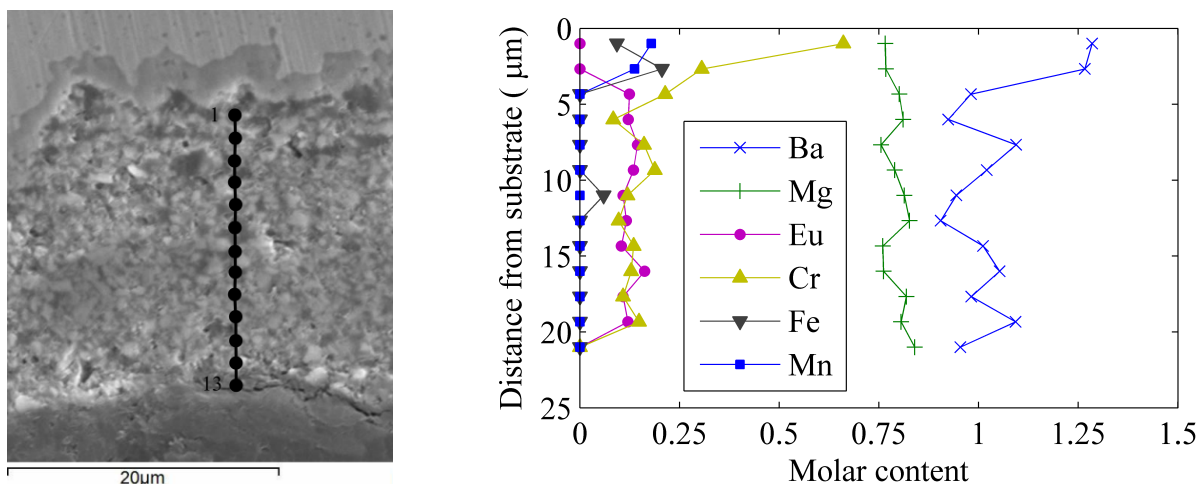
Figure 6.14. Molar content of elements across the thickness of a single-layer coating after heat treatment at 1100 °C for 20 minutes as detected by SEM EDS. The molar content of aluminium in BAM:Eu (10) is considered as a reference.

The peak at 513 nm can therefore be ascribed to emission of Mn^{2+} as this ion is present in the coating and it is well-known to have an emission peak at that wavelength in the BAM host [173]. The broad band that appears above 640 nm can be caused by emission of Mn^{4+} but additional contributions from Cr^{3+} and Fe^{3+} are possible as these two ions are also present in the BAM layer. This is especially the case of Cr^{3+} which is present across the whole thickness in a concentration comparable to that of the Eu dopant.

In order to identify the ion or ions responsible for this broad band emission, samples were prepared that contained 1 mg of BAM:Eu powder and 0.02 mg of one of the powder metal precursor (Cr, Fe or Mn). The powder mixture was thoroughly ground and then heat treated at 1000 °C for 20 minutes. The emission spectra of these samples were then measured at room temperature and are shown in Figure 6.15. Potential reaction between the material used for the interlayer (SSZ) and BAM were investigated by analysing the emission spectrum of a mixture of BAM:Eu powder with 2 wt % of SSZ ink after heat treatment in air at 1000 °C for 20 minutes, which is also shown in Figure 6.15. Finally, a powder sample was heat treated under the same temperature and time conditions in close proximity to an Inconel 625 substrate tile. This was done to account for possible gaseous diffusion of elements from the substrate, and the emission spectrum of this sample is thus labelled as "substrate".
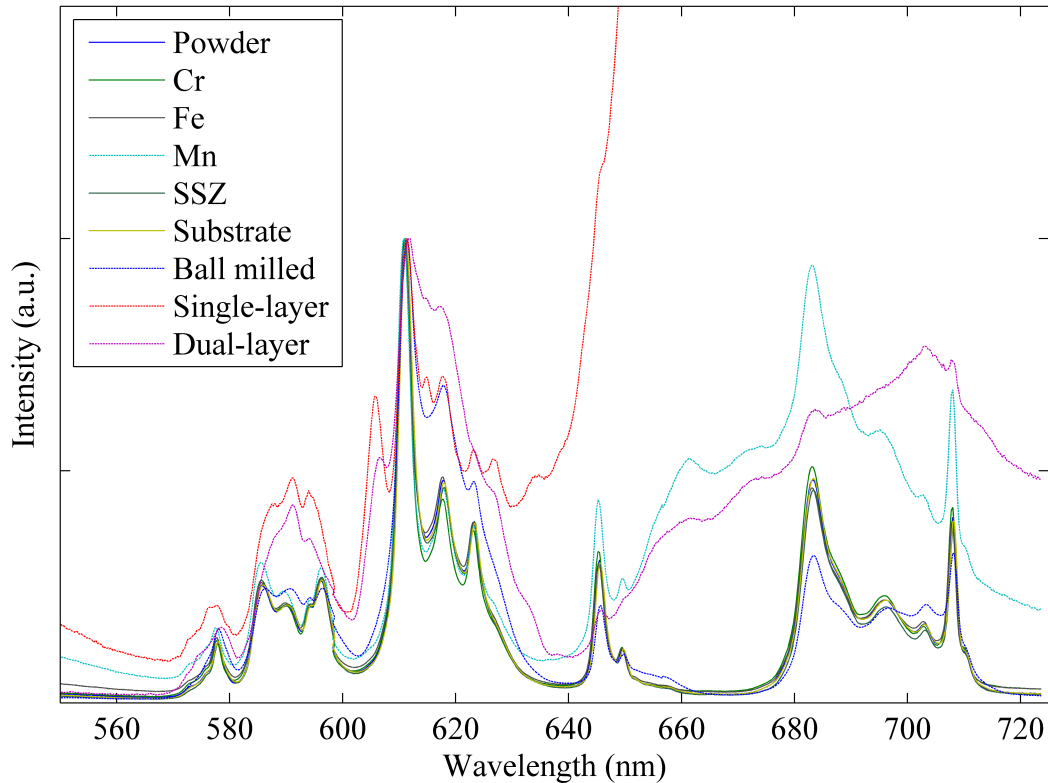
Figure 6.15. Emission spectra of various BAM:Eu samples normalised to the 611 nm peak. The samples include commercial powder, mixture of commercial powder with a transition metal ion (Cr, Fe, Mn), and with SSZ, commercial powder located near an Inconel 625 substrate, ball milled commercial powder, and single and dual-layer coatings.

Figure 6.15 includes for comparison the emission spectra of the commercial powder, the ball milled powder used in the manufacture of the coatings, and the single and dual-layer coatings; all of which were heat treated at 1000 °C for 20 minutes.

Analysis of the emission spectra of all samples indicates that the presence of Cr, Fe, SSZ, and the nearby substrate does not affect the shape of the emission spectrum of Eu^{3+} ions. All these samples show the same emission peaks and the same relative intensity of these peaks compared to the commercial powder. When the powder is ball milled, all the emission peaks of Eu^{3+} are still present but the relative intensities slightly change. In particular, the emission intensity between 605 nm and 635 nm, due to the $^5D_0 \rightarrow ^7F_2$ transition, increases relative to the insensitive emission between 585 nm and 600 nm due to the $^5D_0 \rightarrow ^7F_1$ transition. This indicates a reduction of the symmetry of the sites occupied by Eu^{3+} ions caused by the ball milling of the powder. This effect due to the ball milling of the powder can be also observed in the coated samples, in which the powder is ball milled during the manufacture process.

The sample mixed with Mn shows all the Eu^{3+} emission peaks accompanied by a broad band emission that extends from approximately 640 nm up to 725 nm. On top of this broadband the peaks of Eu^{3+} transitions are still distinct and two additional peaks arise at 661.5 nm and 672 nm. This broadband and the two peaks are also observed in the single and dual-layer coating samples. However, in these samples the peaks from Eu^{3+} possess a much lower intensity compared to the broad band. The broad band is especially intense in the single layer coating, in which the integrated intensity in the range 640 – 720 nm is nearly 10 times higher than the integrated intensity in the range 580 – 640 nm. In the dual-layer coating this ratio is only 1.6. Furthermore, additional peaks are visible in the range 605 – 635 nm: at 606 nm, 615 nm and 627 nm. This is likely to occur due to the different environments created around the Eu^{3+} as a result of the substitution of Mg ions in the spinel block by transition metal ions. The intensity of these peaks is significantly lower in the dual-layer coating since the diffusion of manganese is prevented.

It can be concluded from the analysis of this figure that the diffusion of Mn in the BAM:Eu lattice is the main cause of changes in the emission spectrum of BAM:Eu. Other transition metal ions and components have a negligible effect in the shape of the emission spectra of the BAM:Eu samples. However, the presence of these ions within the BAM:Eu layer has been confirmed by EDS and they may act as luminescence quenchers even though they do not emit light. As a consequence, the emission intensity of BAM:Eu might be affected and therefore ρ measured after heat treatment differ from that of the calibration with the powder material. This hypothesis was confirmed by the intensity ratios calculated for the samples discussed earlier, which are plotted in Figure 6.16 together with the calibration curve of the commercial powder. In this figure, not only the intensity ratio of the sample mixed with Mn differs from that of the single powder but also the sample mixed with Fe presents a significantly lower value of ρ. The sample with Cr shows a value of ρ slightly lower than the powder calibration but within the limits of the measurement accuracy. The samples placed near the substrate and mixed with SSZ do not show any changes with respect to the powder sample, which further confirms that neither vapour diffusion of any element or reaction with SSZ occurs during the heat treatment in air.
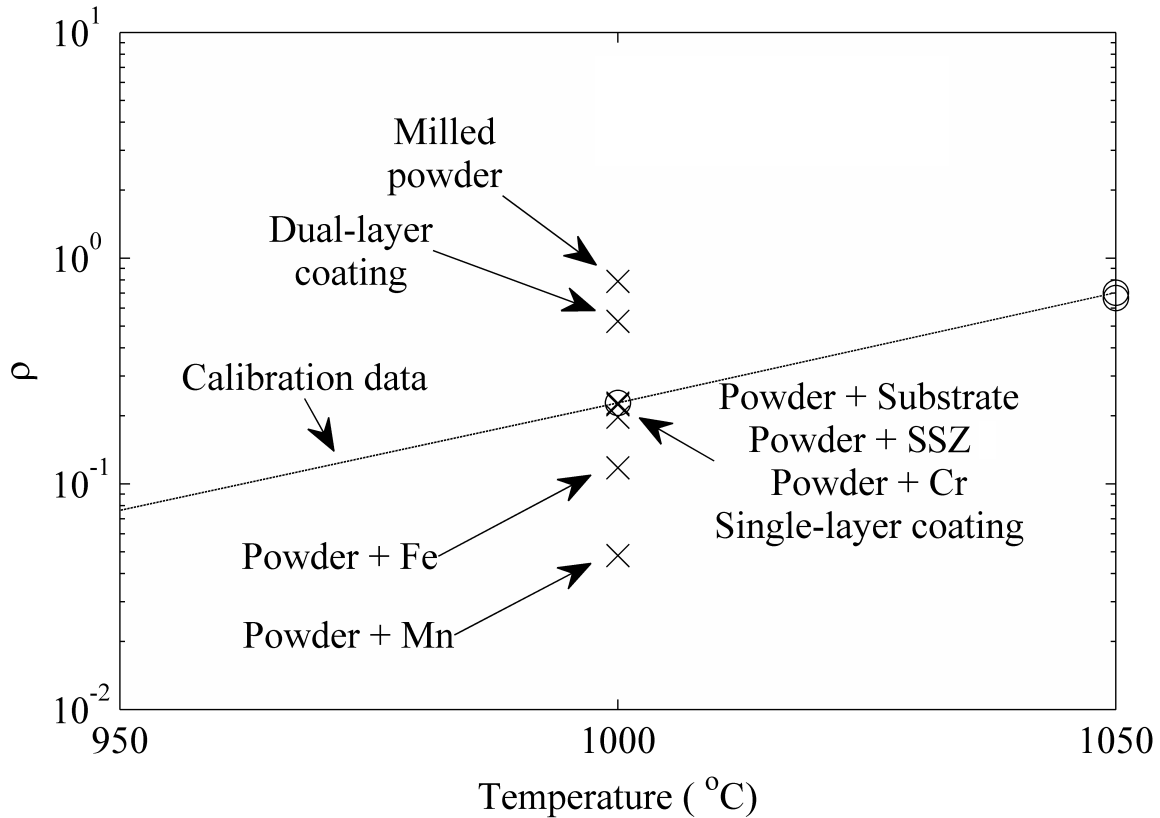
Figure 6.16. Intensity ratio of samples heat treated in air at 1000 °C for 20 minutes. The samples are the same as for Figure 6.15, see text for further details.

The ball milled powder shows a higher value of ρ as was discussed in section 5.2.7. The single and dual-layer coatings should present similar intensity ratios to that of the ball milled powder since the particles were ball milled during the manufacture of the coatings and therefore have the same particle size. Additionally, no sintering process is evident from the SEM image of the surface of manufactured coatings and therefore the structure is similar to that of a stack of powder. However, the intensity ratio of the single layer coating is about 4 times lower than expected and close to the one of the commercial powder. This is the result of the luminescence quenching of the transition metal ions that diffused through the phosphor layer. On the other hand, the dual-layer coating shows a value of ρ much closer to that of the ball milled powder, which suggests that the diffusion of elements is much weaker even though it is still detectable in its emission spectra in Figure 6.15.

The quenching effect caused by the diffusion of transition metal ions greatly affects the ability to measure temperatures with the single-layer coatings as depicted in Figure 6.17. In general, the absolute value of ρ of single-layer coatings is lower than in the commercial powder and thus much lower than the ball milled powder used in the coating. This was already expected

from the examination of Figure 6.16. However, most of the change in ρ occurs between 900 °C and 1000 °C, which is reflected in a higher sensitivity of the measurement in this temperature range and a significantly reduced sensitivity at other temperatures. Additionally, the repeatability of the measurement is poor, which was confirmed by measuring a different set of single-layer samples heat treated at the same temperature (not shown in Figure 6.17). This is possibly due to differences during the manufacture of the coatings that leads to distinct levels of diffusion.
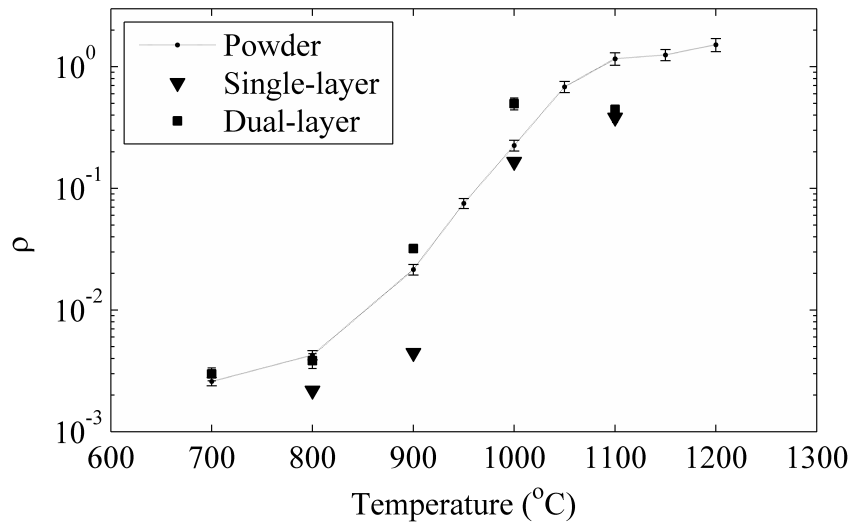
Figure 6.17. ρ of single-layer samples heat treated in air for 20 minutes compared to the calibration curve obtained with the BAM:Eu powder.

The dual-layer coatings, on the other hand, have a value of ρ higher than the commercial powder and closer to the ball milled powder, as shown in Figure 6.17. Furthermore, the sensitivity in the temperature range 900 - 1000 °C is similar to that of the powder and the overall emission intensity of these coatings is higher than the single-layer coatings, although this was only qualitatively estimated. This indicates that the diffusion of elements is prevented by the presence of the interlayer. In particular, the peak at 513 nm is no longer visible in any of the dual-layer coatings after heat treatment and the relative intensity of the Eu^{3+} (580 - 640 nm) emission to the Mn^{4+} broad band (640 – 720 nm) is 3.7 and 5.4 times higher in the dual-layer coatings than in the single-layer coatings, after heat treatment at 900 °C and 1000 °C respectively (see Figure 6.18).
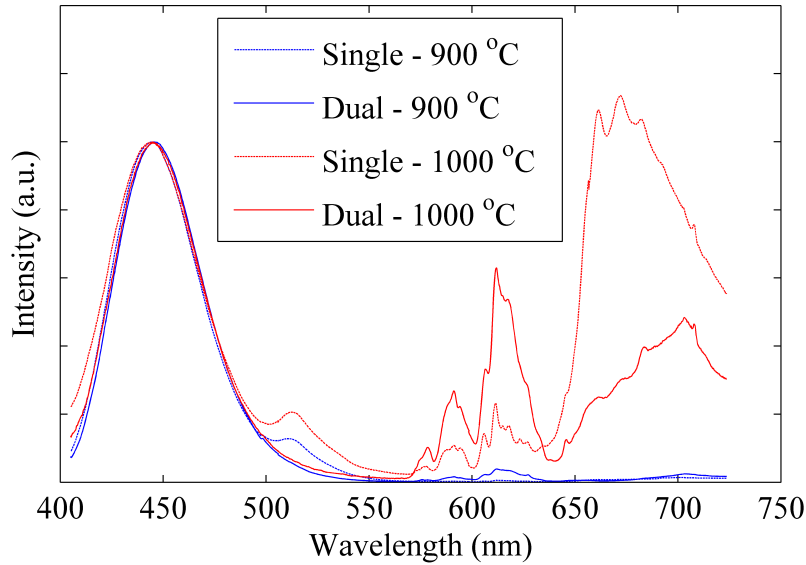
Figure 6.18. Normalised emission spectra of dual-layer samples heat treated for 20 minutes at 900 °C and 1000 °C compared to the emission spectra of single-layer samples heat treated in the same conditions.

6.1.3. Conclusions

The deposition of a BAM:Eu paint was achieved by simply air-spraying an aqueous mixture of the phosphor and a binder on the surface of metallic substrates. The samples were examined after heat treatment at high temperatures but no phosphorescence could be observed. The reasons for the loss of luminescence were identified as chemical reaction between the phosphor and the silicate binder. The use of a binder with a different composition, such as alumina-based, is suggested as a solution.

A binderless coating was manufactured by the screen printing method. This method permits the simple fabrication of a coating by using the commercial phosphor powder as the initial material, and it provides flexibility in the structural composition of the coating. Investigations in screen printed coatings suggest that diffusion of elements from the substrate to the phosphor layer occurs unless a suitable diffusion barrier is introduced. The diffusion of elements such as Cr, Fe and Mn, which was confirmed by EDS and spectroscopy, quenches the luminescence from the phosphor and modifies the emission spectrum thus affecting a potential temperature measurement using the phosphorescence sensor. By simply including an intermediate layer of 2 μm of SSZ, the diffusion of elements was significantly reduced and results similar to those of the powder material obtained. Due to the similarities between SSZ and the standard TBC material (i.e. YSZ), it is considered that the BAM:Eu sensor could be deposited on top of a YSZ TBC in real applications.

6.2. Thermal gradients in phosphor thermometry

The presence of protective coatings and complex internal cooling systems in modern gas turbines imposes a thermal gradient across the sensor/protective coating and the metallic component. This thermal gradient is normally in the order of 1 °C/µm and can affect the temperature measurement performed by using thermographic phosphor coatings [42, 54] due to the contribution to the overall luminescent signal of phosphor layers at different temperatures. Although a thin phosphor layer can be used to minimize the effect of thermal gradients, this is detrimental for the signal intensity and the signal-to-noise ratio and a compromise must be sought.

The effect of laser penetration within phosphor coatings and the effect of thermal gradients on the measurement accuracy have recently been studied theoretically for the lifetime decay method as explained in section 2.2. In this section the theoretical model is compared to experimental results as part of a collaboration project with SCS, and the results are discussed in reference [2]. Additionally, in the second part of this section the model will be extended to the intensity ratio technique to make predictions of the temperature error expected in the use of a BAM:Eu sensor coating under thermal gradient conditions and emphasise the relevance of this effect on the measurement accuracy.

6.2.1. Experimental set-up

The investigation of the effects of thermal gradients was performed on a sample which consisted of a 30 mm circular disk of nickel alloy with a thickness of 3 mm and coated with a layer of YSZ:Eu/Dy of about 100 µm, which was deposited by APS. In order to generate a thermal gradient the sample was placed on a thermal gradient cycling rig owned and operated by SCS. A complete description of the rig can be found in [178]. To create the thermal gradient, the coated surface was exposed to an oxyfuel flame while the back surface was cooled by a current of compressed ambient air. The thermal gradient was thus controlled by adjusting the oxygen-fuel ratio of the flame and the pressure of the cooling air jet. Control of these parameters also permitted adjustment of the maximum temperatures achieved during the test.
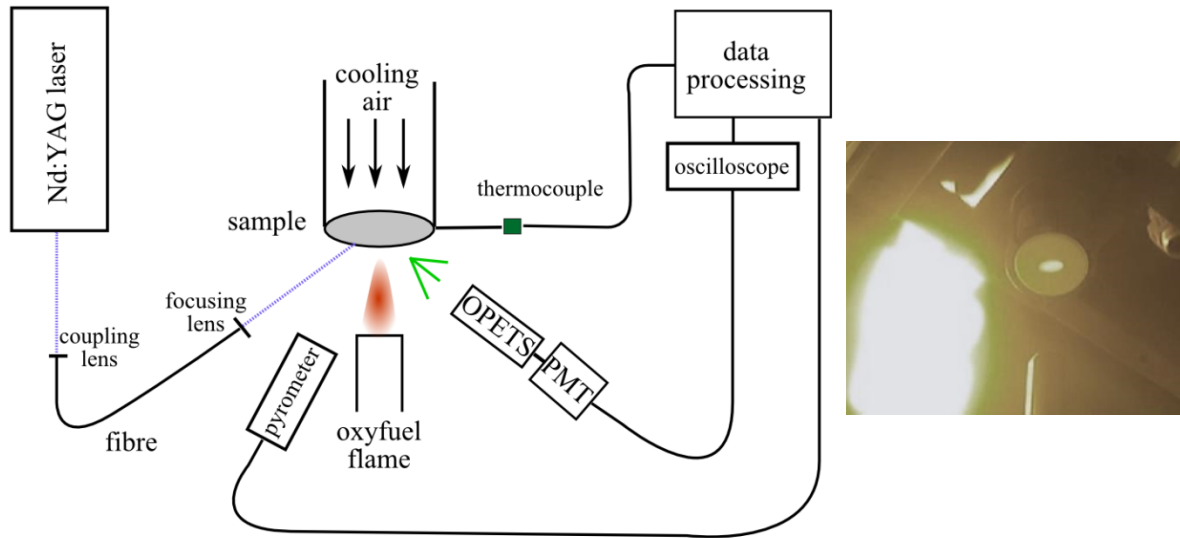
Figure 6.19. Experimental set-up for the temperature measurements in the thermal cycling test rig and image of the illumination of the sample after exposure to the flame.

The temperature of the sample was continuously monitored throughout the tests at three locations. The surface temperature (T_p) of the coating was measured using a long wavelength pyrometer (spectral range: 9.6 - 11.5 μm) to overcome the transparency of the coating at shorter wavelengths. The pyrometer was located at a distance such that the circular area of the measurement was of about 5 mm in diameter. It is well known that pyrometers are subjected to several sources of uncertainty, which include uncertainty in the determination of the emissivity of the surface to be measured, the effect of background radiation due to flames or reflected ambient light, and the contamination of the optical path that results in a change of the irradiance detected by the pyrometer.

In this work, the emissivity of the phosphor sample was estimated using two different set-ups as described in reference [6]. Firstly, the sample was uniformly heated up to 280 °C on a hot plate and the emissivity setting of the pyrometer was modified until its temperature reading matched that of a K-type thermocouple embedded within the sample. Secondly, the phosphor sample was heated to approximately uniform conditions in the thermal gradient test rig (as previously described) to a temperature of about 600 °C. Then, the temperature reading of the pyrometer was matched to the temperature measured using the phosphorescence of the sample by modifying the emissivity setting. In both cases the best results were obtained for an apparent emissivity of 0.93. The uncertainty in the estimation of the emissivity of YSZ TBCs using pyrometry has previously been reported to be of about ±5 % [26] and this level of uncertainty was therefore assumed for the current emissivity value.

According to [179], the main emission from a Bunsen flame (similar to that used in this work) is due to H_2O and CO_2 molecules. CO_2 main emission lines are located in the 4.4 µm and 15 µm region, whereas the H_2O emission lines are located at 2.7 µm, 6.26 µm and in the region from 10-24 µm. Therefore, of these, only emission from water can affect the reading of the pyrometer, which collects light from 9.6 - 11.5 µm. However, the emission lines of water at these wavelengths are at least an order of magnitude less intense than the main lines in the near infra-red. It can be concluded that the contribution of the flame radiation to the uncertainty of the measurement is negligible compared to the uncertainty related to the calculation of the emissivity discussed in the previous paragraph. This is further supported by the manufacturer's claim that the pyrometer is well-suited to make measurements with a long signal path length because the wavelengths observed by it are not strongly absorbed by atmospheric gases.

Measurements were performed in surroundings at room temperature. Therefore, background radiation reflected from the sample to the detector was expected to be low. The worst case was when the sample was heated on the hot plate, where the sample temperature was about 280 °C. This was the lowest temperature considered and hence was that with the lowest signal to contamination ratio with contamination generated by surroundings at the ambient temperature of 25 °C. If we assume an emissivity of 1 for the surroundings, the irradiance emitted by the ambient is approximately 12 % of the irradiance of the sample. However, given the high emissivity of the sample (~0.93), and assuming that the Kirchoff's law is valid at the temperatures of interest ($\varepsilon_{\lambda,\theta}(T) = \alpha_{\lambda,\theta}(T)$), the reflectance of the sample is low ($\alpha + \rho + \tau = 1$, where α is absorptivity, ρ is reflectivity and τ is transmittance). It can thus be assumed a reflectivity of approximately 0.1 applies, which implies that the background radiation collected by the pyrometer is, in the worst case, of about 1.2% of the total irradiance.

An additional source of uncertainty specified by the manufacturer is related to the temperature difference between the sample and the housing of the pyrometer. According to specifications, 0.7 % of this temperature difference should be added to the uncertainty of the measurement.

The uncertainties related to the pyrometer measurement are summarised in Table 6.1. In this table, individual uncertainties at 900 °C (which is the maximum temperature measured with the pyrometer in the experiments) of all the contributing factors are included, and these individual uncertainties are used to calculate the combined standard uncertainty following

equation (6.1) obtained from the procedure in the "Guide to the expression of uncertainty in measurement" [180].

$$u_c^2(y) = \sum_{i=1}^{N} \left(\frac{\partial f}{\partial x_i}\right)^2 u^2(x_i) \tag{6.1}$$

In this equation, u_c is the combined uncertainty of the measurand estimate y, f is the functional relationship between the measurand and all the other variables (derived here from Plank's law), $u(x_i)$ is the standard uncertainty of each of the input estimates x_i. It is assumed for this calculation that all the factors are independent, and Planck's law is used with values of $T = 1200$ K, $\varepsilon = 0.93$ and $\lambda = 10$ μm.

Table 6.1. Estimated uncertainties of various components affecting the pyrometer measurements

Component	Uncertainty at 927 °C	Reference
Calibration	± 0.5 °C	Manufacturer specification
Temperature difference between sample and pyrometer	± 6.5 °C	Manufacturer specification
Emissivity	± 0.0465	[26]
Flame	-	[179]
Reflected irradiance	± 1.2 %	This work
Combined standard uncertainty	± 36.4 °C	This work

The substrate temperature (T_{TC}) was measured by using a K-type thermocouple located at the centre of the disk and 1 mm beneath the TBC/bond coat interface. The temperature measurement using the phosphorescence of the sensor (T_s) was performed by exciting the sample with the third harmonic (355 nm) of a Nd:YAG laser. The laser beam was in this case delivered through an optical fibre (FT1000UMT-CUSTOM, Thorlabs) of 1 mm in diameter. Energy losses throughout the fire were estimated to be of 20 %. The output of the fibre was focused onto the sample by a plano-convex lens to form a spot size of approximately 9 mm so that the fluence of the excitation was typically below 10 mJ/cm^2. The emitted light was collected by an optical probe (OPETS) designed by SCS [51, 181]. This probe coupled the light into a PMT by using a narrowband interference filter centred at the wavelength of the main dysprosium emission line (592/43, Edmund Optics). The signal from the PMT was processed using a single-exponential algorithm as described in section 4.1.3.2. A description of the full set-up is shown in Figure 6.19.

The lifetime decay of the sample was previously calibrated against temperature in an optically accessible furnace in isothermal conditions and the calibration curve is shown in Figure 6.20. Uncertainties in the calibration of the phosphor are typically of approximately ± 10 °C. The sample was located inside the furnace and the temperature rose to the maximum value of interest. After equilibrium was reached, the furnace was switched off and the sample slowly cooled down. The temperature of the sample was continuously monitored by a K-type thermocouple and the lifetime decay measured using the same laser light and collection optics from the rig tests. The recorded signal was processed and fitted by a single-exponential algorithm. The fitting parameters were set to $c_1 = 0.25$ and $c_2 = 9$ both for the tests and calibration.
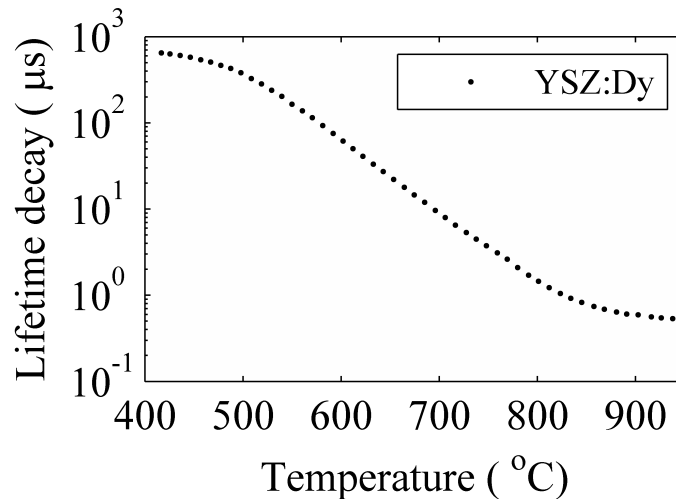
Figure 6.20. Lifetime decay calibration curve of YSZ:Dy. Uncertainties in the calibration of the phosphor are typically of approximately ± 10 °C.

The theoretical results for the conditions tested in the experiments were modelled by Pilgrim et al. [54, 95] following the model described in section 2.2.2. The optical coefficients of the coating, i.e. scattering and absorption coefficients that are the necessary input to the model, were selected from the literature available for YSZ TBCs as indicated in [54]. An extensive discussion on the selection of optical coefficients for the model was reviewed in detail in [95]. A linear thermal gradient across the coating was utilised for calculations, which assumed steady state conditions and the presence of heat transfer only by conduction. The experimentally measured temperatures of the coating were used as inputs to calculate this gradient.

6.2.2. Experimental and modelled results

Two separate types of tests were performed in the sample with a forced thermal gradient. In the first one, the thermal gradient, defined as the temperature difference from the surface to the substrate ($T_p - T_{TC}$), was kept constant at about 100 °C while the temperature of the substrate was increased from 500 °C to 800 °C. The temperature readings of the pyrometer (T_p), the luminescent sensor (T_s) and the substrate thermocouple (T_{TC}) are shown in Figure 6.21. The temperatures calculated by the theoretical model and the temperature difference defined as the temperature gradient from the surface to the sensor ($T_{diff} = T_p - T_s$) are also included, both for experimental and modelled temperatures.
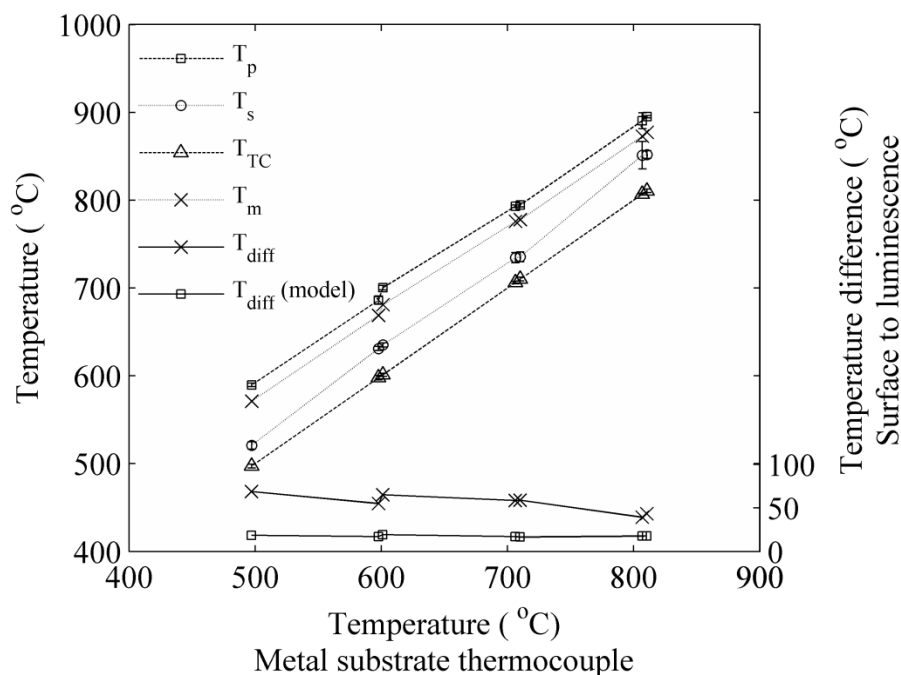
Figure 6.21. Average temperatures read by the pyrometer, luminescence and thermocouple, when the gradient is kept constant and the absolute temperatures increased. Modelled results are also included.

The first aspect to notice is that T_s remains between T_p and T_{TC}, which indicates that the luminescence measurement under thermal gradient conditions provides a value of temperature at a certain effective depth within the coating. However, the temperature actually measured, T_s, is closer to the substrate temperature than predicted by the model. The apparent depth of the temperature reading, which can be deduced from the calculated thermal gradient, is estimated to be of 79 μm from the surface of the coating. This depth is larger than expected from the theoretical approach.

The offset between T_p and T_s is relatively constant, which is in agreement with the theoretical model. This can be explained by referring to the calibration curve of the phosphor shown in Figure 6.20. When the thermal gradient is constant and the range of temperatures lies within the same region of the calibration curve, the change of the decay time across the coating remains the same and therefore the equivalent depth of the measurement also stays invariable.

In the second test, the temperature of the metallic substrate was kept at a constant temperature of about 750 °C, while the thermal gradient across the coating gradually increased from 60 °C to 160 °C. All the temperature readings are plotted in Figure 6.22 against the thermal gradient. T_{diff} as defined before is also included in the graph.
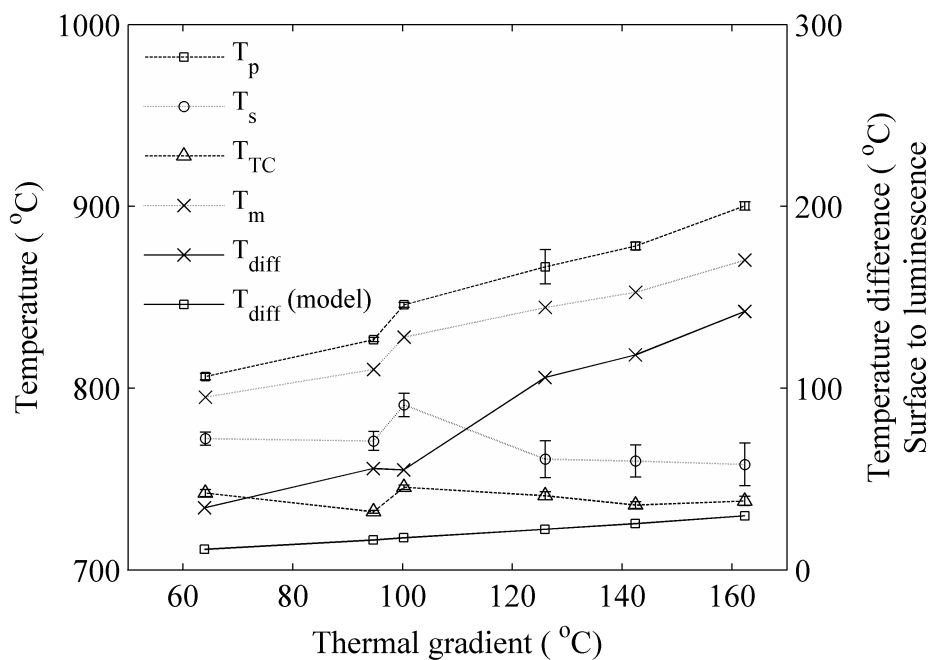
Figure 6.22. Average temperatures read by the pyrometer, luminescence and thermocouple, when temperature is kept constant and the gradient is increased. Modelled results are also included.

Similarly to the previous test, T_s remains inside the coating and closer to T_{TC} than T_p. The luminescent sensor temperatures predicted by the model are again higher than those actually measured. However, the same linear increase of T_{diff} is found for the measured and predicted temperatures. This means that the sensed temperature becomes closer to the bond coat interface for higher thermal gradients. In fact, the depth of T_s increases from 68 μm when the thermal gradient is of 0.5 °C/μm to 111 μm when the thermal gradient is of 1.3 °C/μm. An explanation can be found in the increase of intensity of the phosphorescence at lower temperatures, which makes that contribution to the measured signal from deeper layers of the

coating stronger at the surface thus making the overall decay longer and the measured temperature lower.

The model predicts well the variations of the temperature measurement with the changes of the thermal gradient. However, temperature inaccuracies anticipated by the theoretical model are underestimated since the absolute temperatures predicted by the model are up to 10 % higher than those actually measured. The temperature measured by the luminescence is thus closer than expected to the bond coat interface temperature in all the cases. A possible explanation for this could be related to the consideration of only one mechanism of heat transfer by conduction and the assumption of a constant thermal conductivity across the coating. Radiation effects are significant at these temperatures and the variation of thermal conductivity can introduce further changes to the heat transfer and thus to the thermal gradient. In addition to this, the coefficients of absorption and scattering, which are inputs to the model, are obtained from the literature and might not represent accurately the physical properties of the sample used in the study.

6.2.3. Application to the intensity-ratio method

In this section, the model developed by Pilgrim et al. [54] is adapted so that the intensity ratio signal at the surface of a luminescent coating in a thermal gradient could be theoretically reconstructed rather than the lifetime decay.

6.2.3.1. Model assumptions

A single layer BAM:Eu coating on top of a metallic substrate was modelled. The phosphor was considered to have a quantum efficiency of 0.85, as indicated in [124], and the substrate a reflectivity of 0.15, which is in accordance with data presented for metallic substrates in [54]. The procedure followed to calculate the phosphorescent emission at the surface was the same used by Pilgrim et al. [54]. The single layer coating of BAM:Eu under a thermal gradient is equally divided in multiple thin layers and the contribution to the total luminescence intensity of each of these layers is calculated. Because the various phosphor layers are at different temperatures due to the thermal gradient, the relative intensities at the surface of the two emission wavelengths used to calculate the intensity ratio (445 nm and 611 nm) vary from layer to layer, and therefore the value of ρ of the overall signal at the surface varies accordingly.
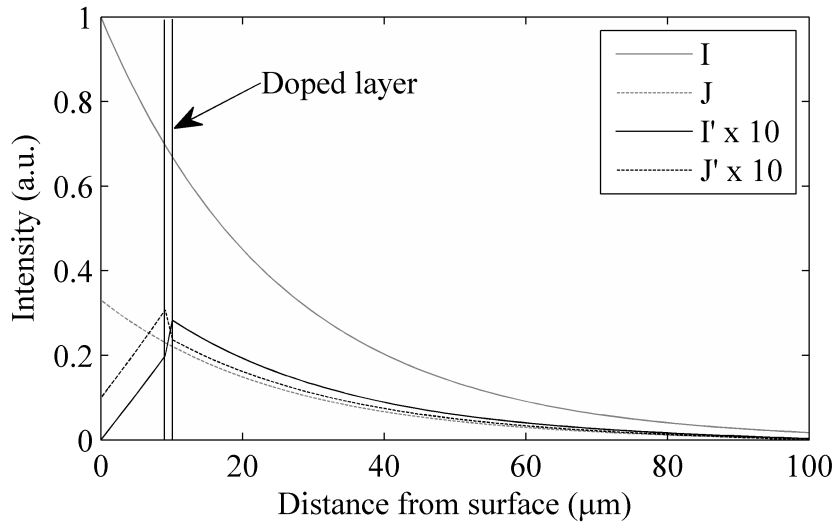
Figure 6.23. Excitation at 266 nm (grey lines) and emission at 445 nm (black lines) light distribution across a 100 μm thick coating when a 1 μm layer is considered to be doped. The emission intensity is multiplied by 10 to improve visibility.

For each doped layer, the distribution of the laser excitation light and the emission at 445 nm across the coating was calculated as depicted in Figure 6.23. The emitted light at the surface of the coating (J'_{445}) due to the contribution of a single layer was used to calculate the intensity of the light emitted at the other emission wavelength (J'_{611}) by multiplying $J'_{445} \cdot \rho$, where ρ corresponds to the temperature of the doped layer. This assumes that light at 445 nm and 611 nm propagates equally across the layer, which might not be true if the scattering and absorption coefficients differ at those wavelengths. Finally, contributions from all the layers were added up for both emission wavelengths and the apparent ρ calculated. From this value of ρ the theoretically measured temperature could be obtained from the calibration curve.

The main limitation for the application of the model was related to the estimation of the optical coefficients that are inputs to the model. To the knowledge of the author no data are available of the scattering and absorption coefficients of BAM:Eu powder layers or coatings. For BAM:Eu powder in thick plaques the remission function is reported in [117]. This function is defined as $m(\lambda) = \mu/\beta$, where μ and β are the absorption and scattering coefficients respectively. This relation between the two coefficients is therefore used to estimate the optical coefficients of BAM:Eu. However, one of the two coefficients must still be determined by other means. Since no other data are available, it was assumed in a first approximation that the scattering coefficient values used in [95] and calculated from [182] for YSZ APS coatings would be representative of a BAM:Eu coating with similar microstructure.

This assumption is made due to the impossibility of obtaining real data for a BAM:Eu coating during this project. The results subsequently obtained are only qualitative and real coating coefficients must be measured before attempting to obtain quantitative results.
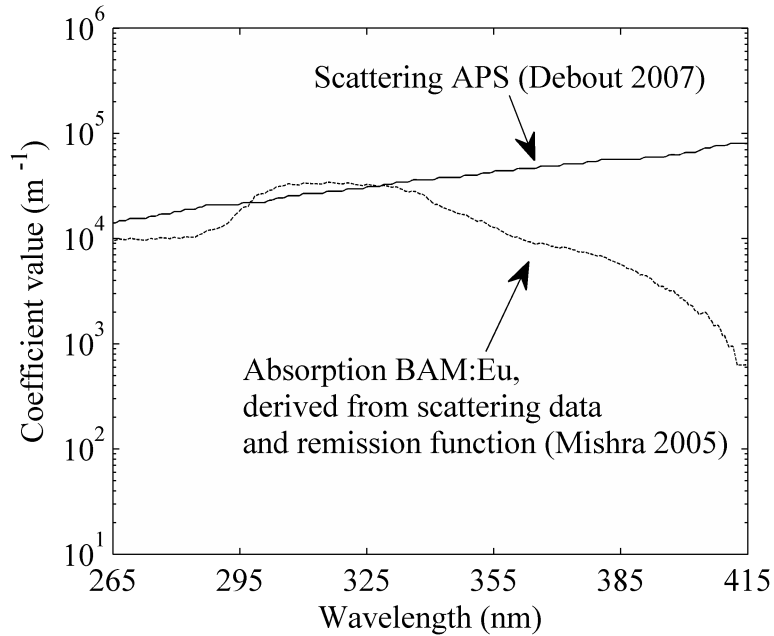
Figure 6.24. Scattering coefficient assumed from YSZ APS coatings [95, 182] and absorption coefficient derived from the scattering coefficient and the remission function of BAM:Eu [117]. These values are a simple assumption to obtain qualitative results.

From the values of the scattering coefficient and the remission function, the absorption coefficient was then calculated. Because the data for the remission function is only available up to wavelengths of about 415 nm, values at 445 nm were assumed to be similar to those at 415 nm. This is consistent with the fact that BAM:Eu is transparent in the whole visible spectrum and thus the absorption coefficient is several orders of magnitude lower than the scattering coefficient. Values for the scattering and absorption coefficients used in this work are shown in Figure 6.24.

6.2.3.2. *Results and discussion*

The effect of coating thickness and thermal gradient was investigated by modelling a single layer BAM:Eu coating with optical properties as described previously. The surface temperature was fixed at 1000 °C, in the region of maximum sensitivity of the sensor, so that the effect of the thermal gradient was the highest possible. The results are shown in Figure 6.25, in which both plots can be compared with the results by Pilgrim et al. [54].
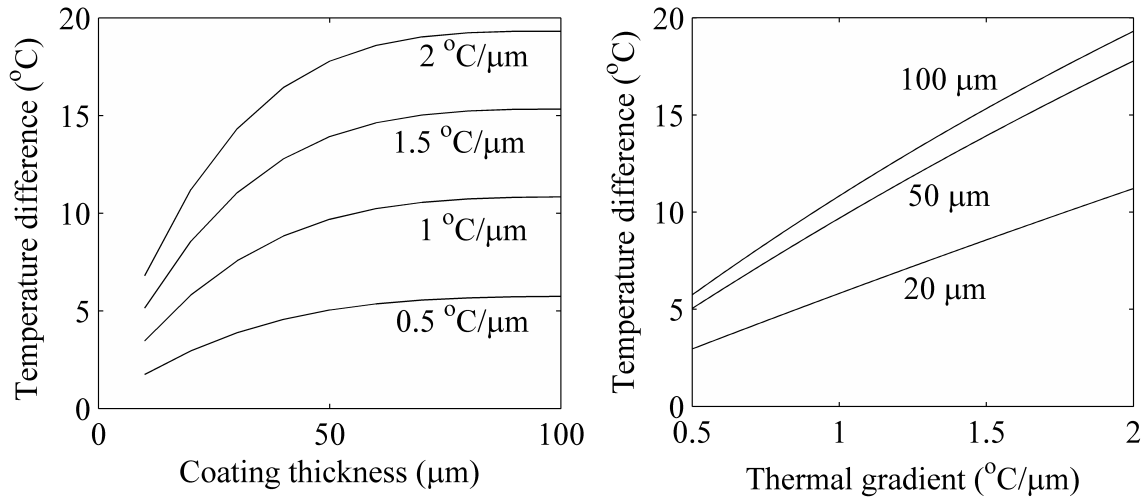
Figure 6.25. Temperature difference between the surface of the coating and the actual measurement as calculated by the model and considering the effect of the coating thickness (left) and thermal gradient (right).

Qualitative analysis of the results shows that the effect of a thermal gradient in the measurement accuracy when the intensity ratio method is employed is similar to that obtained with the lifetime decay method. An increase of the coating thickness increases the temperature difference from the surface to the measurement up to a point when contributions from deep inside the coating are low and the temperature difference remains nearly constant. An increase of the thermal gradient given a fixed coating thickness increases the temperature difference from the surface to the measurement almost linearly. Therefore the same implications deduced in [54] can be applied for the intensity ratio method. This includes that the thinnest possible coating should be used in applications where the thermal gradient is unknown, which is the most common case in practical applications, since the temperature error introduced will be lower than for thick coatings.

Considering the experimental results from section 6.2.2, temperatures are expected to be closer to the interface between the coating and the substrate, and therefore a larger error than the theoretical estimation can be anticipated. This is probably due to the temperature distribution model employed considering only heat transfer by conduction and a constant thermal conductivity. Furthermore, the optical coefficients used in the model are assumed from the reduced data available in the literature and not directly applicable to obtain quantitative results. The temperature differences estimated in this analysis nearly double when the scattering coefficient is reduced by a factor of 10, and they drastically decrease to below 2.5 °C when the scattering coefficient increases by a factor of 10. The variation of these

coefficients between the two emission wavelengths (445 nm and 611 nm) should also be considered for improved accuracy. A large discrepancy in the results can be found if transmission of light through the coating at these two wavelengths is actually very different. This requires estimation of the two coefficients in the whole visible spectrum which is out of the scope of this work.

6.2.4. Conclusions

A theoretical model developed by Pilgrim et al. [54, 95], which describes the propagation of excitation and emission light through a phosphor coating and permits the estimation of the intensity of light coming out of the coating, was used to predict the effect that a thermal gradient across the coating would have on the measured temperature by using the lifetime decay method. In this work, experimental validation of the model was carried out in collaboration with C. Pilgrim and SCS. The validation was done by exposing a YSZ coating sample mounted on a thermal gradient test rig to a controlled thermal gradient. The temperatures at the surface and in the metallic substrate were carefully controlled so that the measurement by luminescence could be compared to those temperatures. It was verified that the temperature measured by luminescence is between the surface and the substrate temperatures. Experimental results are in agreement with the general trends deduced from the theoretical model but suggest that the model underestimates the differences between the surface and the luminescence temperatures. It is argued that some assumptions to the model and the thermal gradient distribution across the coating might be responsible of the discrepancies between experiments and theory. Additionally, the uncertainties related to the temperature measurements performed with thermocouples and pyrometry can affect the results bringing the theoretical model closer or further from the experimental results. If a detailed quantitative analysis is to be done in the future, these uncertainties need to be accounted for with standard procedures such as the "Guide to the expression of uncertainty in measurement" [180].

The model is further extended to account for the effect of thermal gradients when the intensity ratio method is used in a BAM:Eu coating. Despite difficulties to obtain reliable values from the literature for the model input coefficients, the results are qualitatively similar to those obtained for the lifetime decay method. This emphasises the importance of considering thermal gradients when performing temperature measurements with phosphor coatings under thermal gradient conditions.

7. CONCLUSIONS AND OUTLOOK

In this chapter a brief summary of the conclusions derived from the results of the project is provided. The aspects of the research that can be improved or investigated further are discussed, as well as final recommendations for the future development of a sensor coating with BAM:Eu.

7.1. Instrumentation

The equipment and methodology used during the present work to perform reliable luminescence measurements was described in detail. Intensity ratio measurements were performed by using emission spectra recorded at various wavelengths in independent measurements. By using this system the precision of the measurement was typically better than 1 % and the measurement uncertainty lower than 2.5 %. These values are expected to improve if a dual-camera system is employed instead, in which information of the two regions of the spectrum is collected simultaneously. Furthermore, selection of adequate collection filters could also be further investigated to optimise the signal intensity and sensitivity of the intensity ratio. To develop the system for industrial application, a continuous-wave laser at a longer wavelength than the 266 nm used in this study could be used. BAM:Eu is excitable at wavelengths as long as 375 nm, which matches the emission of some continuous-wave lasers available in the market. Alternatively, delivery of the excitation light and collection of the phosphorescent emission could be coupled to an optical fibre and detection made by a compact spectrometer from which the spectrum could be converted into an intensity ratio by numerical post-processing. This would make the equipment small and suitable for in-situ measurements.

The measurement of the lifetime decay method presents some complications that are well known and documented in the literature. Previous recommendations were followed in this work to obtain reliable measurements. Additionally, three algorithms were tested to fit the decay signal, namely a single-exponential, bi-exponential and multi-exponential. The results indicate that a single-exponential algorithm that cuts off the initial part of the decay signal is best in terms of precision. Such an algorithm fails to accurately fit non-exponential decays and is highly sensitive to the fitting parameters. However, this method is acceptable if the fitting parameters are kept constant throughout the measurements.

7.2. BAM:Eu

A thorough review of the literature related to BAM:Eu and its oxidation in air was presented which was a useful guideline during the investigation of the phosphor as a history sensor. Material characterisation studies were summarised and the crystal structure of BAM described in detail. Understanding of this structure is crucial to explain the oxidation mechanism of the phosphor. The large number of studies about thermal degradation of BAM:Eu were reviewed and two types of degradation identified, of which only oxidation in air was relevant for this project. Although the majority of these studies are related to the use of BAM:Eu in lighting applications, which generally involve different experimental conditions, some of the results related to the oxidation process of the phosphor were used to support the conclusions derived from current experiments.

7.3. Thermal history sensing

One of the objectives of the project was to investigate the mechanism by which oxidation at high temperature in air of BAM:Eu phosphor occurs and how the modification of the optical properties as a result of this oxidation can be used as a reliable indication of the past temperature. Insight into the oxidation mechanism was gained by physical, thermal and optical characterisation of the phosphor. The mechanism of oxidation involves adsorption of gaseous oxygen onto the surface of the phosphor, diffusion of the dopant ion through the conduction layer of the BAM lattice and oxidation of the europium ions upon interaction with the adsorbed oxygen. This process occurs progressively in the temperature range investigated from 700 °C to 1200 °C, and it is also dependent on the total time that the phosphor is exposed at high temperatures.

A continuous change of the emission spectrum and phosphorescent decay time was observed upon oxidation that could be used to perform a measurement of the temperature at which the phosphor was exposed. The intensity ratio and lifetime decay were defined and calibrated for the range of temperatures from 800 °C to 1200 °C and exposure times from 5 minutes to 120 minutes. A continuous and predictable change of the measurands was observed as expected from the oxidation mechanism. Above 900 °C, the variation of ρ was well predicted by the KJMA theory, while at lower temperatures additional calibration data was necessary. Various effects that can introduce systematic errors in the measurement technique were quantified. The excitation fluence used to illuminate the phosphor shows negligible influence on the

intensity ratio but affects significantly the lifetime decay. This is possibly due to high order recombination processes that occur between the excited dopant ions and the host lattice.

The time necessary to cool down the sensor after exposure to high temperatures is expected to vary from the calibration to practical applications. In this work, samples were cooled down in ambient air in only 2 - 3 minutes. A slower cooling down time of about 1.5 hours provided an overestimation of the sensed temperature of only 40 °C when the intensity ratio was used and 65 °C for the lifetime decay method. This effect should be considered in practical applications when the calibration of the phosphor is done or by applying a correction after the measurement. By annealing the phosphor in atmospheres with variable concentration of oxygen, it was shown that presence this gas is necessary for the oxidation of BAM:Eu to occur. A minimum threshold for the oxygen partial pressure of 0.1 bar was established so that the uncertainty of the measurement was not affected by the lack of oxygen available for oxidation. Above that partial pressure the adsorption of oxygen was saturated and no changes on the measurement were observed. The cooling down time and oxygen atmosphere studies were performed on samples heat treated at 1000 °C. Although the influence of these effects at other temperatures is expected to be similar due to the continuous nature of the oxidation process, further investigation is necessary to obtain accurate calibration of these effects at all the temperatures of interest.

Investigation of sol-gel manufactured samples showed that the dopant concentration shifts the range of temperatures in which the phosphor exhibits higher sensitivity. At higher dopant concentrations the phosphor was sensitive at higher temperatures and vice-versa. This is believed to permit optimisation of the phosphor for different temperature ranges depending on the application. Further investigation on phosphors manufactured by the solid state method, rather than the sol-gel used in this work, would enable accurate calibration of this effect and also determination of the maximum temperature that can be reliably measured by the phosphor. The appearance of the BAL phase in the sol-gel phosphors manufactured in this project was responsible for the extension of the sensing capabilities to higher temperatures. Future tests with different solid solutions of BAM-BAL phases doped with europium could extend the measurement sensitivity to higher temperatures or increase the dynamic range of the phosphor. In general, the level of crystallinity, stoichiometry and induced defects, which are normally optimised in commercial BAM:Eu to obtain maximum quantum efficiency in lighting applications, should be investigated further with regards to the use of the phosphor in

temperature measurements. Optimisation of these parameters could potentially increase the sensitivity and dynamic range of the phosphor.

The possibility to reuse the sensor after a temperature measurement is performed was investigated. In order to do so, a heat treatment at a relatively high temperature in a reducing atmosphere was necessary. The results indicate that heat treatment at temperatures below 1000 °C could not completely reset the initial state of the phosphor and successive calibrations of the sensor were dependent on the initial annealing temperature. Heat treatment at 1150 °C, on the contrary, proved to be successful to reset the phosphor to an adequate level to perform a new temperature measurement with the same calibration curve initially used. Further investigation of the uncertainty expected after multiple resetting processes is necessary.

The performance of the phosphor as a thermometer (using the intensity ratio method) can be summarised as follows:

- Sensitivity > 0.5 %·°C^{-1} between 700 °C and 1000 °C.
- Possibility to modify this range by modifying the dopant concentration.
- Typical measurement uncertainty < 2 % in the range 700 - 1200 °C.
- Sensitivity with exposure time modelled by KJMA theory above 800 °C.
- Measurement not affected by excitation fluence.
- A cooling down time of 1.5 h can introduce a systematic error of up to 40 °C at 1000 °C.
- Measurement not affected by the oxygen partial pressure when it is above 0.1 bar.
- A change of 1 order of magnitude in the particle size can introduce a temperature error of up to 70 °C.

7.4. Coating development

The investigation of conventional ceramic film deposition techniques that could be used to create a thermal history coating and the thermal characterisation of such a sensor was one of the aims of this work. The phosphor was successfully deposited by air spraying it in the form of paint. However, the use of this paint was restricted by chemical reaction between the binder and the BAM:Eu at high temperatures. This reaction eliminated any phosphorescence signal from the phosphor that could be used for a temperature measurement. Further

investigation with other paints that are not based on a silicate binder, for example alumina-based binders, is expected to provide better results.

Screen printed coating samples exhibited element diffusion from the substrate after heat treatment. Chromium, iron and manganese were detected in the BAM:Eu layer after exposure to high temperatures. The presence of these ions is important because it quenches the luminescence from the phosphor thus affecting any subsequent temperature measurement. The use of a SSZ diffusion barrier of only 2 μm drastically reduced the diffusion of ions and improved the emission efficiency. A diffusion barrier between the metallic substrate and the BAM:Eu layer is thus necessary for the application of the sensor. Further investigations with a thicker interlayer are desirable to determine the minimum required thickness of this diffusion barrier. Additionally, deposition of BAM:Eu on top of YSZ should be investigated since this is the standard TBC material of gas turbines.

PVD deposition methods seem particularly suitable for the deposition of BAM:Eu. This deposition should be carried on in a vacuum or a reducing atmosphere. The stoichiometry should be carefully controlled to obtain the desired phase. Modification of the porosity of the coating would enable control over the surface area in contact with air so that the oxidation of the phosphor is facilitated or inhibited. The possibility to adjust the temperature range that can be measured by controlling the porosity should be investigated. The PLD method offers a good control of these parameters and it should be explored as a suitable method to obtain a thin film of BAM:Eu on top of a YSZ substrate. The results of screen printed coatings indicated that enough signal intensity is obtained from a 12 μm thick coating and thus thinner coatings could be tested if required by the deposition method.

When measuring temperatures with a ceramic sensor coating, the thermal gradient existent across the sensor due to internal cooling systems can dramatically affect the accuracy of the measurement. This effect was investigated and experimental results indicated that the temperature sensed was actually closer to the interface between the phosphor layer and the substrate, rather than close to the surface of the phosphor.

7.5. Further recommendations

In the future development of phosphors as a thermometry tool, proper use of metrological terms needs to be enforced. This can be done by adopting the International Vocabulary of Metrology (VIM) [183], which is internationally recognised and provides consistent

definitions for terms such as precision, accuracy, uncertainty and error. This will promote standardisation of the technique and facilitate the comparison of this relatively new technique with existing temperature detection methods.

In addition to this, a rigorous uncertainty analysis of the various contributing factors in phosphor thermometry, which should include the experimental methods used to characterise the phosphors, needs to be undertaken. In order to do so, reliable metrological practice should be followed such as the ISO Guide to the Expression of Uncertainty in Measurement [180].

8. REFERENCES

1.   Yañez Gonzalez, A., Ruiz-Trejo, E., Van Wachem, B., Skinner, S., Beyrau, F., and Heyes, A., *A detailed characterization of BaMgAl$_{10}$O$_{17}$:Eu phosphor as a thermal history sensor for harsh environments,* Sensors and Actuators A: Physical, **234** 339-345, (2015).

2.   Yañez Gonzalez, A., Pilgrim, C.C., Feist, J.P., Sollazzo, P.Y., Beyrau, F., and Heyes, A.L., *On-Line Temperature Measurement Inside a Thermal Barrier Sensor Coating During Engine Operation,* Journal of Turbomachinery, **137**(10) 101004-101004, (2015).

3.   Yañez Gonzalez, A., Skinner, S., Beyrau, F., and Heyes, A., *Reusable Thermal History Sensing via Oxidation of a Divalent Rare Earth Ion Based Phosphor Synthesized by the Sol-Gel Process,* Heat Transfer Engineering, **36**(14-15) 1275-1281, (2015).

4.   Yañez Gonzalez, A., Ruiz-Trejo, E., van Wachem, B., Skinner, S., Beyrau, F., and Heyes, A.L. *Development of an optical thermal history sensor based on the oxidation of divalent rare earth ion phosphor*, Proceedings of the 14th UK Heat Transfer Conference, Edinburgh, UK, (2015).

5.   Araguas Rodriguez, S., Feist, J.P., Pilgrim, C.C., Berthier, S., Biswas, S.K., Skinner, S., Yañez Gonzalez, A., and Heyes, A.L. *Luminescent Thermal History Sensors: Fundamentals and Applications for Thermal Profiling*, NATO AVT Symposium, Rzeszów, Poland, (2015).

6.   Yañez Gonzalez, A., Pilgrim, C., Feist, J., Sollazzo, P., Beyrau, F., and Heyes, A. *On-line Temperature Measurement Inside a Thermal Barrier Sensor Coating during Engine Operation*, Paper No. GT2014-25936, Proceedings of the ASME Turbo Expo, Düsseldorf, Germany, (2014).

7.   Yañez Gonzalez, A., Skinner, S., Beyrau, F., and Heyes, A. *A reusable thermal history sensor based on the oxidation of a divalent rare earth ion based phosphor synthesized by the solgel process*, IET & ISA 60th International Instrumentation Symposium, London, UK, (2014).

8.   Yañez Gonzalez, A., Pilgrim, C., Sollazzo, P., Heyes, A., Feist, J., Nicholls, J., and Beyrau, F. *Temperature Sensing inside Thermal Barrier Coatings using Phosphor Thermometry*, IET & ISA 60th International Instrumentation Symposium, London, UK, (2014).

9.   Yañez Gonzalez, A., Skinner, S., Beyrau, F., and Heyes, A.L. *Optical Thermal History Sensing via Oxidation of Divalent Rare Earth Ion Based Phosphors Synthesized by the Sol-Gel Process*, Proceedings of the 13th UK Heat Transfer Conference, London, UK, (2013).

10. *Updated energy and emissions projections 2014*, Department of Energy & Climate Change, (September 2014).

11. Capros, P., De Vita, A., Tasios, N., Papadopoulos, D., Siskos, P., Apostolaki, E., Zampara, M., Paroussos, L., Fragiadakis, K., and Kouvaritakis, N., *EU Energy, Transport and GHG Emissions: Trends to 2050, reference scenario 2013*. (2013).

12. Boyce, M.P., *Gas Turbine Engineering Handbook*. (Burlington : Elsevier Science, 2011), 4th ed.

13. Petek, J. and Hamilton, P., *Performance monitoring for gas turbines,* Orbit, **25**(1) 64-74, (2005).

14. Schilke, P.W., *Advanced Gas Turbine Materials and Coatings*, GE Energy: Schenectady, NY, (2004).

15. Feuerstein, A., Knapp, J., Taylor, T., Ashary, A., Bolcavage, A., and Hitchman, N., *Technical and economical aspects of current thermal barrier coating systems for gas turbine engines by thermal spray and EBPVD: a review,* Journal of Thermal Spray Technology, **17**(2) 199-213, (2008).

16. Vaßen, R., Jarligo, M.O., Steinke, T., Mack, D.E., and Stöver, D., *Overview on advanced thermal barrier coatings,* Surface and Coatings Technology, **205**(4) 938-942, (2010).

17. Trunova, O., Beck, T., Herzog, R., Steinbrech, R., and Singheiser, L., *Damage mechanisms and lifetime behavior of plasma sprayed thermal barrier coating systems for gas turbines—Part I: Experiments,* Surface and Coatings Technology, **202**(20) 5027-5032, (2008).

18. Madhwal, M., Jordan, E.H., and Gell, M., *Failure mechanisms of dense vertically-cracked thermal barrier coatings,* Materials Science and Engineering: A, **384**(1) 151-161, (2004).

19. TC-direct, *Guide to thermocouple and resistance thermometry*, (2013).

20. Bird, C., Mutton, J., Shepherd, R., Smith, M., and Watson, H. *Surface temperature measurements in turbines*, AGARD Conference Proceedings, (1998).

21. Franco, G.A., Caron, E., and Wells, M.A., *Quantification of the surface temperature discrepancy caused by subsurface thermocouples and methods for compensation,* Metallurgical and Materials Transactions B-Process Metallurgy and Materials Processing Science, **38**(6) 949-956, (2007).

22. Li, D. and Wells, M.A., *Effect of subsurface thermocouple installation on the discrepancy of the measured thermal history and predicted surface heat flux during a quench operation,* Metallurgical and Materials Transactions B-Process Metallurgy and Materials Processing Science, **36**(3) 343-354, (2005).

23. Tszeng, T. and Saraf, V., *A study of fin effects in the measurement of temperature using surface-mounted thermocouples,* Journal of Heat Transfer-Transactions of the Asme, **125**(5) 926-935, (2003).

24. Kerr, C. and Ivey, P., *An overview of the measurement errors associated with gas turbine aeroengine pyrometer systems,* Measurement science and technology, **13**(6) 873, (2002).

25. Alaruri, S.D., Brewington, A.J., Thomas, M.A., and Miller, J.A., *High-temperature remote thermometry using laser-induced fluorescence decay lifetime measurements of Y_2O_3:Eu and YAG:Tb thermographic phosphors,* IEEE Transactions on Instrumentation and Measurement, **42**(3) 735-739, (1993).

26. Alaruri, S., Bianchini, L., and Brewington, A., *Effective spectral emissivity measurements of superalloys and YSZ thermal barrier coating at high temperatures using a 1.6 μm single wavelength pyrometer,* Optics and lasers in engineering, **30**(1) 77-91, (1998).

27. Cassady, L. and Choueiri, E. *High accuracy multi-color pyrometry for high temperature surfaces*, 28th International Electric Propulsion Conference, Toulouse, France, (2003).

28. Allison, S.W. and Gillies, G.T., *Remote thermometry with thermographic phosphors: Instrumentation and applications,* Review of Scientific Instruments, **68**(7) 2615-2650, (1997).

29. Khalid, A.H. and Kontis, K., *Thermographic phosphors for high temperature measurements: Principles, current state of the art and recent applications,* Sensors, **8**(9) 5673-5744, (2008).

30. Khalid, A.H., Kontis, K., and Behtash, H.Z., *Phosphor thermometry in gas turbines: consideration factors,* Proceedings of the Institution of Mechanical Engineers Part G-Journal of Aerospace Engineering, **224**(G7) 745-755, (2010).

31. Kissel, T., Baum, E., Dreizler, A., and Brübach, J., *Two-dimensional thermographic phosphor thermometry using a CMOS high speed camera system,* Applied Physics B, **96**(4) 731-734, (2009).

32. Fuhrmann, N., Schild, M., Bensing, D., Kaiser, S.A., Schulz, C., Brubach, J., and Dreizler, A., *Two-dimensional cycle-resolved exhaust valve temperature measurements in an optically accessible internal combustion engine using thermographic phosphors,* Applied Physics B-Lasers and Optics, **106**(4) 945-951, (2012).

33. Heyes, A.L., Seefeldt, S., and Feist, J.P., *Two-colour phosphor thermometry for surface temperature measurement,* Optics and Laser Technology, **38**(4-6) 257-265, (2006).

34. Feist, J.P., *Development of Phosphor Thermometry for Gas Turbines*, PhD Thesis, Imperial College London, (2001).

35.   Aldén, M., Omrane, A., Richter, M., and Särner, G., *Thermographic phosphors for thermometry: A survey of combustion applications,* Progress in energy and combustion science, **37**(4) 422-461, (2011).

36.   Brubach, J., Pflitsch, C., Dreizler, A., and Atakan, B., *On surface temperature measurements with thermographic phosphors: A review,* Progress in Energy and Combustion Science, **39**(1) 37-60, (2013).

37.   Brubach, J., Dreizler, A., and Janicka, J., *Gas compositional and pressure effects on thermographic phosphor thermometry,* Measurement Science & Technology, **18**(3) 764-770, (2007).

38.   Allison, S.W., Cates, M.R., Scudiere, M.B., Bentley, H.T., Borella, H., and Marshall, B. *Remote thermometry in a combustion environment using the phosphor technique*, Technical Symposium Southeast, (1987).

39.   Tobin, K., Allison, S., Cates, M., Capps, G., and Beshears, D., *High-temperature phosphor thermometry of rotating turbine blades,* AIAA Journal, **28**(8) 1485-1490, (1990).

40.   Feist, J.P., Heyes, A.L., and Seefelt, S., *Thermographic phosphor thermometry for film cooling studies in gas turbine combustors,* Proceedings of the Institution of Mechanical Engineers Part A-Journal of Power and Energy, **217**(A2) 193-200, (2003).

41.   Seyfried, H., Richter, M., Aldén, M., and Schmidt, H., *Laser-induced phosphorescence for surface thermometry in the afterburner of an aircraft engine,* AIAA Journal, **45**(12) 2966-2971, (2007).

42.   Knappe, C., Andersson, P., Algotsson, M., Richter, M., Linden, J., Alden, M., Tuner, M., and Johansson, B., *Laser-induced phosphorescence and the impact of phosphor coating thickness on crank-angle resolved cylinder wall temperatures,* SAE International Journal of Engines, **4**(1) 1689-1698, (2011).

43.   Choy, K.-L., Heyes, A.L., and Feist, J., *Thermal barrier coating with thermoluminescent indicator material embedded therein*, WO2000006796, (1999).

44.   Feist, J., Heyes, A., and Nicholls, J., *Phosphor thermometry in an electron beam physical vapour deposition produced thermal barrier coating doped with dysprosium,* Proceedings of the Institution of Mechanical Engineers, Part G: Journal of Aerospace Engineering, **215**(6) 333-341, (2001).

45.   Steenbakker, R.J.L., Feist, J.P., Wellman, R.G., and Nicholls, J.R., *Sensor Thermal Barrier Coatings: Remote In Situ Condition Monitoring of EB-PVD Coatings at Elevated Temperatures,* Journal of Engineering for Gas Turbines and Power-Transactions of the ASME, **131**(4), (2009).

46.   Feist, J.P. and Nicholls, J.R., *Multi-functional material compositions, structures incorporating the same and methods for detecting ageing in luminescent material compositions*, WO2009/141623, (2008).

47.   Feist, J. and Heyes, A., *Coatings And An Optical Method For Detecting Corrosion Process In Coatings,* GB. Patent, **318929**, (2003).

48.   Pilgrim, C.C., Berthier, S., Feist, J.P., Wellman, R.G., and Heyes, A.L., *Photoluminescence for quantitative non-destructive evaluation of thermal barrier coating erosion,* Surface & Coatings Technology, **209** 44-51, (2012).

49.   Eldridge, J.I., Singh, J., and Wolfe, D.E., *Erosion‑Indicating Thermal Barrier Coatings Using Luminescent Sublayers,* Journal of the American Ceramic Society, **89**(10) 3252-3254, (2006).

50.   Eldridge, J.I., Bencic, T.J., Spuckler, C.M., Singh, J., and Wolfe, D.E., *Delamination‑Indicating Thermal Barrier Coatings Using YSZ: Eu Sublayers,* Journal of the American Ceramic Society, **89**(10) 3246-3251, (2006).

51.   Feist, J., Sollazzo, P., Berthier, S., Charnley, B., and Wells, J., *Application of an Industrial Sensor Coating System on a Rolls-Royce Jet Engine for Temperature Detection,* Journal of Engineering for Gas Turbines and Power, **135**(1) 012101-012101-9, (2013).

52.   Sollazzo, P., Feist, J., Berthier, S., Charnley, B., Wells, J., and Heyes, A. *Application of a production line phosphorescence sensor coating system on a jet engine for surface temperature detection*, AIP Conference Proceedings, (2013).

53.   Eldridge, J.I., Bencic, T.J., Allison, S.W., and Beshears, D.L., *Depth-penetrating temperature measurements of thermal barrier coatings incorporating thermographic phosphors,* Journal of Thermal Spray Technology, **13**(1) 44-50, (2004).

54.   Pilgrim, C., Feist, J., and Heyes, A., *On the effect of temperature gradients and coating translucence on the accuracy of phosphor thermometry,* Measurement Science and Technology, **24**(10) 105201, (2013).

55.   Omrane, A., Petersson, P., Aldén, M., and Linne, M., *Simultaneous 2D flow velocity and gas temperature measurements using thermographic phosphors,* Applied Physics B, **92**(1) 99-102, (2008).

56.   Rothamer, D. and Jordan, J., *Planar imaging thermometry in gaseous flows using upconversion excitation of thermographic phosphors,* Applied Physics B, **106**(2) 435-444, (2012).

57.   Fond, B., Abram, C., Heyes, A.L., Kempf, A.M., and Beyrau, F., *Simultaneous temperature, mixture fraction and velocity imaging in turbulent flows using thermographic phosphor tracer particles,* Optics Express, **20**(20) 22118-22133, (2012).

58.   Abram, C., Fond, B., Heyes, A.L., and Beyrau, F., *High-speed planar thermometry and velocimetry using thermographic phosphor particles,* Applied Physics B-Lasers and Optics, **111**(2) 155-160, (2013).

59.   Fond, B., Abram, C., and Beyrau, F., *On the characterisation of tracer particles for thermographic particle image velocimetry,* Applied Physics B, 1-7, (2015).

60. Cowling, J., King, P., and Alexander, A.L., *Temperature-indicating paints,* Industrial & Engineering Chemistry, **45**(10) 2317-2320, (1953).

61. Watson, H. and Hodgkinson, E., *Temperature indicating paint*, Patent US 10/229,002, (2002).

62. *Technical Service Brochure*, Rolls-Royce Deutschland Ltd & Co KG, (2011).

63. Rabhiou, A., *Phosphorescent Thermal History Sensing for Advanced Condition Monitoring in High Temperature Environment*, PhD Thesis, Imperial College London, (2012).

64. Lempereur, C., Andral, R., and Prudhomme, J.Y., *Surface temperature measurement on engine components by means of irreversible thermal coatings,* Measurement Science & Technology, **19**(10), (2008).

65. Smith, M., *Interpretation of thermal paint*, Patent US 6/434,267, (2002).

66. REACH, *Registration, Evaluation, Authorisation and Restriction of Chemicals (REACH), Regulation (EC) No 1907/2006 of the European Parliament and of the Council*, in *OJ of the European Union L 396/1* (18.12.2006).

67. Feist, J., Nicholls, J., and Heyes, A., *Determining thermal history of components*, Patent WO/2009/083,729, (2007).

68. Rabhiou, A., Feist, J., Kempf, A., Skinner, S., and Heyes, A., *Phosphorescent thermal history sensors,* Sensors and Actuators A-Physical, **169**(1) 18-26, (2011).

69. Rabhiou, A., Kempf, A., and Heyes, A., *Oxidation of divalent rare earth phosphors for thermal history sensing,* Sensors and Actuators B-Chemical, **177** 124-130, (2013).

70. Heyes, A.L., Rabhiou, A., Feist, J.P., and Kempf, A.M. *Phosphos Based Temperature Indicating Paints*, ASME Turbo Expo 2012: Turbine Technical Conference and Exposition, (2012).

71. Feist, J.P., Biswas, S.K., Pilgrim, C., Sollazzo, P.Y., and Berthier, S. *Off-Line Temperature Profiling Utilising Phosphorescent Thermal History Paints and Coatings*, ASME Turbo Expo 2014: Turbine Technical Conference and Exposition, (2014).

72. Lo, K.-H., Shek, C.-H., and Lai, J.K.-L., *Metallurgical temperature sensors,* Recent Patents on Mechanical Engineering, **1**(3) 225-232, (2008).

73. Fair, G.E., Kerans, R.J., and Parthasarathy, T.A., *Thermal history sensor based on glass-ceramics,* Sensors and Actuators A: Physical, **141**(2) 245-255, (2008).

74. Yokota, K., Kizaki, Y., Sakamoto, Y., and Motohiro, T., *Method and sensor for detecting thermal history*, US5975758 A, (1999).

75. Nicholls, J., *Advances in coating design for high-performance gas turbines,* MRS Bulletin, **28**(09) 659-670, (2003).

76. Martin, P.M., *Handbook of deposition technologies for films and coatings: science, applications and technology*. (William Andrew, 2009), 3rd ed.

77. Carter, C.B. and Norton, M.G., *Ceramic Materials: Science and Engineering*. (2013), 2nd ed.

78. Brinker, C.J. and Scherer, G.W., *Sol-gel science: the physics and chemistry of sol-gel processing*. (Gulf Professional Publishing, 1990).

79. Brinker, C.J., Frye, G.C., Hurd, A.J., and Ashley, C.S., *Fundamentals of sol-gel dip coating,* Thin Solid Films, **201**(1) 97-108, (1991).

80. Besra, L. and Liu, M., *A review on fundamentals and applications of electrophoretic deposition (EPD),* Progress in Materials Science, **52**(1) 1-61, (2007).

81. Horwood, R., *Towards a Better Understanding of Screen Print Thickness Control,* Active and Passive Electronic Components, **1**(2) 129-136, (1974).

82. Von Dollen, P. and Barnett, S., *A Study of Screen Printed Yttria-Stabilized Zirconia Layers for Solid Oxide Fuel Cells,* Journal of the American Ceramic Society, **88**(12) 3361-3368, (2005).

83. Zhang, Y., Huang, X., Lu, Z., Liu, Z., Ge, X., Xu, J., Xin, X., Sha, X., and Su, W., *A study of the process parameters for yttria-stabilized zirconia electrolyte films prepared by screen-printing,* Journal of Power Sources, **160**(2) 1065-1073, (2006).

84. Burgin, J., Jubera, V., Debéda, H., Glorieux, B., Garcia, A., and Lucat, C., *Screen-printed phosphor coatings for white LED emission,* Journal of Materials Science, **46**(7) 2235-2241, (2011).

85. Yu, S., Yang, L., Bin, C., Zheng, H., Chen, M., and Liu, S. *Development process of phosphor coating with screen printing for white LED packaging*, 12th International Conference on Electronic Packaging Technology and High Density Packaging (ICEPT-HDP), (2011).

86. Qiao, B., Tang, Z., Zhang, Z., and Chen, L., *Study on $ZnGa_2O_4:Cr^{3+}$ a.c. powder electroluminescent device,* Materials Letters, **61**(2) 401-404, (2007).

87. Moon, H., Kim, S.D., Hyun, S.H., and Kim, H.S., *Development of IT-SOFC unit cells with anode-supported thin electrolytes via tape casting and co-firing,* International Journal of Hydrogen Energy, **33**(6) 1758-1768, (2008).

88. Hotza, D. and Greil, P., *Review: aqueous tape casting of ceramic powders,* Materials Science and Engineering: A, **202**(1) 206-217, (1995).

89. Takahashi, S., *Longitudinal mode multilayer piezoceramic actuators,* Piezoelectricity, (5) 337, (1992).

90. Henderson, B. and Imbusch, G.F., *Optical spectroscopy of inorganic solids*. (Clarendon Press, Oxford, 1989).

91. Atkins, P. and De Paula, J., *Atkins' Physical Chemistry*. (Oxford University Press, 2006), 8th ed.

92. Shionoya, S. and Yen, W.M., *Phosphor handbook*. (CRC Press, 1999).

93. DeShazer, L. and Dieke, G., *Spectra and energy levels of Eu^{3+} in $LaCl_3$,* The Journal of Chemical Physics, **38**(9) 2190-2199, (1963).

94. Chambers, M. and Clarke, D., *Doped oxides for high-temperature luminescence and lifetime thermometry,* Annual Review of Materials Research, **39** 325-359, (2009).

95. Pilgrim, C., *Luminescence for the non-destructive evaluation of thermal barrier coatings*, PhD Thesis, Imperial College London, (2014).

96. Blasse, G. and Grabmaier, B.C., *Luminescent materials*. (Springer-Verlag, Berlin, 1994).

97. Verstegen, J., *A survey of a group of phosphors, based on hexagonal aluminate and gallate host lattices,* Journal of the Electrochemical Society, **121**(12) 1623-1627, (1974).

98. Verstegen, J., Radielović, D., and Vrenken, L.E., *A new generation of "deluxe" fluorescent lamps, combining an efficacy of 80 lumens/W or more with a color rendering index of approximately 85,* Journal of the Electrochemical Society, **121**(12) 1627-1631, (1974).

99. Oshio, S., Matsuoka, B., Tanaka, S., and Kobayashi, H., *Mechanism of luminance decrease in $BaMgAl_{10}O_{17}$:Eu^{2+} phosphor by oxidation,* Journal of the Electrochemical Society, **145**(11) 3903-3907, (1998).

100. Lacanilao, A., Wallez, G., Mazerolles, L., Dubot, P., Binet, L., Pavageau, B., Servant, L., Buissette, V., and Le Mercier, T., *Structural analysis of thermal degradation and regeneration in blue phosphor $BaMgAl_{10}O_{17}$:Eu^{2+} based upon cation diffusion,* Solid State Ionics, **253** 32-38, (2013).

101. Smets, B. and Verlijsdonk, J., *The luminescence properties of Eu^{2+}-and Mn^{2+}-doped barium hexaaluminates,* Materials Research Bulletin, **21**(11) 1305-1310, (1986).

102. Boolchand, P., Mishra, K., Raukas, M., Ellens, A., and Schmidt, P., *Occupancy and site distribution of europium in barium magnesium aluminate by ^{151}Eu Mössbauer spectroscopy,* Physical Review B, **66**(13) 134429, (2002).

103. Dunn, B. and Farrington, G., *Fast divalent ion conduction in Ba^{++}, Cd^{++} and Sr^{++} beta" aluminas,* Materials Research Bulletin, **15**(12) 1773-1777, (1980).

104. Ellens, A., Zwaschka, F., Kummer, F., Meijerink, A., Raukas, M., and Mishra, K., *Sm^{2+} in BAM: fluorescent probe for the number of luminescing sites of Eu^{2+} in BAM,* Journal of Luminescence, **93**(2) 147-153, (2001).

105. Pike, V., Patraw, S., Diaz, A.L., and Deboer, B.G., *Defect chemistry and VUV optical properties of the BaMgAl$_{10}$O$_{17}$:Eu^{2+}-Ba$_{0.75}$Al$_{11}$O$_{17.25}$:Eu^{2+} solid solution,* Journal of Solid State Chemistry France, **173** 359-366, (2003).

106. Lambert, J., Wallez, G., Quarton, M., Le Mercier, T., and van Beek, W., *Searching for the dopant ion in Eu^{2+}-activated BaMgAl$_{10}$O$_{17}$ phosphor with synchrotron diffraction,* Journal of Luminescence, **128**(3) 366-372, (2008).

107. Zhu, P.F., Di, W.H., Zhu, Q.R., Chen, B.J., Zhu, H.Y., Zhao, H.F., Yang, Y.J., and Wang, X.J., *Luminescent properties and thermal stability of BaMgAl$_{10}$O$_{17}$:Eu^{2+} synthesized by sol-gel route,* Journal of Alloys and Compounds, **454**(1-2) 245-249, (2008).

108. Wu, Z. and Cormack, A., *Defects in BaMgAl$_{10}$O$_{17}$:Eu^{2+} blue phosphor,* Journal of Electroceramics, **10**(3) 179-191, (2003).

109. Zhang, S.X., Kono, T., Ito, A., Yasaka, T., and Uchiike, H., *Degradation mechanisms of the blue-emitting phosphor BaMgAl$_{10}$O$_{17}$:Eu^{2+} under baking and VUV-irradiating treatments,* Journal of Luminescence, **106**(1) 39-46, (2004).

110. Howe, B. and Diaz, A.L., *Characterization of host-lattice emission and energy transfer in BaMgAl$_{10}$O$_{17}$:Eu^{2+},* Journal of luminescence, **109**(1) 51-59, (2004).

111. Kim, K.B., Koo, K.W., Cho, T.Y., and Chun, H.G., *Effect of heat treatment on photoluminescence behavior of BaMgAl$_{10}$O$_{17}$:Eu phosphors,* Materials Chemistry and Physics, **80**(3) 682-689, (2003).

112. Sohn, K.S., Kim, S.S., and Park, H.D., *Luminescence quenching in thermally-treated barium magnesium aluminate phosphor,* Applied Physics Letters, **81**(10) 1759-1761, (2002).

113. Yamada, H., Shi, W.S., and Xu, C.N., *Lattice deformation in thermally degraded barium magnesium aluminate phosphor,* Journal of the Electrochemical Society, **151**(12) E349-E351, (2004).

114. Bizarri, G. and Moine, B., *On BaMgAl$_{10}$O$_{17}$:Eu^{2+} phosphor degradation mechanism: thermal treatment effects,* Journal of Luminescence, **113**(3-4) 199-213, (2005).

115. Kim, Y. and Kang, S., *Investigation of the degradation mechanisms in BaMgAl$_{10}$O$_{17}$:Eu^{2+} phosphor: on the influence of thermal process on operational durability,* Applied Physics B-Lasers and Optics, **98**(2-3) 429-434, (2010).

116. Liu, B.T., Wang, Y.H., Wang, Z.F., Zhou, J., and Gao, X.L., *Photoluminescence Properties and Degradation Mechanisms of BaMgAl$_{10}$O$_{17}$:Eu^{2+} Phosphor under Baking Treatment,* Electrochemical and Solid State Letters, **13**(3) J15-J17, (2010).

117. Mishra, K., Raukas, M., Marking, G., Chen, P., and Boolchand, P., *Investigation of fluorescence degradation mechanism of hydrated BaMgAl$_{10}$O$_{17}$:Eu^{2+} phosphor,* Journal of The Electrochemical Society, **152**(11) H183-H190, (2005).

118. Mishra, K.C., Johnson, K.H., and Schmidt, P.C., *Theoretical investigation of intercalated water molecules and hydroxyl groups in BAM ($BaMgAl_{10}O_{17}:Eu^{2+}$) phosphor and associated degradation processes,* Journal of the Electrochemical Society, **153**(11) H202-H208, (2006).

119. Wang, Y.H. and Zhang, Z.H., *Luminescence thermal degradation mechanism in $BaMgAl_{10}O_{17}:Eu^{2+}$ phosphor,* Electrochemical and Solid-State Letters, **8**(11) H97-H99, (2005).

120. Zhang, Z.H., Wang, Y.H., Li, X.X., Du, Y.K., and Liu, W.J., *Photoluminescence degradation and color shift studies of annealed $BaMgAl_{10}O_{17}:Eu^{2+}$ phosphor,* Journal of Luminescence, **122** 1003-1005, (2007).

121. Mishra, K., Raukas, M., Ellens, A., and Johnson, K., *A scattered wave model of electronic structure of Eu^{2+} in $BaMgAl_{10}O_{17}$ and associated excitation processes,* Journal of Luminescence, **96**(2) 95-105, (2002).

122. Yoshida, H., Yamazaki, T., Toyoshima, H., Watanabe, S., Ogasawara, K., and Yamamoto, H., *Experimental and Theoretical Investigations for Excitation Properties of $Ba_{1-x}Eu_xMgAl_{10}O_{17}$,* Journal of The Electrochemical Society, **154**(7) J196-J200, (2007).

123. Zych, E., Goetz, W., Harrit, N., and Spanggaard, H., *Spectroscopic properties of sintered $BaMgAl_{10}O_{17}:Eu^{2+}$ (BAM) translucent pellets: Comparison to the commercial powder,* Journal of alloys and compounds, **380**(1) 113-117, (2004).

124. Kim, K.-B., Kim, Y.-I., Chun, H.-G., Cho, T.-Y., Jung, J.-S., and Kang, J.-G., *Structural and optical properties of $BaMgAl_{10}O_{17}:Eu^{2+}$ phosphor,* Chemistry of Materials, **14**(12) 5045-5052, (2002).

125. Sarner, G., Richter, M., and Alden, M., *Investigations of blue emitting phosphors for thermometry,* Measurement Science & Technology, **19**(12), (2008).

126. Fond, B., *Simultaneous temperature and velocity imaging in turbulent flows using thermographic phosphor tracer particles*, PhD Thesis, Imperial College London, (2014).

127. Lakshmanan, A., *The Role of Sintering in the Synthesis of Luminescence Phosphors*, *Sintering of Ceramics - New Emerging Techniques*, Chapter 15, (D.A. Lakshmanan), (2012).

128. Liu, B., Wang, Y., Zhou, J., Zhang, F., and Wang, Z., *The reduction of Eu^{3+} to Eu^{2+} in $BaMgAl_{10}O_{17}:Eu$ and the photoluminescence properties of $BaMgAl_{10}O_{17}:Eu^{2+}$ phosphor,* Journal of Applied Physics, **106**(5), (2009).

129. Lu, C.H., Chen, C.T., and Bhattacharjee, B., *Sol-gel preparation and luminescence properties of $BaMgAl_{10}O_{17}:Eu^{2+}$ phosphors,* Journal of Rare Earths, **24**(6) 706-711, (2006).

130. Sharma, P.K., Dutta, R.K., and Pandey, A.C., *Performance of YAG:Eu^{3+}, YAG:Tb^{3+} and BAM:Eu^{2+} plasma display nanophosphors,* Journal of Nanoparticle Research, **14**(3), (2012).

131. Lu, C.H., Hsu, W.T., Huang, C.H., Godbole, S., and Cheng, B.M., *Luminescence characteristics of europium-ion doped BaMgAl$_{10}$O$_{17}$ phosphors prepared via a sol–gel route employing polymerizing agents,* Materials Chemistry and Physics, **90**(1) 62-68, (2005).

132. Jung, K.Y., Lee, D.Y., Kang, Y.C., and Park, S.B., *Size-dependent luminescent properties of hollow and dense BaMgAl$_{10}$O$_{17}$:Eu blue phosphor particles prepared by spray pyrolysis,* Korean Journal of Chemical Engineering, **21**(5) 1072-1080, (2004).

133. Ekambaram, S. and Patil, K., *Synthesis and properties of Eu^{2+} activated blue phosphors,* Journal of Alloys and Compounds, **248**(1) 7-12, (1997).

134. Park, S. and Kang, S., *Combustion synthesis of Eu^{2+}-activated BaMgAl$_{10}$O$_{17}$ phosphor,* Journal of Materials Science: Materials in Electronics, **14**(4) 223-228, (2003).

135. Golego, N., Studenikin, S.A., and Cocivera, M., *Thin-film BaMgAl$_{10}$O$_{17}$:Eu phosphor prepared by spray pyrolysis,* Journal of the Electrochemical Society, **147**(5) 1993-1996, (2000).

136. Sohn, K.S., Cho, S.H., Kulshreshtha, C., and Shin, N., *Preparation of blue emitting BaMgAl$_{10}$O$_{17}$:Eu^{2+} thin-film phosphors by pulsed laser deposition,* Electrochemical and Solid-State Letters, **9**(12) 115-117, (2006).

137. Linden, J., Knappe, C., Richter, M., and Alden, M., *Precision in 2D temperature measurements using the thermographic phosphor BAM,* Measurement Science & Technology, **23**(8), (2012).

138. Wu, Z., Dong, Y., and Jiang, J., *Thermal treatment effects on degradation of BaMgAl$_{10}$O$_{17}$:Eu^{2+} phosphor for PDP,* Materials Science and Engineering: B, **150**(3) 151-156, (2008).

139. Hamamatsu-Photonics, *Characteristics and use of FFT-CCD area image sensor. Technical information SD-25*, (2003).

140. Hamamatsu-Photonics, *Photomultiplier tubes - Basics and applications*, (2006).

141. Knappe, C., Abou Nada, F., Richter, M., and Alden, M., *Comparison of photo detectors and operating conditions for decay time determination in phosphor thermometry,* Review of Scientific Instruments, **83**(9) 094901, (2012).

142. Knappe, C., Linden, J., Abou Nada, F., Richter, M., and Alden, M., *Investigation and compensation of the nonlinear response in photomultiplier tubes for quantitative single-shot measurements,* Review of Scientific Instruments, **83**(3), (2012).

143. Seefeldt, S., *Development of phosphor thermometry with application to film cooling in gas turbines*, PhD Thesis, University of London, (2005).

144. Brubach, J., Janicka, J., and Dreizler, A., *An algorithm for the characterisation of multi-exponential decay curves,* Optics and Lasers in Engineering, **47**(1) 75-79, (2009).

145. Fuhrmann, N., Brübach, J., and Dreizler, A., *Spectral decomposition of phosphorescence decays,* Review of Scientific Instruments, **84**(11) 114902, (2013).

146. Newbury, D.E., Joy, D.C., Echlin, P., Fiori, C.E., and Goldstein, J.I., *Scanning electron microscopy and X-ray microanalysis*. (Springer, 2003).

147. Mehta, R., *Interactions, Imaging and Spectra in SEM, Scanning Electron Microscopy*, (D.V. Kazmiruk), (2012).

148. *Quantitative EDS X-ray microanalysis using SEM*. Web. 7 May 2015; Available from: http://www.ammrf.org.au/myscope/analysis/eds/.

149. Langford, J. and Wilson, A., *Scherrer after sixty years: a survey and some new results in the determination of crystallite size,* Journal of Applied Crystallography, **11**(2) 102-113, (1978).

150. Scardi, P., Leoni, M., and Delhez, R., *Line broadening analysis using integral breadth methods: a critical review,* Journal of Applied Crystallography, **37**(3) 381-390, (2004).

151. Hall, W., *X-ray line broadening in metals,* Proceedings of the Physical Society. Section A, **62**(11) 741, (1949).

152. Williamson, G. and Hall, W., *X-ray line broadening from filed aluminium and wolfram,* Acta Metallurgica, **1**(1) 22-31, (1953).

153. James, J., Spittle, J., Brown, S., and Evans, R., *A review of measurement techniques for the thermal expansion coefficient of metals and alloys at elevated temperatures,* Measurement Science and Technology, **12**(3) R1, (2001).

154. Hayashi, H., Saitou, T., Maruyama, N., Inaba, H., Kawamura, K., and Mori, M., *Thermal expansion coefficient of yttria stabilized zirconia for various yttria contents,* Solid State Ionics, **176**(5) 613-619, (2005).

155. Tietz, F., *Thermal expansion of SOFC materials,* Ionics, **5**(1-2) 129-139, (1999).

156. Engberg, C.J. and Zehms, E.H., *Thermal Expansion of Al_2O_3, BeO, MgO, B_4C, SiC, and TiC Above 1000 °C,* Journal of the American Ceramic Society, **42**(6) 300-305, (1959).

157. Coats, A. and Redfern, J., *Thermogravimetric analysis. A review,* Analyst, **88**(1053) 906-924, (1963).

158. Montgomery, K., *Type N versus type K thermocouple comparison in a brick kiln,* Temperature: its Measurement and Control in Science and Industry, **6** 601-5, (1992).

159.   Schmechel, R., Kennedy, M., Von Seggern, H., Winkler, H., Kolbe, M., Fischer, R., Xaomao, L., Benker, A., Winterer, M., and Hahn, H., *Luminescence properties of nanocrystalline Y_2O_3:Eu^{3+} in different host materials,* Journal of Applied Physics, **89**(3) 1679-1686, (2001).

160.   Suzuki, H., Iseki, T., and Maruyama, T., *Study of the Cubic‑to‑Monoclinic Transformation in Eu_2O_3,* Journal of the American Ceramic Society, **59**(9-10) 451-451, (1976).

161.   Weinberg, M.C., Birnie, D.P., and Shneidman, V.A., *Crystallization kinetics and the JMAK equation,* Journal of Non-Crystalline Solids, **219** 89-99, (1997).

162.   Ruitenberg, G., Woldt, E., and Petford-Long, A., *Comparing the Johnson–Mehl–Avrami–Kolmogorov equations for isothermal and linear heating conditions,* Thermochimica Acta, **378**(1) 97-105, (2001).

163.   Christian, J.W., *The theory of transformations in metals and alloys*. (Newnes, 2002).

164.   Kohout, J., *An alternative to the JMAK equation for a better description of phase transformation kinetics,* Journal of Materials Science, **43**(4) 1334-1339, (2008).

165.   De Leeuw, D. and Hooft, G.t., *Method for the analysis of saturation effects of cathodoluminescence in phosphors; applied to Zn_2SiO_4:Mn and $Y_3Al_5O_{12}$:Tb,* Journal of Luminescence, **28**(3) 275-300, (1983).

166.   Brubach, J., Feist, J.P., and Dreizler, A., *Characterization of manganese-activated magnesium fluorogermanate with regards to thermographic phosphor thermometry,* Measurement Science and Technology, **19**(2) 025602, (2008).

167.   Hirosawa, I., Honma, T., Kato, K., Kijima, N., and Shimomura, Y., *Oxidation of doped europium in $BaMgAl_{10}O_{17}$ by annealing studied by x‑ray‑absorption fine‑structure measurements,* Journal of the Society for Information Display, **12**(3) 269-273, (2004).

168.   Kurz, R. *Gas turbine performance*, Proceedings of the Thirty-Fourth Turbomachinery Symposium, Houston, TX, (2005).

169.   Zyp-Coatings, *Personal communication*, (2015).

170.   Jones, R., *Scandia-stabilized zirconia for resistance to molten vanadate-sulfate corrosion,* Surface and Coatings Technology, **39** 89-96, (1989).

171.   Ruiz-Trejo, E., *Personal communication*, (2014).

172.   Chen, Y., Orlovskaya, N., Klimov, M., Huang, X., Cullen, D., Graule, T., and Kuebler, J., *Layered YSZ/SCSZ/YSZ electrolytes for intermediate temperature SOFC Part I: design and manufacturing,* Fuel Cells, **12**(5) 722-731, (2012).

173.   Yang, P., Yao, G.-Q., and Lin, J.-H., *Energy transfer and photoluminescence of $BaMgAl_{10}O_{17}$ co-doped with Eu^{2+} and Mn^{2+},* Optical Materials, **26**(3) 327-331, (2004).

174. Chao, C.-C., *Charge-transfer luminescence of Cr^{3+} in magnesium oxide,* Journal of Physics and Chemistry of Solids, **32**(11) 2517-2528, (1971).

175. Wojtowicz, A., *Luminescence of Cr^{3+} in kyanite,* Journal of Luminescence, **50**(4) 221-230, (1991).

176. Pott, G. and McNicol, B., *Zero-Phonon Transition and Fine Structure in the Phosphorescence of Fe^{3+} Ions in Ordered and Disordered $LiAl_5O_8$,* The Journal of Chemical Physics, **56**(11) 5246-5254, (1972).

177. Shannon, R., *Revised effective ionic radii and systematic studies of interatomic distances in halides and chalcogenides,* Acta Crystallographica Section A: Crystal Physics, Diffraction, Theoretical and General Crystallography, **32**(5) 751-767, (1976).

178. Sollazzo, P.Y., Pilgrim, C., Feist, J.P., and Nicholls, J.R., *Operation of a Burner rig for thermal gradient Cycling of Thermal Barrier Coatings,* Paper No. GT2014-26325, Proceedings of the ASME Turbo Expo, Düsseldorf, Germany, (2014).

179. Plyler, E.K. and Humphreys, C., *Infrared Emission Spectra of Flames,* Journal of Research of the National Bureau of Standards, **40**(6) 449-456, (1948).

180. Bipm, IEC, IFcc, IsO, IuPAc, and IUPAP, *OIML, Guide to the Expression of Uncertainty in Measurement,* International Organization for Standardization, Geneva. ISBN, 92-67, (1995).

181. Feist, J., Sollazzo, P., Berthier, S., Charnley, B., and Wells, J., *Application of an Industrial Sensor Coating System on a Rolls-Royce Jet Engine for Temperature Detection,* The 6th Gas Turbine Conference, Gas Turbines in the Markets of Tomorrow, The Institution of Diesel and Gas Turbine Engineers, **Volume: 1**, (2011).

182. Debout, V., Vardelle, A., Abelard, P., Fauchais, P., Meillot, E., Bruneton, E., Enguehard, F., and Schelz, S., *Investigation of in-flight particle characteristics and microstructural effects on optical properties of YSZ plasma-sprayed coatings,* High Temperature Material Processes: An International Quarterly of High-Technology Plasma Processes, **11**(3), (2007).

183. *International vocabulary of basic and general terms in metrology (VIM),* International Organization, **2004** 09-14, (2004).

APPENDIX

Permissions for third party copyright

Page number	Type of work	Reference	Copyright holder	Permission
25	Figure	[12]	Elsevier	X
34	Figure	[64]	IOP Publishing	X
45	Figure	[81]	Hindawi Publishing Corporation	X
55	Figure	[94]	Annual Reviews	X
68	Figure	[102]	American Physical Society	X
72	Figure	[110]	Elsevier	X
74	Figure	[126]	Benoit Fond	X
179 - 186	Full paper	[2]	ASME	X

Evidence of permission for re-use of figure in [12]:

ELSEVIER LICENSE
TERMS AND CONDITIONS

Jun 02, 2015

This is a License Agreement between Alvaro Yanez ("You") and Elsevier ("Elsevier") provided by Copyright Clearance Center ("CCC"). The license consists of your order details, the terms and conditions provided by Elsevier, and the payment terms and conditions.

All payments must be made in full to CCC. For payment instructions, please see information listed at the bottom of this form.

Supplier	Elsevier Limited The Boulevard,Langford Lane Kidlington,Oxford,OX5 1GB,UK
Registered Company Number	1982084
Customer name	Alvaro Yanez
Customer address	City and Guild Building
	London, SW7 2AZ
License number	3640731133324
License date	Jun 02, 2015
Licensed content publisher	Elsevier
Licensed content publication	Elsevier Books
Licensed content title	Gas Turbine Engineering Handbook
Licensed content author	Meherwan P. Boyce
Licensed content date	2012
Number of pages	22
Start Page	493
End Page	514
Type of Use	reuse in a thesis/dissertation
Portion	figures/tables/illustrations
Number of figures/tables /illustrations	1
Format	both print and electronic
Are you the author of this Elsevier chapter?	No
Will you be translating?	No
Original figure numbers	Figure 11-2 Firing temperature increase with blade material improvement.
Title of your thesis/dissertation	Phosphorescent thermal history sensors for extreme environments
Expected completion date	Sep 2015
Estimated size (number of pages)	210
Elsevier VAT number	GB 494 6272 12
Permissions price	0.00 GBP

Evidence of permission for re-use of figure in [64]:

Dear Dr Yanez Gonzalez,

Thank you for your request to reproduce IOP Publishing material in your thesis.

Regarding:

Figure 1 (Meas. Sci. Technol. 19 (2008) 105501 (11pp))

We are happy to grant permission for the use you request on the terms set out below.

Conditions

Non-exclusive, non-transferrable, revocable, worldwide, permission to use the material in print and electronic form will be granted **subject to the following conditions:**

- Permission will be cancelled without notice if you fail to fulfil any of the conditions of this letter.

- You will make reasonable efforts to contact the author(s) to seek consent for your intended use. Contacting one author acting expressly as authorised agent for their co-authors is acceptable.

- You will reproduce the following prominently alongside the material:

o the source of the material, including author, article title, title of journal, volume number, issue number (if relevant), page range (or first page if this is the only information available) and date of first publication. This information can be contained in a footnote or reference note; or

o a link back to the article (via DOI); and

o if practical and IN ALL CASES for works published under any of the Creative Commons licences the words "© IOP Publishing. Reproduced with permission. All rights reserved""

- The material will not, without the express permission of the author(s), be used in any way which, in the opinion of IOP Publishing, could distort or alter the author(s)' original intention(s) and meaning, be prejudicial to the honour or reputation of the author(s) and/or imply endorsement by the author(s) and/or IOP Publishing.

- Payment of £0 is received in full by IOP Publishing prior to use.

Evidence of permission for re-use of figure in [81]:

▤ Abstract

🄰 Full-Text PDF

🄱 Citations to this Article

? How to Cite this Article

Towards a Better Understanding of Screen Print Thickness Control

R. J. Horwood

Electronic Technology Department, British Aircraft Corporation Ltd., Guided Weapons Division, GPO Box 77, Filton House, Bristol BS99 7AR, UK

Evidence of permission for re-use of figure in [94]:

Evidence of permission for re-use of figure in [102]:

American Physical Society
License Details

Aug 26, 2015

This is an Agreement between Alvaro Yanez ("You") and American Physical Society ("Publisher"). It consists of your order details, the terms and conditions provided by American Physical Society, and the payment instructions.

License Number	3682551157243
License date	Aug 05, 2015
Licensed Content Publisher	American Physical Society
Licensed Content Publication	Physical Review B
Licensed Content Title	Occupancy and site distribution of europium in barium magnesium aluminate by $\{\}^{151}\mathrm{Eu}$ M\"ossbauer spectroscopy
Licensed copyright line	Copyright © 2002, American Physical Society
Licensed Content Author	P. Boolchand et al.
Licensed Content Date	Oct 31, 2002
Volume number	66
I would like to...	Thesis/Dissertation
Requestor type	Student
Format	Print, Electronic
Portion	chart/graph/table/figure
Number of charts/graphs /tables/figures	1
Portion description	Figure 1
Rights for	Main product
Duration of use	Life of current edition
Creation of copies for the disabled	no
With minor editing privileges	no
For distribution to	Worldwide
In the following language(s)	Original language of publication
With incidental promotional use	no
The lifetime unit quantity of new product	0 to 499
The requesting person/organization is:	Alvaro Yanez Gonzalez
Order reference number	None
Title of your thesis / dissertation	Phosphorescent thermal history sensors for extreme environments
Expected completion date	Sep 2015
Expected size (number of pages)	210
Total	**0.00 GBP**

Evidence of permission for re-use of figure in [110]:

**ELSEVIER LICENSE
TERMS AND CONDITIONS**

Jul 30, 2015

This is a License Agreement between Alvaro Yanez ("You") and Elsevier ("Elsevier") provided by Copyright Clearance Center ("CCC"). The license consists of your order details, the terms and conditions provided by Elsevier, and the payment terms and conditions.

All payments must be made in full to CCC. For payment instructions, please see information listed at the bottom of this form.

Supplier	Elsevier Limited The Boulevard,Langford Lane Kidlington,Oxford,OX5 1GB,UK
Registered Company Number	1982084
Customer name	Alvaro Yanez
Customer address	City and Guild Building
	London, SW7 2AZ
License number	3678790847553
License date	Jul 30, 2015
Licensed content publisher	Elsevier
Licensed content publication	Journal of Luminescence
Licensed content title	Characterization of host-lattice emission and energy transfer in BaMgAl10O17:Eu2+
Licensed content author	Brandon Howe,Anthony L. Diaz
Licensed content date	July 2004
Licensed content volume number	109
Licensed content issue number	1
Number of pages	9
Start Page	51
End Page	59
Type of Use	reuse in a thesis/dissertation
Intended publisher of new work	other
Portion	figures/tables/illustrations
Number of figures/tables /illustrations	1
Format	both print and electronic
Are you the author of this Elsevier article?	No
Will you be translating?	No
Original figure numbers	Figure 1
Title of your thesis/dissertation	Phosphorescent thermal history sensors for extreme environments

Expected completion date	Sep 2015
Estimated size (number of pages)	210
Elsevier VAT number	GB 494 6272 12
Permissions price	0.00 GBP
VAT/Local Sales Tax	0.00 GBP / 0.00 GBP
Total	0.00 GBP

Evidence of permission for re-use of figure in [126]:

Dear Alvaro,
It is my pleasure to grant you permission to use this figure in your dissertation.
Regards,
Benoit

On 31 Jul 2015, at 16:45, Yañez Gonzalez, Alvaro wrote:

Dear Dr Fond,

I would like to re-use Figure 3.7 of your PhD thesis entitled "Simultaneous temperature and velocity imaging in turbulent flows using thermographic phosphor tracer particles" in my PhD thesis entitled "Phosphorescent thermal history sensors for extreme environments" to be submitted at Imperial College London on September 2015.

Thank you for your cooperation,

Alvaro Yanez

Evidence of permission for re-use of figure in [2]:

Dear Mr. Gonzalez,
It is our pleasure to grant you permission to use **all or any part of** the ASME paper "On-Line Temperature Measurement Inside a Thermal Barrier Sensor Coating During Engine Operation," by A. Yañez Gonzalez; C. C. Pilgrim; J. P. Feist; P. Y. Sollazzo; F. Beyrau; A. L. Heyes, J. Turbomach. 2015; 137(10), cited in your letter for inclusion in a PhD thesis entitled Phosphorescent thermal history sensors for extreme environments to be published by Imperial College London.

Permission is granted for the specific use as stated herein and does not permit further use of the materials without proper authorization. Proper attribution must be made to the author(s) of the materials.   **Please note**: if any or all of the figures and/or Tables are of another source, permission should be granted from that outside source or include the reference of the original source. ASME does not grant permission for outside source material that may be referenced in the ASME works.

As is customary, we request that you ensure full acknowledgment of this material, the author(s), source and ASME as original publisher. Acknowledgment must be retained on all pages printed and distributed.
Many thanks for your interest in ASME publications.

Sincerely,

Beth Darchi
Publishing Administrator
ASME
2 Park Avenue, 6th Floor
New York, NY 10016-5990
Tel 1.212.591.7700
darchib@asme.org